THE DEVELOPING OF A SMART ELBOW PROSTHESIS FOR LOOSENING DETECTION

MUHAMMAD MOID KHALID KHAN

Doctor of Philosophy

ASTON UNIVERSITY

July 2021

Aston University

DEVELOPING OF A SMART ELBOW PROSTHESIS FOR LOOSENING DETECTION

Muhammad Moid Khalid Khan

Doctor of Philosophy

2021

Abstract

Total Elbow Arthroplasty (TEA) is an effective surgical procedure for restoring elbow joint function and improve a patient's quality of life by relieving pain suffered from various musculoskeletal disorders. Despite new designs for prostheses and improved surgical procedures, TEA still suffers today from mid-to-long-term complications such as aseptic loosening, infection, dislocation, and pre-prosthetic fractures. With aseptic loosening followed by infection being the most persistent reason for TEA revision, investigating methods for early diagnosis of implant loosening and differentiating between the infection and aseptic loosening is necessary to address this problem. This thesis aims to develop a novel diagnostic tool that can be embedded into the prosthetic and provide a quantitative measurement for early signs of the implant loosening without any usage of radiographs or any contact with the implant.

In this study, three types of sensor configurations along with detection algorithms were developed, designed, and tested along with a functional prototype to detect the migration of the elbow prosthesis (Aseptic loosening). The detection system was validated under realistic conditions through experiments with a custom-designed mechanical testing rig. Finally, for infection detection, a biocompatible chemical sensor (Hydrogel) was synthesised and was linked with the aseptic loosening detection system to investigate the early signs of infection. Among the three sensor configurations, the single sensor configuration detected the implant migration at a resolution of 0.3 mm with a detection error of less than 3 %. The configuration was able to detect angular motion up to 3 degrees with a detection error of 5 %. The quad sensor configuration, an arrangement of four closely packed sensors, enhanced the overall detection performance by increasing system resolution to 0.15 mm in multiple axes along with increasing the signal to noise ratio, reducing root mean square error, and compensating the tilt effect of the single sensor. While the dual sensor configuration, two sensors arranged in-line but 42 mm apart, downgraded the detection performance by introducing a detection error of 30 %. The detection system showed negligible effect on the biomaterial used in TEA and was able to differentiate between different migrations types (Linear, Angular, Static and Dynamic). The difference in three fixation scenarios (grossly loose, partially loose, and fully fixed) was identified evidently by the detection system with the grossly loose fixation showed a displacement of 0.187 ± 0.061 mm on the x-axis and 0.387 ± 0.059 mm on the y-axis. The chemical sensor (Hydrogel) was able to detect the change in its surrounding pH level (highlighting the potential to detect infection) and by the amalgamation with the detection system, pH change was detected without the use of an imaging technique. Further improvement in the synthesis of the hydrogel and the optimisation of the detection system has also been suggested.

The quad sensor system implies that it has the potential to be used to continually or intermittently monitor implant behaviour without hospital visitation or x-ray exposure. This could be applied more widely to other major joints such as the hips and knees, giving in-situ biomechanical insight into joint replacement behaviour over time.

Acknowledgments

Above all else, all praise and acknowledgment goes to Almighty Allah my creator, for his blessing all through my entire career to accomplish my goals.

During this research journey, many people deserve my thanks, firstly to my father Dr. Muhammad Khalid Khan, and my mother Goher Khalid for their unending support and help at every stage of the Ph.D. and for sending their prayers and love all the way from home.

I am immensely grateful to my mentor and supervisor Dr. Sarah Junaid for her consistent gaudiness, trust, ideas, and knowledge during the entire course of this project. Without this help, this work would not have been possible. I offer my profound gratitude to my second supervisor Dr. Laura Leslie for her support, guidance, and patience.

I would like to thank my clinical supervisor Dr. Subodh Deshmukh and Dr. Kanthan Theivendran for bringing this project and explaining the clinical perspective of this work.

I acknowledge and thank Dr. Anisa Mahmood, for training me on how to synthesis hydrogels and helping in writing and securing an AIMR Seed Corn grant application.

I acknowledge and thank Luke Southan for supporting and trusting my research and helping in securing the Innovate UK ICURe grant, along with introducing me to the commercial aspect of the research.

Finally, thanks to my colleagues and friends for all the good times and support.

List of Publications

This research led to the filling of a GB patent in April 2020. This is being further pursued the commercialisation.

- **Muhammad Moid Khalid Khan**, Subodh Deshmukh, Kanthan Theivendran, Laura J Leslie, Sarah Junaid, 'System and Method for Tracking Migration of a Structure'. **Submitted**

The research output of the work is being presented in the following conference and journal publications along with various national and international podium/poster presentations.

- **Muhammad Moid Khalid Khan**, Subodh Deshmukh, Kanthan Theivendran, Laura J Leslie, Sarah Junaid, "A New Diagnostic Technique to Detect Early Migration of Elbow Prostheses", IEEE Access, DOI: 10.1109/ACCESS.2021.3049170.

- **Muhammad Moid Khalid Khan**, Subodh Deshmukh, Kanthan Theivendran, Laura J Leslie, Sarah Junaid, "Implantable Sensors for Non-Radiographic Micro-Motion Detection in Joint Prostheses", IEEE Sensors, Under Review.

- **Muhammad Moid Khalid Khan**, Subodh Deshmukh, Kanthan Theivendran, Laura J Leslie, Sarah Junaid, "Loosening of Elbow Prostheses- A review of complications and current diagnostic tools used to detect loosening" Journal of Arthroplasty, Under Review

- 2nd February – 5th February 2019, Orthopaedic Research Society 2019 Annual Meeting, Austin, Texas, USA, **Muhammad Moid Khalid Khan**, Subodh Deshmukh, Kanthan Theivendran, Laura J Leslie, Sarah Junaid, 'Detection of Loosening of the Humeral Component of Elbow Prosthesis'.

- 8th February – 11th February 2020, Orthopaedic Research Society 2020 Annual Meeting, Phoenix, Arizona, USA, **Muhammad Moid Khalid Khan**, Subodh Deshmukh, Kanthan Theivendran, Laura J Leslie, Sarah Junaid, 'Non-Invasive, Non-radiographic Technique for Detecting Micro-Motion in Total Joint Replacement Loosening'.

- 7th July – 10th July 2019, 25th Congress of the European Society of Biomechanics, Vienna, Austria, **Muhammad Moid Khalid Khan**, Subodh Deshmukh, Kanthan Theivendran, Laura J Leslie, Sarah Junaid, 'Development of a Diagnostic Tool for Detecting Aseptic Loosening of Elbow Prosthesis'.

- 6th September – 7th September 2018, BioMedEng18 Conference, Imperial College London, United Kingdom, **Muhammad Moid Khalid Khan**, Subodh Deshmukh, Kanthan Theivendran, Laura J Leslie, Sarah Junaid, 'Development of Smart Elbow Prosthesis'.

Table of Contents

List of Abbreviations

TEA	Total elbow arthroplasty
UHMWPE	Ultra high molecular weight polyethylene
PMMA	Polymethylmethacrylate
Ti	Titanium Alloy
JRF	Joint reaction force
RSA	Radiostereometric analysis
Bx	Magnetic Field in x-axis
By	Magnetic Field in y-axis
Bz	Magnetic Field in z- axis
Z-Distance	Distance between sensor and magnet
PCB	Printed circuit board
SDA	Serial data pin
SCL	Serial clock pin
S.Golay	Savitzky Golay
WT	Wavelet Transform
SNR	Signal to noise ratio
RMS	Root mean square error

List of Tables

List of Figures

Chapter 1

Introduction and Outline of the Thesis

1.1 Introduction

The human elbow joint is a complex structural joint that provides a mechanical link between the upper extremity i.e., the shoulder, and wrist and has evolved into a mechanism capable of achieving a large range of motion to perform highly complex tasks. When impaired from this function, it may restrict its performance in doing simple daily tasks and may also lead to severe disability. Loss of elbow motion is considered more disabling than the loss of shoulder and wrist movement since normal elbow function is required for positioning the hand in space, which is crucial in the performance of daily life activities [1].

The elbow joint can perform two different types of motion namely flexion-extension and pronation-supination. Under normal conditions, the human elbow functional arc for flexion-extension motion ranges from 30 to 130 degrees and for pronation-supination 50 to -50 degrees [2]. Medication and physiotherapy are primarily used to relieve pain and improve range of motion when the elbow joint suffers from any complication but if a range of the motion is less than 100 degrees for flexion-extension then surgical intervention will be needed because the loss of 50% of the elbow mobility represents the loss of 80% of upper limb function [2]. In such a scenario total elbow arthroplasty (TEA) is an appropriate treatment for relieving pain and improving range of motion.

Joint arthroplasty is becoming the widely performed solution for the elbow pathologies, in which a part of, or entire elbow joint is replaced by a prosthetic/implant. The aim of these prosthetics is primarily to relieve pain and restore the elbow's functionality. The development of this surgical procedure was mainly for the treatment of rheumatoid arthritis and tuberculosis arthritis. At the end of the nineteenth century and the beginning of the twenty century, the main causal factor for this joint replacement was tuberculosis. With the introduction of effective antibiotics drugs tuberculosis, arthritis decreased considerably and the only primary cause for the elbow joint replacement was osteoarthritis 2% and

rheumatoid arthritis 20-60% [3]. In recent decades, the trend has changed due to the utilisation of disease-modified anti-rheumatoid drugs[4] which has decreased the number of elbow arthroplasty cases affected by rheumatoid arthritis. According to the National Scottish autoplastic registry, Norwegian Arthroplasty registry and the State wide Planning and Research Cooperative System (SPARCS) database from New York shows that the trend of TEA affected by rheumatoid arthritis has decreased and a concomitant increase is seen in arthroplasty for trauma cases [5-7]. In the last decade, the usage of elbow arthroplasty to treat acute trauma cases has increased.

To understand the functionality of elbow implants, a brief insight into the human elbow anatomy, elbow pathology, and treatment is due:

1.1.1 Human Elbow Joint

The human elbow (cubital joint or synovial hinge joint) is fundamental to daily activities. In the human elbow, three bony parts meet; the humerus (long bone), radius (smaller bone), and ulna (medial bone) as shown in figure 1.1 [8]. The elbow joint consists of three articulations i.e. humero-ulnar, humero-radial, and proximal radioulnar highlighted in figure 1.1. The former articulation is the result of joining the humeral condyle and semilunar notch of the ulna. It is an arthrodial, uni-axial joint with one degree of freedom: flexion-extension [9]. The role of the humeroulnar is to bend and straighten the elbow. The middle articulation is the result of joining the humeral condyle and the head of the radius. Its role is also flexion-extension and it can perform the complex movement that is supination and pronation. The final articulation is a result of joining the circumference of the head of the radius and the radial notch of the ulna. The contact area between the three bones is covered with a capsule which is a dense collagenous connective tissue that surrounds the joint lying the synovial membrane in the middle of synovial fluid. This creates a pocket of fluid and generates a negative pressure, which helps in keeping the bones together [10].

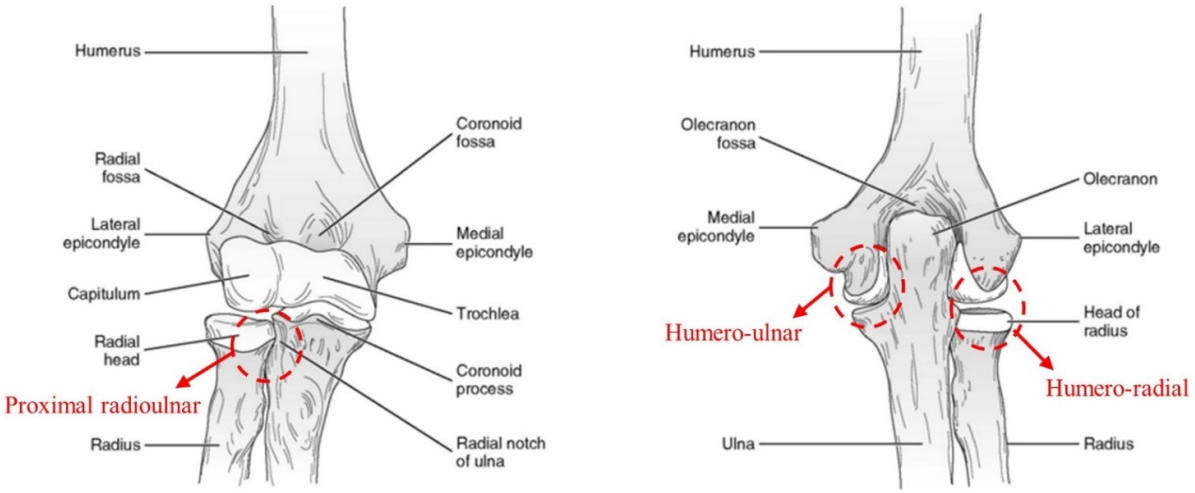

Figure 1. 1: The Osseous Anatomy of the Elbow Joint and three elbow joints labelled. (Adapted from: [8])

The ligaments are bundles of strong, dense, and flexible connective tissue, which connects the articulating bones together and helps in stabilising the elbow. The elbow joint comprises of three ligaments namely: medial, lateral, and annular ligament. The medial (ulnar) collateral ligament has two triangular bands posterior and interior (Figure 1.2). Both bands arise from the medial epicondyle and pass inside the elbow joint, the anterior band attaches to the front part of the ulna (coranoid process) and posterior to the back of ulna (olecranon process) and helps in keeping the normal relation of humerus with ulna [11]. The lateral (radial) collateral ligament, consists of a single short narrow band which is stretches from the lateral epicondyle to the annular ligament. It helps in the movement of extension and flexion but averts any lateral movement of the elbow joint. The annular (orbicular) ligament is a U-shaped ligament that is composed of a strong band of fibres that encircle the radius head and helps in maintaining the contact between radius and humerus [10, 11].

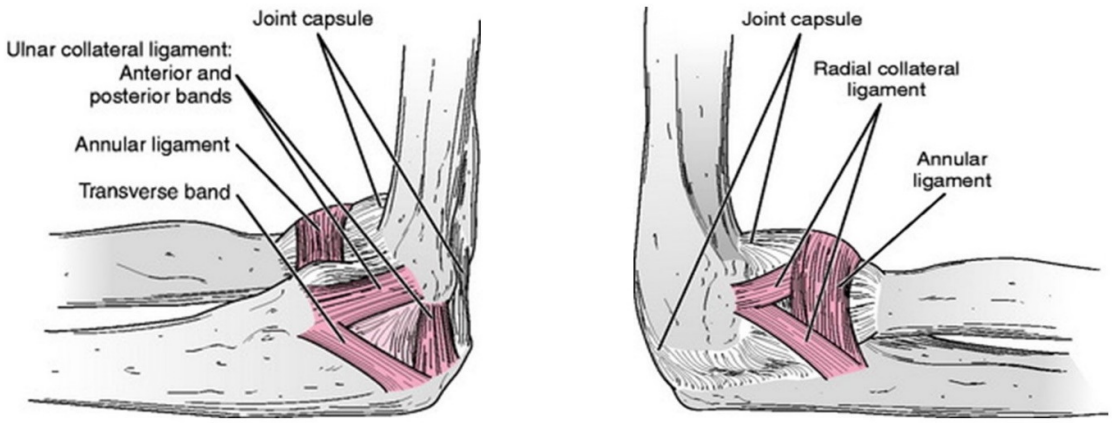

Figure 1. 2:The Ligaments of Elbow Joint (Adapted from : [8])

The elbow motion includes two active anatomical planes (Flexion- Extension and Pronation-Supination) and one passive plane (varus/valgus). During the Flexion – Extension the elbow movement was described by Richard Snell [10] as following: "As the lower end of the humerus contains a round capitulum and pulley-shaped trochlea for the articulation with the head of a radius and the trochlear notch of the ulna. Starting from the full extension, the olecranon fossa which is posteriorly above the trochlea of the humerus receives the olecranon process of the ulna and its movement is limited by the tension of the brachialis muscle and anterior ligament" as shown in figure 1.3.

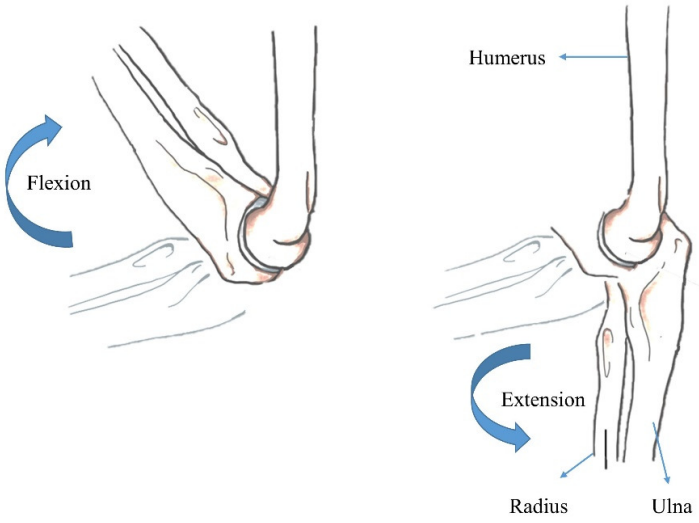

Figure 1. 3: Flexion- Extension of Forearm (Adapted from: [12])

During flexion coronoid fossa which is anteriorly above the trochlea receives the coronoid process of the ulna. When fully flexed the radial fossa situated above the capitulum receives the head of the radius (figure 1.3). The human elbow can be fully flexed up to 140-150 degrees and its movement is limited by the anterior surface of the forearm [10]. During rotation movement i.e., Pronation-Supination, very little motion occurs at the ulna. In pronation, the radius rotates at the elbow joint and comes on top of the Ulna. This action turns the forearm 180 degrees while in supination it rotates in opposite direction by crossing the radius over the ulna (figure 1.4). During these two movements, the head of the radius rotates inside the ring which is formed by a radial notch of the ulna and annular ligament [10].

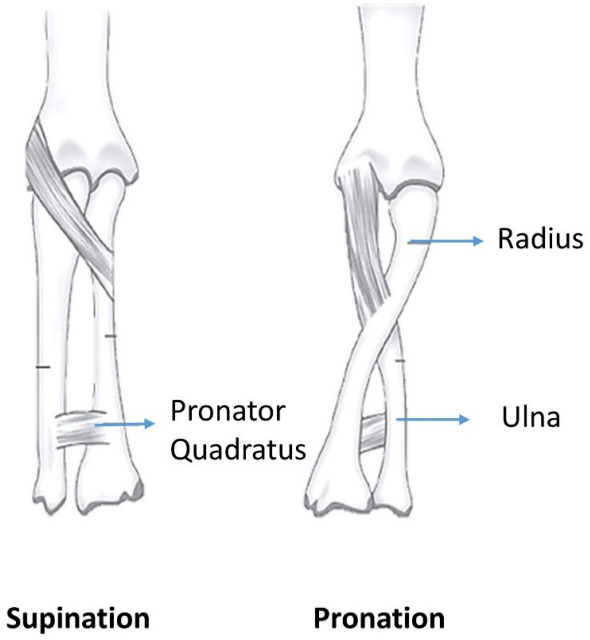

Figure 1.4: The Pronation-Supination of Forearm

The varus/valgus stress occurs due to the mechanical structure of the elbow as highlighted in figure 1.5 [3]. The valgus moment is countered by the varus moment, which is primarily distributed among the muscle-tendon that are crossing around the ulnar collateral ligament, osseous articulation at the medial side of the elbow joint.

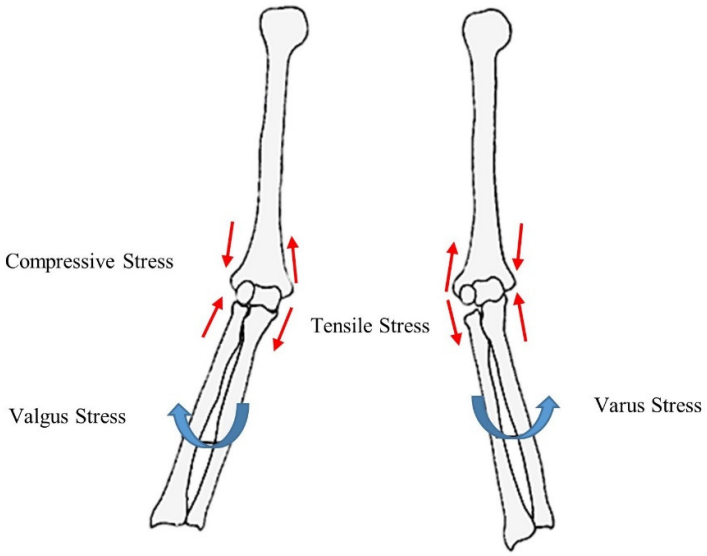

Figure 1. 5: The Varus-Valgus of Forearm

1.1.2 Muscles of the Elbow

The four major muscles responsible for elbow joint movements is the Brachialis (strongest elbow flexor) located anteriorly, the bicep brachii located superiorly, the Brachio-radialis located at laterally, and the triceps brachii (strongest elbow extensor) located anteriorly [10, 11] (Table1). The major muscles responsible for radio-ulnar joint movement is the two-pronator muscles: pronator teres located proximal to the joint, pronator quadratus located at a distal end of the joint, and two supinator muscles: supinator and bicep brachii.

Table 1. 1: Elbow Joint Muscle, Primary Functions and Movements [3,5]

Elbow Joint Muscle	Primary function	Movement
Brachialis	To bend the forearm	Flexion
Bicep brachii	Bi-articular muscle which helps in controlling motion of Shoulder and Elbow Joint	Flexion and supination
Brachio-radialis	To flex the forearm when quick movement is required	Flexion and supination
Flexor carpi radialis	Bending and radial deviation of wrist, weak flexion of the elbow.	Flexion
Pronator teres	Assist in Flexion	Flexion, Pronation
Triceps brachii	To extend the elbow joint and to fixed elbow joint to perform fine movement i.e. writing	Extension
Radio-ulnar Joint Muscle		
Pronator teres	To rotate the forearm palm downward.	Pronation, Flexion
Pronator quadratus	To assist pronator teres in pronation	Pronation
Supinator	To rotate the forearm palm upward	Supination
Biceps brachii	To assist in controlling the movement of the elbow	Flexion and supination

These muscles also act as a source for primary and secondary stabilisers of the elbow. The ulnohumeral joint provides osseous stability while the medial and lateral ligament stabilises the elbow. The secondary stabilisers are the radiohumral articulation, flexor-pronator muscle, and extensor muscle. These muscles also provide dynamic stability to the elbow as shown in figure 1.6 [13]. Muscles and ligaments of the

elbow joint make up three stabilizing systems: (A) the primary stabilizers consists of the ulnohumeral articulation and the medial and lateral ligaments, (B) the secondary has a radiohumral articulation with flexor and extensor tendons while (C) the dynamic stabilizing originates from humeral shaft via bicep and triceps.

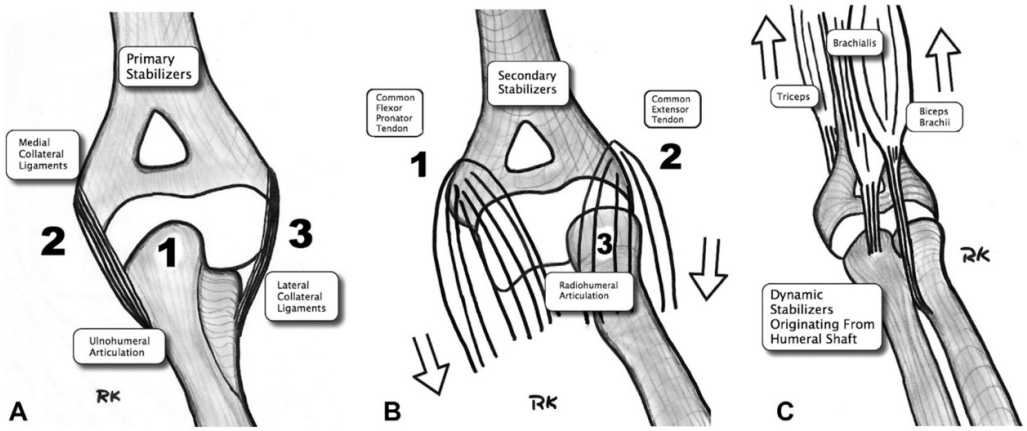

Figure 1. 6: Muscles and ligaments of Elbow Joint with the three stabilising systems: (A) primary, (B) secondary (C) and dynamic stabilisers. (Adapted from:[13])

1.1.3 Elbow Joint Forces

The elbow joint is a non-weight-bearing joint, yet it is subjected to considerable force delivered from the daily activity transmitted through a small surface area. These forces are typically caused solely by muscle actions. These complex muscles across the joint exerted a large compressive force on the joint especially the humeral ulna joint while performing flexion and extension. The resulting joint reaction force (JRF) are magnified per unit weight in hand while performing a various activity of daily living (ADL)[14]. The elbow joint experiences a load of approximately one times body weight (1 x BW) while performing normal daily activities, this increases to 3 times bodyweight when lifting a heavy object and goes up to 6 times of bodyweight during pounding and throwing activates[15]. The evaluation of these JRF is determined by performing the two- and three-dimensional studies. Limited experimental studies have been conducted to validate the computational results obtained. Nicol *et al (1977)* reported that the maximum JRF of 300 N during normal ADL while a maximum of 2094 N with extreme ADL [16]. The stress distribution across the humeral ulna and radiocapellar joints were 43 % and 57 % respectively[17].

1.1.4 Common problems in the Elbow Joint

The elbow joint is susceptible to the development of acute injuries and different joint diseases due to its location and usage to perform a variety of tasks which could leave patients with pain and a reduction in mobility. The most common pathologies of elbow arthritis are rheumatoid arthritis, post-traumatic arthritis, instability, severe fracture, and osteoarthritis [6].

From the early 1970s to the late 1990s rheumatoid arthritis was the most frequently diagnosed pathogen of elbow arthritis because of its progressive nature and its effects on the capsuloligamentous tissue. Rheumatoid arthritis (RA) is also known as inflammatory arthritis of the elbow, an autoimmune condition that leads to the thickening and inflammation of the synovial membrane surrounding the elbow joint. With chronic inflammation, the cartilage can be damaged and can cause pain, cartilage loss, and stiffness[18].

From 2000 to date, the development of effective biological drugs such as anti-TNF a medication for the treatment of RA has shown a remarkable result in decreasing the number of patients suffering from this disease[19]. However, other conditions have become a more prominent problem in elbow joints that cause discomfort and disability. The most commonly occurring are osteoarthritis and post-traumatic arthritis.

By 2020, Osteoarthritis will represent the fourth leading cause of disability worldwide. This will place a major burden on individual social and health care systems [20]. Osteoarthritis (OA) is characterised as degenerative joint disease resulting from the wear and tear in joints, in the elbow this manifests by damaging the protective cartilage which covers the bones. Three main pathologic processes involved in elbow osteoarthritis: Loose bodies form from the fragmentation of cartilage; bony osteophyte formation leads to impingement and also leads to progressive joint capsular contracture. Advanced arthritis leads to the destruction of the joint space which results in impairment of elbow function and affects the quality of a person's life [21].

In severe OA or trauma cases where the patient is suffering from a chronic and severe pain and quality of life is affected, TEA is performed. Elbow arthroplasty is a procedure to alleviate pain and restore joint movement.

1.2 Total Elbow Arthroplasty

1.2.1 Surgical Approach

The most common technique used for total elbow arthroplasty is the standard posteromedial approach [22]. The surgery starts by exposing the back of the elbow by making an incision. Then the muscles are displaced gently to one side of the elbow and the ulna nerve is protected. Then on the distal side of the humerus, the origin of the medial and lateral collateral ligaments is dissected. For the clear assessment of the humerus dimension, Humerus is rotated externally. The central portion of the trochlea is resected using a bone saw [22]. The humeral canal is exposed at the proximal base of the olecranon fossa and the lateral and medial side of the humerus are cut using humeral cutting guides and the humeral component of the prosthesis is inserted into the humeral canal. Then the forearm is moved proximally and a mandibular canal is exposed in which the ulna component of the prosthesis is inserted [23]. Polymethylmethacrylate (PMMA) cement may be used to fix these metallic parts of the prosthesis with the bone and finally high molecular weight polyethylene is inserted between the components of the prosthesis [22, 23].

1.2.2 Elbow Implant Fixation

The Elbow implant can be fixed in the bone via three different ways i.e. Cemented fixation, cementless fixation, and hybrid fixation. In hybrid fixation, one component of the implant is cemented and the other is cementless. Nowadays most elbow prostheses are cemented. The fixation in the cemented elbow prosthesis uses PMMA and depends upon the stable interface between the cement and the implant component along with the firm mechanical bond between bone and cement[24]. Comparing to the hip and knee arthroplasty surgery in which the cement mantle is between 2 -5 mm [25]. In TEA the cement mantal is considered thinner and it is suggested that the cementing passes the tip of a humeral and ulna component of a prosthesis to decrease the component loosening rate [26].

1.2.3 Types of Elbow Prosthesis

The elbow prosthesis is predominantly limited to replacing the humero-ulna joint and consists of a humeral stem and ulna stem that articulate. Most of the elbow prostheses therefore omit the other two joints; the humeroradial and the proximal radioulnar joints. There are two main categories of elbow prostheses available to replace elbow joint that relate to the articulation and these are:

I. Linked/unlinked

II. Constrained/semi-constrained/ unconstrained

In the linked elbow prosthesis there is a physical linkage between the humerus and ulna component of the implant which allows this prosthesis not to dislocate unless structural failure occurs. An example of this is the Coonrad Morrey prosthesis (figure 1.9). While in the unlinked prostheses the humerus and ulna component are physically separated from each other[19], such as the Souter-Strathclyde design (figure 1.8). The unlinked prosthesis is chosen depending on the sufficient bone stock as well as capsular and ligament structure to set the prosthesis and provide stability to the joint[23].

The term constrained/ semi-constrained / unconstrained refers to the degree of freedom of articulation and relates to conformity and tolerances at the articulation surfaces between the humero-ulna joint.

Depending upon the design, both linked and unlinked elbow prosthesis can be constrained, semi-constrained or unconstrained. The humeral and ulna stems can be made long or short depending upon the surgeon requirement and these stems can be fixed into the bones with or without PMMA bone cement, with cemented designs being most common[27]. To help with longevity of the fixation, sections of the humerus and ulna stems are coated with different materials such as titanium spray, porous beads, or plasma spray to improve fixation strength.

The implant's survivorship and its clinical outcome vary from one implant type to another. There is no consensus that which type shows better results because both types have some advantages and disadvantages as shown in table 1.2.

Table 1. 2: Advantages and Disadvantages between Linked and Unlinked Elbow Prostheses

Types	Advantages	Disadvantages
Linked	• High stability. • It depended on bone stock • Can be used when there is ligamentous insufficiency • Better range of motion (ROM)	• High risk of mechanical loosening due to higher tension on the interface • Complicated revision surgery due to extensive canal invasion.
Unlinked	• Lower risk of implant loosening and Osteolysis. • As Unlink requires less bone invasion, beneficial for revised surgery.	• Highly depended upon bone stock and ligament structure. • Higher rate of dislocating the joint. • Require accurate positioning for proper articulation of the implant.

Currently, there are three basic elbow prosthesis subtypes: a resurfacing one (unlinked, semi-constrained, short stem), a loose hinge (linked and semi-constrained), and hybrid (depending upon need can be changed from unlinked to link)[19]. The selection of the prostheses type is based on the joint stability and available bone stock.

1.3 Total Elbow Arthroplasty History

In the sixteenth century, the first recorded salvage surgery of the elbow was performed by Ambroise Pare by surgically removing the soft tissue along with its nearby affected bone to prevent amputation due to an incurable joint infection [28]. In the nineteenth century, when anaesthesia became commonly used, the surgical procedure of excision and creating a pseudo–arthrosis began to evolve. In which the incapacitating elbow disease was cured by resecting the distal humerus [28].

However, the first documented total elbow arthroplasty was in 1925 and was carried out by Robineau using vulcanized rubber and metal anatomical prosthesis. In 1941, a non-anatomical hinged prosthesis completely made of metal was used by Boerema[28]. Different researchers (Venable (1952), Prevo (1954), Weiss (1970), Dee (1972)) worked on different methodologies and materials to develop fully constrained prostheses. All the attempts for treating the elbow joint showed unsatisfactory outcomes, resulting in loosening of the prosthesis and deep infection [29].

Then, came the era of the semi-constrained and non-constrained prosthesis. In 1973 Dee reviewed his results of a constrained prosthesis and came with a modification with his prosthesis by making a hinged prosthesis semi-constrained with lateral movement up to 15^{o} along with a simple surface replacement for the preservation of bone (figure 1.7). The clinical results were satisfactory but only for a short period [30].

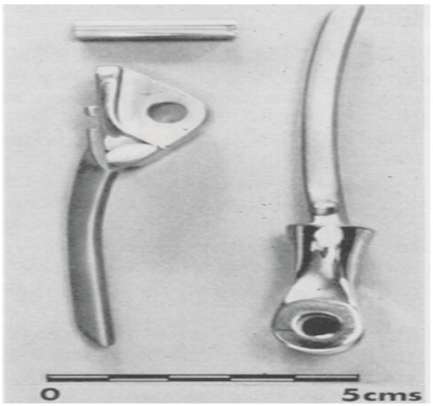

Figure 1. 7: Dee Prosthesis [31]

In 1973 a non-constrained prosthesis was introduced named Souter- Strathclyde. In which the humeral and ulnar components were made of Vitallium and ultra-high molecular weight polyethylene (figure 1.8) . The main advantage of this prosthesis was that a small amount of bone was removed but this created a high loosening rate [32].

Figure 1. 8: Souter-Strathclyde Prosthesis [31]

Also, In 1973 Coonrad developed a prosthesis that consists of titanium stem, polyethylene hinge, and pin for central locking with only 2^0 - 3^0 of laxity [33] (figure 1.9). This prosthesis was used until 1978 when Morrey found out that this prosthesis has a high rate of loosening in patients having rheumatoid arthritis. Soon after that Coonrad- Morrey Type II prosthesis was made which allowed 7^0 of Varus-valgus laxity at the articulation but this prosthetic also has some biomechanical problems and therefore was only used from 1979 till 1981 [33, 34]. To compensate for the problem Type III was invented and this type is currently in use ever since. The Type III prosthesis included an anterior flange with an associated bone graft to improve cement fixation and to decrease the rate of loosening. The distal and proximal parts of the humerus and ulna components were coated with titanium spray. This prosthesis showed good clinical results however to date, it is encountered by some complications among which the loosening is the main [30].

Figure 1. 9: Coonrad- Morrey Type III Prosthesis [31]

In 1978 Gschwnd/Scheier/Bahler (GSB) III (figure 1.10) was made from the failure of constrained GSB I and GSB II. In GSB III the humeral part is made of Prostal-10 and ulna of Protasul-2 alloy with polyethylene coated articulation [35]. An oval link connection between these two components allowed 5^{o} of rotation, flexion, and extension. Although this prosthesis showed satisfactory results with post-operative Mayo elbow, it still encounters the main complication of loosening [35, 36].

Figure 1. 10: GSB III Prosthesis [35]

In 1978 Wadsworth a non-constrained elbow prosthesis was invented because of a non-satisfactory result of a constrained prosthesis. Both the humeral and ulna component were fixed with cement. The humeral component was made of polyethylene and ulna of chrome-cobalt alloy [37]. During insertion of this prosthesis very small bone needed to be removed but the main reason for the failure of this

prosthesis was a high rate of loosening of the humeral component 68.4%. Due to this problem it was no longer used after 1982 [38].

Figure 1. 11: WadsWorth Prosthesis [37]

The first Kudo Prosthesis Type –I was used from 1971-1975 and this prosthesis was placed in the non-constrained way in which the humeral component was made of titanium and ulna of high-density polyethylene and an articulating surface made of titanium[39]. Gradually modification came in this type and the latest design which is also still being used is Kudo Prosthesis, type V invented in 1990 in which the ulna component is made of polyethylene with a metal backing coated and humeral component made of cobalt-chromium alloy with the porous-coated half stem. The result of type V was very satisfying which allowed Range of Movement (ROM) improvement of up to 15^{o} along with stability and pain relief. In respect to other prostheses, the complication rates were also low and the major problem which was loosening was seen in 17 % of the study population [40].

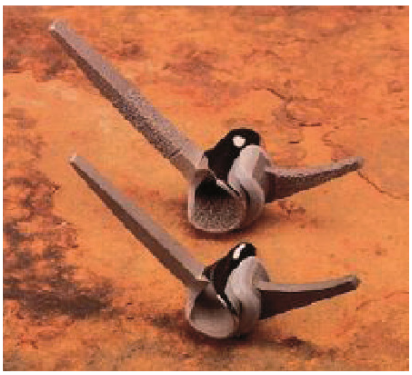

Figure 1. 12: Kudo Prosthesis [40]

Based upon the types of elbow prosthesis explained, to develop a prosthesis for TEA which can mimic all the elbow functions along with stabilising the articulation of the elbow and radio-ulnar joint still poses a significant challenge. One of the major drawbacks of the anatomical prosthesis was its lack of intrinsic stability which required the integrity of muscles and ligaments. As mentioned, the humeroradial and radioulnar joints are not preserved in the majority of elbow prosthesis. It is not clear how much impact this biomechanical shift will have on the biomechanics of the joint. Table 1.3 highlights the clinical mayo score of different elbow prosthesis devices and how much they improve the elbow's range of motion.

The Mayo elbow performance score highlights the performance index for evaluating the clinical outcome of the elbow joint after TEA. The score is calculated by assessment of pain, range of motion, and patients rating for daily life activity. The score ranges from 0 to 100, with a higher score indicating better performance [41].

Table 1. 3: Clinical Score and Improved ROM of Different Elbow Prostheses [29-39]

Elbow Prosthesis	Clinical Assessed Prosthesis	Follow Up Years	Loosening rate	Infection rate	Improved Range of Motion	Mayo Elbow Score
Discovery Elbow	48	02	10.41%	8.33%	25.2	86.25/100
Coonrad- Morrey	41	10-15	14.63%	4.87%	24	91/100
Souter-Strathclyde	44	06	9.09%	2.27%	18	86/100
Wadsworth	19	1-2	68.4%	5.3%	8.7	36.80/100
GSB III	82	06	15.2%	1.1%	31	88.5/100
iBP	9	3-4	7.7%	-	-	95/100
Kudo V	89	06	16.9%	-	15	-
Dee	12	1-2	--	-	-	10/100

1.4 Utilisation of TEA

Thousands of elbow prostheses have been implanted in Europe and the USA and their use has almost doubled between 1998 and 2011 [42]. In the USA the incidence of TEA surgery performed is 1.4 in every 100,000 of the population. Day *et al (2010)* reported that in the USA there is a rise of 6.4 % annually in the procedure of TEA and a 7.6 % annual growth between 1993 and 2007 [43]. Figure 1.13 highlights the utilisation rate of the elbow arthroplasty from 1997-2011, the utilisation was greater in females than males, with females having better surgical outcomes [42] as shown in figure 1.13.

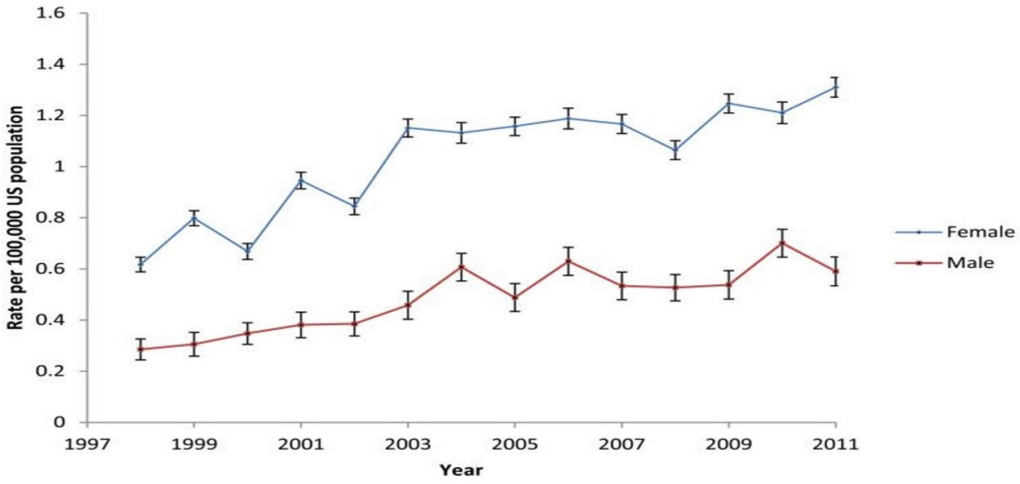

Figure 1. 13: Utilisation rate of TEA from 1997-2011 [42]

Although, compared with knee and hip joint registries there are limited registries establish for the elbow and less is known about the current surgical utilisation of the TEA. The first national joint registry for the elbow and the shoulder were introduced in the first decade of the twenty century. The oldest registry is the Finnish Arthroplasty which was established in 1980 followed by Norway, New Zealand, Sweden, Australia, Denmark, and United Kingdom. Figure 1.14 highlights the trend of elbow implantation at different joint registries at three time points over a 10 year period from 2008 to 2018.

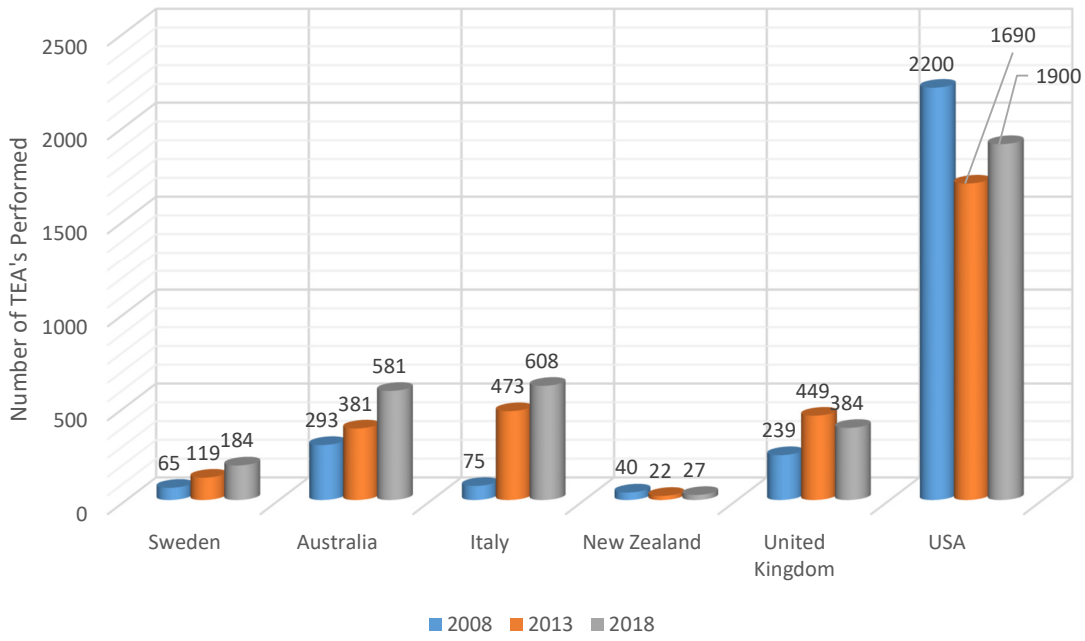

Figure 1. 14: Utilisation rate of TEA at different Elbow Joint Registries [44]

Highlighting the trends of the utilisation of the TEA based upon gender. In females, the utilisation rate was high [42, 45]. Also, it has been reported that the mortality rate and the hospital stay of the females were lower as compared to the males, even though on average the female groups were older [46]. According to Zhou *et al (2016)* in the USA the TEA utilisation of the white females (74%) was much higher as compared to other race female patients [47].

1.5 Change in Quality of Life after TEA

The increase in the number of TEA procedures. It is likely to place a considerable financial strain on the health care system. In terms of quality of life and cost/utility ratio, few studies have been conducted and limited data is available regarding the efficacy of the treatment.

Giannicola *et al (2013)* studied 33 elbow arthroplasty performed between 2007 to 2013 to quantify the improvements in the quality of the life of patients who underwent TEA therapy [48]. He reported 91 % of the satisfactory outcome of the patients and highlighted the significant improvement between pre and post-operative scores and an increase in the range of motion. Pain reduction was the factor that most

affected the patient's quality of life. The author conducted the cost/utility ratio and 70 % of the patients showed satisfaction postoperatively

Angst *et al (2005)* studied 79 elbow arthroplasty performed from 1984 to 1996 to qualitatively assess the outcome after TEA. He reported a low pain level, good elbow stability, and overall 82 % were satisfied with the TEA while 8 % of patients were not satisfied as the TEA did not meet their preoperative expectations.

Zhou et al (2016) studied 3146 patients and evaluated their hospital stay, cost, and rate of readmission within 30-days. He reported that the mean hospital stay was 4.2 ± 5 days and the mean total hospital cost was 16.300 ± 4000 US dollars per case. The rate of re-admissions within 30 days was 4.4 % [47].

1.6 Problem Associated with TEA

While TEA is a versatile procedure that can be performed in both trauma and elective situation for relieving pain and increasing patient's elbow range of motion, yet the survival rates of the elbow implants ranges from 70% to 81 % [49]. These low survival rates are due to the problems associated with the TEA which leads to implant revision. The most persistent problem associated with the TEA is the mechanical failure of the components of the implants. These failures can occur soon after surgery (inadequate surgical technique or patient's non-compliance) or after few years (implant instability, fracture, loosening). The revision surgery caused by the mechanical failure cannot be avoided till there is any mechanism to detect the early failure.

Therefore, understanding the cause of these problems and detecting them at early stage is necessary to avoid revision surgery. These early signs of loosening detection will also aid hospitals by reducing their operational check-up cost which ranges from $135.20 ± $190.5 per visit along with reducing the burden on the clinicians [50]. In addition to that, it will allow the clinicians to form a standardised management system in which they categorise their patients depending upon their implant performance. By this management system, they will able to focus on the patients in which early signs of loosening are detected that can be treated effectively with systematic drugs and rehabilitation protocol along with antibiotic treatment to prevent their implant for further loosening.

1.7 Outline of the Thesis

This thesis is organised in 7 chapters and a brief description about these chapters are as follows:

Chapter 1 briefly introduces the human elbow joint anatomy, function, exerted forces, different arthritis problems, and elbow replacement as the most widely and effective treatment for the end-stage of arthritis. History of the elbow replacement and the evolution of various types of prosthesis and their design. Finally, this chapter summarises the elbow arthroplasty utilisation, its effect on the quality of life, an outline of the thesis.

Chapter 2 reviews the current complications that are associated with elbow arthroplasty and the factors involved in causing those complications. It also highlights the clinical need for the instrument prostheses and the limitation of the current diagnostic technique for detecting prostheses loosening. Consequently, the existing system and the new proposed system for detecting loosening were reviewed and their drawbacks were described.

Chapter 3-6 contains the technical contribution of this thesis.

Chapter 3 proposes a magnetic measurement system that can be integrated into the existing elbow prostheses making it "Smart/Instrumental". This new measuring system is able to detect prostheses aseptic loosening in multiple axes at different motion (linear & angular) and different states (Static & Quasi-Static movement). Also, the effect of various biomaterials on the detection system was analysed. The designed detecting system was validated against a reference displacement measurement device (Electro Force 3300, TA Instruments, Boston, USA).

Chapter 4 introduces a sensor configuration design and the use of the wavelet filtering technique to estimate the migration of the prostheses and improve its resolution, sensitivity, and signal-to-noise ratio. The proposed system is validated similar to chapter 3 against the reference displacement measurement device. A specific sensor selection criteria defined which result in compensating the tilting effect that was observed in chapter 3.

Chapter 5 introduces the mechanical testing rig design, realisation, and its use to validate the measurement of smart elbow prostheses. This chapter highlights the description of mechanical rig design and the humeral component of the elbow prostheses (embedded with sensors). Different prostheses fixation configurations were tested (un-cemented, semi- cemented, and fully cemented) and its performance was analysed at different joint reaction forces. Similar to chapter 4, a multi-sensor configuration was used and the data were analysed with the reference force and displacement measurement device (Electro Force 3300, TA Instruments, Boston, USA)

Chapter 6 proposes the development of a chemical sensor (Hydrogel) to detect the septic loosening due to bacterial infection in the smart elbow prostheses by integrating the chemical sensor with the magnetic measuring system. This chapter includes the synthesis of the biocompatible hydrogel and its effect on various pH changes. Different modes of hydrogel were synthesized and integrated with the magnetic measuring system to analyse its effect with a change of pH level.

Finally, chapter 7 provides the conclusion of this thesis along with a general discussion on the achievements and the perspective for future work.

2 Chapter 2: Literature Review and Background

Loosening of Elbow Prostheses- A Review of Complications and Current Diagnostic tools used to Detect Loosening

Summary

Disease and trauma of the elbow joint have led to the design and use of a range of implantable Total Elbow Arthroplasties (TEAs). The demand for long-lasting TEAs is evident through the modifications in implant design and surgical techniques, alongside new engineering technologies being applied to existing diagnostic tools. Aseptic loosening, along with septic loosening, are the most recognised reasons for the revision of TEAs because of their different causes of failure and their complexity in diagnosis. This chapter focuses on various factors that cause both aseptic and septic loosening of elbow prostheses along with the current diagnostic techniques that are used to detect loosening. Several imaging and non-imaging diagnostic procedures and promising new techniques for the detection of loosening are discussed to highlight their abilities and shortcomings. It is concluded that the current signs and symptoms of loosening may not be clinically apparent until the late stages of failure due to the lack of accurate and sensitive early diagnosis tools. There is a need for more sophisticated, rapid, and accurate diagnostic tools to be developed which could detect early signs of implant migration along with the broad range of microorganisms that causes septic loosening. Additionally, the diagnostic tools should match the mechanical complexity and biological parameters of the elbow prosthesis.

2.1 Introduction

Total elbow arthroplasty (TEA) has continued to evolve over the past four decades. However, due to the distinctive anatomy and biomechanical properties of the elbow joint, the complication rates of TEA ranges from 11% to 38 % which is 20 to 45 % higher compared to the total hip or knee arthroplasty [51, 52]. Although the prevalence of TEA is not high as compared to hip and knee arthroplasty, different authors have reported a significant increase in the surgical procedure. *Day et al (2015)* reported an annual rise of 7.6 % of TEAs in the United States with a nearly 3 fold increase of primary TEAs and a

5 fold increase of revision TEAs from 1993 to 2007[45]. Klug *et al (2014)* reported the increase of TEA in Germany by 80 % over the last decade[53]. Therefore, the use of TEA is increasing. TEA was primarily used to treat inflammatory (rheumatoid) arthritis (RA) which in the early 1970s and late 1990s was a frequently diagnosed condition[54]. Due to the advancement in medical technology by developing effective pharmaceutical treatment, the prevalence of TEA due to RA has reduced. Gay *et al (2012)* reported a decrease from 48 to 19 % during 10 years [55]. Simultaneously, elbow joints are affected by other musculoskeletal conditions that cause discomfort and disability. Among these the most commonly occurring are osteoarthritis and post-traumatic arthritis. By 2020, osteoarthritis will represent the fourth leading cause of disability worldwide[56] placing a major burden on individuals as well as social and health care systems. Currently, TEA is the sole solution for an effective reconstruction treatment for patients with end-stage arthritic elbow conditions, providing relief from pain and restoring elbow function. However, different factors contribute to implant failure and lead to revision surgery which must be addressed.

Revision surgery is more traumatic, complex, and costly than primary surgery and reveals clinical complexities along with inadequate clinical outcomes as compared with primary TEA. The ratio of primary surgery to revision surgery is known as the revision burden. Worldwide, only a handful of countries keep extensive records of all joint replacement surgeries, including TEA, such as the United Kingdom, New Zealand, Portugal, Norway, and the Netherland. The rest of the national joint registers focus only on hip, knee, and shoulder surgeries. Table 2.1 shows the rate of revision burden of joint replacements from the five national orthopaedic registries mentioned. From the table, it can be seen that the revision burden of TEA is comparatively high (6 – 30 %) compared to all other joint arthroplasties (5 – 12 %). This indicates that irrespective of its small size and low prevalence, the complications that are associated with TEA and lead to revision are relatively high.

Table 2. 1: Revision Burden for Different Replacement Surgeries (THA – Total Hip Arthroplasty, TKA – Total Knee Arthroplasty, TSA – Total Shoulder Arthroplasty, TEA – Total Elbow Arthroplasty) [57-61]

	United Kingdom	**New Zealand**	**Portugal**	**Norway**	**Netherlands**
THA Primary	996,272	118,993	4,384	1,902,08	215,380
THA Revision	106,360	17,348	648	31,515	28,639
Burden %	**9.64**	**12.72**	**12.86**	**14.21**	**11.73**
TKA Primary	1,091,636	93,963	4,110	81,861	201,454
TKA Revision	68,233	7,390	278	7,501	19,045
Burden %	**5.88**	**7.29**	**6.33**	**8.39**	**8.63**
TSA Primary	30,841	8,250	111	7,707	10,174
TSA Revision	3,480	637	9	754	1,104
Burden %	**10.13**	**7.16**	**7.5**	**8.91**	**9.78**
TEA Primary	2,884	515	13	867	508
TEA Revision	820	35	1	451	221
Burden %	**22.13**	**6.36**	**7.14**	**34.21**	**30.31**

Likewise, compared with the survival rates of total hip arthroplasty (THA) and total knee arthroplasty (TKA), which are 95 % and 90 % respectively after 10 years, the survival rate of TEA is lower at just 79.2 % [52]. Prosthesis survival depends upon several factors such as surgical technique, prosthesis design, type, and the age and activity of the patients[62].The main reason for this lower longevity is the high rate of complications that are associated with TEA. Compared with THA and TKA there are a limited number of studies which describes the complications associated with TEA.

2.2 Complications related to TEA

The first report regarding the complications of TEA was reported by Gschwend *et al (1996)*[63] in which the total complication rate of 43 % with an 18 % revision rate was reported. The main factors which contributed to these complications were aseptic loosening, ulnar nerve complications, dislocation,

infection, instability, ectopic bone formation, subluxation, intra-operative fracture, and fracture of the prosthesis. To minimise these complications different surgical techniques and advancements in implant design have been made over the last two decades. The implants have evolved through a series of modifications from fully constrained to unconstrained and linked to unlinked prostheses based upon clinical results and biomechanical properties as reviewed in the previous chapter.

The fully constrained elbow prosthesis is no longer used because of its high rate of loosening. It has been replaced by linked and unlinked prosthesis designs[23]. The linked elbow prosthesis is a semi-constrained design that uses a sloppy hinge to decrease the instability of articulation and the rate of aseptic loosening. But despite that, these prostheses suffer from a higher rate of loosening as compared with an unlinked prosthesis. The unlinked prosthesis is unconstrained and for its stability of articulation, it totally depends upon the soft tissue surrounding the prosthesis. Due to this fact, the unlinked prosthesis has a high rate of instability as compared to a linked prosthesis[23].

Voloshin *et al (2011)*[51] conducted a review of the literature on the complication of TEA which shows that there was a reduction in the rate of complications of TEA as compared with the Gschwend *et al (1996)* report. The overall reduction rate was 18.7 ± 5.8 %. This reduction was attributed to advancements in prosthesis design and better surgical techniques. The type of complications remains the same i.e. loosening, instability, and deep infection but the frequency of its occurrence decreased.

An analysis of three systematic reviews of TEA survival rates published over the last 16 years reveals aseptic loosening and infection as consistent causes of loosening. Little *et al (2003)* conducted a systematic review on TEA survival rates in which 3618 TEA cases found the most common complication rates related to biomechanical instability and loosening (9-14 %) (figure 2.1) with infection occurring in over 4 % of cases on average [64]. The analysis included complications from all types of arthroplasty i.e. constrained, semi-constrained, and un-constrained arthroplasty.

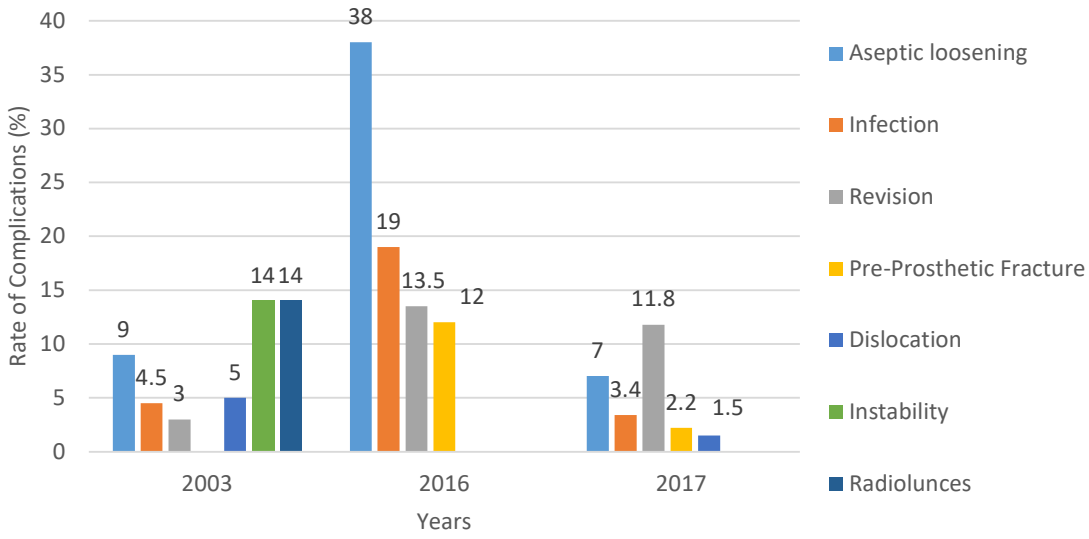

Figure 2. 1 Complication rates of TEA from 2003-2017 in a total of 22,305 TEA cases from three systematic reviews [52, 64, 65]

Prkic *et al (2017)* conducted a similar systematic review on TEA survival rates[65], a review of 9308 implants, where 13.5 % were identified for revision cases with a weighted mean follow-up of 81 months. As shown in figure 2.1 this review also concluded the main reason for the revision was aseptic loosening (38 %) followed by deep infection (19 %) [65]. The aseptic loosening was seen less in linked prostheses than semi-constrained whilst the infection did not differ between these implant groups.

More recently a systematic review conducted by Chantal *et al (2017)* where a total of 9379 elbow implants were examined containing both linked and unlinked prostheses. From figure 2.1 it can be seen that as compared to the previous two reviews, the rate of complication had decreased, ranging between 11 % to 38 % in which clinical loosening was frequently followed by deep infection. There is however, no clarity regarding the design of prosthesis (linked, unlinked) to show which had a better survival rate [52].

2.3 Mechanism of Aseptic loosening

Total elbow arthroplasty (TEA) consists of two main stems, namely the humeral stem and the ulna stem. These metallic stems are made of either cobalt-chromium alloys CoCrMo (ASTM F75) or CoNiCrMo (ASTM F562), stainless steel 316L (ASTM F138, F139) or a titanium alloy Ti-6Al-4V (ASTM F136)[66, 67]. Their articulating surfaces are sometimes made from ceramics such as calcium phosphate, zirconia, alumina, and their composite[67]. These stems are largely secured in the bone cavity by the use of bone cement, Polymethylmethacrylate (PMMA)[68]. In the case of linked designs, these stems are joined together with a plastic bearing made of ultra-high-molecular-weight polyethylene (UHMWPE) that allows the prosthesis to hinge. Aseptic loosening occurs to both of the stems of TEA but the cause of this loosening is different. The main cause of aseptic implant failure of TEA includes wear, elbow kinematics, and loss of bone stock.

2.3.1 Wear Effect

Wear debris in TEA is generally generated when the components of the implant are degrading due to the relative motion of component surfaces with each other under shear force. This degradation causes material loss from one or both surfaces. As described by Mckellop *et al (1995)*, four modes of wear can be observed in total joint replacement as shown in table 2.2 [69, 70]. These modes of wear are caused by different mechanisms such as adhesion, abrasion, and fatigue wear. These wear processes can occur at the articular surface at the UHMWPE bushing and axis pin, as well as at the bone-cement and cement-implant interface.

Table 2. 2: Different Modes of Wear in Total Joint Arthroplasty

Modes	Contacting Surfaces
1	Bearing Versus Bearing
2	Bearing Versus Non-Bearing
3	Bearing verses Bearing versus third body material
4	Non-Bearing versus Non-Bearing

Goldberg *et al (2008)* reported a retrospective analysis of 16 semi-constrained (Coonrad-Morrey) prostheses in which both mode 1 and 3 types of wear were observed at the humeral and ulna UHMWPE bushing. Mode 2 type of wear is shown in the metal axis pin and metallic ulna base [70]. Lee *et al (2005)* reviewed 919 elbow replacements with semi-constrained implants. They found that an angle greater than 10° of total varus-valgus laxity indicated complete wear of the bushing [71].

2.3.2 Position and Kinematics of the Elbow

The success of TEA depends on the correct placement of the implant along with the balancing of the soft tissue to regain the biomechanical properties of the joint. The migration of the prosthesis from its original position remains the leading cause of the failure of TEA. Therefore, a properly positioned implant is necessary to avoid loosening. In the newest development during the surgery both distal and proximal centralisers are used for optimum positioning/alignment of the implant's component. These centralisers also help in equal distribution of the cement around the implant [72] as shown in figure 2.2.

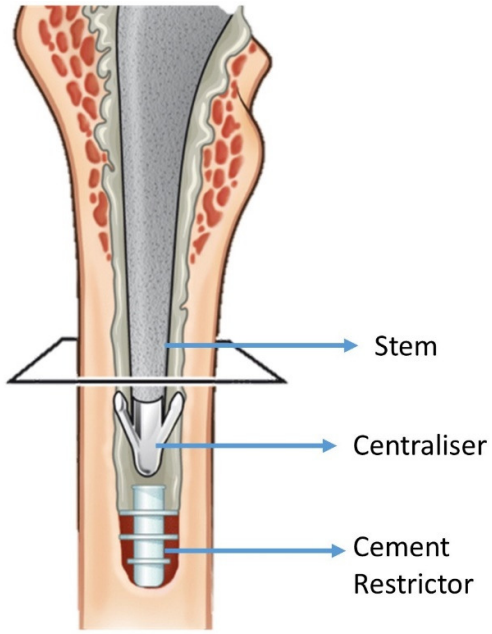

Figure 2. 2 : Allignment of the stem using stem centraliser for proper positioning. (Adapted from [73]).

Properly reflecting elbow kinematics can minimise the stress and energy dissipation at bone-implant interface. Even with a correctly positioned joint replacement, there is the question of what long-term

impact the alteration of the joint from the surgery has on implant survivability. The procedure for the majority of TEA implants requires the excision of the head of the radius, thus removing the proximal radioulnar joint and humeroradial joint. The force transmission at the elbow is anatomically altered. Up to 60 % of the loads are transferred across the humeroradial joint during flexion (0 ° - 30 °) [74]. This reduction in the joint articulations will inevitably alter the biomechanics and load dynamics of the joint.

2.3.3 Quality and Quantity of Bone Stock

For the longevity of an elbow prosthesis, the quality of prosthesis positioning and bone stock plays a vital role. Different types of bone loss can be observed in TEA which leads to misplacement of the prosthesis. Compared to the femur and tibia bones of the hip and knee respectively the cancellous bone is limited around the elbow. For better fixation of the prosthesis, the cancellous bone should have better stock for better cement interdigitating, which has been shown to improve cement/bone interfacial strength [75]. Furthermore, inflammatory erosion and osteolysis causes bone loss surrounding the implant or cement mantle which eventually causes cortical bone thinning and in more severe cases ballooning of cortical bone before implant fracture. Bone loss can occur both in the ulnar and humeral bone. Based on the intensity of the bone loss, Stanley classified three different types of bone loss [76].

- Type 1- Minimal bone loss
- Type 2 – intramedullary bone loss
- Type 3- structural cortical bone loss.

For poor bone stock, allograft placement and impaction bone grafting are used. More than 50 % of patients receive a bone graft for better fixation, yet implant loosening persists in one in every five patients.

2.3.4 Causes of Aseptic loosening in different Prosthesis Types

The contributing factors for aseptic loosening differ from one prosthesis type to another. Cesar *et al.* (2007), reported long-term outcomes (postoperative beyond 10 years) of the GSB III prostheses [36]. In the study, a higher loosening rate was noted on the humeral side, which was attributed to increased forces at the posterior side. This increase of force was due to the prostheses humeral hinge and distal stem posterior translation during lifting[36]. Also, the finite element analysis was carried out on the GSB III prosthesis which confirmed that at a 120^{o} flexion between the humeral stem and hinge the maximum distribution of the Von Mises stress was observed at the posterior side of the humeral component [77].

Kodama *et al (2017)* studied Kudo Type V elbow prosthesis and found no loosening of the humeral component. The possible reason for this could be the the titanium porous plasma-sprayed stem which becomes adequately osseointegrated with the surface of bone and metal to prevent loosening[78]. However, the studies show that in a well-fixed and well-placed humeral component, the ulnar component experiences high loads due to all the loosening forces transferring from the humeral to the ulnar component which leads to the failure of the ulnar component[78]. In unlinked elbow prostheses, Ljung *et al (1993)* describe the reason for the substantial loosening of the implant as it is due to a multi-axial force that is exerted by the elbow at the implant-cement and cement-bone interface[79].

Similarly, the studies on Souter-Strathclyde TEA showed that the failure of the ulnar component was the main cause of loosening[80]. The ulnar component is wholly made of polyethylene (PE) and an elasticity difference between the PE layer and the cement layer can lead to a fracture of the ulna component [78, 80]. According to Herren *et al* (2001), in semi-constrained unlinked elbow prostheses, the failure was believed due to a release of collateral ligament during surgery which contributes to neglecting stability of implant[81]. Also, Robert *et al (2018),* highlighted that in semi-constrained prostheses the substantial bone resorption is due to the non-anatomic forces which are resulted from the ligament deficiency (release of the medial and lateral collateral ligament from their humeral), radial head resection, and fixation of the stem [13]. This bone resorption results in increasing the moment arm

between the hinges where the maximum load is transferred. Which not only loosens the stem but also increases the likelihood of arthroplasty failure[82].

Furthermore, in resurfacing and semi-constrained TEAs the common problem for early aseptic loosening was the high contacting stress resulting from indirect articular rotational torque at the implant-bone and implant-cement interfaces[83].

2.4 Septic Loosening

Septic loosening i.e. deep infection after TEA has been shown to be the second most prevalent form of TEA failure. Septic loosening is a devastating complication that leads to revision surgery, significant morbidity, and puts a substantial burden and cost on the patients and health services. The rate of infection with TEA has been greater than other major joints arthroplasties as shown in table 2.3. Mohajer *et al (2014)* showed that the rate of infection after primary surgery ranges from 1 to 9 %. While the infection rate is considerably higher after revision (<40 %) in a TEA[84]. It is believed that the elbow joint is more frequently affected by the infection than the other main joint replacements because of the joint's relatively close proximity to the skin and therefore the exposed wound site. [85].

Table 2. 3: Rates of Infection in Different Joints 2014 [84]

Joint	Rate of Infection
Elbow	<9%
Knee	<2%
Shoulder	<1%
Hip	<1%

Prevention methods have been developed for the past two decades to lower the risk of infection. These methods include postoperative immobilisation, antibiotic-impregnated cement, laminar airflow with ultraclean air, and anti-microbial coating[86]. Due to these prevention steps, the rate of infection in TEA

has decreased to 3.3 ± 2.9 %[51]. Despite these improvements, the prevalence of septic loosening in the elbow joint is consistently higher as compared to the knee and hip joints.

There is no consensus on the definition of infection that is associated with prostheses. It varies from one study to another [87]. According to the Infection Diseases Society of America (IDSA), the prosthetic joint infection can be defined as[88]:

I. The existence of a sinus tract communicating with the prostheses.
II. Presences of purulence surrounding the prostheses.
III. The existence of acute inflammation seen on a histopathologic exam at the time of surgery.
IV. At least two or more intraoperative culture or a combination of aspiration and intraoperative culture that yield the same organism

It must be taken into consideration that infection can still be possible even if the above criteria are not met [88].

2.4.1 Route and Classification of Infection

Infection predominately originates from perioperative or post-operative exposure of the surgical site to pathogens. Most of the infection that occurs early after implantation is because of perioperative inoculation, where pathogens are introduced directly into the surgical site during or soon after surgery, and this type of infection is known as exogenous infection. This often leads to acute early-onset infection, which is identified and managed in the first few weeks to months post-procedure.

There is another type of infection that can occur due to pathogens from the bloodstream known as haematogenous infection, which is more difficult to manage. This infection can be most commonly acquired from dental infections, lungs, and urinary tract infections and more commonly associated as chronic or “low-level” infection[89]. It may occur soon after surgery or may take years to occur post-surgery. Depending upon the sign and symptoms after implantation, an infection can be classified according to the time of manifestation after implantation as shown in table 2.4 [90].

Table 2. 4: Classification of Infection with Respect to Time

Classification	Time of Occurrence
Early Infection	<3 months
Delayed Infection	3-24 months
Late Infection	>2 years

The early and delayed infection mostly occurs due to exogenous infection while the late infection is typically caused by haematogenous seeding. This traditional classification is not clinically useful however another classification guiding the optimal surgical management was presented. According to that, an early infection can be defined as an infection that manifests within 1 month after joint implantation. Acute haematogenous can occur within 3 weeks of the postoperative period. Chronic infection can either be an exogenous infection diagnosed 1 month after surgery or a haematogenous infection with signs continuing for 3 weeks[90].

2.4.2 Pathogens that Causes Septic Loosening

Infection-causing pathogens are mostly bacterial and generally mono-microbiota in nature [91]. Figure 2.3 summarises the microorganism that causes infection in the joint prostheses. Nearly all prostheses-associated infections are caused by gram-positive bacteria, with Staphylococcus Aureus (S. Aureus) and other Staphylococci being the most common bacteria. For patients with rheumatoid arthritis, S. Aureus is the most prevailing bacteria (37 %). Whereas Aerobic cocci, mycobacteria, fungi, and Polymicrobial haematogenous infections were the least found [84, 90].

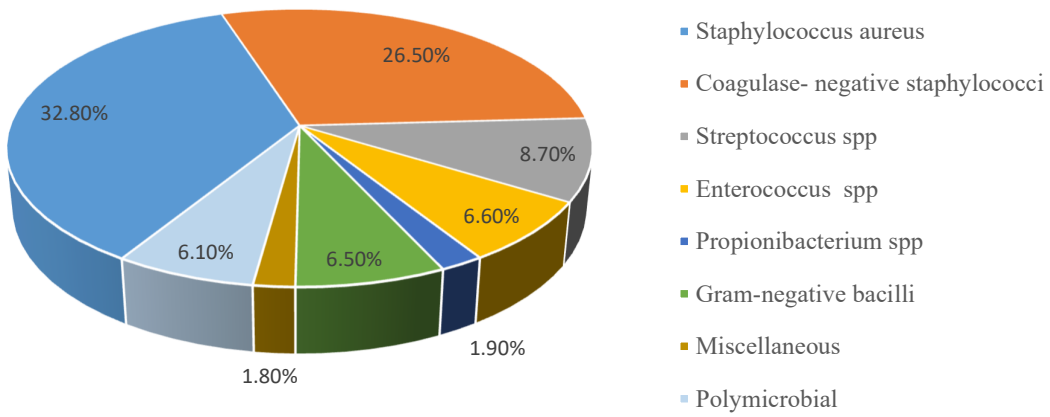

Figure 2. 3: Microorganism Causing Infection in the Joint Prostheses [84, 90]

2.4.3 Bacterial Biofilm (Pathogenesis)

Microorganisms are categorised into two different forms of life i.e. planktonic microorganisms and biofilms. Planktonic microorganisms are free-floating microorganisms and can replicate rapidly. These planktonic microorganisms are introduced into the surgical site via exogenous or haematogenous route and adhere to the surface of the prosthetic implant, which then develops fibrous exopolysaccharide material creating a protective biofilm. A biofilm is a coherent cluster of planktonic microorganisms embedded in a matrix having more resistance to antimicrobials [92]. Prosthetic implants provide an ideal environment for the microorganism to flourish[91]. Within the biofilm the microorganisms organize themselves into groups of a complex three-dimensional matrix, resembling multicellular organisms and producing extracellular polymeric substances namely polysaccharides [84]. They are metabolically less active and in the stationary phase of growth. In this biofilm stage they can withstand host immune response as well as different anti-microbial agents. The formation of biofilm is the critical step for the development of periprosthetic joint infection (PJI). A major complication in treating a biofilm is its high resistance to antimicrobial treatments compared to planktonic bacteria [84, 90, 91].

2.4.3.1 Development of Biofilm

Biofilm formation is completed through several stages namely cell adhesion, cellular aggregation, biofilm maturation, and cellular detachment as shown in figure 2.4. In cell adhesion, the planktonic bacteria adhere to the implant surface using its Flagella or Pilli [93].

Cellular aggregation is the second stage in which there are cell-to-cell adhesion and multilayer cellular proliferation, forming a microcolony. These colonies are surrounded by a self-secreted viscous fluid, which results in increasing the microbial density. Thus, a biofilm is formed on the surface of these colonies but at this stage, it's still relatively unstable and susceptible to eradication [94, 95].

The third stage is biofilm maturation, this maturation is achieved by physiological changes occurring within the biofilm i.e. regulation of flagella and Pilli. The accessory gene regulator (Agr) mainly regulates this stage (Quorum-Sensing). When mature the size of the biofilm is increased and has more resistance to eradication. The final stage is cellular detachment, where the mature biofilm releases planktonic bacteria from the surface. These planktonic bacteria then adhere to a different site of the implant surface, thus initiating an entirely new cycle [94, 95].

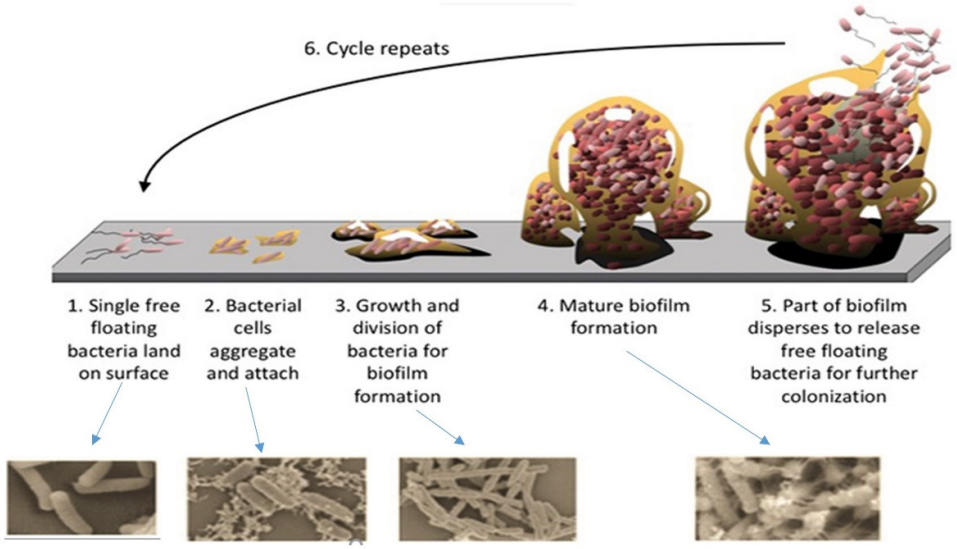

Figure 2. 4: Biofilm Life Cycle. Adapted from [96]

Understanding the formation of biofilms in PJI will not only aid in diagnostics but can explain the latency of infection after arthroplasty and identifying the pathogens responsible for the PJI.

2.5 Diagnostic Methods for Detecting Aseptic and Septic Loosening

Aseptic and septic loosening are the major reasons which limit the longevity of elbow prostheses. This lower survival rate of the elbow prostheses leads to revision surgery which poses a higher risk for the patients. Early detection is key for implant survival as it will allow the clinician to act accordingly depending upon the type of loosening. For the early sign of aseptic loosening the patients will be subjected to systematic drugs (parathyroid hormone peptides and prostaglandin EP4 receptor antagonists) to enhance the bone metabolism which will prevent the implant for further loosening. Also, the patients will be under rehabilitation protocol to avoid high impact activities [97]. In cases of septic loosening antibiotic treatment will be prescribed to the patients which will help in preventing the development of biofilm.

Different methods are used to detect loosening in elbow prostheses, which can be categorised by the condition and location of the usage. There are limited numbers of studies that describe the methods used to detect loosening (aseptic or septic) in elbow prostheses. However, these complications have been studied much more extensively in knee and hip arthroplasty. Figure 2.5 describes the current methods which are used to detect loosening (aseptic or septic) based on the data from total knee arthroplasty (TKA) and total hip arthroplasty (THA) experience along with the combination of TEA where possible.

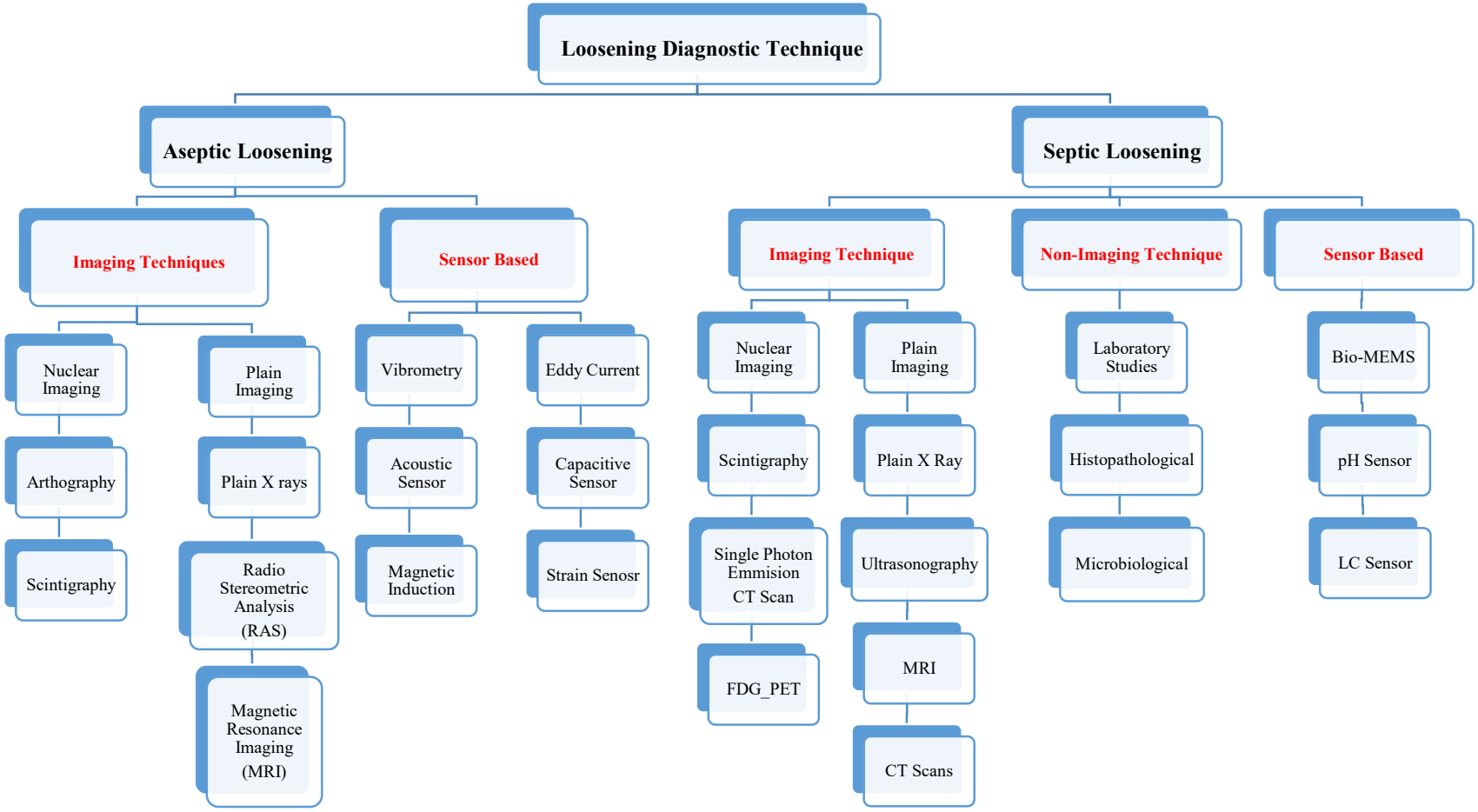

Figure 2. 5: Current Diagnostic Techniques to Detect Septic and Aseptic Loosening in the Total Joint Arthroplasty (Hip, Knee, and Elbow).

2.5.1 Imaging Techniques used to access Aseptic Loosening

2.5.1.1 Plain Radiography (X-rays)

Plain radiographs (X-rays) are the first method and most often used to identify the loosening of the elbow prostheses. X-ray is an imaging modality that remains quick, informative, and less cost-intensive than any other imaging technique to detect loosening. The limitation of this technique is that there are different radiographic criteria for implant loosening and interpretation of the X-ray requires adequate clinical experience, making it prone to subjectivity [98]. The radiological evaluation of implant loosening based on the presence of radiolucent lines is described by Morray, Adams, and Bryan [99]. Radiolucent lines are noted as a 'translucent' dark line that usually appears at the implant/cement or cement/bone interface on a 2D radiograph and has been associated with aseptic loosening of the prostheses. Table 2.5 shows the classification of radiolucent lines.

Table 2. 5: Different Types of Radiolucent Lines.

Types	Description
Type 0	No Radiolucency or < 1 mm thick line.
Type I	≥1 mm thick radiolucent line with <50% bone-cement interface.
Type II	>1 mm thick radiolucent line with >50% bone-cement interface.
Type III	>2 mm thick radiolucent line with a whole bone-cement interface.
Type IV	Gross loosening

However, X-rays remain a 2D assessment for the 3D disease process and are often inaccurate with low sensitivity and specificity. The implant is considered definitely loose at the late stages, type III or IV, in the radiolucent lines classification, any earlier stages are considered possibly or partially loose with no real certainty as to the extent of loosening. The use of machine learning (artificial intelligence) is gaining more interest in the assessment of radiographs. Currently the radiographs are assessed manually, which sometimes results in poor inter- and intra-observer reliability and low accuracy. More research is

conducted on analysing the radiographic automatically by the use of machine learning algorithms. Using this method, various data sets of the radiographs of different modes of loosening are collected and the system is trained to do the assessment of the plain radiograph and predict the aseptic loosening. Recently, Alireza *et al (2019)* developed a new deep learning algorithm which was able to predict the displacement in the position of the hip implant (mechanical loosening) automatically. The trained neural network achieves higher sensitivity (0.94) and fewer false-positive results than human observers [100].

2.5.1.2 Radio Stereometric Analysis (RSA)

RSA is a potentially powerful imaging technique that can provide a highly accurate and precise 3D assessment of the elbow prostheses' movement. In this technique, the surgeon embeds vitallium and titanium markers in the relevant bony structure and the specified area of the implant during surgery in order to establish a rigid body segment for analysis. Two X-rays at two different views along with a calibration box are used simultaneously for radiographic examination [101]. There are limited numbers of studies on RSA of the elbow joint, with the mean precision reported at 0.29 mm translation and 0.66 degrees rotation migration [102]. This achievable accuracy makes an ideal tool for surgeons to study the micro-motion of the implant humeral component in total elbow prostheses[103]. However, the limitation of this method is that it is only accepted as a clinical research tool and can therefore only be used on a limited number of patients that meet the inclusion criteria. Another reason for its limited use in the elbow joint is the limited size of the surrounding bone, which leads to over projection and metal artifacts.

2.5.1.3 Arthrography

This technique is used in addition to X-rays when there is a case of unsolved pain in an artificial joint [104]. In this technique, the periprosthetic membrane around the implant and cement-bone interface is visualized by inserting a contrast agent into the joint. The contrast agent role is to enhance the image accuracy, to identify area of loosening which are not visible on plain radiographs. The criteria of loosening are based on the infiltration or leakage of the contrast agent [105]. Compared to the plain radiographs it has higher sensitivity and specificity (about 4 % higher) [106]. The sensitivity of this

technique can be increased by using the digital subtraction method. The limitation of this method is the reduced resolution of the arthrogram as a result of joint motion [107].

2.5.1.4 Bone Scintigraphy

In recent years, to find certain abnormalities in the bone where a prosthetic is implanted, a nuclear medicine technique known as bone scintigraphy is used. It is a nuclear scanning test in which the patient is injected with a radioactive drug that emits gamma rays[108]. Then the patient is scanned through gamma cameras that detect the radiations. This technique is sensitive to those areas where unusual bone rebuilding activity is occurring. Limitations of this technique include time consumption, relatively expense, and expertise required for interpretation of images [108, 109].

2.5.1.5 Magnetic Resonance Imaging (MRI)

MRI technique is an effective method that allows comprehensive imaging for assessing the tissue surrounding the elbow prostheses. By providing important information which could aid in detecting any complication regarding elbow arthroplasty. In this method, a homogenous magnetic field is applied to the specific area of the body where the prosthesis is implanted. The region where the implant is situated shows magnetic field heterogeneity due to implant ferromagnetic properties [110]. This method provides 3D imaging with good soft-tissue contrast and no ionisation radiation. Limitations of this method are varying sequencing protocol, time consumption, cost, metal artefact, and adequate clinical expertise for interpreting MRI images [111].

2.5.1.6 Computed Tomography (CT)

CT scans are relatively cost effective, easy to perform, readily available, and provides a superior spatial localisation to the plain radiographs. The scan uses computers and rotating X-rays to create a cross-sectional image and provides detailed information about various parts of body i.e. soft tissue, bone and blood vessels. In orthopaedic implants X-rays usage was limited due to radiographic imaging artefact produced by the metal implants, but the development of dual energy acquisition combined with metal artefact reduction algorithm (MAR) have improved the quality of CT scans by reducing these metal artifact [112].

Currently, these CT scans are combined with single photon emission computed tomography (SPECT) to increase the sensitivity offered by bone scintigraphy. SPECT combined with CT allows to investigate the bone's metabolic activity surrounded the prosthesis and is less prone to the MRI to image degradation due to metal artefact [113]. Although there has been an optimising technique to reduce the metal artifact but this method is limited by the creation of different pattern of artefacts by various metals of the prostheses that need to be minimised [113].

2.5.2 Sensor Based techniques used to detect aseptic loosening

2.5.2.1 Vibrometery

The use of sensors for the detection of loosening was first investigated and tested on total hip arthroplasty and was based on measuring resonance frequency and damping[114]. This method relies on the principle that when the implant is inserted into the bone it forms a bonded unit having its own natural frequency and when harmonics forced vibration is applied resonance occurs. This method uses a non-invasive technique to monitor the natural frequency where an external accelerometer is used to measure the vibration at the hip while an external shaker is used for the exciting force vibration at the condylar region of the knee as shown in figure 2.6. In resonance frequency analysis the acoustic behaviour of a well-fixed implant is linear while the loosened is nonlinear[114]. The method is restricted by the accelerometer's low-signal to noise ratio and its sensitivity and specificity are only 20 % greater than plain radiographs[115]. Similar to the previous two imaging methods, one of the limitations is the training required to correctly interpret signals.

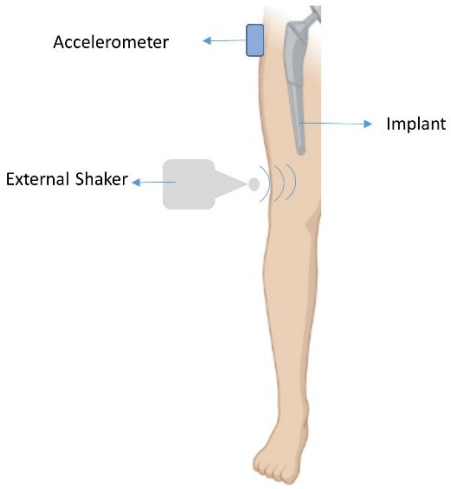

Figure 2. 6: Illustration of the Vibrometry Method for the Detection of Aseptic Loosening.

2.5.2.2 Magnetic Induction Approach

Similar to the vibrometry approach, Ruther *et al (2013)* introduced a new diagnostic technique. Instead of using an external shaker for introducing mechanical excitation, the excitation was driven by magnetic induction and the piezo crystal oscillators were embedded into the stem of the implant as shown in figure 2.7. The variation in the damping frequency of the piezo crystal oscillator determines the state between the bone-implant interfaces. The crystal is vibrated by the use of the external magnetic field coil. The vibration generated by the crystal produces different damping frequencies which are measured by the accelerometer externally located at the skin. The outputs signals can distinguish between the various states of the bone implant when it is excited by the constant frequency [116].

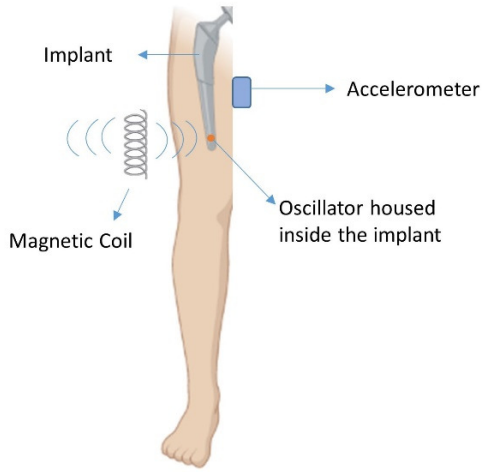

Figure 2. 7: Illustration of Magnetic Oscillator Method for diagnosing Aseptic Loosening.

The limitation of this method is that due to resonance frequency shift it is difficult to distinguish between the various states of loosening also this method cannot be used for continuous monitoring as it will require an external source for excitation and measuring [116].

2.5.2.3 Acoustic Signals

There is another method for the detection of the stability of the implant which is similar to the vibrometry approach. In this technique instead of using an external shaker (providing input vibration). The implant is struck hard with a metallic device to provide external excitation as highlighted in figure 2.8. This excitation is detected by the use of a microphone attached to the other side. The loosening of the implant is identified by the variation in the frequency of the excitation. As the stability of the implant increases the resonance frequency increase. Unger *et al (2009)* observed the increase in frequency from 400-800Hz [117].

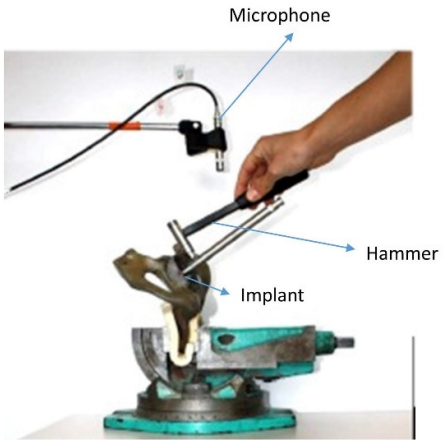

Figure 2. 8: Illustration of Acoustic Method Adapted from [118] .

Another study by Davies *et al (1995)* used an ultrasonic approach to identify the bone implant interfaces shown in figure 2.9. In this method the ultrasonic wave is emitted through the cement and implant and the reflected wave is analysed by its amplitude and arrival time. In this technique only two phases were identified the bonded and debonded one [119].

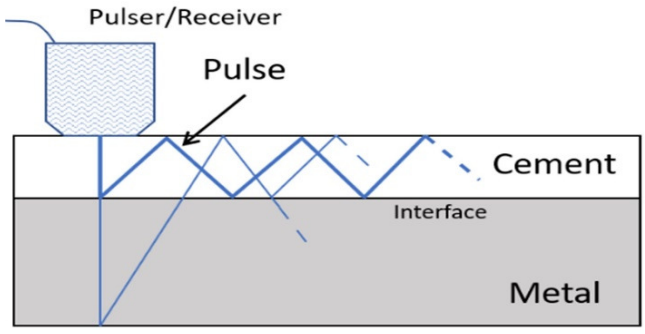

Figure 2. 9: Illustration of Acoustic Method using ultrasonic excitor and receiver [118].

The major limitation of this technique is that it is patient–dependent and for each patient it will require optimisation because of the surrounding tissue on wave propagation. Other drawbacks include the external excitor and reader units, which prohibit its range and the possibilities of continuous monitoring.

As these electromechanical components are attached to the patient's body, it will cause discomfort to the patients while performing daily life activities.

2.5.2.4 Eddy Current Sensor

Recently this new sensor technology is being developed as an implantable system to detect the micromotion of the joint prostheses by using inductive sensors based on eddy currents as shown in figure 2.10. In this technique an inductive coil is placed near the surface of the prosthesis that generates a primary magnetic field. When the prosthesis comes in its proximity due to implant migration, the eddy current flows into it and it generates a secondary magnetic field that opposes the primary one. This results in changing the impedance characteristics of the coil and means prosthesis migration can be predicted. Under laboratory conditions, a resolution of 0.3 mm can be achieved. This technique seems quite promising and can be placed in the guided holes of the bone (entryway that surgeon uses to guide their instrument) thus, no alteration will be required in the prostheses design [120].

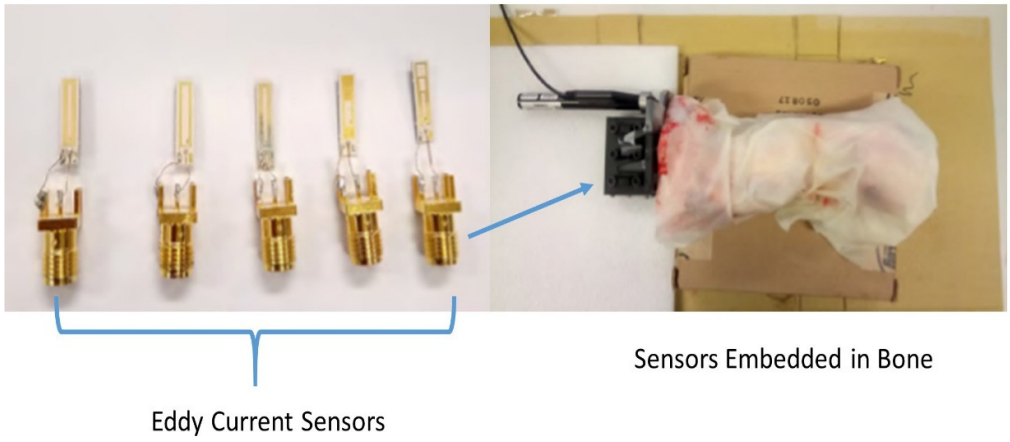

Figure 2. 10: Illustration of Eddy Current Sensor Adapted from [120].

However, this work is in its experimental phase and will require further development before clinical use. The main shortcoming of this technique that needs to be overcome is its lack of biocompatibility. Another limitation is its sensitivity which reduces as the distance between the coil and prostheses increases [120].

Similarly, in another study a eddy current sensor was combined with the tunnel magneto resistive sensor (TMR) for further enhancing its detection sensitivity by measuring the indirect magnetic field generated by the coils [121]. The result showed that by combining these two methods increased the relative change in detection by 1.5%.

Measuring the direct change in magnetic field to detect implant migration has not been explored yet and it is an untapped field of research for detecting micro motion in-vivo and that could be explored further.

2.5.2.5 Electrical Impedance Tomography

The use of the electrical impedance spectroscopy to assess the bone-implant interface was conducted by Arpaia *et al (2007)*. In which they used two electrodes attached to the outer surface of the skin. The electrodes provide the variable current on the skin's surface and measure the voltage drop between the electrodes as shown in figure 2.11. The results state that the impedance increases for a decreased level of integration [122].

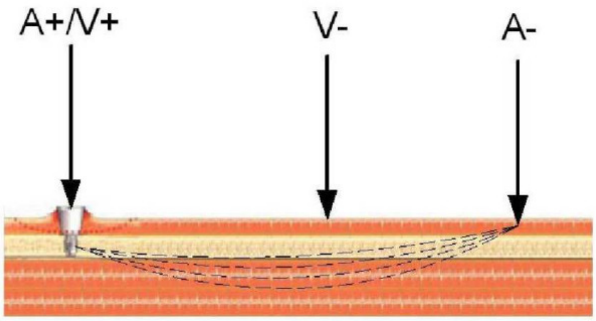

Figure 2. 11: Illustration of the electrical impedance technique and its working principle [123].

Using the same concept Hamid *et al (2020)* developed a new method for detecting the micromotion of the prostheses by using self-sensing bone cement in combination with Electrical Impedance Tomography (EIT) figure 2.12. In this technique, micro/nano-sized piezoresistive material particles are combined with the bone cement. Using EIT, conductive imaging is produced which can monitor the bone-implant interface. This technique is only implemented via computer simulations and it still requires

experimental trials to be published along with the fabrication of piezoresistive bone cement composites [124].

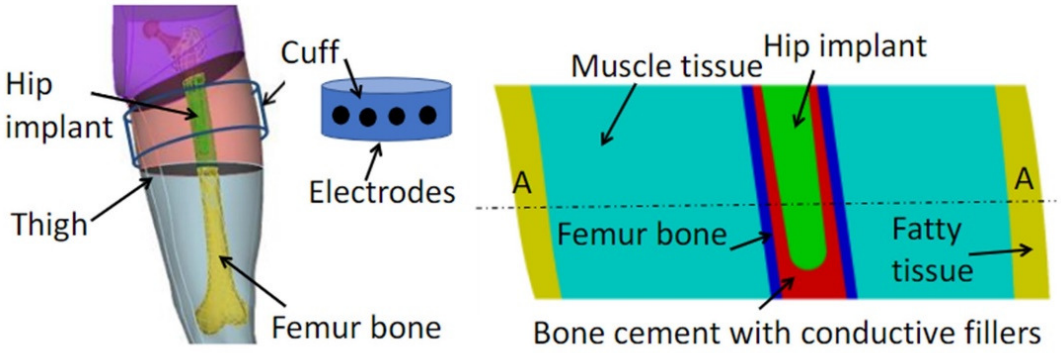

Figure 2. 12: Illustration of Electrical impedance technique by using nano piezoresistive materials [124].

The limitation of this technique is that it is currently carried out *In Vitro* and it requires an external component to be attached to the patients which is impractical for continuous monitoring.

2.5.2.6 Strain Sensors

In this diagnostic technology, the implant loosening was observed by the change in the strain of the bone growth. Burton *et at (2019)* developed a co-surface sensing technology that was able to measure radial and axial strain of the bone. The sensors were attached to the parallel plate capacitors. Their dielectric charge varied according to the change in the strain [125].

Similar to this concept McGivray *et al (2015)* developed a biocompatible sensing technology to detect fracture healing in the implanted fracture fixation plate by using planar capacitors and resonance circuits to monitor any physical loading. In both strain sensing technologies, powering of the sensors was performed through magnetic induction and the change in the capacitance was measured by the change in the resonance frequency [126].The limitation of this technology is that it requires an external power source for monitoring and requires a controlled environment to detect any change, as electromagnetic noise can alter the results.

2.5.2.7 Capacitive Sensors

Marco *et al (2021)* developed a new diagnostic technique to detect the bone-implant interface by using co-surface capacitive sensors. This technique is similar to the strain sensor but instead of measuring the change in capacitance by applied strain. In this technique, the capacitance is changed as the bonding between the bone and implant starts to vary as shown in figure 2.13. This technique is only used *in vitro* and the limitation of this method is that it needs to be attached to the implant surface which might affect the biocompatibility of the implant. Further work is required in this technology to resolve these factors along with the powering and data transmission [127].

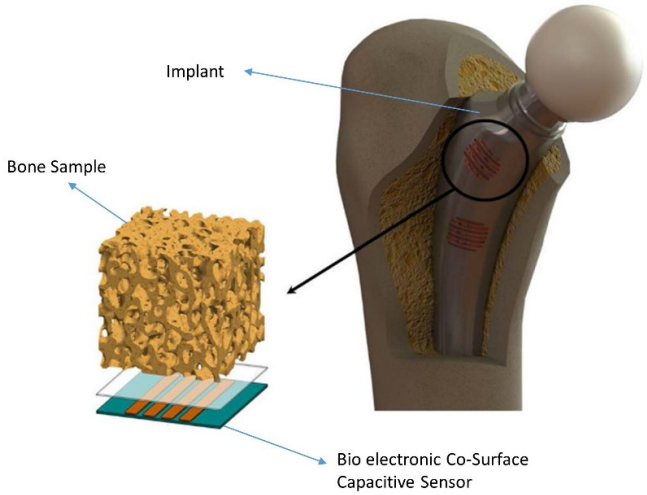

Figure 2. 13: Illustration of Capacitive sensor Adapted from [127].

2.5.3 Imaging Techniques for detecting Septic loosening

Imaging offers the easiest, most patient-friendly, and non-invasive screening process to detect any abnormalities of the bone and its surrounding tissue which helps in the prediction of implant-associated infection. These imaging techniques/radiographs range from various wavelengths and mechanisms and are capable to visualise the functional localisation of the infection around the implant that plays a significant role in the clinical diagnosis of the infection. There are two types of radiographic technique which are used to detect infection in the joint prostheses: radioisotopic and non-radio isotopic imaging

technique. Among non-radioisotopes 4 methods are used in the diagnostic approach to septic loosening[128]:

- *Normal radiographs (x-ray),* they are used to assess any sinus track surrounding the prostheses. These radiographs have a sensitivity of 14 % and specificity of 70 % in the detection of any infection that is associated with the implants [129]. They only provide a crude analysis of the soft tissue and bone and serve as a reference to monitor any abnormalities. It has also been reported that 50 % of the radiographs remain normal regardless of the existence of the infection [129].
- *Magnetic resonance imaging (MRI),* used for providing information on the soft tissue around the prostheses.
- *Computed tomography (CT),* gives an accurate assessment of bone structure along with the method for removing any prostheses-related artifact. Depending upon the type and material of the implant the severity of the artifact will vary. Due to recent technical improvement, the striking artifact of the x-rays is reduced by the use of beam hardening. Cyteval et al *(2012)* reported that if only one soft tissue abnormality is considered as an infection criterion then the CT demonstrates 100 % sensitivity and 87 % specificity. If joint distention is used the sensitivity is 83 % and the specificity 94 %. Detection of the sinus tracks is quite difficult in the CT scans [129].
- *Ultrasonography,* is used for detecting joint effusions and guide arthrocentesis[130]. They are mostly used for the analysis of those soft tissues area where lesions are accessible i.e. knee, elbow, ankle but less in the hip and spine where the depth and bone structure limits the acoustic window.

The shortcomings of these imaging techniques are that they cannot be used to determine that the infection is present or not. They can only help to support other techniques used to confirm infection such as microbiology swabs and symptoms consistent with infection. In MRI and CT detecting periostitis has 100 % sensitivity but for detecting infection the sensitivity is 16 %.[130].

In radioisotopic imaging techniques, the following are methods that are used to identify infection:

- ^{18}F-fluoro-2-deoxyglucose positron emission tomography (FDG-PET), having a sensitivity of 91-100 % and specificity of 9-97 % in diagnosing infection[130].
- Single-photon emission computed tomography (SPECT), enables more localisation to the radiotracers uptakes as compared to other radionuclide methods.
- Scintigraphy using radiolabelled neutrophils, can show increased uptake of (^{99m}TC)-labelled diphosphonate on the surface of the bone in cases of prostheses infection[84].

There are also other investigational methods that are used as a nuclear imaging technique for diagnosing infection. The main drawback of this radioisotopic imaging technique is that they are laborious, expensive, and limited data limits value due to artifact and data inconsistency[84].

2.5.4 Non- Imaging Techniques for detecting Septic loosening

2.5.4.1 Laboratory Studies

Routine blood tests, particularly raised erythrocyte sedimentation rate (ESR), white blood cell count, and C-reactive protein (CRP) may suggest the identification of infection but these markers will give high false-positive rates in the early postoperative phase [89, 131].

ESR combined with CRP yields better results than an individual one. The different threshold of CRP and ESR has been defined to predict infection. However they are non-specific and their measurement is affected by several factors such as age, sex, medication, severity, underlying diseases, and other unknown factors [132].

It should be noted that the normal result from these tests does not mean that the infection is excluded, and the abnormal result may be because of infection elsewhere in the body.

2.5.4.2 Histopathological Studies

Histopathological analysis of intraoperative frozen specimens of periprosthetic tissue is an important tool for a diagnosis of infection. It has excellent accuracy in predicting infection but moderates in ruling out a diagnosis. It has sensitivity of >80 % and specificity of >90 % [133]. Acute inflammation in

periprosthetic tissue varies from 1-10 neutrophils per high-power field in x 40 magnification but >5 neutrophils are indicative of periprosthetic joint infection (PJI) [87].

The limitation of these studies is insufficient information reported about the degree of inflammatory cell infiltration, which varies from one specimen to another from the same patient. Inter-observer variability is also high, the process is time-consuming and no information regarding the bacteria causing the infection [84, 87, 133].

2.5.4.3 Microbiological Studies

Conventional microbiological studies include synovial fluid aspiration, gram staining, and culture testing to positively identify microorganisms' specific to the infection site. In synovial fluid aspiration, the pathogens can be detected between 45-100 % [134]. Synovial Fluid aspiration along with differential cell count showed good results in predicting infection in the preoperative phase. It has sensitivity up to 75 % and a specificity of 95 %[131].

Gram Staining of periprosthetic tissue and synovial fluid is not recommended because it has a low sensitivity of 26 % and high selectivity at 97 %. Similarly, Swab culture should also be avoided because of its low sensitivity[84]. Although microbiological cultures are the most reliable in identifying the microbes and therefore determine the most appropriate antibiotics to use, due to time constraints, a course of antibiotics is often administered before the results are received. This adds to the growing global problem of antimicrobial resistance, thus calling for a more rapid and time-effective method of positively identifying infection. There is a new diagnostic method introduced in the field of microbiological studies to rapidly detect the microorganism causing the problem. These new diagnostic tools are:

Micro-calorimetry

This technique measures the amount of heat produced by the bacteria in small quantities (1 to 10 CFU/mL). It is a promising tool for the rapid detection of micro-organism but the limitation of this technique is potentially high cost, lack of standardisation, and method complexity[135].

Sonication

Cultured samples obtained from the sonication of a removed prosthesis provide more sensitivity than conventional tissue culture for disrupting adherent bacteria from the biofilm. In this method extracted orthopaedic implant (implant failed due to septic loosening) is sonicated in a saline solution to extract microorganisms from the surface of the implant, followed by culturing of the sonication fluid to identify the type of biofilms that had adhered to the surface. According to Trampuz *et al (2007)*, this technique has a sensitivity of 78.5 % and a specificity of 98.8 % [136]. The drawback to this method is that it requires removal of the implant (revision surgery) and can therefore only be used in the late stages of infection to confirm the bacterial culture.

2.5.5 Sensor-based techniques for detecting septic loosening

There is limited data published on detecting septic loosening via the use of in-vivo sensors. The following are implantable sensors-based diagnostic techniques that are currently in experimental trials to detect infection associated with the joint prostheses.

2.5.5.1 Bio-MEMS Sensor

Garth *et al (2005)* proposed an engineering approach for detecting infection in the joint prostheses by developing a MEMS biosensor. The working principle of this biosensor was based on quorum sensing. According to the paper, when the bacteria start to form a biofilm they communicate with each other through quorum sensing. Interference with their quorum-sensing signalling system (RAP-TRAP) will help in predicting and curing the infected prostheses [137].

2.5.5.2 pH Sensor for Infection Detection

Arifuzzaman *et al (2019)* developed a chemical-based pH sensor (hydrogel), which can detect the local change of pH around the prostheses. According to the study, the tissue and surrounding environment around the prostheses is in the acidic range of 4 – 7 pH when it is subjected to bacterial colonisation (infection) [138]. The sensor was able to detect the change in pH by varying its diameter which was measured radiographically. The sensor showed a promising response in the cadaveric experiment but one of the limitations of this method was the size of the gel should be at least 1mm so that the change

in diameter can be visible. Another limitation was that it cannot be used for continuous monitoring and requires a physical barrier to protect from a direct application of force [138].

2.5.5.3 Wireless (LC) Temperature Sensor

Karipott et *al (2018)* developed an embedded wireless temperature sensor to detect infection for orthopaedic implants. The working principle of the sensor was based on the inductive capacitive resonating sensor (LC sensor) that can be remotely detected via an external detection coil. The sensor was able to detect a change in temperature via a change in the sensor Q factor. This method is still in experimental trials and yet to test in medical-grade polymers. Furthermore, the mechanical properties of this sensor need to be quantified [139].

2.6 Summary of Findings

In this chapter, literature was reviewed in detail in terms of the complications that are associated with TEAs, major factors that leads to revision surgery and currently available diagnostic tools to detect both aseptic and septic loosening. After reviewing published studies in these intersecting fields, the following knowledge gaps were identified:

- The most common factor that leads to revision surgery is aseptic loosening followed by septic loosening (Figure 2.1). In the elbow implant the revision burden is higher as compared to the other major orthopaedic implants (Table 2.1). The currently available diagnostic tools are not feasible for detecting early sign of loosening (Table 2.6).

Table 2. 6: Comparison of Non-Imaging based Diagnostic technique to detect Loosening.

Techniques	Operative Non-Invasively	Biocompatible	Integration in Exciting Implants	Continuous Monitoring	Sensitivity	Multiple Axes Detection	Differentiate between Aseptic and Septic
				Aseptic Loosening			
Vibrometry	✔	✔	✔	✖	✖	✖	✖
Acoustic	✔	✔	✔	✖	✖	✖	✖
Eddy Current	✔	✖	✔	✔	✖	✖	✖
Electric Impedance	✖	✖	✔	✖	✔	✖	✖
Strain Sensor	✔	✖	✖	✖	✖	✔	✖
Capacitive Sensor	✔	✖	✔	✔	✔	✖	✖
				Septic Loosening			
Bio Mems Sensor	✖	✔	✖	✖	✖	✖	✖
pH Sensor	✔	✔	✔	✖	✔	✖	✖
LC Sensor	✔	✔	✖	✖	✖	✖	✖

- The imaging-based techniques are used as a gold standard to monitor the implants but they are not suitable for constant monitoring, as it will require patients to have regular visits to the radiologist and regular radiation, which would be unfavourable to the patients' health long-term. The field of bioelectronics medicine has recently attracted a lot of research to address these shortcomings. The reduction in the revision surgery is possible by developing a highly sophisticated implantable device that not only detect early signs of loosening but can also be continuously monitored.
- There has been progress in the development of the electronic devices to detect loosening. Table 2.6 shows the comparison of sensor-based orthopaedic implant diagnostic tools. From this comparison it seems that there is a need of a sensor-based diagnostic tool that can be easily integrated within the existing orthopaedic implant along with detecting early sign of loosening at multiple axes, along with differentiating between septic and aseptic loosening. Currently, there is no such tool available that can differentiate between septic and aseptic loosening.
- The use of magnetic fields has some promise and already been explored in the form of indirect eddy current sensors however there is potential to explore this field more.

2.7 Conclusion

In conclusion, there is a need for a rapid and accurate diagnostic tool that could detect early loosening of the prosthesis without any radiographic exposure, which matches both the mechanical and biological complexities of the elbow prosthesis. The task of developing such a tool will require innovative multidisciplinary approaches and effective engineering solutions to overcome the considerable technical and technological challenges that must be overcome. The recent developments in this field show promise and suggest the solution for detecting early septic and aseptic loosening is to embed sensors in the existing prosthesis making it "smart". The advantage of embedding sensors will be that firstly, it will allow for continual remote monitoring and that will provide feedback without any exposure to

radiographs and visits to the hospital. Secondly, the data collected will reveal valuable dynamic information about the prosthesis and joint behaviour, which has not been done to date and will help drive more effective prosthesis designs in the future.

2.7.1 Diagnostic System Functional Requirements

The detection technique needs to fulfill the following specification requirement to overcome the limitation of existing and developing diagnostic tool.

- As highlighted in the literature, less than 150 μm movement between the implant and bone is required to avoid fibrous tissue and promote ingrowth of bone. Beyond this limit, there is a risk of loosening. Standard X-ray can detect loosening up to 2 mm. Therefore, the new diagnostic tool should be able to detect aseptic loosening with a resolution of 150 μm or less, without using any radiographic exposure.
- The technique needs to be non- invasive with minimal modification in the implant design and can be easily integrated with the existing orthopaedic implants.
- The majority of the new tools encounter biocompatibility issues along with detection in single axis only. The new tool needs to be biocompatible with loosening detection capability in multiple axes.
- The technique should be able to differentiate between septic and aseptic loosening.
- The system should have a low power consumption and easily be integrated with the existing data processing units.

2.8 Ph.D. Aim and Objectives

The aim of this Ph.D. is to develop a prototype diagnostic technique encompassing sensors that will have the ability to detect aseptic and septic loosening in the elbow prosthesis.

The objectives in order to achieve this aim are as follows:

1. Develop a sensing technique, prototype, and algorithm that interprets inputs into displacement under static and dynamic movement at micron or sub millimetre level
2. Design and build a test rig that mimics the real bone implant interface scenario and can test the prototype system at various applied loads.
3. Analyse the effect of different biomaterials and how different movement patterns (linear and angular) will affect the system.
4. Analyse the effect of implant movement at various scenarios (un-cemented, semi-cemented, and fully cemented).
5. Develop a biocompatible chemical sensor that can inform of the presence of infection, testing its performance at various pH levels that can be integrated with the displacement sensor.
6. Evaluate the developed prototype sensors and suggest future development.

3 Chapter 3:

Development of a Diagnostic Technique to Detect Early Migration of Elbow Joint Prostheses

Summary

Migration of an implanted prosthesis due to aseptic loosening is difficult to detect without regular radiographic imaging. In this chapter, a low-cost, non-radiographic, robust diagnostic technique is designed and validated to detect the migration of the humeral component of an elbow prosthesis. The system consists of a single magnet with a single sensor and migration data is based on the variation in the magnetic field. The magnetic sensor was enclosed in titanium alloy and a magnet was embedded within a cement restrictor in the humeral bone enclosed in ultra-high molecular weight polyethylene (UHMWPE). A layer of bone cement was then placed between the enclosed magnet and sensor. An algorithm linked with a Savitzky-Golay (SG) filter was developed that could decouple, convert, and filter the magnetic field signal to provide both the linear and angular displacement measures. Magnetic field distribution of different size of magnets were also analysed to see which one provide a wider and stronger field. The system was also designed to eliminate the crosstalk and non-linearity effect of the magnet. The highest resolution the sensor achieved was 0.3 mm with a detectable linear migration range of 0.3 mm to 4 mm in the x/y axis and between 8-15 mm in the z-axis (the axis of the humeral canal). The detectable rotational range was 0.5 to 3.0 degrees in the x/y axis. The repeatability of the calibrated sensor was analysed and showed a standard deviation of 0.05 mm over 150 cycles. The resolution was dependent upon the operating conditions and sensor positioning. There was no interference from the titanium alloy, bone cement nor the UHMWPE. This sensor system offers an alternative non-radiographic option for measuring the migration of implanted prostheses. The work presented in this chapter forms the basis for a paper that is now published in the peer-reviewed journal IEEE Access [140].

3.1 Introduction

Aseptic loosening of the elbow prosthesis is considered to be the key contributor in the failure of total elbow arthroplasty (TEA) encountering 47 % of the revision [28, 51, 52, 63, 64, 141]. To date, the conventional method to detect aseptic loosening is by plain radiography. Particularly in the higher risk stratification group as recommended by the Australian Orthopaedic Registry [142]. The main limitation of these imaging methods is they do not have the needed temporal resolution in detecting the early signs of loosening along with non-intrusiveness as most of them can only be carried out in clinical laboratories which makes them unable to maintain the continuous monitoring of the prosthesis throughout the daily life routine of patients. Furthermore, these techniques expose the patients to ionizing radiation, and in some cases require injections for additional radio-opaque agents and have limited applicability for inter-operative assessment.

Considering that the TEA have a 20 - 40 % higher rate of complications when compared to TKA and THA [102] a solution is required, that can effectively monitor the prosthesis position remotely and detect early signs of loosening without using any radiographic exposure, which will aid in minimising the revision procedures. Embedding sensors in prostheses have been performed in other joints to measure force, kinematics, and temperature. However, an approach to detecting aseptic loosening using embedded sensors in existing prostheses with minimal modification of implant design making the prostheses "smart" or "instrumented" has not previously been explored. The first instrumented prosthesis was designed for the hip by Bergmann et al. *(1993),* which included strain gauges to measure force [143]. Recently Soares et.al. *(2021)* developed an effective microscale sensing technology that can detect the changes in the bone-implant interface using capacitive sensing [127]. Similar sensors were designed for the knee to measure the tibiofemoral compression force. Arami, A., et al *(2013)* designed a smart instrument for the knee prosthesis that has been developed for estimating the kinematics of knee prostheses during different movements. Also, another instrumented knee prosthesis was developed with self-powered force measuring capabilities [144, 145].

To date, no instrumented prosthesis has been designed for the TEA or other joints that can monitor the prostheses' performance and give feedback despite its high complications and loosening rate compared to other joints (detailed in chapter 2). Therefore, the work presented in this chapter focuses on the development of a low-cost, non-contact, X-ray-free technique to detect aseptic loosening of the elbow prosthesis using a system of embedded sensors.

In order to develop such type of detection technique that has sensors embedded in a prosthesis, the selection of suitable sensors that fulfill the requirement (aseptic loosening detection) is needed. The following section describes the sensors that have the capabilities to detect loosening (position/displacement) and can easily be embedded in the existing prosthesis.

3.1.1 Sensor Selection

There are various sensors available that can determine the spatial position of the target without any contact. They are classified as position sensors, displacement sensors, proximity sensors, and vibration sensors. Position sensors give the position of the targeted object with respect to the specified co-ordinate system. Displacement sensors gives the relative displacement of the targeted object. Proximity sensors report a binary presence or absence of stimulus with limited scope for interpolation of movement, and the vibration sensors provide the amplitude and frequency of the targeted object that is under oscillation [146-148]. To detect the migration of the implant (aseptic loosening) at micron level displacement sensors or position sensors are required. So, that they can detect the position or motion of the implant without any contact.

These sensors can be categorised into 5 different types based on their sensing mechanisms; capacitive sensors, inductive sensors, optical sensors, ultrasonic sensors, and magnetic sensors. Table 3.1 highlights the benefits and shortcomings of each sensing mechanisms.

Table 3. 1: Comparison of different types of Displacement/Position sensors [146-148]

Sensors	Advantages	Disadvantages
Capacitive	Highly sensitive	Short Range and performance effected by Biomaterials
Inductive	Long Range	Low Sensitivity and effected by Biomaterial
Optical	Highly sensitivity and resolution	Requires line of sight and short-range
Ultrasonic	Not affected by Biomaterials and high range. Non-Contact.	High losses in Bone.
Magnetic	High Sensitivity, detect in multiple axes, differentiate between various displacements. Non-Contact.	Short Range, Performance Affected by Ferrous material

The multi-axis sensitivity, distance measurement capability and limited range of the magnetic sensor are promising characteristics that fulfill the application of the instrumented prosthesis for loosening detection. The magnetic sensor was selected for this study, and the type of sensor chosen is mentioned below.

3.1.2 Magnetic Sensor Selection

There are different types of magnetic sensors which utilise a variety of techniques and technologies to detect and measure the magnetic field. Recent development in commercially available magnetic sensors also permit the estimation of the intensity and orientation of the magnetic field in multiple axes with compensating thermal and low-frequency noise effects [149].

The different types of magnetic sensor techniques include Hall Effect, anisotropic magnetoresistance (AMR), giant magnetoresistance sensor (GMR), Fluxgate effect, induction coil effect, MEMS Lorentz force, and other magnetic phenomena, which has the capability to measure the magnetic field with resolution from pico Tesla (pT) to milli Tesla (mT) with a bandwidth from DC to MHz. The performance of these technologies used in different magnetic sensors can be found in Lenz & Edelstein 2006 [150]. Among all these techniques and technologies, the Hall Effect sensor is most commonly used in industrial

applications (current sensing, proximity sensing, and position sensing) because of its compact size, low cost, and ability to easily integrate with any data acquisition system [151].

Hall Effect sensors consists of a thin sheet of semiconductor known as Hall element, a continuous current is flowing across it and when there is no magnetic field the current distribution is the same, no potential difference is seen. However, when this sensor is subjected to any magnetic field(B), a Lorentz force(F) deflects the charge carriers(e) due to the electromagnetic field (equation 1) [152].

$$F = e(E + V \times B) \qquad (1)$$

Where E is an electromagnetic field and V is voltage. This deflection changes the direction of the current in the medium and results in an electrical field and a potential difference is seen i.e. Hall voltage. This voltage (V_H) is directly proportional to the magnetic field (B) and current (I) and inversely proportional to the carrier charge (e), its density (n), and thickness (h) of the film.

$$V_H = \frac{IB}{neh} \qquad (2)$$

The Hall voltage can be measured by inserting two metallic plates across the medium as shown in figure 3.1.

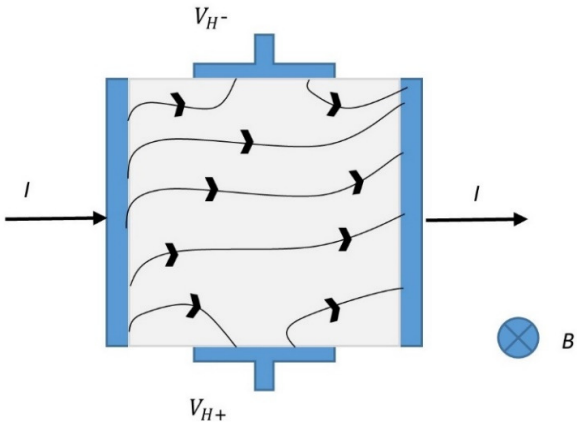

FIgure 3. 1: Working principle of the Hall Effect sensor to measure Hall voltage across two metallic plates.

One issue with the Hall sensor is that to increase the sensitivity of the sensor higher current is required which increases the power consumption but now the commercially available Hall Effect sensors have compensated that issue and can measure the magnetic field in 3- axes by utilising very low power. The sensor also includes a temperature sensor for thermal drift compensation and digital output via I2C or SPI bus to integrate with data acquisition. All these are embedded on a single chip typically 3 mm x 3 mm x 1 mm size.

Magnetic sensors can further be divided into two types based upon their excitation method: coils and permanent magnets. In the majority of the relative displacement detection, magnets are used. Depending upon the type of detection the magnet magnetisation is selected e.g. radially magnetised magnets are used for circular rotation detection while axially magnetised for linear/angular detection. The sensors are fabricated in such a way to output orthogonal signals with respect to the magnetic field [153, 154].

In addition to these features, the magnetic sensors do not require any free line of sight if intended to used inside the human body because the human body has transparency to the magnetic field [155], which make them suitable to be used in orthopaedic implant to provide the position or any micro displacement of the implant. Based on these characteristics a 3 axis Hall Effect magneto resistive sensor (TLV493D, Infenion, Austria) was selected for this study it has a resolution of 98 μT/LSB and sensitivity of 7.7 to 30.8 LSB12/mT which satisfies the specification requirement for detecting any small change. Also, as the device will be embedded in the human body the power consumption needs to be minimum. This sensor provides low operating current consumption along with simple integration with data acquisition device via I2C communication which satisfies the specification requirement of the diagnosing system (Chapter 2, section 2.7.1).

A limited number of studies have been carried out on embedding magnetic sensors in prostheses to detect kinematics and force [144, 155]. From the literature review, it is apparent that the use to this technique to detect early migration of the prosthesis is a novel introduction to the field and could therefore provide an early diagnosis of aseptic loosening.

Therefore, the aim of the work presented in this chapter is to develop a novel, low-cost, and radiograph-free detection technique to detect aseptic loosening of elbow prostheses using magnetic sensors.

To achieve this aim the following objectives are listed below:

- Analysing the effect on the variation of the magnetic field of the magnet due to change in displacement.
- Developing an algorithm that can convert the raw data received from the sensor to prosthesis position parameter in multiple axes.
- Differentiating between different types of movement (linear/angular and static/dynamic) and understanding the resolution and accuracy of the system.
- Analysing the signal noise in the detection measurement and linking the algorithm with the filtering technique to improve the system detection performance.
- Comparing the effect of different biomaterials on the sensing technology.

3.2 Material and Method

3.2.1 System Overview

As the literature highlights both components of the elbow prostheses (humerus and ulna) are subjected to loosening depending upon the prosthesis type (Chapter 2, section 2.3.4). The majority of the radiolucent lines are observed at the tip of each component after loosening [156-158]. Therefore, the position of the sensor was selected near the vicinity of the elbow prosthesis component's tip. As described above, these sensors detect the magnetic field, and to provide a constant source of a magnetic field that doesn't require any power, a permanent magnet was used. The magnet was placed in a cement restrictor. The cement restrictor was chosen because during TEA these restrictors are used for pressurising the cement and improve prostheses fixation and are placed distal to the tip of the stems [62]. Considering the position of the sensor near the tip of the stem, the restrictor showed an ideal place for the insertion of a magnet and for the alignment of the sensor and magnet stem centralisers can be

used. This study focuses on the humeral component loosening and the same method can be replicated for the ulna component as well.

The proposed diagnostic technique used for the detection of aseptic loosening of the elbow prosthesis is shown in figure 3.2.

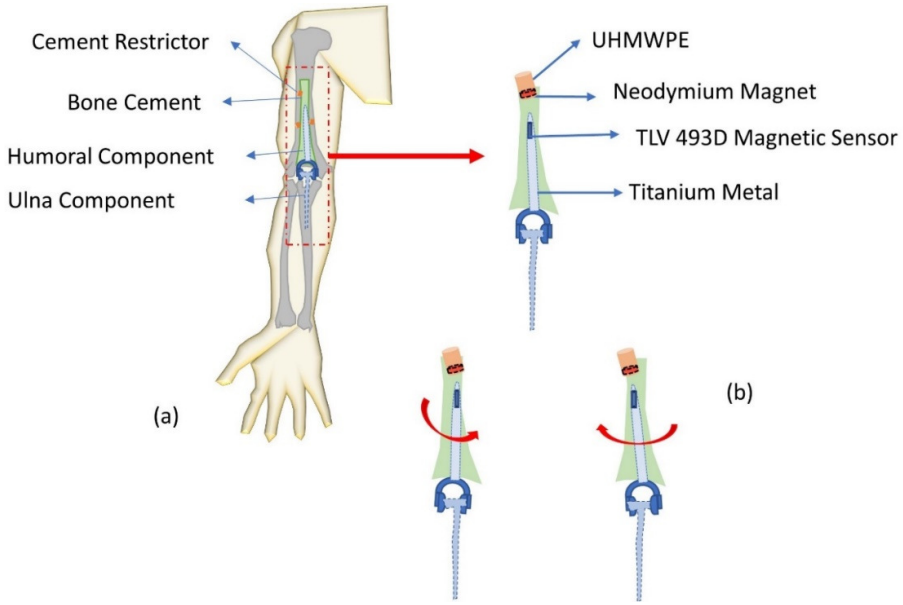

Figure 3. 2: (a) Proposed diagnostic system overview (b) Sensor and Magnet placement in the system Adapted From[140].

The measuring system consists of a sensory component and a magnetic component. The sensory component choose for this study was a 3-axis magneto-resistive sensor (TLV 493D, Infineon, Austria) which was embedded in the humeral stem of the elbow prosthesis, made of cobalt-chromium (ASTM F75) or titanium alloy (Ti-6Al-4V). As these metal alloys have a negligible effect on the magnetic field [155], the sensor will be able to detect the magnetic field without any attenuation. The magnetic component (axially-magnetised magnet) was placed at a reference point through a cement restrictor in the humeral bone. The magnet was enclosed in UHMWPE and acts as a source for detecting any translational or rotational loosening.

Finally, the area between the sensor and magnet was filled with bone cement and body tissue or fluid. The sensor detects the magnetic field emitted from the magnet and the raw data is sent to a PC via a USB cable. A software program is written in LabView (National Instruments, Austin, TX, USA) and MATLAB (The Mathworks Inc., Natick, MA, USA) calculates the position of the humeral stem relative to the magnet.

The fundamental idea behind this diagnostic technique is the calculation of the distance between the magnet and sensor, based on the magnetic field measurement detected by the sensor. Figure 3.1 highlights the position of the sensors that will be responsible for detecting any micro motion along the three axes. Also, the magnetic field decays with distance from the magnetic source, however, this decay is unaffected by human tissue or biomaterials (titanium alloy, cobalt-chromium alloy, UHMWPE, and PMMA bone cement). Furthermore, the human body has shielding properties that have been shown to be identical to free space [159].

3.2.2 Magnetic Field Distribution

To develop a micro motion detection technique, analysis was required on how the magnetic field of a magnet will respond at different displaced positions. As, the remanence (strength) of the magnet depends upon the magnet's size, material, forming process, and temperature which have been kept constant except the size of the magnet in this study. In this section, the magnetic field of an axis-magnetised cylindrical magnet was investigated to obtain the magnetic position sensor behaviour. According to Schott et al. *(2002),* whenever a magnet is displaced from its original position, the relevant direction and distance between the sensor and magnet changes, which is equivalent to the displacement of the sensor in the magnet field of a magnet with a fixed position [160].

The selection of magnet size was limited by its insertion in the humeral bone and was based on the dimension of the commercially available Hardinge cement restrictor as shown in figure 3.3. According to the dimension, three different sizes of magnets having a diameter of 3mm, 5mm, and 7mm were selected with a height of 3 mm. Each magnet was of the same type i.e. rare earth neodymium (NdFeB-

42) which provides the highest available remanence to size ratio [159]. Each magnet magnetic field was analysed to understand which size will be more suitable for the detection system.

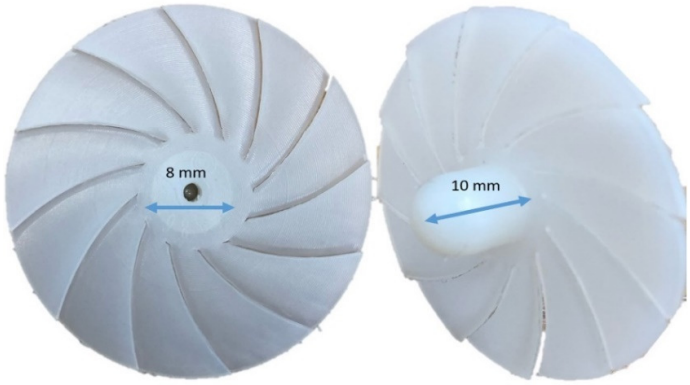

Figure 3. 3: Dimension of Commercially available Harding cement restrictor

To investigate the magnetic field of the magnet that will be embedded in the cement restrictor, an axisymmetric finite element model was used to simulate the magnetic field (Quick Field 6.3.1.2049, Tera Analysis Ltd., and Svendborg, Denmark). The simulation of the magnet was investigated in an air medium have a relative permeability of 1.0. The permeability of the magnet was selected based on the coercive force 9300 A/m and the remanence flux density of 11300 of the magnets. A mesh size of 250 was selected. Figure 3.4 shows the magnetic field vector distribution in the z-r plane of one of the selected magnets. As the simulated magnetic field is axisymmetrical the 3D model can be described in a 2D map.

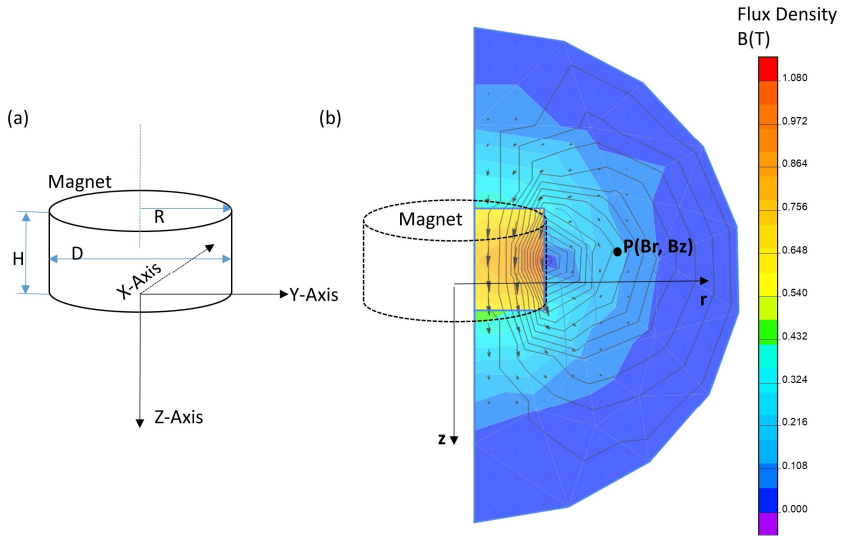

Figure 3. 4: (a) Dimensions of the magnet where R is the radius, D is the diameter and H is the height (b) Magnetic field of the magnet in a z-r plane as simulated for a magnet radius of 3.5 mm and height 3mm.

The magnetic field at any point P in the 2D map can be calculated by using equations (3)-(7) as described in detail by Schott e al. *(2002)* [160]. The validity and application of these equations to determine distance as a function of a magnetic field is described in the paper, where the authors report experimental errors as low as 10-40 µm (0.5 – 2 % error) at 0 to 2 mm testing range [29].

$$\frac{B_x}{B_y} = \frac{x}{y} \tag{3}$$

$$B_r = \sqrt{B_x^2 + B_y^2} \tag{4}$$

$$r = \sqrt{x^2 + y^2} \tag{5}$$

Where B_x and B_y are the magnetic fields measured in x-y axis, x and y are the coordinate positions, B_r is the magnetic field in the x-y plane and r is the radius in the x-y plane. Thus, the coordinate of the magnetic field at point P can be calculated in the 2D model by using the following equations, which have been derived previously [29]:

$$x = r.\frac{B_x}{B_y} \tag{6}$$

$$y = r.\frac{B_y}{B_x} \tag{7}$$

So, to obtain the three-axis displacement of the sensor from the three-axis magnetic field the relationship between (B_z,B_r) and (z, r) is enough where B_z is the magnetic field in the z-axis.

3.2.3 Configuring the Magnetic Sensor

In this study the Infineon TLV493-D magnetic sensor was used to detect magnetic field intensity in 3 orthogonal directions and from this, the prosthesis position can be determined. A custom printed circuit board (PCB) was designed for the sensor and then the PCB was enclosed in 2 mm thick titanium alloy (Ti-6AL-4V). Before calibrating the sensor according to the working envelope, the sensor needed to be configured with the data acquisition device, since this sensor is a digital sensor, it utilises an I2C communication protocol. A National Instruments (NI) MyRio was used as a data acquisition device to retrieve data from the magnetic sensor via its SDA (Serial Data pin) and SCL (Serial Clock pin). As the magnetic sensor has the output via the I2C protocol, two pull up resistors were required on the I2C line (SDA and SCL) as shown in figure 3.5. These resistors are necessary because the device has an open-collector configuration.

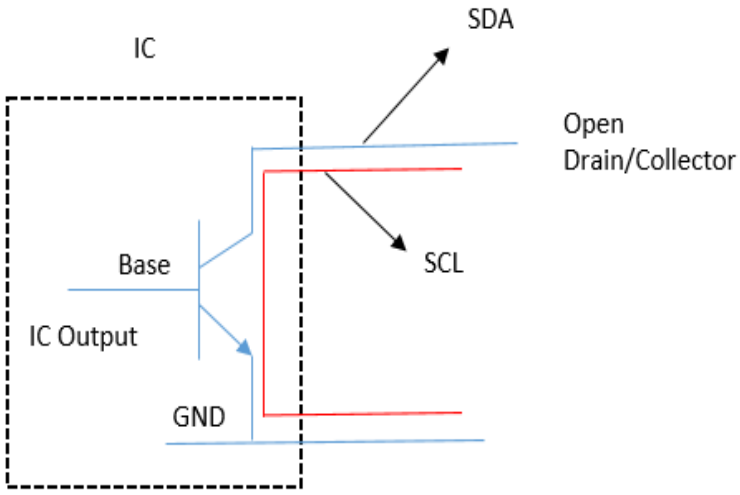

Figure 3. 5: Schematic of the Open collector configuration [140]

In open collector configuration, the system can only connect to the clock line (SCL) or signal data line (SDA) to the ground, but it cannot drive the lines to high. For the line to be able to go to the high voltage the pull-up resistor must be inserted because it needs a stable voltage state to define the two-binary state of bits i.e., 0 V as 0 bit and 3.3V as 1 bit.

The value of the pull-up resistor is important for the design configuration because an incorrect value of the resistor can lead to signal loss. By using the following equations the values of the pull-up resistor can be calculated [161].

$$R_{min} = \frac{V_{cc} - V_{OL\,(Max)}}{I_{OL}} \qquad (8)$$

Where R_{min} is the minimum pull up resistor value, V_{cc} is the supply voltage, $V_{OL\,(Max)}$ and I_{OL} are low-level output voltage and current respectively.

$$R_{max} = \frac{t_r}{0.8473 \ * \ C_b} \tag{9}$$

Where R_{max} is the maximum value of the pull-up resistor, t_r is the rise time and C_b is the bus capacitance. Therefore, the pull-up resistor value can be selected between R_{min} and R_{max}.

The next step was retrieving data from sensor specified registers as the magnetic sensor consists of 4 sensing elements (3 hall plates and 1 temperature sensor). Their data is stored in a specific register as described in the sensor bit map. Each register can store up to 8 bits of data but for the correct magnetic field value, the sensor must measure 12 bits of data. To achieve this, an appropriate code was written in LabView, which can read the data from the specific register and arrange it into 12 bits of data (Appendix A4).

3.2.4 Sensor Calibration

A technique is defined for the calibration of the magnetic sensor which will be used to find the migration of the implant relative to its original position. As the magnetic sensor has the capability of measuring magnetic field along three orthogonal axes simultaneously, the sensor can be used to measure field direction in two different planes. By using this concept, the sensor can be calibrated and identify its starting position. For the axially magnetised cylindrical magnet, the magnetic field along its axis can be derived from Camacho [162].

$$B(z) = \frac{\mu_o M}{2}\left(\frac{z + H_m}{\sqrt{(z + H_m)^2 + \left(\frac{D_m}{2}\right)^2}} - \frac{z}{\sqrt{z^2 + \left(\frac{D_m}{2}\right)^2}}\right) \tag{10}$$

Where M is the magnetisation of the magnet axially, μ_o is the relative magnetic permeability, H_m is the height of the magnet, z is the distance from the pole of the magnet and D_m is the diameter of the magnet.

According to Chao Hu [163] the theoretical localisation of a magnet can be found by using the equation:

$$B = Bx\,\hat{\imath} + By\,\hat{\jmath} + Bz\,\hat{\mathrm{k}} = \frac{\mu_o M}{2}\left(\frac{z + H_m}{\sqrt{(z + H_m)^2 + \left(\frac{D_m}{2}\right)^2}} - \frac{z}{\sqrt{z^2 + \left(\frac{D_m}{2}\right)^2}}\right) \tag{11}$$

Where (Bx, By, Bz) are the 3 components of the magnetic flux intensity of the magnetic sensor and ($\hat{\imath}$, $\hat{\jmath}$, $\hat{\mathrm{k}}$) are the vector components of the magnetic field. For the localisation of the magnet the z component of the vector equation will be considered. In this study to find the distance from the measured magnetic field values, an algorithm was used as shown in Figure 3.6.

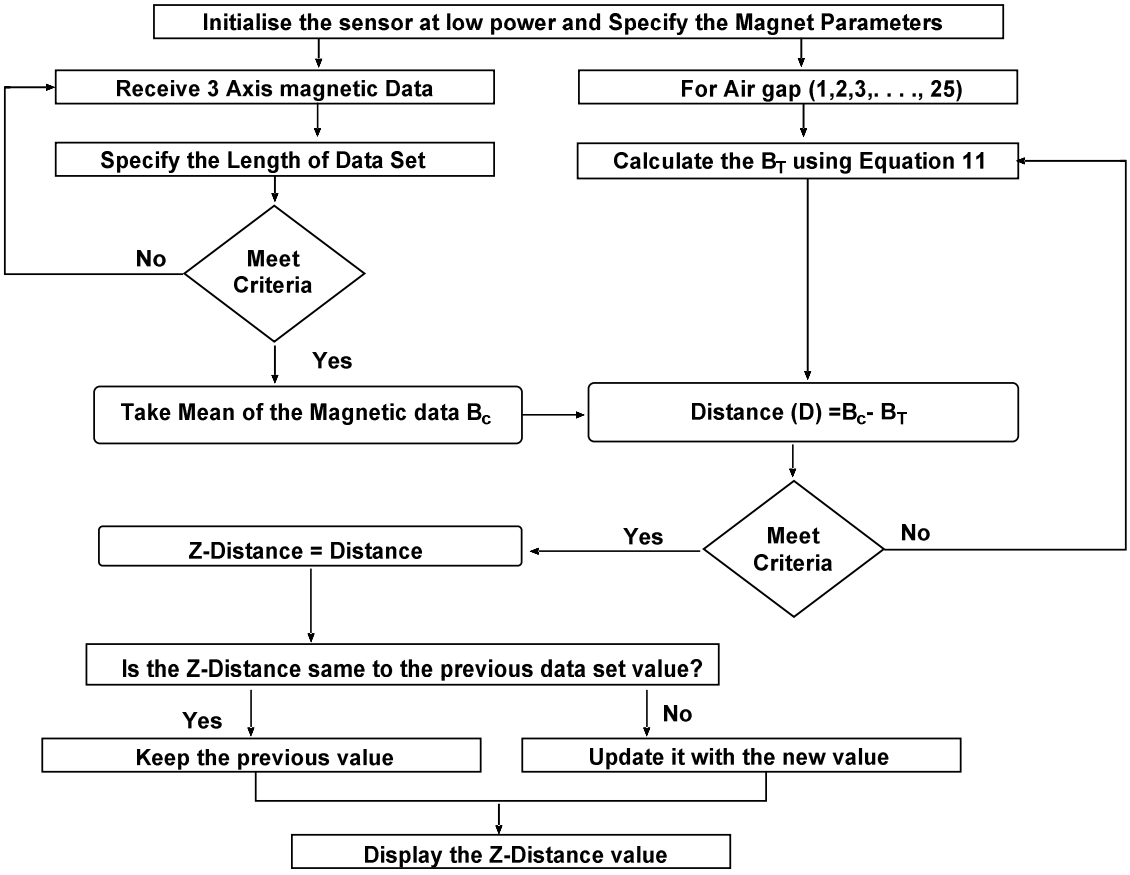

Figure 3. 6: Flow chart for the algorithm for the detecting of the distance between sensor and magnet (Z-Distance)

The magnetic field values from the sensor data are compared to the theoretical distance values as shown in the algorithm (figure 3.6). The algorithm looks for a match to identify the Z-Distance between the magnet and the sensor. If at the value of z, the difference between the magnetic field and theoretical value is zero or close to zero that value of z will be considered as the distance between sensor and magnet. Once the Z-distance is determined, the linear/angular displacements in the x and y axes are determined (figure 3.7).

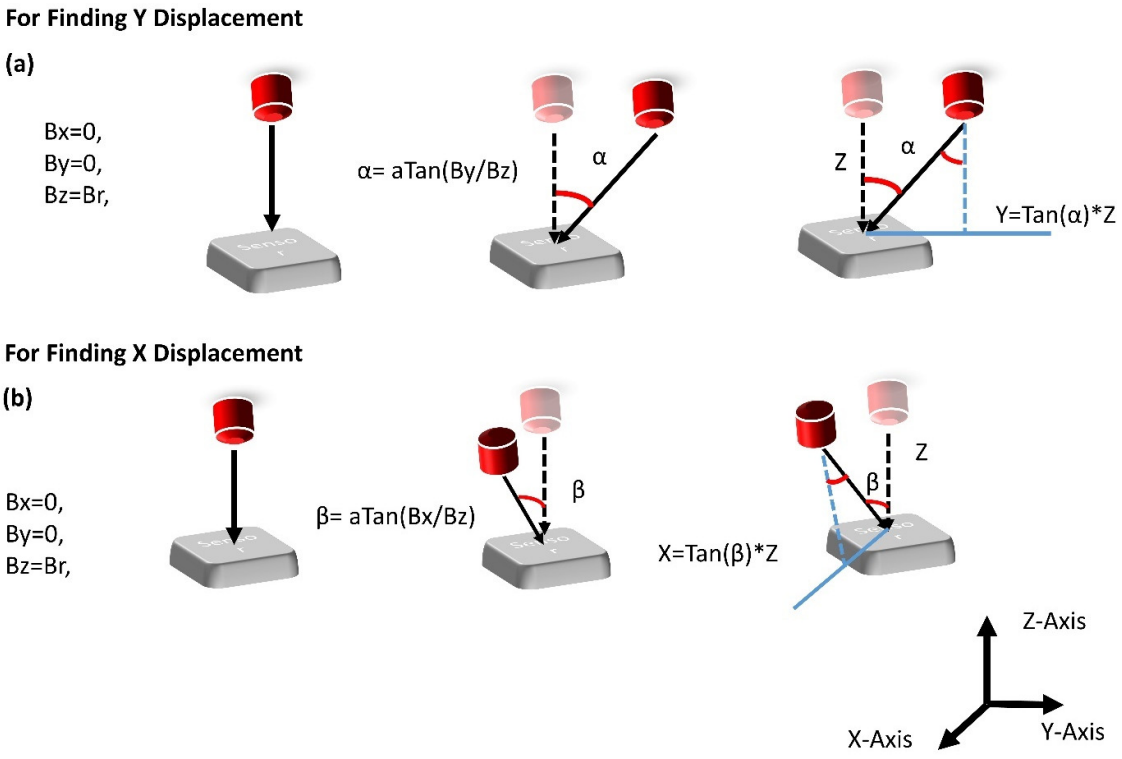

Figure 3. 7: (a) Linear/Angular movement detection mechanism in the y-axis. (b) Linear/ Angular movement detection mechanism in the x-axis [140].

According to figure 3.7a, when the magnet is displaced in the Y direction it makes an angle α with respect to its previous position, and wherever this change occurs only the magnetic field in the y-z axis changes. Similarly, in figure 3.7b, when the magnet is displaced radially (x-direction) it makes an angle β by altering the magnetic field in the x-z axis. To find α and β the following equations were used.

$$\alpha = \tan^{-1}\left(\frac{B_y}{B_z}\right) \qquad (12)$$

$$\beta = \tan^{-1}\left(\frac{B_x}{B_z}\right) \quad (13)$$

To find the relative displacement of the sensor from its original position, α and β angles will be multiplied with the Z-distance (the distance between the sensor and magnet). That will yield the displacement of the sensor in the Y and X directions.

$$Y\ Distance = \tan\alpha * Z\ Distance \quad (14)$$

$$X\ Distance = \tan\beta * Z\ Distance \quad (15)$$

3.2.5 Signal Filtering Technique

The data received from the sensor must be smoothened as it contains high frequency content that cannot be removed by a plain FIR average filter. To achieve the high degree of noise removal from the desired signal, the length (N) of the signal must be larger so that the signal bandwidth becomes greater than the filter passband frequency (ω_c).

$$\omega_c = \frac{\pi}{N} \quad (14)$$

In the current study Savitzky-Golay (SG) filter also known as least-square or polynomial smoothing filter is used to smooth the desired signal. The SG filter is basically a low pass filter, or it can be also considered as a type of finite impulse response FIR digital filter that can preserve better the high-frequency content of the desired signal (100 -3.3 KHz). The main advantage of selecting SG filter was

its capacity to retain the shape of the signal which is not possible compared to the moving average filter [164]. Figure 3.8 highlights the basic working principle of the SG filter.

The SG filter approximates the signals locally in the time domain within the moving windows by using a polynomial fitting with fixed order as shown in figure 3.8. The coefficients of the polynomials are obtained by the least square method and the final smooth signal data points are calculated from the value of the polynomial at the centre index of the moving window. The final filtered signal is obtained by repeating the said procedure for each set of data points [165].

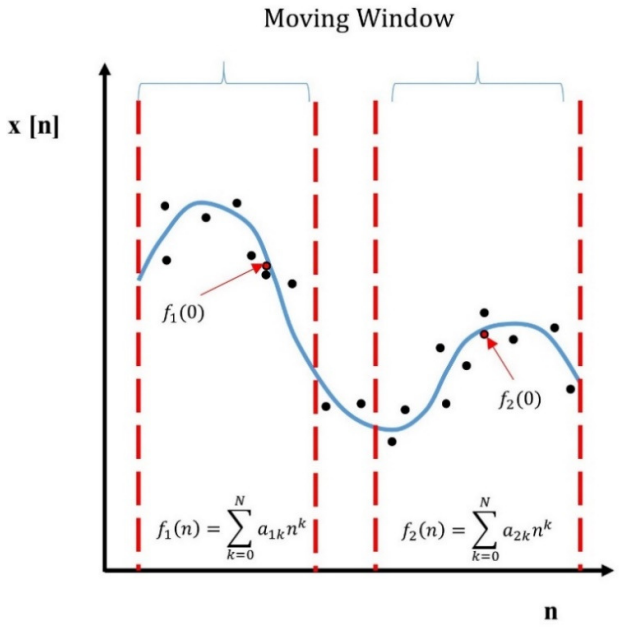

Figure 3. 8: Working principle of Savitzky Golay filter.

Using this filtering technique on the obtained data from the magnetic sensors is as follows:

The output signal from the sensor can be represented as:

$$y(n) = x(n) + w(n) \qquad (17)$$

Where $x(n)$ represents the magnetic field signal with high-frequency content while $w(n)$ is the associated noise with magnetoresistive sensor i.e., Johnson (thermal noise), shot noise, 1/f (flicker) noise.

The SG filter can be defined by two parameters that are denoted as K for a degree of polynomial and M for sequence. Following assumptions are made in the SG filter.

I. All data points of the signal should be natural numbers.

II. The length of the signal should be N=2M+1 and is odd for the sequence of M.

III. Data points should be positioned symmetrically about the origin x_o as follows:

$$x_N = [x_{-M}, \ldots, x_{-1,} x_o\,, x_1, \ldots, x_M] \qquad (18)$$

Polynomial smoothing of N samples of data is equivalent to replacing them by the values that lie on smooth polynomial curves drawn between the noisy samples.

$$\hat{x}_m = c_0 + c_1 m + \ldots + c_k m^k, -M \leq m \leq M \qquad (19)$$

Where $\hat{x}_m$ represent the m[th] smooth data point. The coefficients c_i are determined optimally by a least square fit that minimises the least square error and also fits the given data on a corresponding polynomial curve. For N data samples the performance index can be minimized as follows:

$$E \sum_{m=-k}^{k} e_m^2 = \sum_{m=-k}^{k} (x_{m-}(c_0 + c_1 m + \ldots + c_k m^k)^2 \qquad (20)$$

Similarly, we define the K+1 polynomial basis vector as follows:

$$S = [s_0, s_1, \dots, s_k] \tag{21}$$

Hence, the smooth data can be represented in vector form as:

$$\hat{x} = \sum_{i=0}^{k} c_i s_i = B_x \tag{22}$$

As the data points should be symmetrically about the origin. So, the middle-smoothed value $y_0 = \hat{x}_0$ is given in terms of middle SG filter b_0.

$$y_0 = b_0^T x = \sum_{m=-M}^{M} b_0(m) x_m \tag{23}$$

The N-dimensional vector x can be shifted to n instants of time as follows:

$$x \rightarrow [x_{n-M}, \dots, x_{n-1}, x_n, x_{n+1}, \dots, x_{n+M}] \tag{24}$$

The resulting length N, order K, SG filter for smoothing a noisy sequence $x(n)$ will be, in its steady-state form as:

$$y(n) = \sum_{m=-M}^{M} b_0(-m)x(n-m) \qquad (25)$$

Where b_0 is the middle SG filter, as all data points should be symmetrical around the origin, m is the m^{th} point of the filter window and n is the number of data points.

3.2.6 Bone Cement Preparation

PALACOS (Heraeus Noblelight Ltd, UK) low viscosity Polymethylmethacrylate (PMMA) bone cement[68] with and without antibiotic (Gentamicin) was used for this study. There are several types of bone cement that vary by their viscosity and anti-biotic content. In TEA the low viscosity cement is commonly used with or without antibiotics depending upon the surgeon's preference [70]. The bone cement comes in two components made up of a powder (copolymer) and liquid (monomer). The cement was prepared as per the manufacturer's instructions. Using the first-generation cementing technique (hand mix, manual insertion) [166], the two components were mixed at a ratio of 2:1 in a bowl in a fume cupboard (Airone FC 750 model, Safelab systems Ltd. Somerset, UK) for 2-3 minutes to form PMMA cement. Before becoming a hard dough, it goes to the following steps. The first step is called polymerisation, which is a chemical reaction in which the powder (copolymer) and liquid (monomer) undergoes an exothermic reaction and starts to heat up with the maximum temperature of 40° C to 47° C. The second phase is the waiting phase which usually lasts for several minutes and the cement achieves a suitable viscosity for handling. The third phase is the working phase, where the viscosity starts to increase, and the cement can be poured down into any container. The last phase is the setting phase in which the cement hardens and settles. The cement goes into both thermal and volumetric shrinkage as it gets cooled [166].

In this study, when the bone cement was in its third phase, it was poured into a pre-made mould to create a PMMA sections with thicknesses of 2.5 mm, 5 mm, and 7.5 mm. The PMMA cement was left in the mould for 5 minutes to completely polymerise and harden before removing it from the mould.

3.2.7 Performance Testing

To evaluate the performance of the sensor and to obtain the correlation between the magnetic field and displacement, a mechanical testing system (Electro Force 3300, TA Instruments, Boston, USA) was used to provide input migration of the implant via its two motorised stages i.e., linear, and rotational, with a resolution of 0.5 μm linearly, 0.01 degrees angularly and 0.01 Hz frequency. To provide a repeatable simulation of implant migration, an adjustable fixture/bracket for holding the sensor and magnet embedded in a UHMWPE was designed and fabricated. The fixture was attached to the Electro-force machine (see figure 3.9). The sensor bracket could be moved linearly in the y-axis and rotationally in the x-z plane. In order to move the magnet bracket linearly in the z-axis, an external linear actuator (P-16, Actuonix, Canada) was attached with a resolution of 1 mm and this was used to adjust the distance between the sensor and the magnet. The Electro-Force machine was programmed to move in the y-axis quasistatically (3-minute intervals) at amplitudes of 0.15 mm to 4 mm using square waveforms and dynamically using a sine waveform at 0.1 Hz. A rotational movement in the x-z plane was programmed quasistatically at 3 minute intervals at increments of 0.5 degrees. The z-axis direction was controlled via the linear actuator, which was programmed using an external DAQ card (NI MyRio). The DAQ card was also used to communicate and acquire data with the sampling rate of 10 Hz from the magnetic sensor and to record data into a measurement file.

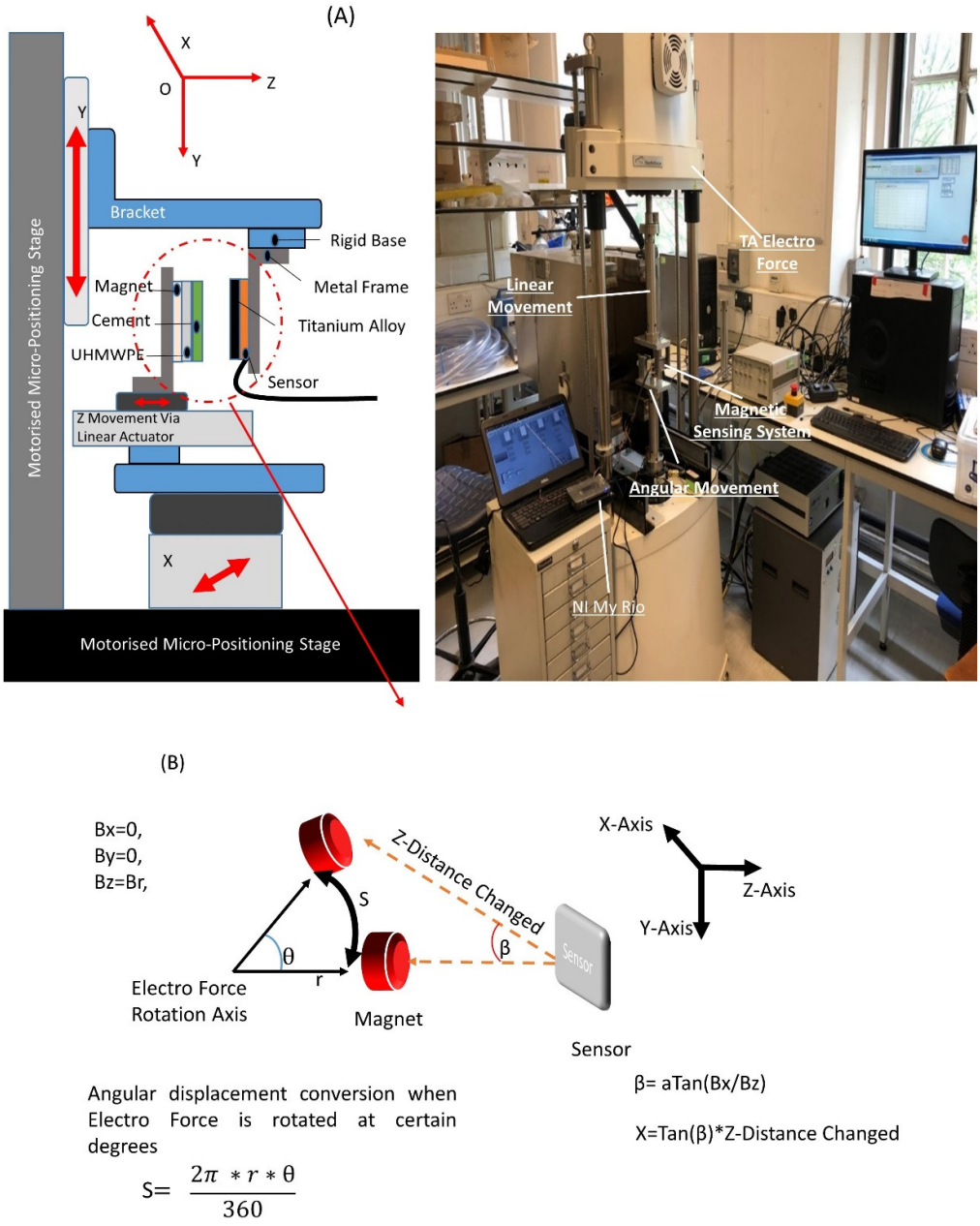

Figure 3. 9: (a) Schematics of the experimental setup.(b) Mechanism for detecting angular displacement when the Electro Force machine is operated in rotation mode.

Figure 3.9b highlights the calculation process of the conversation of the angular degrees movement of the Electro Force to angular displacement when operated in rotation mode.

3.2.8 Statistical Analysis

The statistical analysis of the different test parameters was conducted using SPSS software (version 20.0, SPSS, Chicago, IL, USA). A paired t-test was carried out for each displacement position tested (0, 0.3, 0.5, 1. 1.5, 2. 2.5 mm) before and after applying the SG filter to test any significant changes to the raw versus filtered data sets from the filtering process. Also, Levene's test was performed to check the homogeneity of variance. A non-parametric test was carried out using Linn's Concordance Correlation Coefficient.

3.3 Results

3.3.1 Magnetic Field Distribution

Figure 3.10 highlights the magnetic field distribution and its spatial gradients distribution for all three sizes of the magnet in the z-r plane. It was observed that the magnetic field of the larger magnet has the stronger magnetic field and larger distribution area along the z axes, whilst having a smaller gradient of B_z component dB_z/dz. Similarly, in r axes, the larger magnet has the wider distribution of the field and the larger gradient of Br component dB_r/dr.

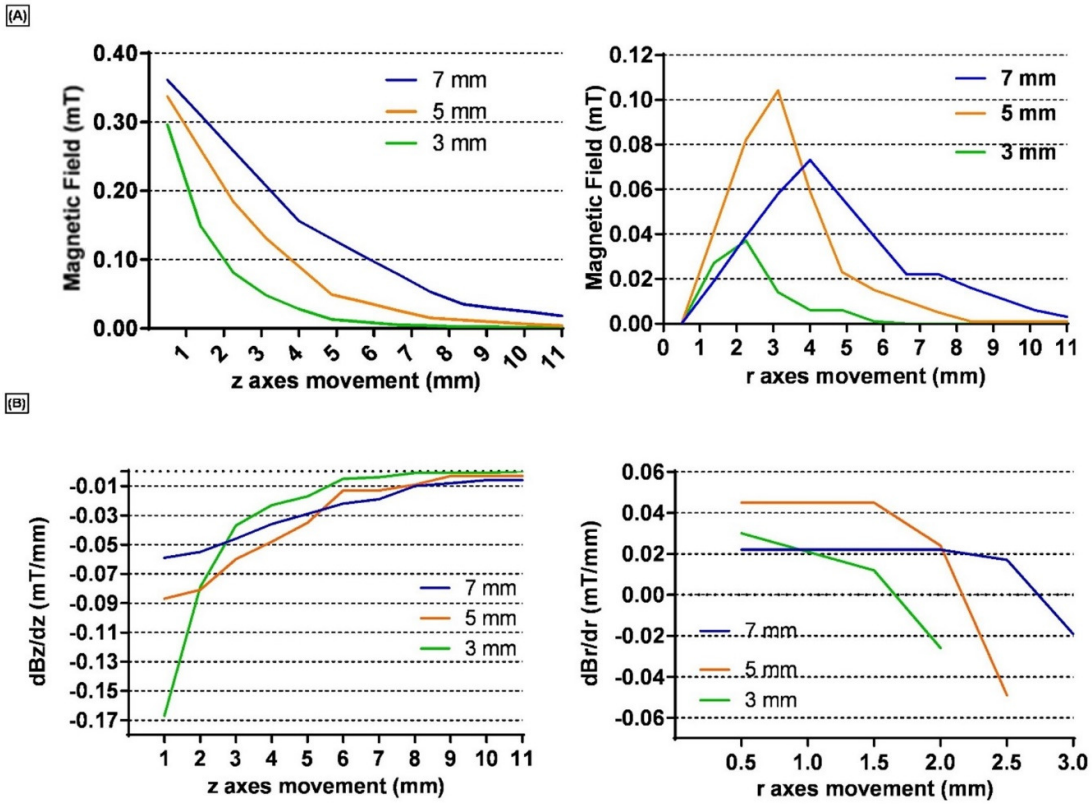

Figure 3. 10: (a) Magnetic field distribution of the 3 different sizes of magnet in a z-r plane (b) Magnetic field gradient distribution.

Looking into the dimensional effect of all the selected magnets, the magnet having a larger diameter has a wider and stronger magnetic field in z-axes and is highly effective for position/ displacement sensing. Figure 3.10 also highlights that both the magnetic field density and the magnetic field gradient decrease as both the z-axis and r-axis movement is increased. Thus, for effective sensitivity, the starting position of the sensor should be within the magnet's magnetic distribution range. Based upon the magnetic field results the magnet with a diameter of 7 mm was selected as it has a stronger and wider field distribution in the z-r axis.

Also, figure 3.11 shows the contour plot simulation of the magnetic field density of the selected magnet (B_r and B_z) in the z-r plane. Figure 3.11a indicates that the value of B_z increases when r is increased. It reaches its maximum value when r=Radius of the magnet, then B_r decreases as r is increased and

eventually moves towards zero. Also, Figure 3.11b indicates that the value of B_z decreases when z is increased and at distance z >20mm the value of B_z is zero. To avoid multiple results when determining r and z from the magnetic field, it was determined that the movement of the magnet in the r plane should not exceed the specified regions as showed in the plots and all the movement should be restricted between these regions.

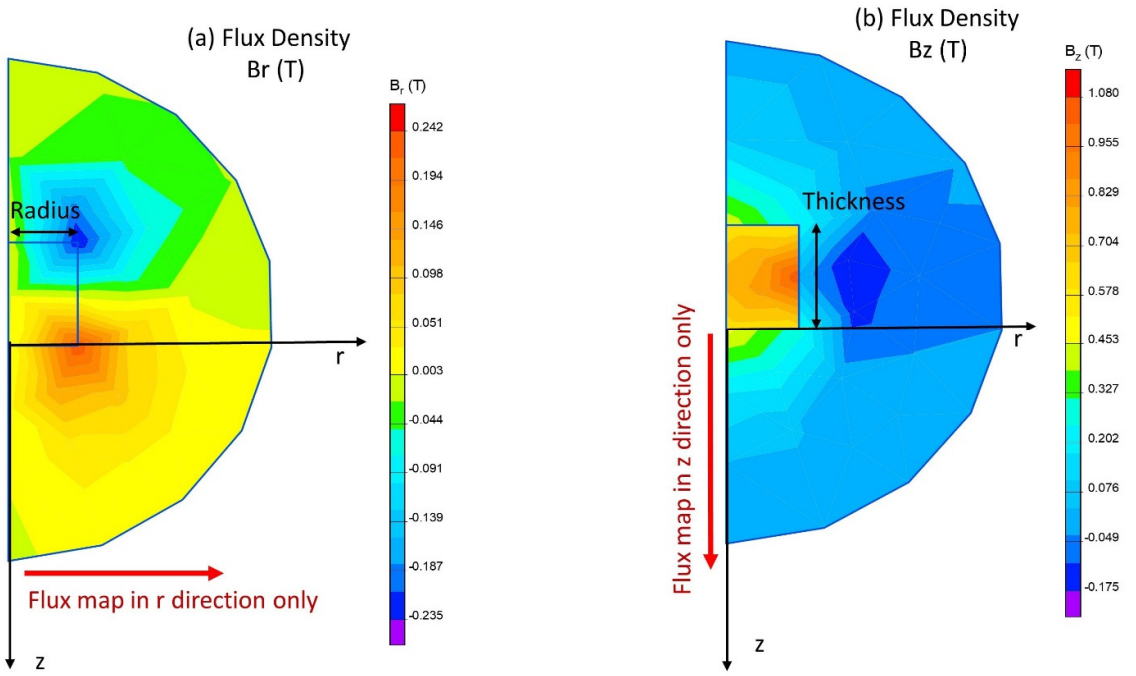

Figure 3. 11: The magnetic field was simulated for the magnet having a radius of 3.5 mm and a height of 3 mm.(a) Plane contour plot of the simulated magnetic field in r-plane (b) Contour plot in z-r plane.

The Magnetic Flux density B_z and B_r of the cylindrical magnet in the z-r plane is shown in figure 3.12, in which the magnetic field data points were observed along the z plane only from the center of the magnet to the external boundary of the simulated field. As observation distance along the z plane started to increase both B_z and B_r showed variability. This change of both magnetic flux (B_z and B_r) while moving along a single plane is termed as crosstalk effect. Also, both the flux densities showed a non-linear behaviour with increasing observation distance.

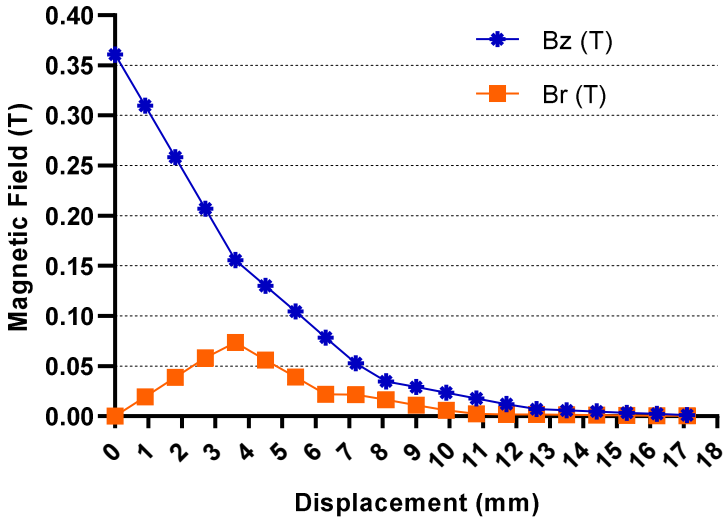

Figure 3. 12**:** The magnetic field distribution of the magnet in a z-r plane from the center of the magnet to a distance of 18mm.

3.3.2 Sensor Calibration

Following the flow chart, as described in figure 3.6, the sensor was first calibrated in the z-axis only in order to detect the distance between the sensor and magnet. The magnet was placed perpendicularly to the z-axis of the sensor (note that the North Pole was facing towards the sensor, if the poles change the magnetic field sign changes from positive to negative) and was moved linearly within the range of 8-20 mm at a step size of 1 mm. The resultant data set was processed with the algorithm as shown in figure 3.6 to determine the coefficients as shown in equations 12 and 13. Figure 3.13 shows the comparison of the detected distance with the actual distance. The detected distance value is the average of 3 measurements and the error bars represent ± one standard deviation. The output of the detected distance showed how well the algorithm fitted the actual value with an R^2 value of 0.9991. The standard deviation was less than 0.5 mm.

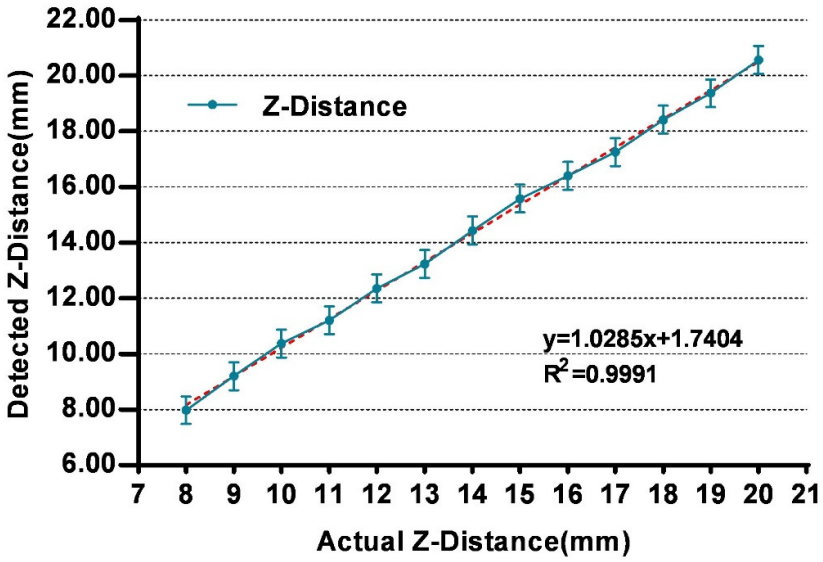

Figure 3. 13: Validation of an algorithm to calculate the distance between sensor and magnet.

A similar set of experiments were conducted to analyse how the system will perform to detect the displacement of the sensor/magnet if they were moved in the other axes. The sensor was first tested linearly in the y-axis ranging from 0.1 mm to 4.0 mm with a step size of 0.5 mm (at z=15 mm). It was then tested angularly around the y-axis ranging from 0 to 4.0 degrees. Figure 3.14 shows that the system was able to detect the displacement of the magnet in the y-axis with no change in the x or z-axis with a resolution of 0.3 mm. Displacement detection at different actual movements is provided in Table 3.2 for both filtered and unfiltered signals. The filtered version has a standard deviation of 0.079 mm as compared to the unfiltered standard deviation of 0.390 mm at 0.3 mm of displacement. A similar result was seen during the x-axis linear movement where the value does not change.

Table 3. 2: Mean ±Standard Deviation of Quasi-Static Linear Movement of the Magnet.

Actual movement (mm)	Detected Movement without filtering (mm)	Detected Movement with filter (mm)
0.30	0.321±0.390	0.328±0.079
0.50	0.527±0.393	0.530±0.075
1.00	1.078±0.386	1.082±0.089
1.50	1.627±0.384	1.632±0.074
2.00	2.126±0.372	2.133±0.079
2.50	2.660±0.371	2.665±0.080
3.00	3.169±0.380	3.173±0.079
3.50	3.701±0.371	3.705±0.078
4.00	4.191±0.369	4.195±0.085

Table 3.2 shows both the raw and filtered signals have similar mean values with the filtered data showing lower variance (standard deviation). A paired t-test showed no significant differences between the raw and filtered data sets. The Levene test shows that there is no homogeneity of variance between the raw and filtered data ($p < 0.05$). Therefore, the assumption of homogeneity was not met. The non – parametric analysis of Linn's Concordance Correlation Coefficient was performed. The analysis showed that the filtered signal has strong concordance with the actual displacement (0.9913) while the unfiltered has a moderate (0.948).

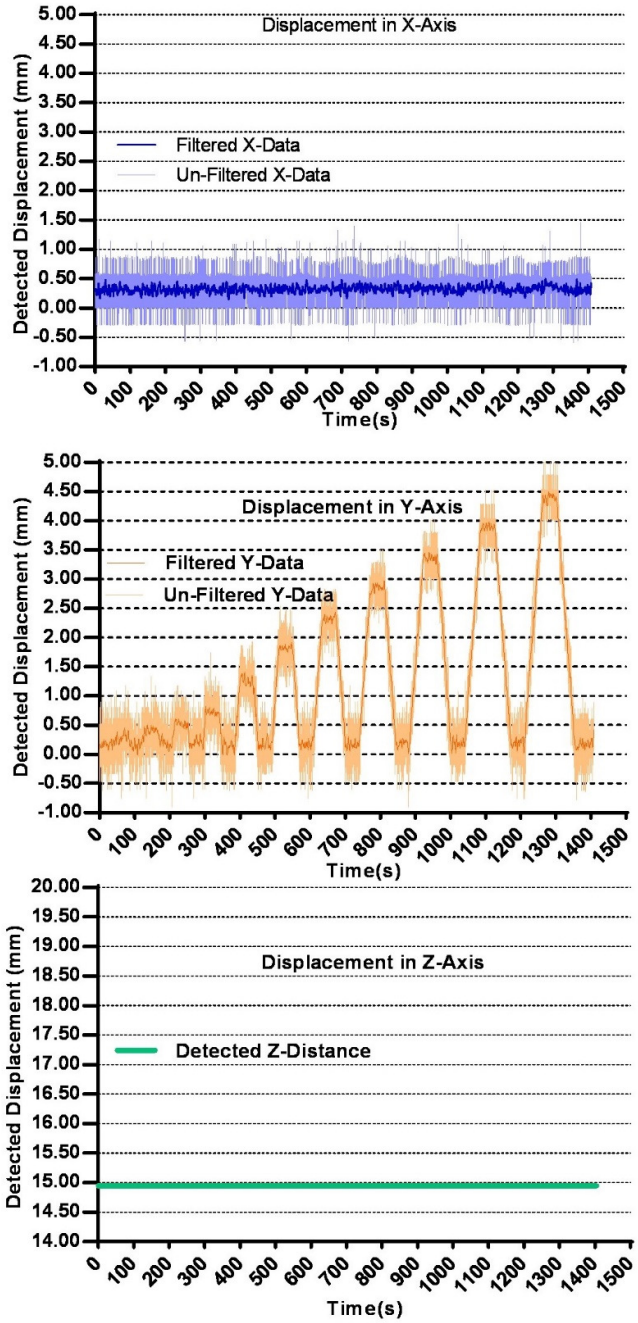

Figure 3. 14: Quasi-Static Linear Movement of Magnet in the y-axis, keeping x-axis and z-axis position constant.

Figure 3.15 shows the angular movement of the magnet around the sensor. Firstly, the system was able to detect angular displacement up to 3 degrees (approximately 2 mm). Secondly up to 1-degree rotation (1.2 mm angular displacement) showed no change in the Z-distance but beyond 1 degree the Z-

displacement starts to change depending upon the movement of the system. Finally, it was observed that beyond 3 degrees the sensor was able to detect the magnetic field, but it introduced an error in the tracking algorithm. This error was due to the tilting effect of the sensor, therefore for accurate displacement measures the sensor and magnet are required to be in parallel alignment with less than 3 degrees tilt.

Table 3. 3: Mean ±Standard Deviation of Quasi-Static Angular Movement of the Magnet.

Actual Movement (Degrees)	**Magnet-Sensor Aligned Error in Detection**	**Magnet-Sensor Misaligned Error in Detection**
0.5	0.007±0.087	0.037±0.108
1.0	0.056±0.076	0.095±0.096
1.5	0.094±0.079	0.156±0.098
2.0	0.158±0.078	0.221±0.091
3.0	0.263±0.076	0.366±0.092
4.0	0.475±0.90	0.552±0.097

Table 3.3 shows that when the magnet was aligned with the sensor, it was able to detect the angular movement with minimum error and as it exceeds after 1.5 degrees of movement. This rise in the error after 1.5 degrees of movement was because of the tilting of the magnet causing changes in the magnetic field that results in an increase in error. Table 3.3 also highlights that when the magnet was placed offset to the sensor and a similar set of angular displacements were performed, the error was the estimation of the displacement, which was higher as compared with the aligned one.

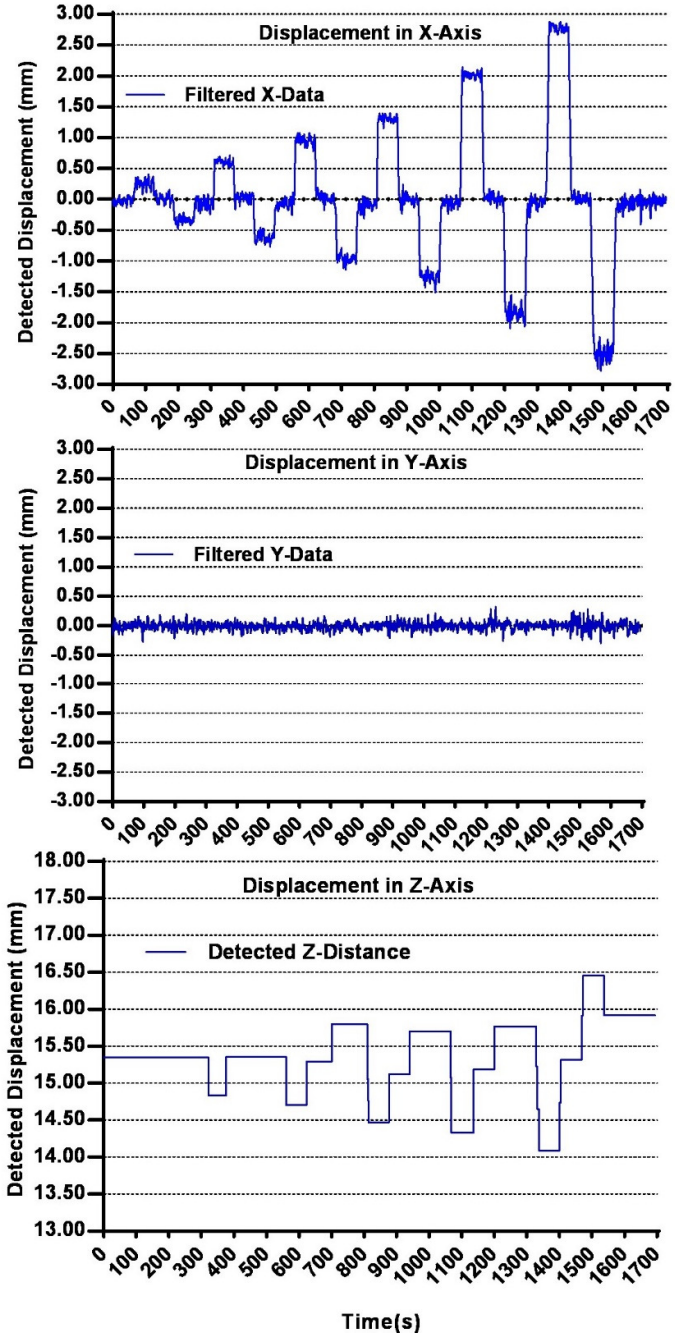

Figure 3. 15: Quasi-Static Angular Movement of the Magnet in the x-axis, keeping y-axes and z-axes movement constant.

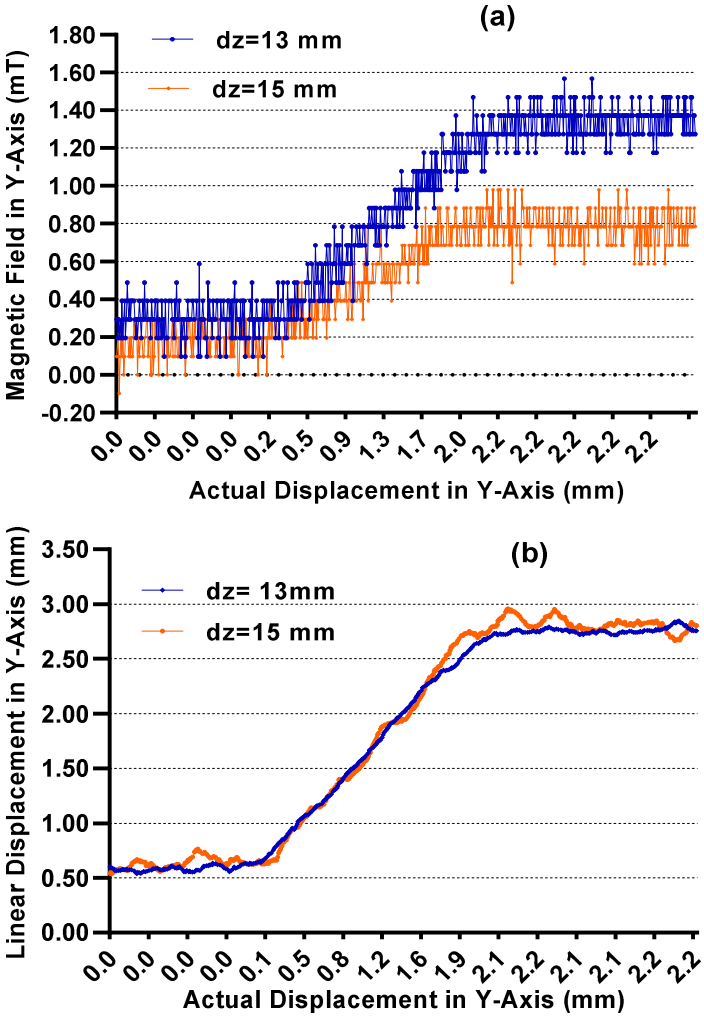

Figure 3. 16: (a) B_y during the y-axis displacement with different Z displaced values (b) Calibrated y values during different Z displaced values.

Figure 3.16 (a, b) shows the comparison of the magnetic field (By) with the calibrated sensor output during the y-axis displacement at different z values. It was observed that during the y-axis displacement at different z values the magnetic field (By) changes showing a strong crosstalk effect while the output from the calibrated sensor showed a close resemblance with the actual y-axis displacement across different z values, meaning that for the tested values the crosstalk effect was eliminated.

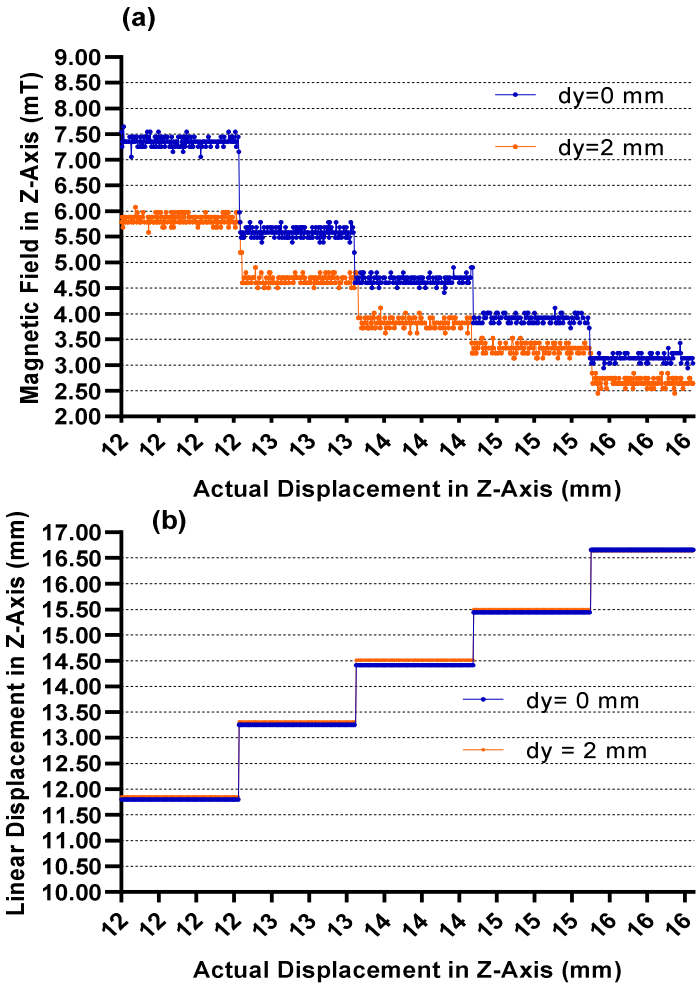

Figure 3. 17: (a) B_z during the z-axis displacement with different Y displaced values (b) Calibrated z values during different Y displaced values.

Also, figure 3.17(a, b) shows that during z-axis displacement at different y displaced values, similar effects were observed with strong crosstalk in a magnetic field (Bz) and eliminated crosstalk in calibrated sensor output in the z-axis.

3.3.3 Performance Testing at Different Biomaterials

The calibration steps earlier were performed without introducing any material between the sensor and magnet. To further investigate the performance of the sensor, the system was tested by introducing different sets of biomaterials that are presently used in the elbow prosthesis, namely, PMMA cement, UHMWPE, and Titanium alloy (Ti-6Al-4V). The system performance was checked under both static and dynamic movement. The system was moved dynamically at 0.1 Hz with an amplitude of 0.3 mm and then quasi-statically at 3 minute intervals with the same amplitude. Figure 3.18 shows that the sensor was able to detect both dynamic and quasi-static movement. It also shows that the biomaterials had a negligible effect on the measuring system.

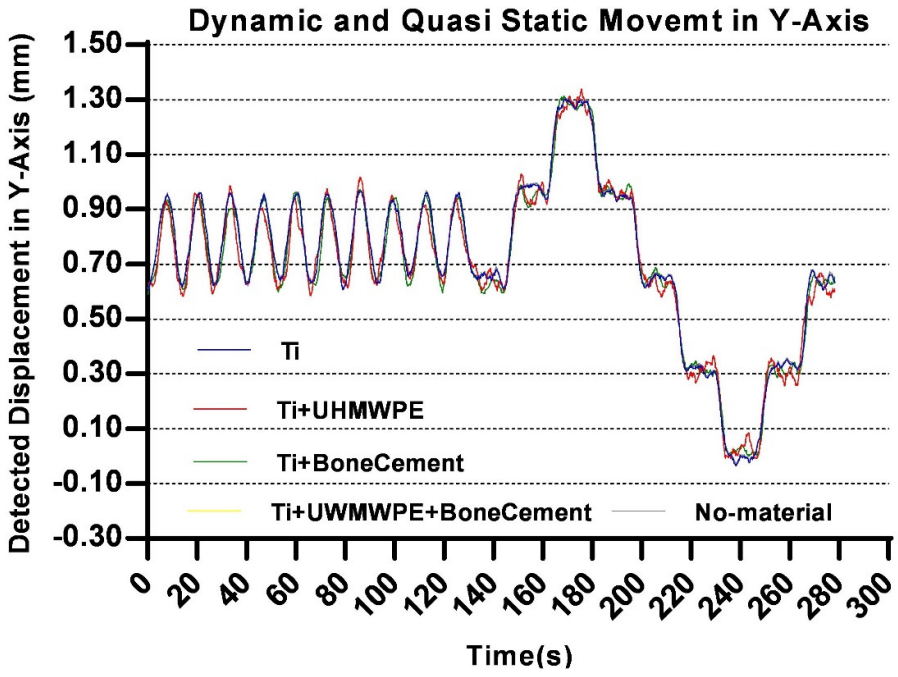

Figure 3. 18: Performance of system at different Biomaterials under dynamic movement (0.1 Hz, 0.3 mm amplitude) and quasistatic movement (3-minute intervals at 0.3 mm increments)

Table 3.4 shows the displacement detected by the sensors at different movements under different biomaterials. It was observed that under the static movement the calculated displacement is much more accurate having an error of approximately 3.1 % while in dynamic movement the error is 10 %.

Table 3. 4: Mean ±Standard Deviation of Static and Dynamic Movement at different materials along with its percentage error

Materials	**STATIC MOVEMENT (0.3 MM)**	**PERCENTAGE ERROR**	**DYNAMIC MOVEMENT (0.3 MM)**	**PERCENTAGE ERROR**
No Material	**0.3091±0.023**	**2.93 %**	**0.3133±0.1012**	**4.24%**
Titanium	0.3121±0.023	3.87%	0.3231±0.1040	7.14%
Titanium and Bone cement	0.3085±0.033	2.75%	0.3305±0.1212	9.22%
Titanium and UHMWPE	0.3090±0.028	2.91%	0.3323±0.11175	9.72%
Titanium, Bone cement, and UHMWPE	0.3085±0.033	2.75%	0.3317±0.1221	9.5%

3.3.4 Performance Testing: Sensitivity

According to the literature, there is no specific information on the minimum distance between the humeral component and cement restrictor in TEAs. However, in shoulder arthroplasty, the minimum distance between the restrictor and humeral component is 10 mm [38]. To check the sensitivity of the developed system the restrictor was placed at the reference point starting from 10 mm and showed the system performance under static and dynamic linear movement in the y-axis ranging from 0.15 mm to 1 mm. Figure 3.19 shows that as the distance between the sensor and magnet is increased, the resolution of the system decreases also the accuracy of the detection measurement decreased as well, and more noise content is introduced to the signal.

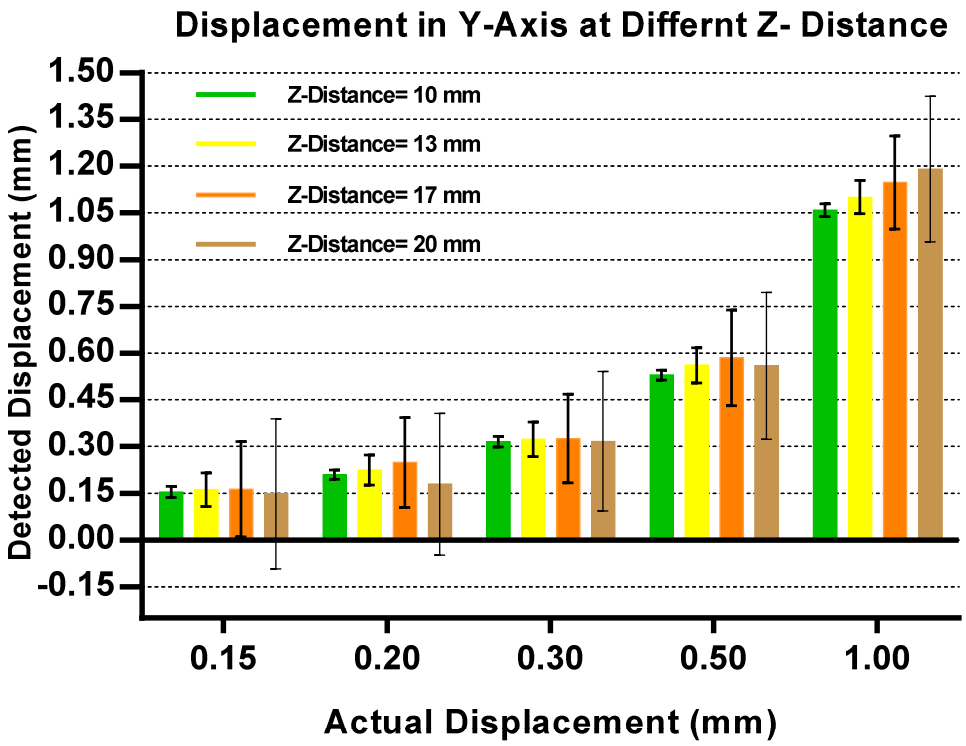

FIgure 3. 19: The sensitivity of the detecting displacement ranging from 0.15 to 1.00 mm at different Z-Distance. Mean with standard displacement error bars

Figure 3.20 shows that at z=13 mm, the system was able to detect accurately the static and dynamic movements with the detected displacement error of less than 0.05 mm. Beyond this distance, a 0.5 mm static movement was detected but with higher noise content. The results show that the ideal distance between the sensor and magnet for static and dynamic displacement should be below 17 mm.

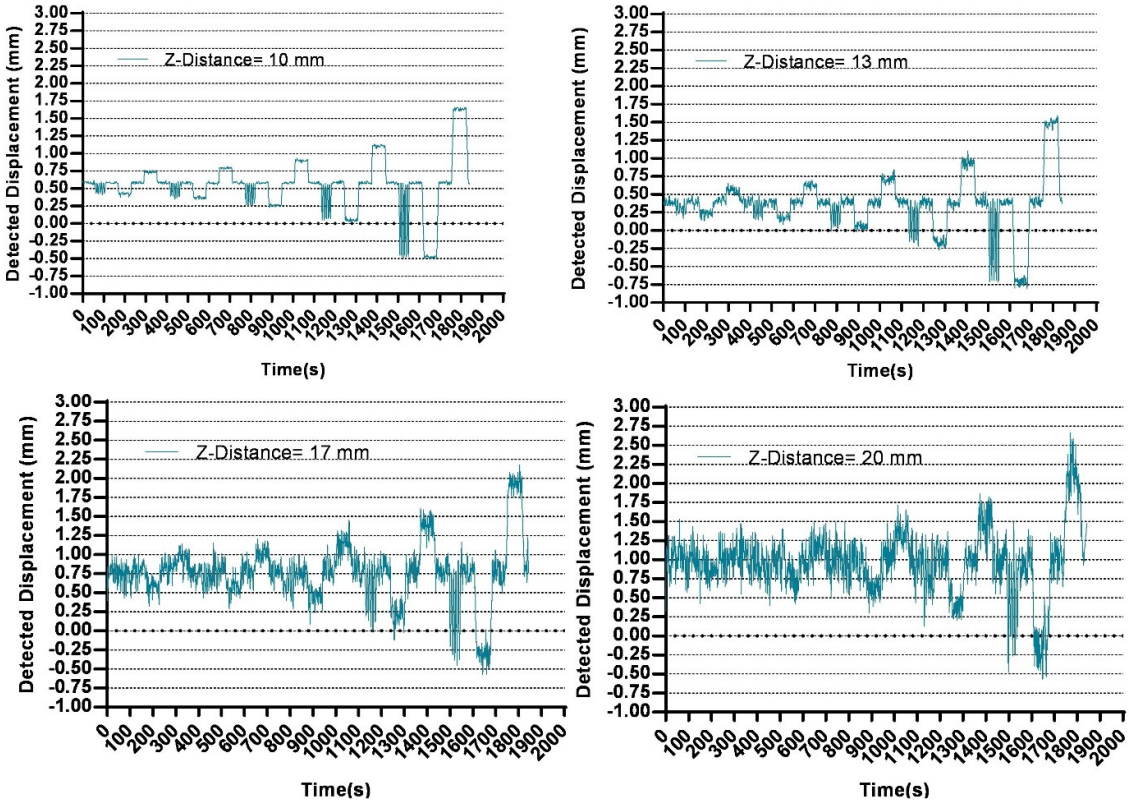

Figure 3. 20: The sensitivity of the detecting system Quasi-Static and Dynamic at different Z-Distance.

3.3.5 Linear and Angular Movement

Figure 3.21 shows that the system was able to detect linear and angular displacement simultaneously. As described previously, there was a change in the Z-distance value when angular displacement exceeded 1.2 mm (1 degree). Also, if the sensor is not properly aligned to the magnet there is a small increment in the y-axis. Figure 3.21 also shows that the system was able to differentiate between a linear and angular movement along with detecting changes in all axes.

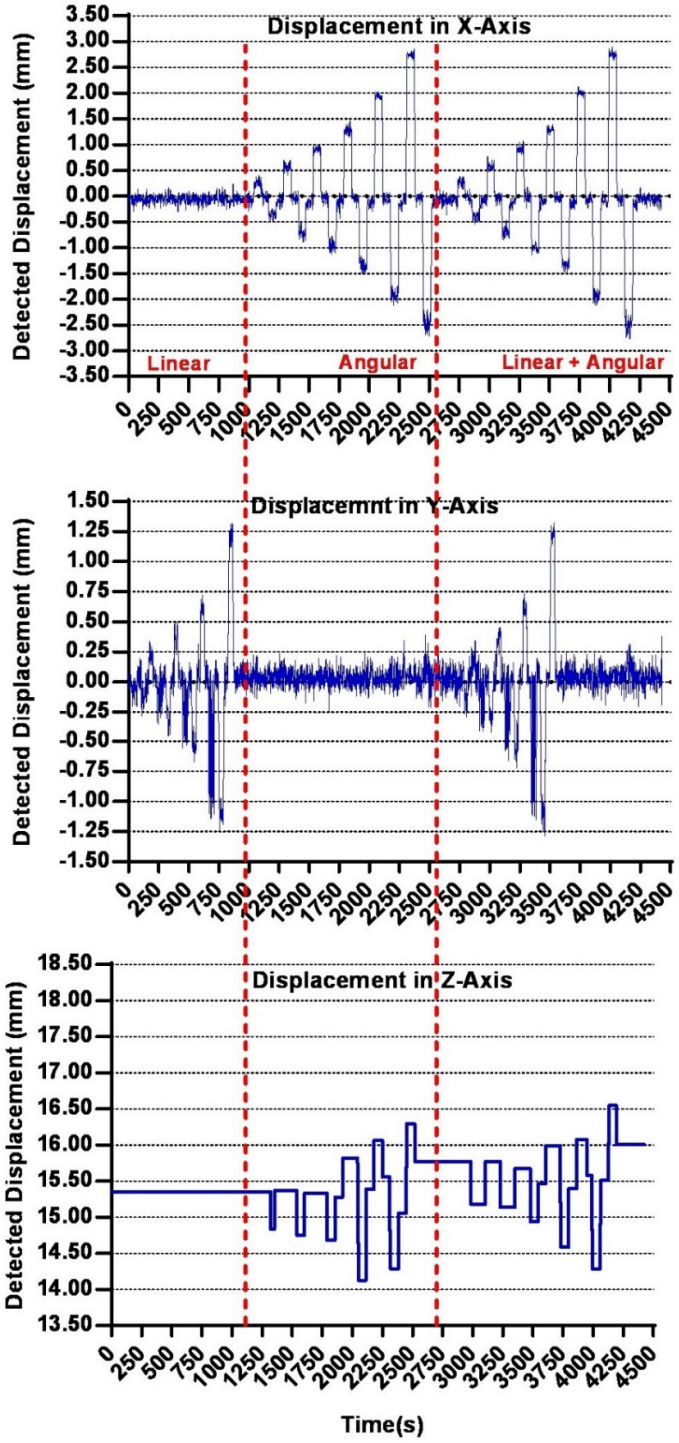

Figure 3. 21: Quasi-Static Linear and Angular Movement. At first 1000 seconds the system was moved linearly in y-axis linear ranging from 0.3- 1.00 mm keeping other axes constant, after 1000 sec the system was moved angularly ranging from 0.5-4.0 degrees keeping other axes constant. At last, the system was moved both linearly in the y-axis ranging from 0.3-1.0 mm and angularly in the x-axis from 0.5 – 4.0 degrees.

3.4 Discussion

The developed system is based on the change in the magnetic field of a magnet embedded in UHMWPE. The difference in the magnetic field measured by the sensor was used to detect displacement as low as 0.3 mm showing the ability to differentiate displacements in increments of 0.5 mm ($p < 0.05$). The biomaterials tested in this study showed negligible effect on the detection technique and the technique was able to differentiate between quasi-static and angular movement. The detecting algorithm also removed the crosstalk effect of the magnetic field along with the nonlinearity and was able to differentiate between linear movement and angular movement.

Compared to the currently available technique, in which RSA is considered to be a gold standard for detecting aseptic loosening having a precision of 0.29 mm translation and 0.66^{o} rotation[102]. However, it has the downside of high cost, x-ray exposure, and limited accessibility. The detection system presented here has several advantages over RSA and other techniques (contact-based), which include low cost, higher accuracy, non-contact, durability, measurement sensitivity, and negligible effects from different materials (liquid and non-magnetic biomaterials). There are no systems to date that can achieve 0.3 mm accuracy without the use of radiographs (RSA technique). Vibrometry has an accuracy of 20 % more than x-rays and the accuracy of standard radiographs is 2 mm detection. The proposed detection technique has a much higher accuracy of detection (0.3 mm) without any radiographic exposure.

The current understanding of the mechanisms of loosening and its causes is still not entirely known due to the lack of continuous monitoring. The implications of developing this system for clinical use is that it could further our understanding of the dynamics of implant loosening behaviour in-situ, implant joint biomechanics, and how implants are designed and managed long-term. However, the system has some limitations that need to be overcome.

One of the limitations in the detection system is the tilt effect during angular motion. There is no compensation for any non-parallel alignment between the sensor and the magnet. Currently, the system carries out a calibration step to check the magnet and sensor are aligned and parallel before proceeding.

If the sensor and magnet are not adequately aligned, it introduces an error in the detection measurement, which increases as the movement increase table 3.3.

A second limitation is possible environmental effects. The system performance may be affected if it encounters an external magnetic field. The magnetic field strength decreases with the increase of distance. However, as long as the external magnetic field variations are at an appropriate distance from the sensor, it will not cause any disturbances to the sensor measurement.

3.5 Conclusion

In this work, a proof-of-concept is presented for a magnetic field-based system to detect the migration of a prosthesis as low as 0.3 mm for post-operative follow-up, using the humeral component of the elbow prosthesis as a case study to demonstrate the system. This is the first magnetic-based system that could be potentially used for prosthesis loosening detection without the use of radiographs and the first of its kind designed for understanding the loosening behaviour of the humeral component in the elbow prosthesis with an achievable accuracy of 0.3 mm. This capability could have a significant impact on how implant loosening is monitored over the life span of the implant. Currently, one of the major limitation is the wireless power and data transmission which restrict its usage in-vivo. By overcoming those limitations, a system such as this could permit studies to develop a new understanding on the dynamics of implant loosening behaviour in-situ, joint biomechanics, and implant designs and how implants are managed long-term.

4 Chapter 4

Developing of an Implantable Multi Sensor Array for Non-Radiographic Micro Motion Detection of Elbow Joint Prostheses

Summary

In this chapter, a method was developed to detect the migration of the humeral component of the elbow prostheses using a single sensor from the previous chapter to using multiple implanted sensors. The sensors integrated into the humeral stem of the elbow prostheses are the 3 axis magneto resistive sensors which are configured by a magnetic field received from the permanent magnet, embedded in the cement restrictor to measure the migration in multiple axis. Two different multiple sensor design approaches were used: dual sensor and quad sensor configurations. Using this multiple sensor approach allows an exploitation of the relationship between measured data from each sensor and develops a method to convert the raw magnetic field data in detecting implant position in multiple axes. The performance for both design configurations were analysed, where the quad sensor configuration delivered a resolution of 0.15 mm with an average error below 0.05 mm linearly. This method also eliminates the tilting effect and increases the sensitivity of the system to 20 mm, which is not possible with the single sensor configuration, along with improving the signal to noise ratio and reducing RMS error. Compared to the single sensor configuration, the dual sensor configuration downgraded the system performance by introducing additional noise in the system while the quad sensor configuration improved the overall system performance. The work presented in this chapter forms the basis for a paper that is now under revision in the peer-reviewed journal IEEE Sensors.

4.1 Introduction

Aseptic loosening of the elbow prostheses is the major contributor to lowering the longevity of the elbow prosthesis. Comparing with the 10 years longevity of the hip and knee prostheses (95% and 90%), the elbow prosthesis has low longevity 79.1 % for 10 years [52]. Early detection of loosening will not only aid in increasing the longevity of the prostheses but will play a key role in providing information for what are the causes of loosening and how prostheses design can be improved. Recently, detection techniques have emerged based on a variety of transducer types i.e., eddy current, capacitive, and strain sensors. However, all these sensing mechanisms have higher sensitivity of detection in a single axis but experience a crosstalk effect while performing multiple axes detection and the effect of the biomaterials are still under-developed [120, 127]. Recently, a capacitive sensor has been investigated, to detect microscale displacement between bone and implant [127]. These capacitive sensors are typically complicated to fabricate and none of the biomaterial effects have been studied. Benefitting from the recent advanced magnetic sensor and their miniature size and with no transparency of the human body, in the previous chapter, a magnetic field based detection technique was developed. The detection technique was low-cost, capable of detecting displacement in multiple axes at a resolution of 0.30 mm linearly and 0.5 degrees angularly, but experiencing an error of tilt effect and environmental noise. Also, the accuracy of detecting measurement was limited to Z-Distance of 15 mm beyond this limit the error in detection measurement and noise increased significantly (Chapter 3, Figure 3.20).

Due to the aforementioned limitations of current techniques, this chapter focuses on a micro-motion detection technique based on varying magnetic fields using multiple sensors embedded in the prostheses and comparing it to our benchmark single sensor configuration developed in the previous chapter, which has also been described in Khan et al. *(2021)* [140]. The multi-sensor uses the same concept of using a sensor to detect the change in the magnetic field of a moving magnet, which can then be translated into displacement and position.

In this study, two different multi-sensor configurations (dual sensor configuration and quad sensor configuration) were investigated to limit the tilting effect of the single sensor, increase resolution and sensitivity along with correlating the raw data from all sensors to a new filtering technique to improve the signal to noise ratio (SNR) and reduce the root mean square (RMS) error.

4.2 Material and Method

4.2.1 System Overview

To measure the radiograph-free migration of the elbow prosthesis, a magnetic measuring system was designed consisting of a magnetic sensing multi-array (Multi-sensor) hermetically sealed in Titanium metal, a sealed magnet embedded in a commercially available cement restrictor made of UHMWPE, and a layer of Polymethylmethacrylate (PMMA) bone cement between them to mimic the original implant position as shown in figure 4.1.

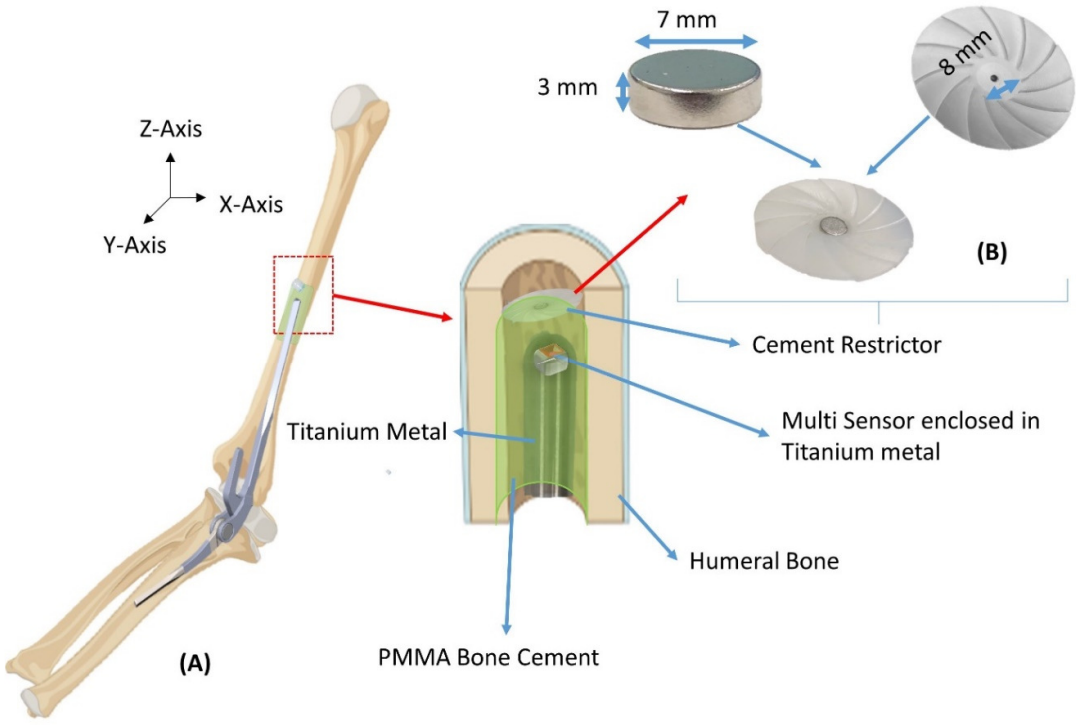

Figure 4. 1: (a) Diagnostic system overview of multi sensor diagnostic system (b) Dimension of a magnet, cement restrictor, and magnet enclosure in cement restrictor

A compact 3D magnetic sensor (TLV 493D, Infineon, Austria) with digital output via the I2C bus was used to detect the position of the implant via measurement of the magnetic field intensity emitted from the magnet in three orthogonal directions as shown in figure 4.1. Two types of multi-sensor configuration were developed; a dual sensor configuration and a quad sensor configuration. The sensors' design configurations were mounted on a custom-designed rigid base (PCB). The size of the rigid base (PCB) was designed based on the dimensions of a commercially available humeral stem. According to the Zimmer Conrad/Morrey implant, the length of the humeral stem varies from 110 mm to 152 mm and its diameter varies from 6 mm to 20 mm [167]. Considering these implant dimensions, the PCB for both configurations were designed and manufactured where the sensors and their auxiliary components were placed accordingly as shown in figure 4.2 and 4.3.

4.2.2 Dual Sensor Configuration

Two 3-axis magneto resistive sensors (TLV493d, Infineon, Austria) were placed longitudinally on the PCB having a distance of 42 mm from each other as shown in figure 4.2. Sensor S1 is positioned to be at the tip of the humeral stem head facing the cement restrictor while sensor S2 would be at the bottom of the stem.

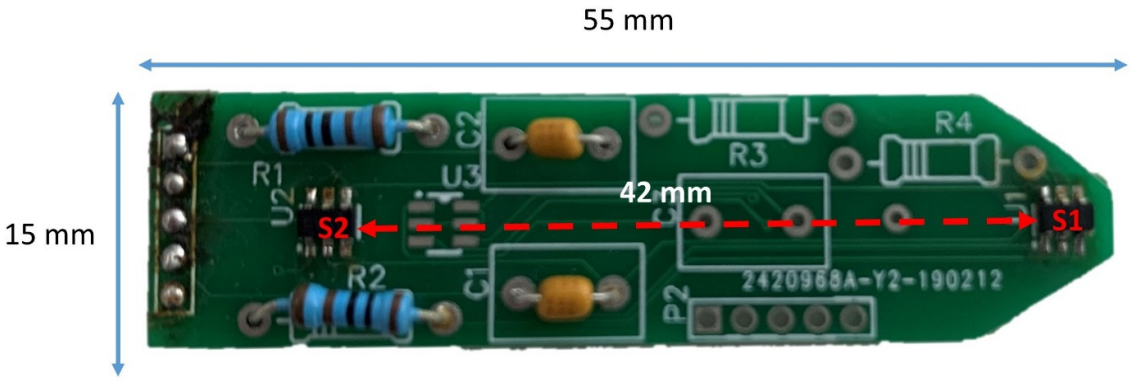

Figure 4. 2: PCB layout of Dual sensor Configuration highlighting the position of the sensors and auxiliary components.

In this dual sensor configuration, S1 will only experience the magnetic field emitted from the magnet embedded in the restrictor, while S2 will only measure the stray/environmental magnetic field. This was the reason that S2 was placed 42 mm away from S1, so that it is unable to detect the magnet's magnetic field. The hypothesis is that the removal of the stray magnetic field from the actual magnet's magnetic field will improve the system detection performance. In order to remove that stray field from the actual field, the subtraction method was used [168] in which the magnetic field received from S1 will be subtracted from the field received by S2 in all three axes. By using equation 1-3 as below:

$$Bxd = Bx1 - Bx2 \quad (1)$$

$$Byd = By1 - By2 \quad (2)$$

$$Bzd = Bz1 - Bz2 \quad (3)$$

Where $Bxd,\ Byd,$ and Bzd are the combined magnetic field of the dual sensor configuration and $Bx1,$ $By1, and\ Bz1$ are the S1 detected magnetic fields in all axes while $Bx2,\ By2, and\ Bz2$ are for S2.

4.2.3 Quad Sensor Configuration

Figure 4.3 shows the layout of the PCB along with the position of the quad sensor (S1 to S4). In the quad sensor configuration, 4 magneto-resistive sensors were placed in a cross formation so that each pair of sensors has one common axes. Sensor S1 and S2 have a common y-axis while sensor S3 and S4 have a common x-axis. Each sensor was placed 3mm apart from the middle common point as shown in figure 4.3, and all of them are facing towards the magnet and receiving magnetic field data from the magnet. Here, the hypothesis is that each sensor will experience the same magnetic field from the magnet

as well as the environment/stray field. By summing up the subtracted field from the pair of sensors it is possible to reduce the noise content and enhance the system performance.

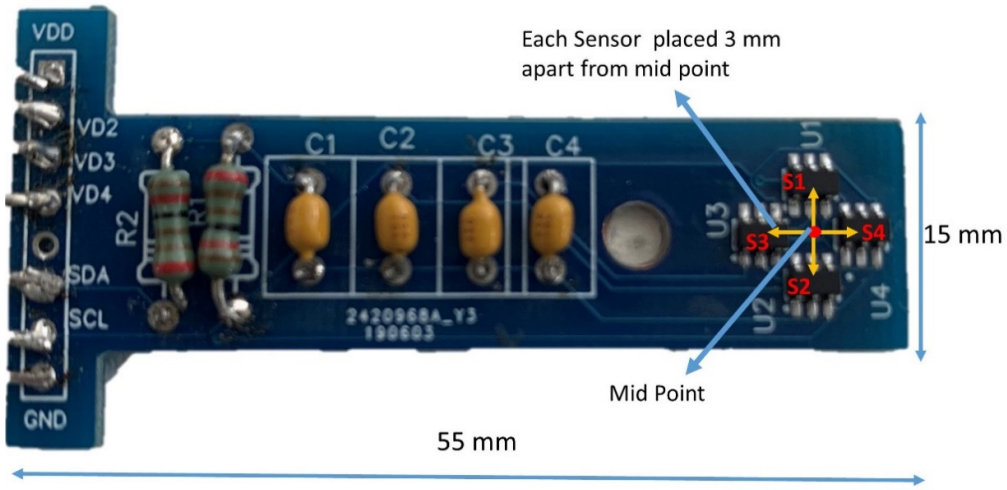

Figure 4. 3: PCB layout of Quad sensor Configuration highlighting the position of the sensors and their auxiliary component.

For the removal of the external stray magnetic field, in quad configuration, the magnetic field of all the sensors in the x and y axes is summed and the mean of the z-axis is taken as shown in equation 4-6. The reason for taking the mean average of the z-axis field is that all sensors have a common z-axis position. So, by subtracting, this will eliminate the magnetic field in the z-axis.

$$Bxq = \sum_{i=1}^{n} B_x(2i-1) - B_x 2(i) \qquad (4)$$

$$Byq = \sum_{i=1}^{n} B_y(2i-1) - B_y 2(i) \qquad (5)$$

$$Bzq = \frac{\sum_{i=1}^{2n} B_z\ (i)}{n} \qquad (6)$$

Where $Bxq, Byq, and\ Bzq$ are the combined magnetic field of the quad sensor in all three axes. n is the sensor pair. $Bx, By, and\ Bz$ are the magnetic field detected by each sensor in all three axes.

4.2.4 Multiple Sensors Bus Configuration with DAQ

For both configurations, NI My RIO 1900 (National Instruments, Austin, TX, USA) was used as a data acquisition device for bus configuration and retrieving data from the multi-sensor set-ups. A total of 8 sensors can be connected to the system via I2C bus communication protocol. The I2C communication and its associated pull up resistors are explained in detail in chapter 3. In the multi-sensor configuration (dual sensor and quad sensor), each sensor needs to be configured via the I2C bus and allocated with a specific 2-bit address. Figure 4.4 describes the configuration process for how to achieve the specific bit address for S1 and S2 for the dual sensor configuration.

For dual sensor configuration the two slave bus communication method was used, in which each sensor is provided with its own separate power line. S1 is powered with the whole system while keeping the S2 power down. During the initial power up, if the voltage on the SDA pin is high, the address bit is set as high “11” (Default case of open drain configuration). If the voltage on the SDA pin is low, the address bit is set low to “00”. These addresses remain fixed until the system is powered downed or at rest. After a 200 milliseconds wait, the system powers up S2 and allocates the opposite bit address to the sensor S1.

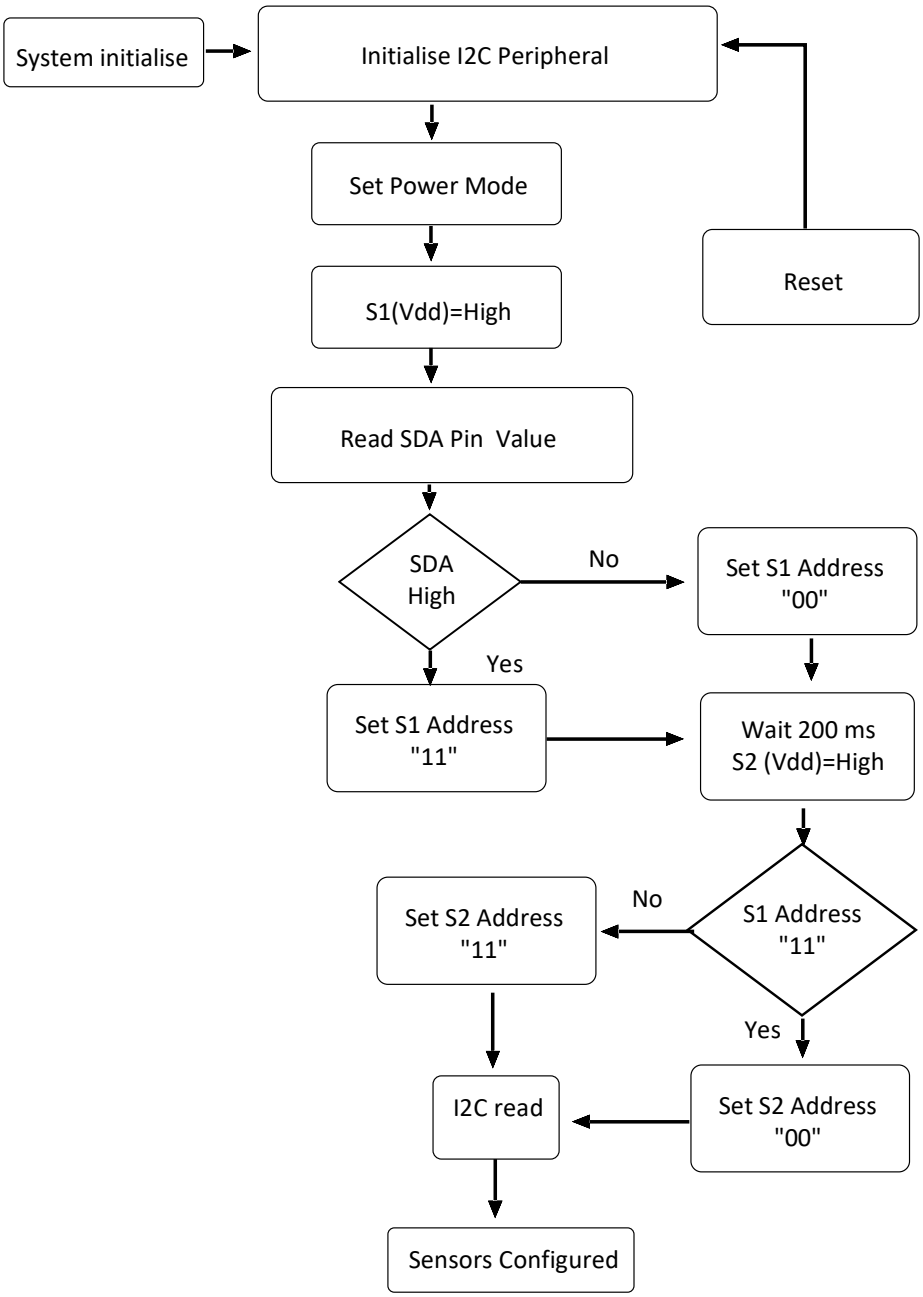

Figure 4. 4: Flow chart for allocating specific bit address for dual sensor configuration.

Figure 4.5 describes the configuration process for how to achieve the specific bit address for more than two sensors i.e. quad sensor.

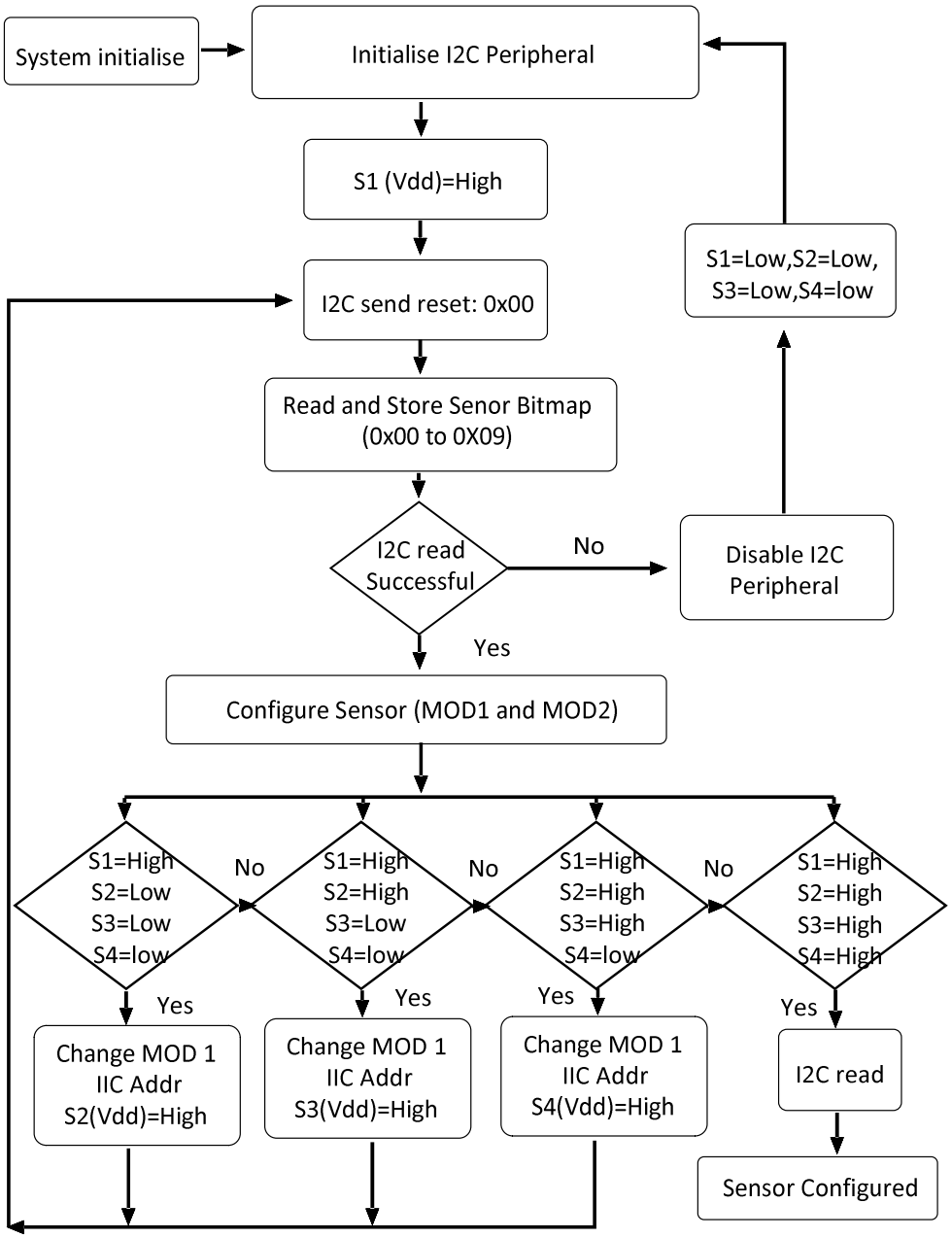

Figure 4. 5: Flow chart for allocating 2-bit address in quad sensor configuration.

First, the system is initialised by powering only sensor S1 and after reading the SDA pin value and allocating the bit address of “11” or “00” depending upon the SDA pin state as describe in 2 slave communication. Once that is done the MOD 1 register (IICAddr bits) needs to be changed from “00” by

default to “01”. This “01” is now a new bit address for the sensor S1. After establishing this, a similar process is followed for sensor S2 to S4 by powering up each sensor when their new bit address is established. For sensor S2 to S4 their new bit address will be “10”, “11”, and “00”.

4.2.5 Magnet Selection and Bone Cement Preparation

Figure 4.1b shows the dimensions of the permanent magnet which was embedded in the commercially available Hardinge cement restrictor (Depuy Synthesis, UK,). The selection of magnet material, size, and shape was based on the magnetic field strength of the magnet and the dimensions of the cement restrictor. Rare earth neodymium magnets provide higher magnetic strength to size ratio [159]. Also, rod and cylindrical shaped magnets produce higher magnetisation in the air as compared to other shaped magnets i.e., ring, sphere, tube, etc. [159]. For these reasons, a neodymium N40 3mm x 7mm cylindrical magnet was chosen for this study. The magnet field distribution is explained in more detail in chapter 3.

PALACOS PMMA bone cement mixture (Heraeus Medical, Hanau, Germany) was used as the fixture medium for the humeral stem. The bone cement consists of solid powder along with a liquid monomer. Both contents were mixed according to supplier instructions with a ratio of 2:1. When the cement was in semi-solid form it was poured in different sized slabs ranging from 5-10 mm.

4.2.6 Calibration of Multi-Sensors

To detect implant displacement, the relationship between the magnetic field and the applied displacement was investigated. The magnetic response of the multi-sensor in determining the localisation of the magnet was investigated at different distances using the same calibration criteria as performed in chapter 3 and also in Khan et al. (2021) to estimate the distance between the sensor and magnet (Z-Distance) [140].

To detect the implant displacement, the position of the magnet with respect to the sensor in all three axes must be determined. The z-axis position (Z-Distance) is the distance between the magnet and the multi-sensor. According to Chao Hu et al. (2007), the theoretical localisation of the axially magnetised magnet can be determined by using equation 7 [163].

$$B = Bx + By + Bz = \frac{\mu_o M}{2}\left(\frac{z + H_m}{\sqrt{(z + H_m)^2 + \left(\frac{D_m}{2}\right)^2}} - \frac{z}{\sqrt{z^2 + \left(\frac{D_m}{2}\right)^2}}\right) \quad (7)$$

Where M is the magnetisation of the magnet axially, μ_o is the relative magnetic permeability, H_m is the height of the magnet, z is the distance from the pole of the magnet and D_m is the diameter of the magnet. Bx, By, and Bz are the magnetic flux intensities of the single magnetic sensor.

With the same working principle described in chapter 3 section 3.2.4, the Z-Distance value in a multi-configuration (dual sensor and quad sensor) was determined by using the sum of the magnetic field intensities of multi-sensor Bxc, Byc and Bzc instead of single sensor magnetic intensity as shown in equation 8.

$$B = Bxc\,\hat{\imath} + Byc\,\hat{\jmath} + Bzc\,\hat{k} = \frac{\mu_o M}{2}\left(\frac{z + H_m}{\sqrt{(z + H_m)^2 + \left(\frac{D_m}{2}\right)^2}} - \frac{z}{\sqrt{z^2 + \left(\frac{D_m}{2}\right)^2}}\right) \quad (8)$$

At the same time, the magnetic field variations detected by the individual sensors of the quad sensor configuration were investigated. After finding the Z-distance value, the migration of the implant in the x and y-axis can be calculated by using equations 9-12.

$$\alpha = \tan^{-1}\left(\frac{B_{yc}}{B_z}\right) \quad (9)$$

$$\beta = \tan^{-1}\left(\frac{B_x}{B_z}\right) \quad (10)$$

$$Y\ Distance = \tan\alpha * Z\ Distance \quad (11)$$

$$X\ Distance = \tan\beta * Z\ Distance \quad (12)$$

4.2.7 Filter Technique

The data received from the multiple sensors were smoothed using a discrete wavelet transform (DWT) de-noising technique to estimate the signal from the sensor and remove the noise component. Comparing to the S.Golay filtering technique used in chapter 3. The S.Golay consist of several assumption parameters (chapter 3, section 3.2.5) if those parameter were not met by the data signal the filtering process didn't work. In addition to that the filtering method work on the moving windows by using a polynomial fitting (figure 3.8) and its computational time was proportional to window length. So for the larger data more computational time will be required. Using such type of filtering for continuous monitoring was not a best options. To overcome this computational problem a DWT was used. DWT provides effective de-noising with minimal computational complexity as it requires minimum number of coefficients. The DWT de-noising technique consists of three steps with five parameters as shown in figure 4.6.

First, the data from the sensor needs to be transformed into a wavelet domain with the length of the signal power of 2. This transformation can be done by selecting a mother wavelet function ($\emptyset$) from the wavelet family. Theoretically, there exists a many type of wavelet function but among them, 22 wavelet types are used most [169]. Selecting a suitable type of wavelet is extremely important for de-noising the data because two similar wavelets may give different de-noising data. After the selection of the wavelet function, the decomposition level (k) needed to be defined. Second, a criterion is selected to reduce or

shrink the coefficient of the wavelet transform. The coefficient of the wavelet transform can be reduced by selecting a specific thresholding function (β).

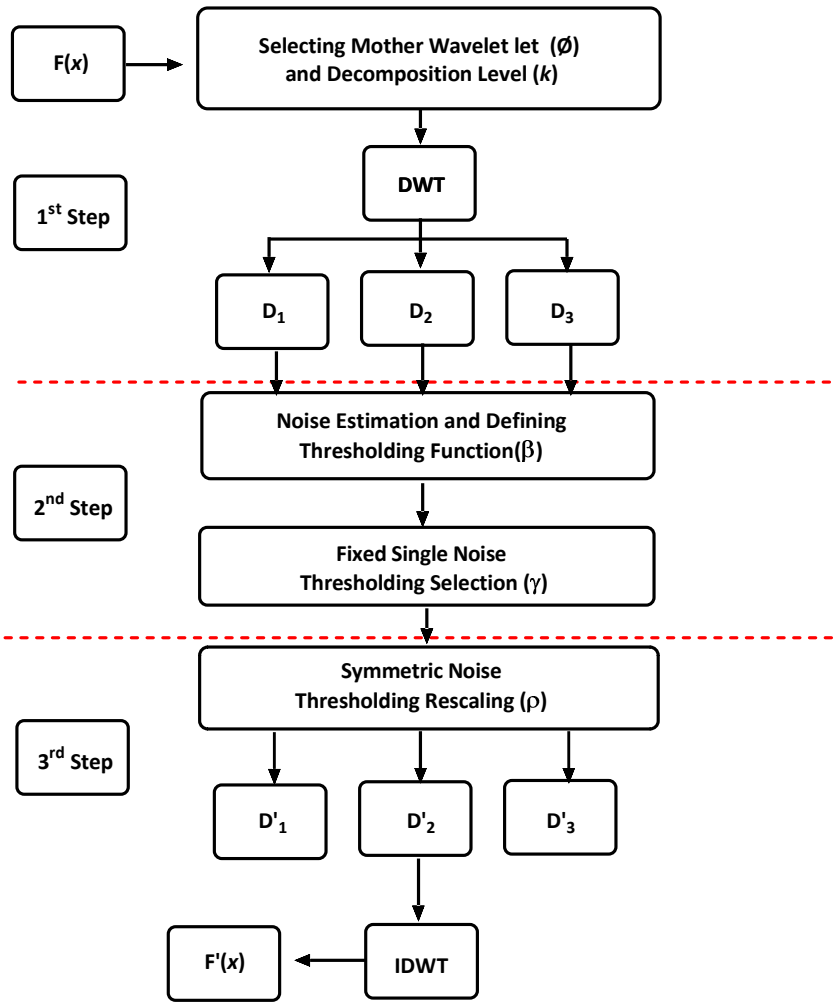

Figure 4. 6: Steps involved in the discrete wavelet transform to de-noise signal.

There are four types of thresholding functions that are commonly used. Among them, Stein's Unbiased Risk Estimate (SURE) threshold is mostly used because of its state-of-the-art decomposition of noise and better performance [170]. The SURE thresholding can be defined as:

$$SURE(t,x) = N - 2 \times M_{(i:|x_i| \le t)} + \sum_{i=1}^{N} (|x_i| \wedge t)^2 \qquad (13)$$

Where x_i is the detailed wavelet coefficient, t is the candidate threshold, N is the length of data and M is the number of the data points less than t. SURE thresholding is usually used to obtain the unbiased variance between the unfiltered and filtered data. After defining the function, the thresholding selection rule (γ) is selected. In DWT, de-noising of the signal depends greatly on the selection of the noise threshold. The wrong choice can result in lowering down the signal strength. Traditional thresholding transforms the coefficient whose magnitude is below the specified value. In the DWT de-noising technique, there are different thresholding selection parameters, but the most commonly used threshold is global thresholding. In global thresholding noise is assumed to have Gaussian distribution, having the same amplitude and frequency distribution that span the same data length[170]. Global thresholding can be further divided into soft and hard thresholding which can be defined in equations 14 and 15. In hard thresholding, the coefficients are either kept or removed from the resultant filtered data while in soft thresholding both positive and negative coefficients are shrunk towards zero.

$$x'_{j,i} = \begin{cases} x_{j,i} : |x_{j,i}| \ge t \\ 0 \quad : |x_{j,i}| < t \end{cases} \qquad (14)$$

$$x'_{j,i} = \begin{cases} sign(x_{j,i)})(|x_{j,i}| - t) : |x_{j,i}| \ge t \\ 0 \qquad\qquad\qquad\quad : |x_{j,i}| < t \end{cases} \qquad (15)$$

Where $x_{j,i}$ and $x'_{j,i}$ are the noise and de-noise coefficients of the wavelet at a j[th] decomposing level and i location. Finally, the shrunk coefficients are first rescaled (ρ) and then inversely transform to the original domain which is the de-noised signal.

To check the performance of the filtered data equations 16 and 17 may be used to determine its signal to noise ratio (SNR) and its root mean square error (RMSE).

$$RMSE = \sqrt{\frac{1}{N}\sum_{n=1}^{N}[x(n) - x'(n]^2} \qquad (16)$$

$$SNR = 10\, log_{10}\left\{\frac{\sum_{n=1}^{N}[x(n)]^2}{\sum_{n=1}^{N}[x(n) - x'(n]^2}\right\} \qquad (17)$$

4.2.8 Experimental Setup

To correlate the relationship between implant displacements with the variation in a magnetic field a mechanical testing system (ElectroForce 3330 Multi-Axial Test System (TA Instruments, Delaware, USA)) was used to provide input displacement as shown in figure 4.7.

The system consists of two motorised stages: linear and rotational with a resolution of 0.5 μm linearly and 0.01 degrees angularly. To provide the repeatable simulation of implant displacement, an adjustable fixture/bracket was designed and fabricated to hold the multi-sensor and magnet with varying layers of bone cement. The fixture was attached to the motorised axial crosshead on the ElectroForce as shown in figure 4.7. The machine crosshead provided the y-axis movement and the machine platform base provided angular motion in the x-z plane.

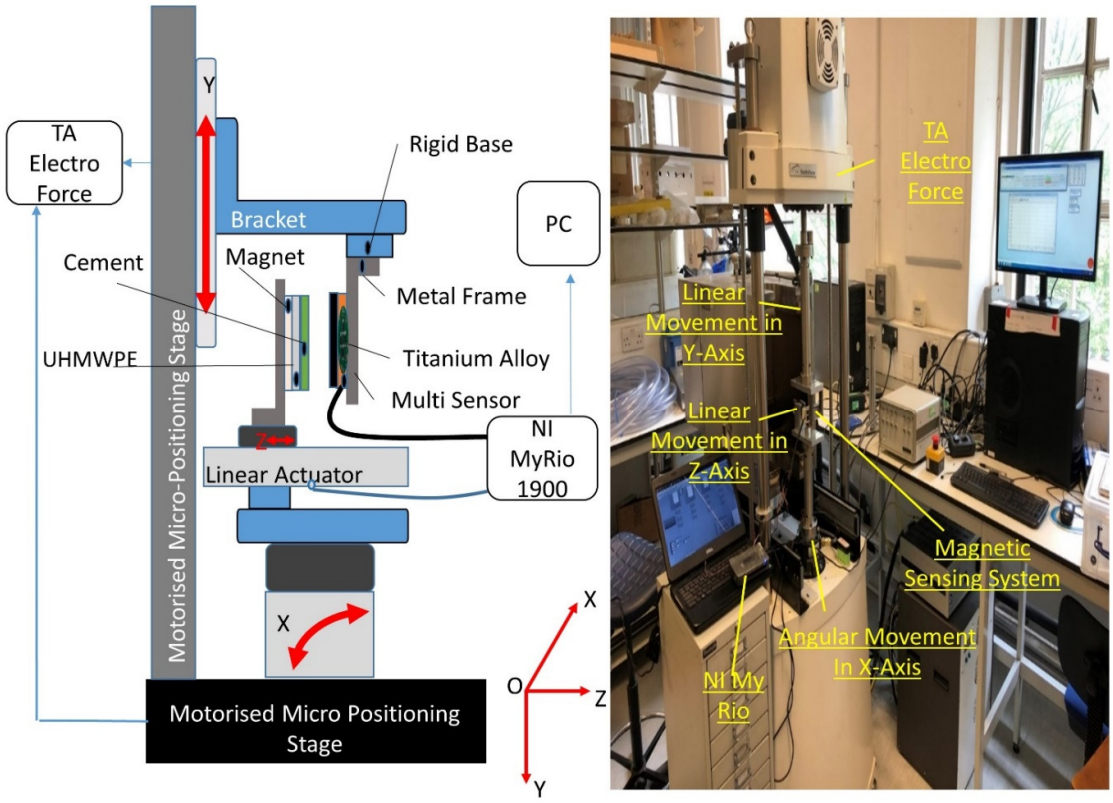

Figure 4. 7: Overview of the Experimental setup Design

The distance between the multi-sensor and magnet i.e. (Z-distance) was adjusted using a linear actuator (Actuonix Inc., Victoria, BC, Canada) with a resolution of 1 mm. The output of the actuator was connected to a My Rio NI DAQ card and LabVIEW (National Instruments) code was written to adjust the Z-distance. The ElectroForce machine was programmed to move the sensor bracket in the y-axis quasistatically (1 min intervals) at amplitudes of 0.15 to 4 mm with a step size of 0.05, 0.3, and 0.5 mm using a square waveform and dynamically using a sine waveform with the frequency of 0.1-0.5 Hz at amplitudes of 0.15 to 4 mm. Similarly, the machine was programmed to move in the x-z plane quasistatically (1 min intervals) with an amplitude of 0.5 degrees to 4 degrees with the step size of 0.5 degrees.

4.3 Results of Dual Sensor Configuration

4.3.1 Noise Reduction Analysis

Figure 4.8 highlights the magnetic field of the dual sensor configuration without applying any filtering technique. It shows that, instead of reducing the noise content, the second sensor increases the level of distortion. Although there was no offset of the magnetic field in any axes, a 10 % increase in noise was observed. To further understand how this additional noise will affect the overall system performance, Experimental tests were conducted on the Z-Distance detection performance along with the linear movement detection as well. Also, the Dual sensor configuration performance was compared with the single sensor performance.

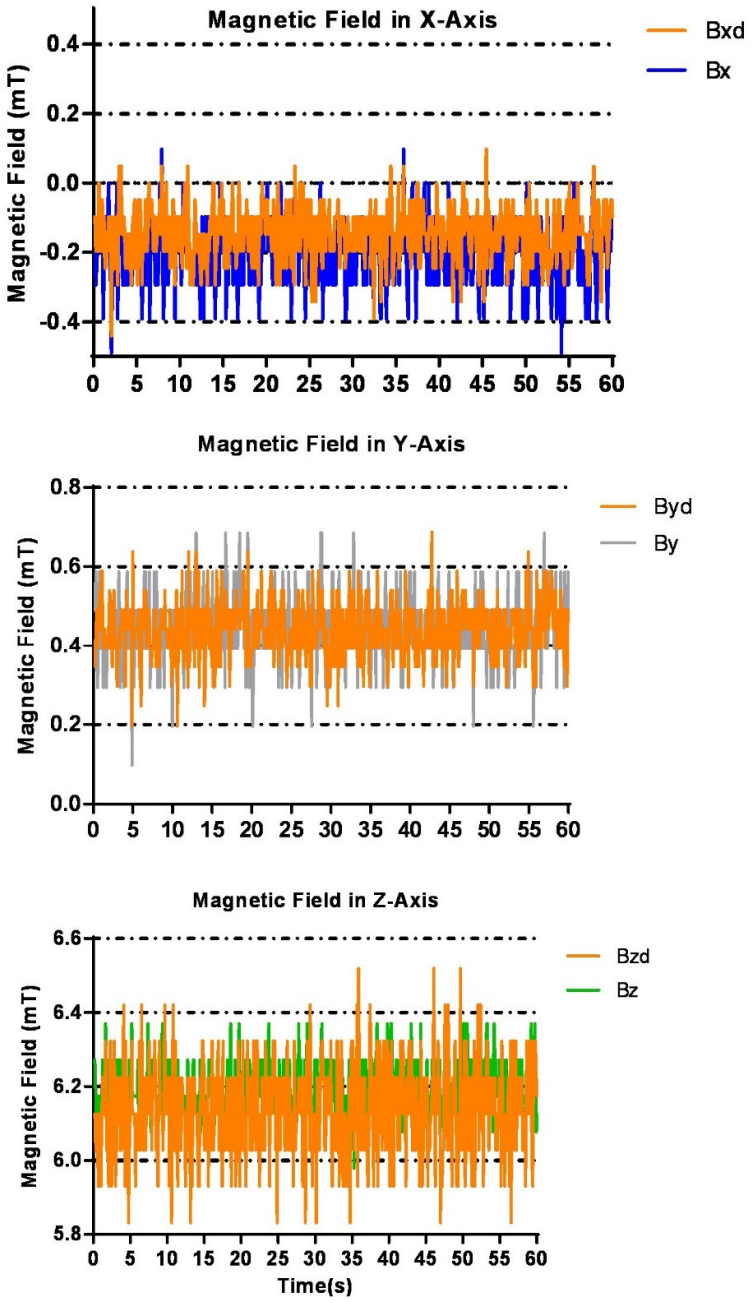

Figure 4. 8: Comparison of the raw magnetic field between a single sensor and dual sensor configuration in all three axes at a fixed Z-Distance of 15 mm. Where Bx, By and Bz are the magnetic field detected by a single sensor configuration while Bxd, Byd, and Bzd are the magnetic field detected by dual sensor configuration.

4.3.2 Z-Distance Detection

For the proposed sensor configuration, the result for the detection of the distance between the sensor and the magnet (Z-Distance) is highlighted in figure 4.9. The Z-Distance results were obtained by placing the magnet perpendicular to S1 of the dual sensor configuration, which was hermetically sealed in the 2 mm titanium metal and was moved at a step size of 1 mm using the linear actuator. After obtaining the combined magnetic field from all three axes, the Z- Distance was calculated by using the same detection algorithm derived for the single sensor configuration (chapter 3) by implementing equation 8.

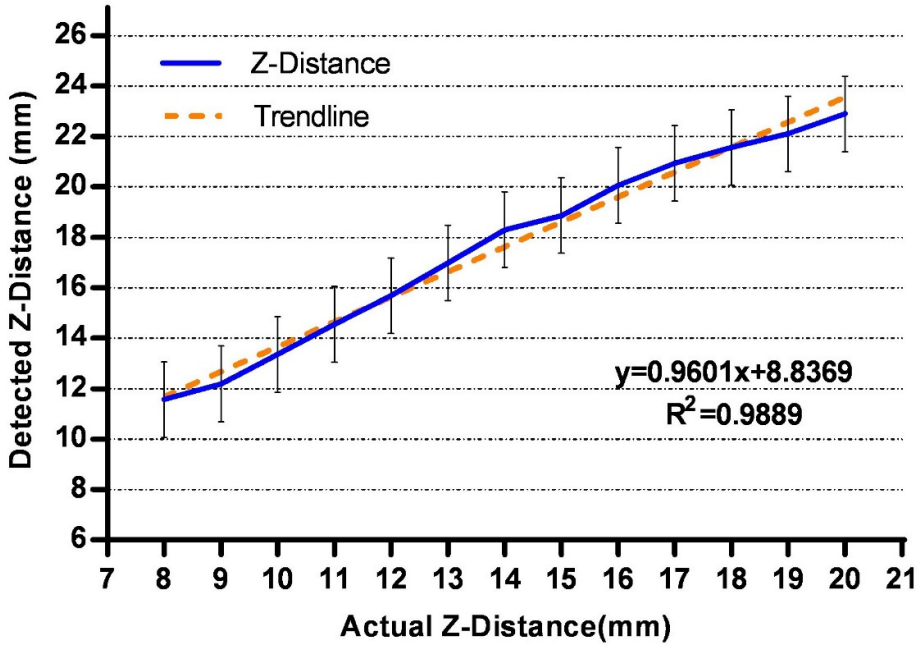

Figure 4. 9: Z- Distance Detection by dual sensor configuration

The Z-Distance detection for the dual sensor configuration provided detection of the distance between the sensor and magnet. A detection error of 3.2 mm and a standard deviation error of ± 1.50 mm were observed. Also, comparing it to the single sensor Z-Distance detection (chapter 3), the correlation with

the straight line equation is not well fitted for the dual sensor configuration has a higher value of intercept and adequate R^2 value.

4.3.3 Linear Movement

In order to check the performance of the dual sensor configuration in detecting the linear migration, the system was moved linearly in the y axis at a step size of 0.3 mm, 0.5 mm, and 1 mm both quasi statically and dynamically at a Z-Distance of 13 mm. Distance in the other two axes remained fixed. As the data contained a high content of noise, a filtering technique was employed by implementing the filtering parameters as shown in table 4.1.

Table 4. 1: Selected Parameters for the DWT Filter

	1st Step		**2nd Step**		**3rd Step**
Parameters	Mother Wavelet	Decomposition level	Threshold Function	Threshold Selection	Threshold rescaling
Selected Parameter	**Sym 6**	**6**	**SURE**	**Hard**	**one**

Figure 4.10 highlights that the filtering technique smoothed out the data by removing the excessive noise. Also, figure 4.10 shows that the dual sensor configuration was able to detect the linear movement of the system in the y-axis, but it also showed changes in the z-axis values as well, keeping the x-axis constant. As the system was only moved linearly, the dual sensor configuration followed the trend of angular detection by changing values in the two axes.

As proven in the Z-Distance detection study (section 4.3.2) the dual sensor configuration has an error of 3 mm. A similar, error was also observed here as well with an error of 3 mm as the actual Z-Distance was 13 mm the system showed 16 mm. Comparing to the single sensor configuration, the dual sensor configuration also had an error in the linear detection. Table 4.2 highlights the comparison of the dual sensor configuration with the single sensor.

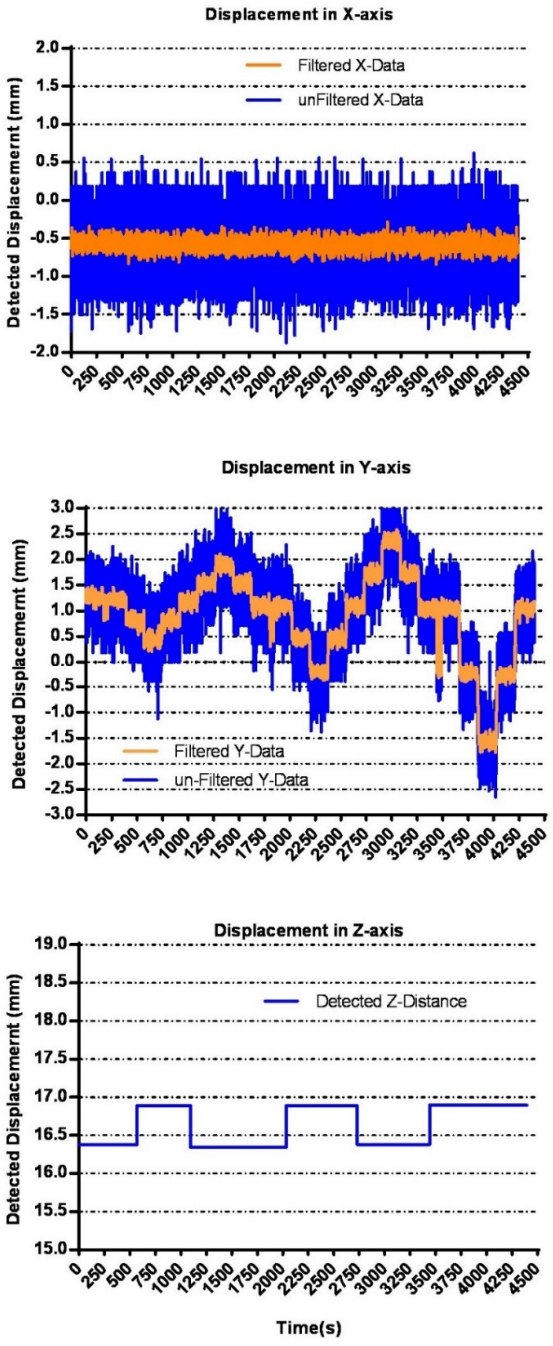

Figure 4. 10: Data from the 2 sensor configuration showing linear movement in Y-axis, keeping x/z axes displacement fixed

Table 4. 2: Comparison of linear detection movement between dual sensor configuration and single sensor

Actual Movement (mm)	**Movement Detection** **Single Sensor Configuration** (Mean ± SD)	**Percentage Error**	**Movement Detection** **2-Single Sensor** (Mean ± SD)	**Percentage Error**
0.3	0.31±0.46	3.33%	0.43±0.092	43.33%
0.5	0.49±0.045	2.04%	0.61±0.090	22.00%
1.0	0.98±0.035	2.04%	1.30±0.070	30.00%
1.5	1.49±0.042	0.67%	1.95±0.083	30.00%
2.0	1.97±0.035	0.52%	2.61±0.711	30.05%
2.5	2.48±0.042	0.60%	3.25±0.082	30.00%
3.0	2.98±0.038	0.67%	3.92±0.086	30.66%

The dual sensor configuration was able to detect linear displacement but had more error and standard deviation error compared to a single sensor. Also, table 4.2 shows that the dual sensor configuration has an overall percentage error of 30.5 % while the single has 1.4 % in detecting linear movement.

Table 4.3 shows that the single sensor has better SNR compared to the dual sensor configuration. Also, in the dual sensor, the SNR remains the same while the RMS error increased as the displacement is increased, while for the single the RMS error is kept to a minimum and SNR improves as displacement increased.

Table 4. 3: Comparison of the RMS error and SNR between the single sensor and dual sensor configuration

	Single Sensor Configuration		**Dual Sensor Configuration**	
Displacement (mm)	**RMSE**	**SNR (dB)**	**RMSE**	**SNR (dB)**
0.3	0.047	44.51	0.162	33.80
0.5	0.045	49.41	0.153	38.72
1.0	0.052	54.19	0.297	38.99
1.5	0.055	57.19	0.453	38.84
2.0	0.053	59.92	0.616	38.68
2.5	0.049	62.52	0.780	38.56
3.0	0.044	65.05	0.939	38.53

4.4 Results of Quad sensor Configuration

4.4.1 Noise Reduction Analysis

First, the effect of the magnetic field on the quad sensor configuration was analysed. As shown in figure 4.3, the sensors are very closely placed to each other. So, if there is any type of magnetic variation all the sensors will read the same effect. Figure 4.11 shows the magnetic field variation of all four sensors (S1-S4) in the y-axis when the magnet was randomly moved.

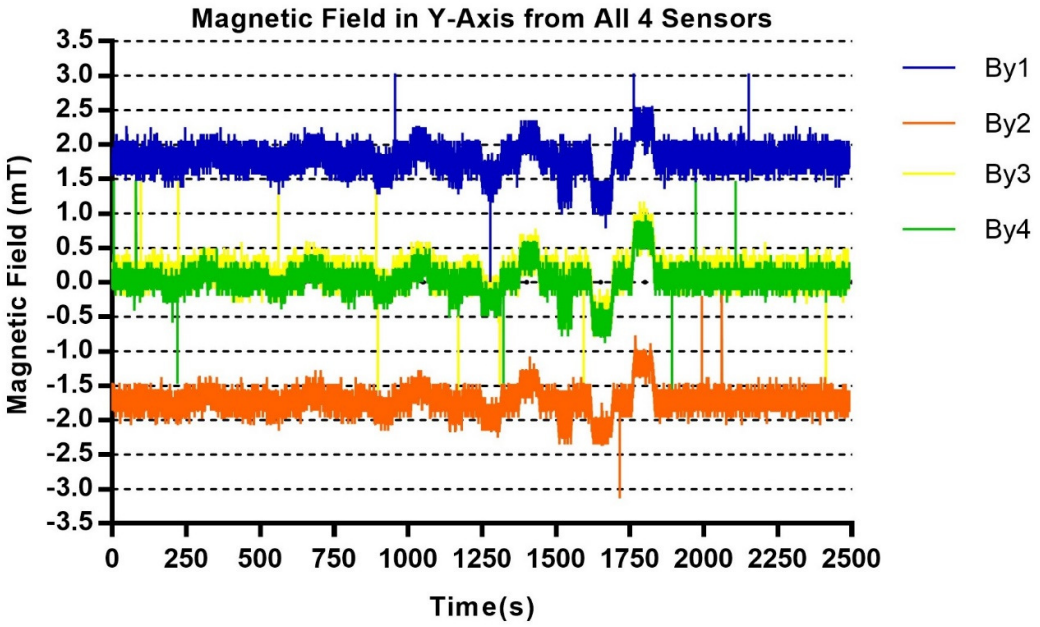

Figure 4. 11: Magnetic Field intensity of quad sensor (S1, S2, S3, and S4) in the y-axis.

It was observed that the y-axis magnetic field of all sensors changed in unison when the magnet was moved in the y-axis, but with different magnitudes because of their position. The magnetic fields of sensors 3 and 4 were almost the same because their y-axis position is the same. Whilst for sensors 1 and 2 their y -axis are not aligned and therefore have a magnetic field magnitude difference. Similarly, when the magnet was moved in the x-axis all the sensors showed the same magnetic field variation response but with different magnitudes.

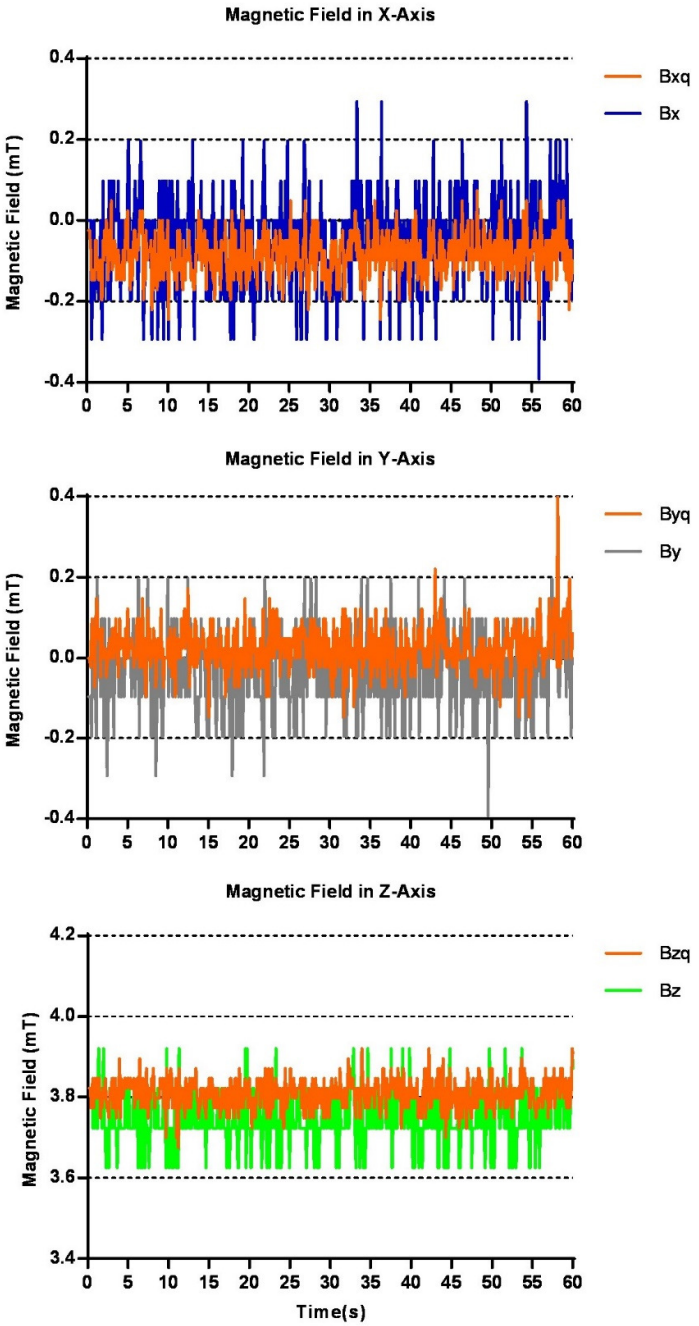

Figure 4. 12: Comparison of the raw magnetic field between a single sensor and dual sensor configuration in all three axes at a fixed Z-Distance of 15 mm. Where Bx, By and Bz are the magnetic field detected by a single sensor configuration while Bxq, Byq, and Bzq are the magnetic field detected by the quad sensor configuration.

The magnetic field measured by the quad sensor configuration showed a reduction in the noise content as compared with the single sensor configuration and dual sensor configuration. This reduction was observed without applying any filtering. Figure 4.12 shows the raw magnetic field measured by the single sensor configuration and quad configuration in all three axes. This reduction in the quad sensor configuration was due to the cancellation of the external magnetic field. All the sensors measure the same amount of external magnetic field, so by combining them, they cancel out the external magnetic field variation. Another reason for the reduction was due to the common mode rejection of electronic noise, as each sensor detected measurements were combined which results in reducing/averaging the random noise associated with the sensors.

4.4.2 Z- Distance Detection

As described in the previous section, the quad sensor must be calibrated to determine the localisation of the magnet and detect distance from the magnet (Z-Distance). Similar steps used for the dual sensor calibration were also performed for the quad sensor, by hermetically sealing it in 2 mm think titanium alloy and moving it perpendicularly to the magnet at a step size of 1 mm using a linear actuator as shown in figure 4.7.

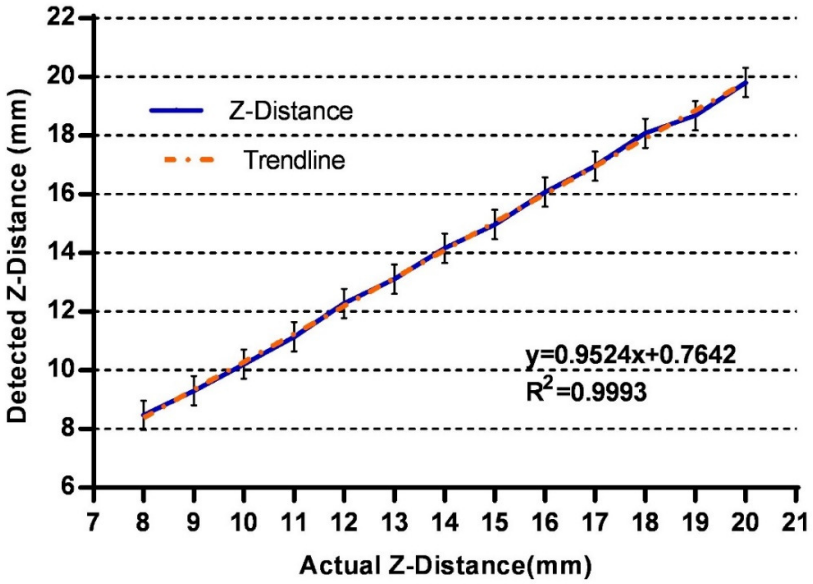

Figure 4. 13: Z-Distance detection by Quad sensor Configuration.

Figure 4.13 shows the correlation between the calculated distance from the quad sensor configuration and the actual distance (R^2 = 0.9993). The quad also showed a lower detection error of 0.35 mm and a lower standard deviation error of ±0.45 compared to a single sensor configuration.

4.4.3 Linear Movement in Y-Axis

As discussed in the calibration section 4.2.6, displacement detection in the x and y-axis can be determined by using equations 9-12. To analyse the performance of the quad sensor in detecting movement in the x and y-axis the sensor was first moved linearly in the y-axis ranging from 0.15 to 4.0 mm with the step size of 0.5 mm, keeping the x-axis movement constant and at a z-distance of 15 mm. Compared with the single sensor configuration the noise content in the quad sensor is lower, however, the data required filtering. The same filter parameters as described in table 4.1 were used. The selection of the mother wavelet and decomposition was based on the signal reconstruction and SNR value. Figure 4.14 shows both filtered and unfiltered x, y displacements along with Z-distance detection values. The results from the quad sensor configuration showed a strong correlation between actual and detected linear displacement with a resolution of 0.15 mm.

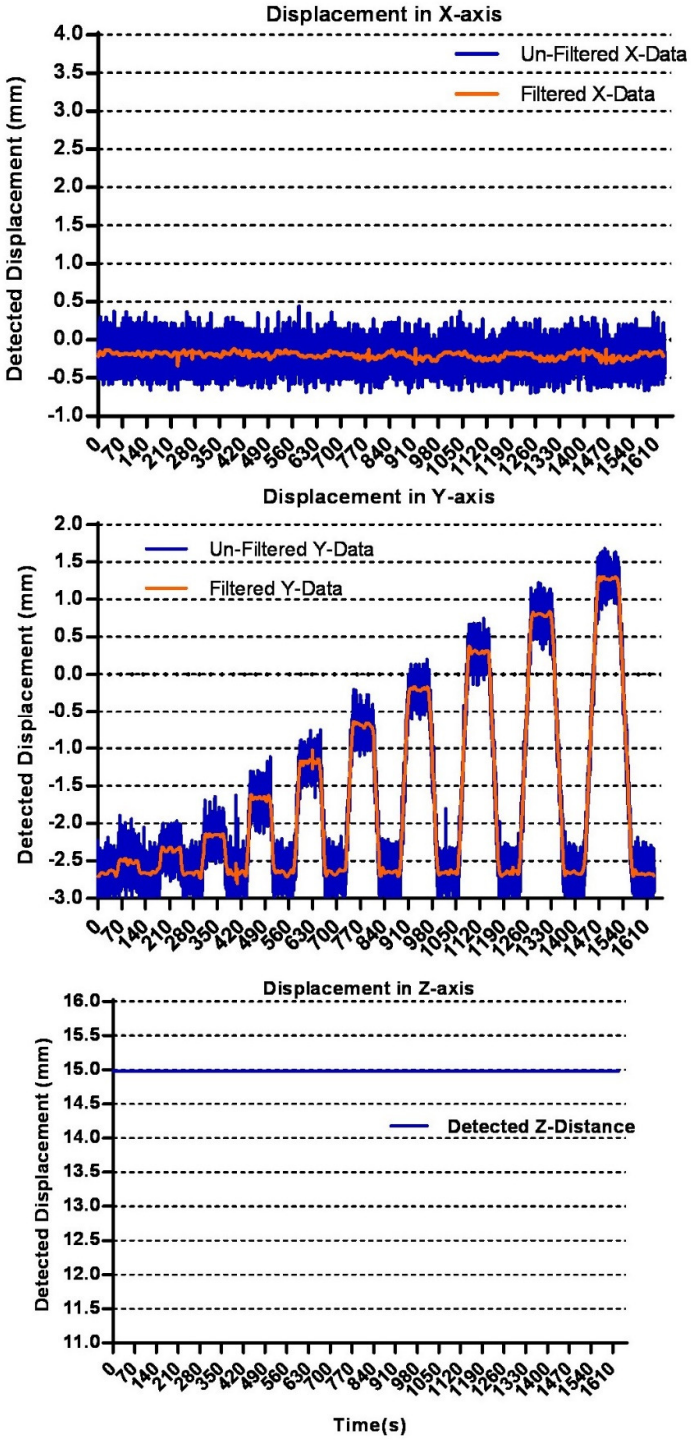

Figure 4. 14: Quasi-Static Linear Movement from 0.15 mm to 4 mm on y-axis keeping x and z axes constant

Figure 4.15 shows the comparison of a single sensor configuration with a quad sensor configuration. By keeping the Z-distance fixed at a 15 mm displacement, the single sensor configuration has a resolution of 0.3 mm while the quad sensor has a 0.15 mm. In the quad sensor configuration, the standard deviation error and mean error remained minimal as compared to the single sensor configuration where the standard deviation error and mean error increased with the increased displacement.

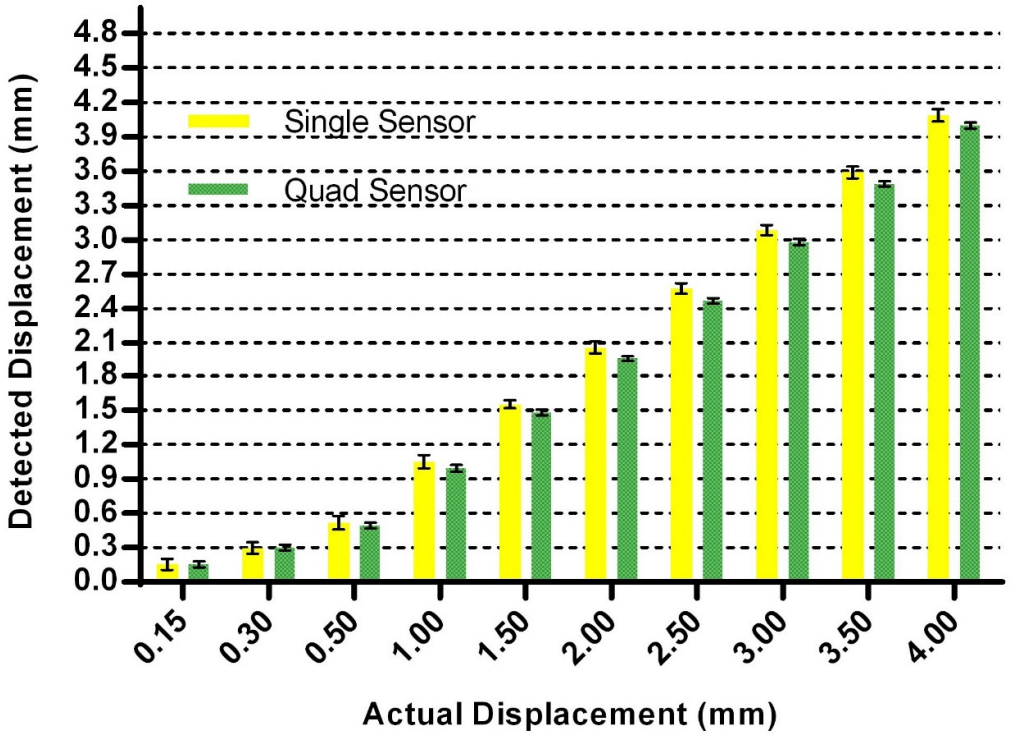

Figure 4. 15: Comparison of Linear Movement Detection between Single Sensor and quad sensor configuration

Table 4.4 describes the RMSE and SNR between single and quad sensor configurations. It was observed that in the single sensor configuration the maximum SNR value was 45 dB at 1.50 mm displacement at Z-Distance of 15 mm and with an increase in distance the RMSE increased. While, in quad sensor configuration with an increase in distance the SNR value increased, and this configuration showed a maximum RMSE of 0.051.

Table 4. 4: Comparison of the RMS error and SNR between Single sensor and Quad sensor configuration when impant is moved along y-axis.

	Single Sensor Configuration		**Quad Sensor Configuration**	
Displacement (mm)	**RMSE**	**SNR (dB)**	**RMSE**	**SNR (dB)**
0.15	0.063	33.27	0.031	39.34
0.30	0.051	41.14	0.032	45.30
0.50	0.066	43.36	0.021	53.51
1.00	0.137	43.03	0.026	57.59
1.50	0.157	45.40	0.035	58.47
2.00	0.222	44.87	0.051	57.72
2.50	0.288	44.55	0.047	60.31
3.00	0.355	44.32	0.033	64.92
3.50	0.390	44.64	0.026	68.41
4.00	0.479	44.21	0.020	71.83

4.4.4 Cross Talk Effect

The magnetic field density of a permanent cylindrical magnet has two features: non-linearity and crosstalk (chapter 3, section 3.3.1). Due to these, the magnetic field does not vary linearly with spatial location, and when the spatial location is moved in only one axis, the magnetic field changes in all axes. These features make a correlation between displacement and magnetic field not significant and tough to resolve.

Figure 4.16 shows the magnetic field measurement of the quad sensor in the y-axis when the magnet was moved to 1 mm with a step size of 0.1mm at different Z-Distance positions. Figure 4.16 (left) shows

that without calibration the magnetic field in the y-axis at different Z-distance shows a strong crosstalk effect along with non-linearity.

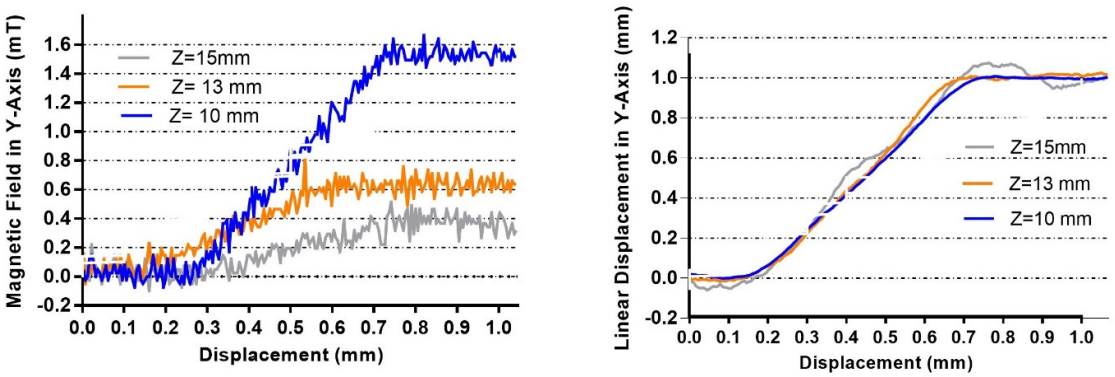

Figure 4. 16: Comparison of the raw magnetic field showing the cross talk effect (left) and the calibrated Quad sensor data in Y-axis at different Z-Distance values where the cross talk effect is eliminated (right).

Figure 4.16 (right) shows that the calibrated output from the quad shows a close agreement with the actual displacement along with eliminating the cross talk effect. A similar set of experiments was conducted to analyse the effect of the correlation of magnetic field with respect to displacement by moving the magnet in the z-axis to 4 mm with the step size of 1mm at different y distances. Figure 4.17 (left) shows the same effect of strong cross-talk and non-linearity as the magnet was moved in the z-axis at different y distance values. Figure 4.17b (right) shows the calibrated sensor output that clearly eliminates the crosstalk effect.

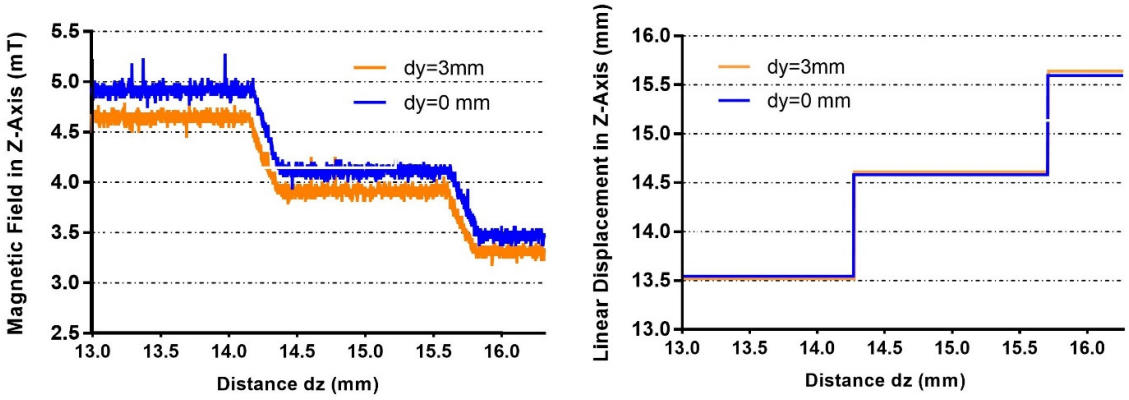

Figure 4. 17: Comparison of raw magnetic field (left) and the calibrated Quad sensor data in Z-axis at different Y-Distance values (right).

4.4.5 Angular Movement Detection

Figure 4.18 shows the results of the quad sensor when the system was moved angularly in the x-axis ranging from 0.5 degrees to 4.0 degrees with a step size of 0.5 degrees, keeping the y-axis constant and at a Z-Distance of 15 mm. Up to 1-degree movement (approximately 0.60 mm), the Z- Distance remains the same, beyond 1 degree there was a change in the Z-Distance value. This change in value was only observed when the magnet was angularly moved in a negative direction (clock wise) until 1.5 degrees. After 2 degrees the same change in Z- Distance was observed in both negative and positive axes. Also, there was a slight change in the y-axis when the magnet was angularly moved beyond 2 degrees.

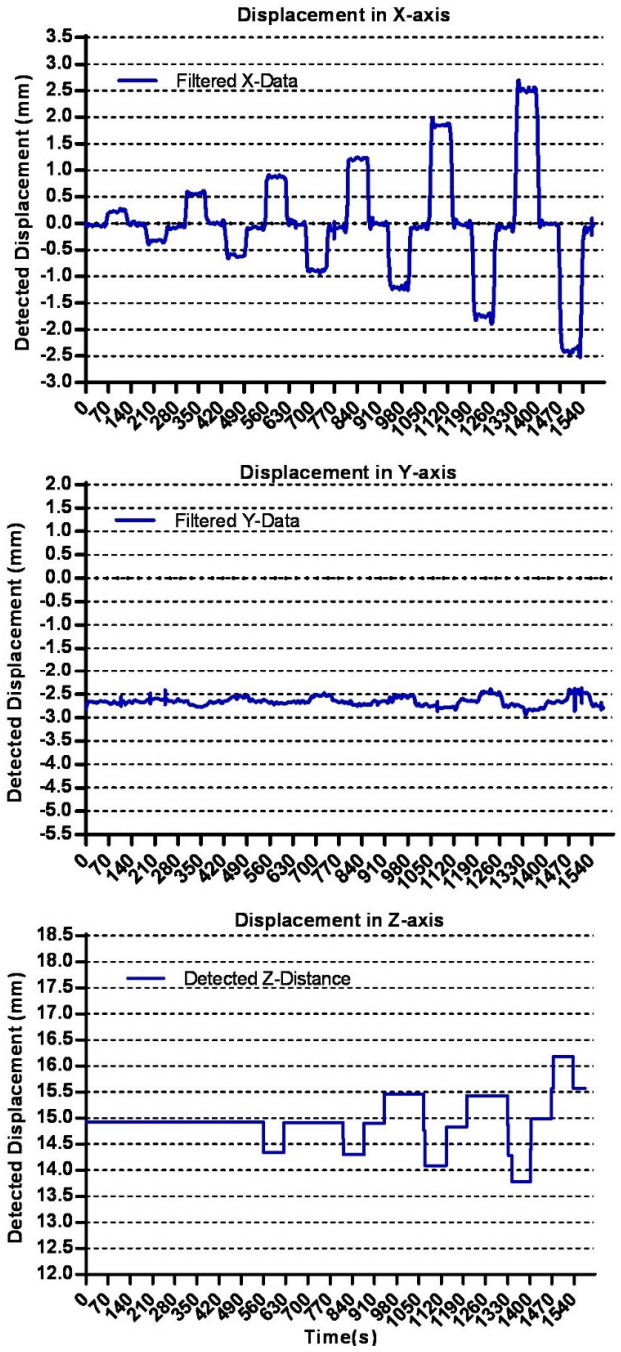

Figure 4. 18: Quasi-Static Angular Movement of the Magnet on the x-axis ranging from 0.5 to 4.0 degrees. Keeping the y and z axes movement constant.

This change in Z-Distance can therefore differentiate between linear movement where there is no Z-Distance change, and angular movement where Z-Distance changes are observed with changes in the x-direction. The change in the y-axis value is due to the orientation of the magnet placement. Currently, this tracking algorithm can detect the position of the magnet but lacks in determining the orientation of the magnet, requiring a correctly orientated starting point. Therefore, during angular motion, only changes in 2 axes are observed.

Figure 4.19 shows a comparison of a single sensor with a quad sensor during angular motion. As described in chapter 3 the main drawback of a single sensor configuration was the tilt effect. Due to this effect, the single sensor configuration was only able to detect up to 3 degrees rotation using a correct starting orientation. In the quad sensor configuration, this tilting effect was resolved. This was achieved by introducing a specific sensor selection criterion.

Figure 4.19a shows the position of the magnet observed by a configuration of four sensors. In figure 4.19a the notations S1, S2, S3, S4 shows the position of the sensors, while SP-S1 to SP-S4 shows the starting position of the magnet when there was no angular movement and EP-S1 to EP-S4 shows the end position of the magnet when it was angularly moved 4 degrees (approximately 2.3 mm) in both positive and negative directions.

Figure 4.19 shows that the quad sensor configuration can detect the position of the magnet using all four sensors. During the angular movement experiment, the starting position of the magnet was at the centre of sensor S1, then moved 4 degrees in the x-z plane showing the end position (EP-S1 to S4) shifting to the positive x-direction (fig. 4.19a, left) and then moving to -4 degrees in the x-z plane showing the end position shifting the negative x-direction (fig. 4.19a, right). As mentioned, the single sensor can detect angular displacement up to 3 degrees depending upon the orientation. In figure 4.19b during the positive x-axis displacement, S1 was only able to measure up to 1.5 degrees. Beyond that, the mean error and standard deviation error started to increase. Similarly, the quad sensor also showed the same response. To overcome this problem a sensor selection criteria was introduced to compensate for this tilting effect.

The sensor selection criteria depend upon the localisation of the magnet. The concept is to only use data from the sensors in closest proximity to the magnet, therefore eliminating the sensors further away that contribute more noise to the data. It can be observed that during positive x-axis displacement the magnet displaced between sensors S1 and S3. Therefore, eliminating S2 and S4 values from the quad sensor configuration gives a well-matched result. Similarly, during the negative x-axis displacement, the single sensor and quad sensor was able to detect the movement with minimum error but as explained previously as the magnet lies between sensor S1 and S4. Therefore, combining the values of these sensors and eliminating S2 and S3 gives better correlation and accuracy of detected displacement.

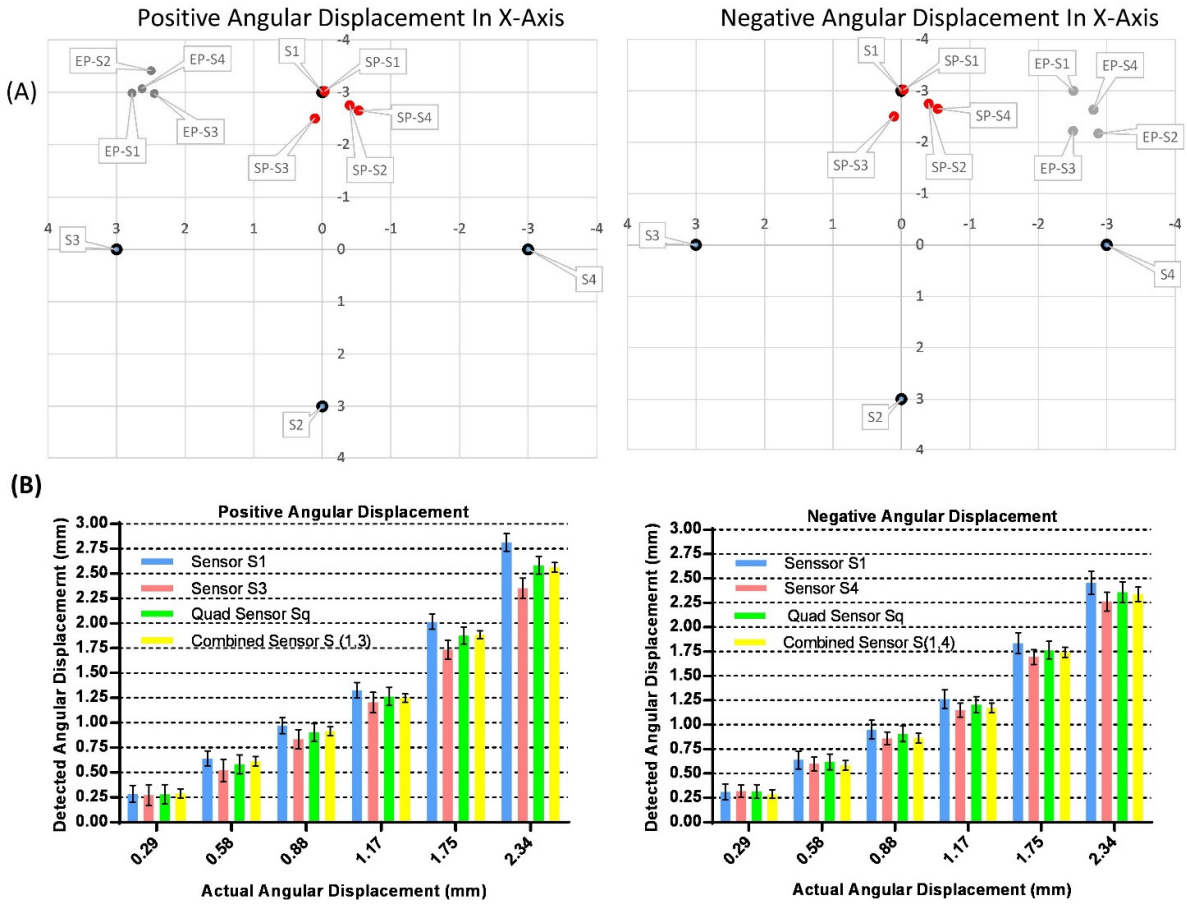

Figure 4. 19: (a) Scattered plot representation of sensors and magnet localisation during positive and negative angular movement. (b) Comparison of Angular Displacement detection between the single and Quad sensor configuration.

4.4.6 System Sensitivity

To analyse the sensitivity of the quad sensor configuration in static and dynamic movement, four sets of experiments were conducted by moving the magnet quasi-statically and dynamically in the y-axis to 1 mm with a set of 0.15, 0.20, 0.30, 0.50, and 1.00 mm at Z-Distance values of 10, 13, 17 and 20 mm. Figure 4.20 shows consistent accuracy to motion from 0.15 mm to 1 mm at the four Z-distance values.

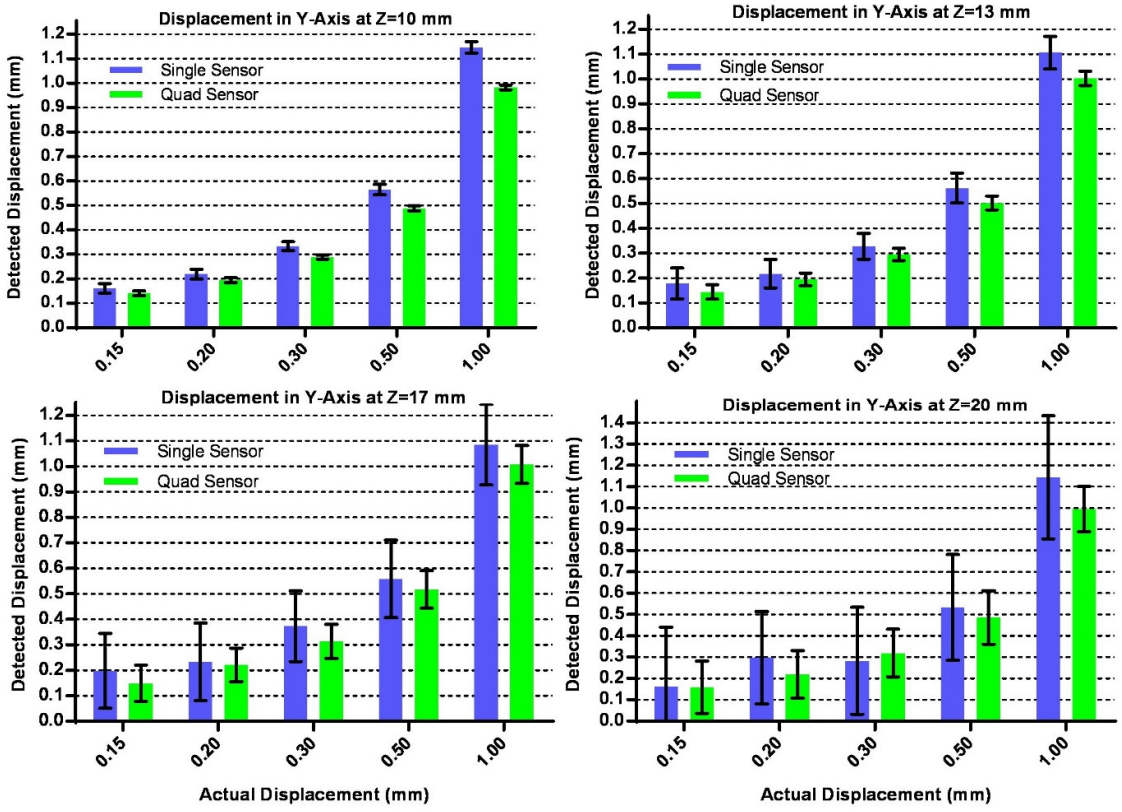

Figure 4. 20: Comparison of the single sensor configuration with Quad sensor configuration at different Z- distance value

As explained in chapter 3, the single sensor can work efficiently when the Z-Distance is ≤ 15 mm. beyond this the accuracy starts to decrease, and also the mean error and standard deviation error also increase which can also be seen in figure 4.20 .As compared to a single sensor sensitivity in detecting

implant movement from 0.15 mm to 1 mm, it ranging from (60% to 10%) when Z-Distance is moved from 10 mm to 20 mm while the quad sensor showed higher accuracy in detection along with higher sensitivity which ranges from (99 % to 60%).

Figure 4.21 also shows that if the system was moved below 0.15 mm, both the single and quad sensor configurations were unable to detect the movement. While 0.15 mm movement both quasi-static and dynamic was only detected by the quad-Sensor configuration.

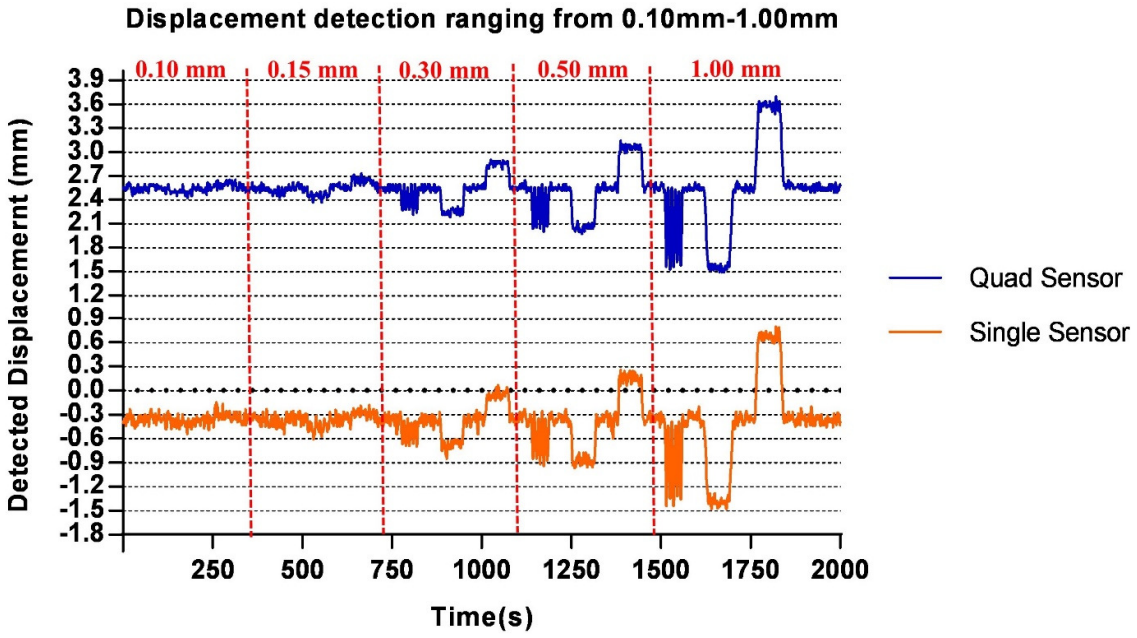

Figure 4. 21: Comparison of the single sensor configuration with Quad sensor configuration at different Quasi-Static and Dynamic displacement at Z-Distance of 15 mm.

4.5 Discussion

This study proposes a micro-motion detection technique for monitoring joint replacements based on magnetic field detection. Multiple sensor configurations were investigated to build on a single sensor configuration (Khan et al. 2021) to achieve sub-millimetre motion detection and to improve on the system's tilting effect, resolution, sensitivity, working range, and signal to noise ratio.

The magnetic field from the magnet embedded in the cement restrictor can be detected by the multi-sensor. Consequently, it is predicted that if embedded in a humeral stem the migration of the humeral component results in a change of the magnetic field which can be measured by the embedded sensors. The feasibility of such a magnetic measuring system has previously been described in chapter 3 and Khan et al. (2021) [140] demonstrating a 0.3 mm linear migration using a single sensor configuration. The work in chapter 3 also describes a negligible effect found from biomaterials on detection. But the limitation of that configuration was a limited working range of between 10-15 mm between the magnet and sensor. Also, the system had a tilt effect, so the system was only able to detect angular motion up to a certain degree of movement depending upon magnet orientation and position.

It was hypothesised that the introduction of a second sensor might be beneficial for the reduction of noise content and will increase the overall system performance. As the second sensor will only measure the stray/environment magnetic field. Removal of these stay fields from the actual magnet's magnetic field might increase the system performance. For that, a dual sensor configuration was designed but instead of increasing the performance, the dual sensor downgraded the detection measurement by introducing 10 % noise to the system and 30% detection error. As both the sensors were placed far from each other. One of the reasons for this down gradation of system performance can be a difference in the stray magnetic fields detected by each sensor along with the inner device variation in noise signature (Johnson noise, 1/f noise), drift, and sensitivity. So, instead of cancelling out the stray field, it added up because the signals were filtered in the time domain whilst the noise from the devices was independent and not linked i.e. one device is subject to a bias field, the other is not biased and as such is more prone to fluctuate and drift. To understand that a new configuration was designed, quad sensor configuration. In this configuration, four sensors were placed in a cross formation having one common axis. Each sensor will detect the magnetic field from the magnet along with the same stray magnetic field and was hypothesised that subtracting the data received from the sensors having a common axis will reduce the noise.

The quad sensor approach system was able to reduce the noise and achieved a displacement resolution of 0.15 mm and a rotational resolution of 0.5 degrees. The system has been shown to detect up to a 4 mm implant shift or 4 degrees tilting, which is the point at which implants are grossly loose and can be detected on a radiograph. This system demonstrates a higher resolution to the current clinical RSA technique, which is considered a gold standard for implant motion detection.

RSA precision for detecting implant movement is reported at approximately 0.29 mm translation and 0.66^{o} rotation [102], however, the downside of this technique is that it is time-consuming, cost-prohibitive, limited accessibility, and exposes the patient to ionizing radiation. RSA works by embedding tantalum beads that act as passive markers in the bone surrounding the implant and using their locations via x-ray imaging to triangulate the position and any subsequent shift of the implant. Issues can also arise from dislodged beads, which impacts the efficacy of the technique. This is particularly important as the total dosage with RSA techniques is relatively high compared to standard x rays and if the beads are insufficiently captured, repeated imaging is needed, exposing the patient to further radiation. The system in this study negates the need for x-ray exposure and repeat readings will have no known detrimental effect on the patient [103].

New developments in implant motion detection have also developed a detection system using eddy current sensing, reporting an accuracy of 0.15 mm, which is comparable to this system [120]. The use of nanoparticles in cement has also recently been developed, with simulations highlighting a resolution of 0.3 mm, however, these systems are still at their early development stage and require further work to address issues of proximity and biocompatibility [15, 29].

Currently, the multi-sensor system (Quad sensor) is only able to locate the implant position in all three axes if the starting orientation is correct and accurate. Further work is needed to develop variable starting orientations as well as the impact of a stray magnetic field emitted from the nearby object in the real scenario, the Helmholtz coil will be used to check its effect on the current system.

4.6 Conclusion

In this work, a magnetic field-based multi-sensor configuration was assembled and implemented to detect the micro-motion of a sensor with respect to a magnet. For the multi-sensor configurations, the Quad sensor configuration shows considerably better repeatability, consistency, no cross-talk, and tilt effect compared to the Dual sensor configuration. This configuration shows the resolution of detectable displacement of 0.15 mm on x/y axes and the sensitivity of detection between 10-18 mm on the z-axis. This system has the potential to be used as an early warning detection for implant loosening. This can lead to more informed clinical decisions and, long term could reduce revision rates and survivorship through more effective and timely intervention.

5 CHAPTER: 5

Development of Mechanical testing Simulator for the Validation of the Smart Elbow Prostheses

Summary

This chapter presents a mechanical testing rig design along with the development of the humeral stem to be used for the validation of multi-sensors (quad sensor configuration) for the detection of early signs of aseptic loosening under different fixation scenarios. The testing rig consists of two actuators operating under force-control. The actuators can be used to simulate the loading cycle. The simulator rig was set up as follows: the humeral proximal end and the cement restrictor containing the magnet were embedded in a synthetic bone substitute cylinder representing the humeral bone. The bone was fixed to the base of the testing rig. The distal end of the humeral stem was loaded vertically via the ElectroForce machine to provide axial cyclic loading and horizontally via an external actuator and load cell to provide a constant joint compressive force. This loading scenario reflected the anterior-posterior loosening mechanism found clinically. To test the performance of multiple sensors the humeral stem was designed and fabricated based on the dimension of the commercially available elbow prosthesis stem. The stem was then hollowed to house the electronics internally and a multi-sensor (Quad-sensor configuration) were integrated into the stem and the PCB was custom-designed to be embedded into the stem. The humeral stem was inserted into the humeral bone containing a magnet embedded in a cement restrictor and three fixation scenarios to simulate different stages of loosening were generated: fully fixed, loose and grossly loose. The stem was placed under cyclic loading and the estimated loosening was validated against the axial actuator displacement sensor. The system showed good performance, particularly by detecting early sign of loosening and differentiating between the three fixation states.

5.1 Introduction

Millions of joint replacement procedures are conducted annually due to rise in the musculoskeletal disorder, registered at various orthopaedic registries around the globe [171, 172]. These musculoskeletal disorders especially osteoarthritis is now the 11th cause of disability in the world [173]. Total joint replacement is an effective procedure for the treatment of these disorders. However, the current implant failure rate is high 10% leading to revision surgery, despite the advancement in the surgical procedure and improvement in the implant design [127]. This highlights the inability of current implant technology for revision-free performance. Over the last 2 decades, there has been a progression in implant technology to enhance longevity but no significant reduction in the revised surgery has been reported [123, 127]. Moreover, the rate of revision surgery increased throughout the years, the probability to undergo a second revised surgery (multiple surgeries) is five to six folds higher than the primary revision surgery [123]. To lowering the increasing rate of revise surgeries and to minimise the burden on the public health system, it is important to develop a method that can improve the surgical outcome and increasing the longevity of the implants.

Compared to all major joint replacement procedures (hip, knee, shoulder), the elbow joint has a higher rate failure despite of its low procedure occurrence. The most common reason for this failure which leads to revision surgery is aseptic loosening. Aseptic loosening is the failure of the integration between the bone and the implant in the absence of infection. For the implant to work as a load-bearing apparatus it needs to have a strong integration/bond with the bone through a mechanically stable interface. The quality of the integration for the non-cemented implants depends upon the osseointegration while for the cemented implants rely on the cement mantle[174].

Currently, the available tools are unable to identifying the early signs of weakening of the bond between implant/cement and cement/bone interface and are only able to detect when the implant is fully loose[175]. The preclinical laboratories testing guidelines and simulators used to analyse the loosening of the implant due to weakening of the cement/bone or implant /cement interface are developed for

major joints (knee, hip, and shoulder) and therefore their loading regimes are specific to their applications and joint-specific design challenges. For example, the wear knee simulator was developed for analysing the knee prostheses performance through a large number of loading cycles and hip joint simulators designed for tribological performance [176, 177]. However, no such guidelines or testing simulator exists for elbow prostheses. The testing machines that have been developed focus on simulating the elbow motion and the force transmission across the elbow joint, while none of simulators address or analyse elbow prostheses loosening [178-180].

The purpose of this study is to design a testing simulator that can mimic clinically-relevant loading behaviour that can lead to implant loosening by varying the fixation/bonding between the cement/bone and implant/cement interface. This testing simulator will also be used to validate the performance of the magnetic field-based diagnostic tool for detecting loosening (chapter 3) with the new capabilities as a multi-sensor system to eliminate the tilting effect and increased precision, described in chapter 4.

5.2 Material and Method

In this section, first, the mechanical testing rig design is described. Followed by the development of the humeral stem integrated with the multiple sensors (quad sensor configuration) and its utilisation for the detection of aseptic loosening under various fixation scenarios. Finally, a validation procedure of the aseptic loosening detection is explained.

5.2.1 Mechanical Testing Rig

Currently, no standard method and protocols exist for the testing of the elbow prostheses as for other major joints i.e. (hip, knee, and shoulder). The majority of the testing systems are focusing on physiological movement and force distribution [178-180]. In this chapter to understand the loosening behavior of the elbow prostheses, a mechanical testing system was designed, in which cyclic load testing was conducted on the humeral stem under different fixation scenarios (fully fixed, loose, and grossly loose). Little information is available in the literature regarding the in vivo joint reaction force on the humeral ulna joint during various activities of daily living (ADL). Brain et al *(2013)* reported the range

of joint reaction force on the elbow joint when performing different ADL. These ADL can range from light duty to extreme high loading tasks. Table 5.1 highlights the joint reaction force on the elbow at various ADL [14].

Table 5. 1: Joint Reaction Force (JRF) on the Elbow during various daily living activities.

ADL Category	Activity Type	Peak JRF (N)
Light duty	Dressing, Eating, personal hygiene	70-350
Moderate	Lifting small weight, opening door	419-698
Strenuous	Lifting heavy objects	768-1396
Extreme	Maximum flexion effort	1466-2094

In this testing protocol, the light duty ADL category was selected and a total joint reaction force of 350 N on the humeral stem of elbow prostheses was applied. The selection of the moderate ADL was selected based on the available instruments/machine force limits.

A testing rig in compliance with ASTM standard (ASTM F2028-17) was used to carry out the cyclic load testing with little modification. This testing standard protocol is used for the fatigue testing of the fixture of the shoulder implant in vitro by using superior and inferior rim displacement measures as a quantities measure of fixation performance[181]. The ASTM F2028-17 sets guidelines for simulating the loosening behaviour of an implant using load-controlled cyclic loading and a constant compressive joint reaction force. With a similar loading scenario in the elbow, the standard was used as a guide in designing the rig In the proposed testing protocol instead of rim displacement, compressive and axial force were applied for the comparative studies of the humeral stem of the elbow prostheses at various fixation conditions.

The mechanical testing rig consists of a base plate and associated three clamps to hold the humeral stem of the elbow prostheses and the porous polyurethane bone substitute (Sawbones Europe, Sweden). A fourth clamp is used to fix the horizontal prismatic linear actuator to the base plate (RS Pro, LD3). The horizontal actuator is controlled in position mode via force feedback, and it applies the compressive joint force on the anterior side of the humeral stem. A strain gauge load cell was sandwiched between the actuator and the implant stem for load feedback. As shown in figure 5.1.

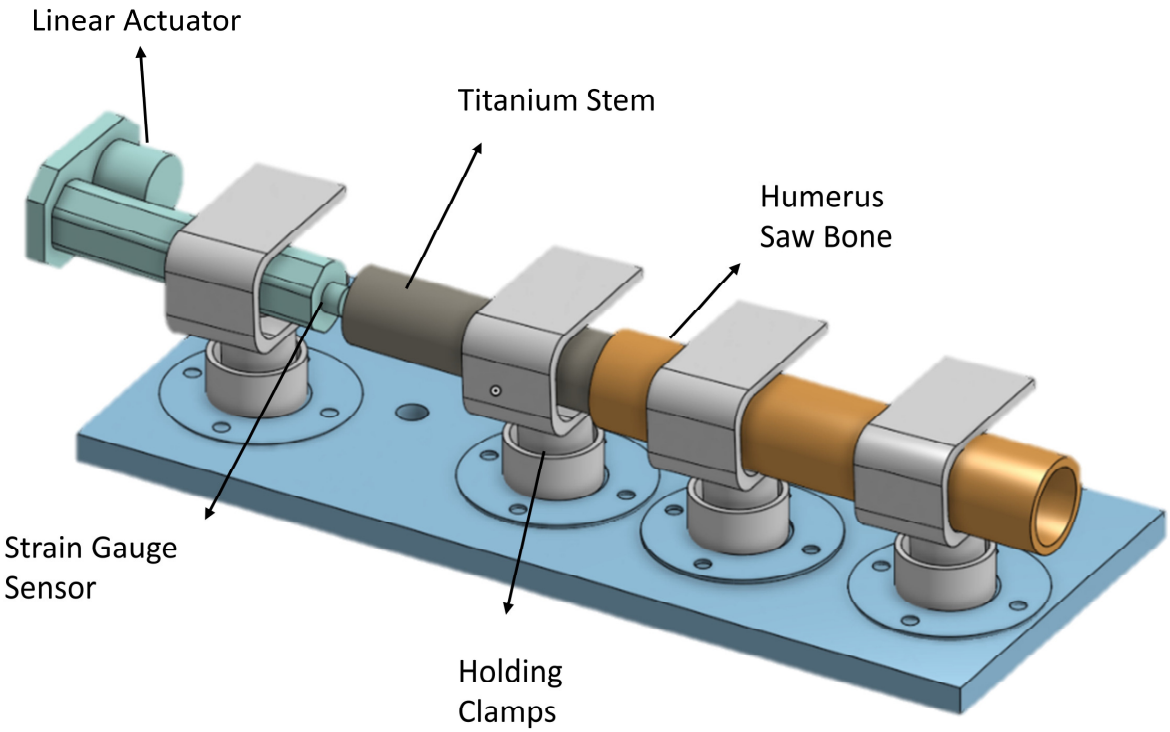

Figure 5. 1: A design of the mechanical testing rig for testing of the humeral stem loosening at different fixation conditions.

In order to provide the axial load on the humeral stem, an axial load unit (ElectroForce 3330, TA Instruments, MA, USA) was used. The axial actuator of the ElectroForce acted as a second actuator of the mechanical testing setup and the six degrees of freedom (6-DOF) load cell was linked with this actuator for detecting the quantitative force exerted on the stem along with delivering the feedback for the load control for the second actuator. The axial actuator was also provided with the displacement

sensor to measure how much the actuator is moved while exerting load on the stem. The whole experimental setup is shown in figure 5.2. Different types of auxiliary mechanical components, including the adjustable fixture for the clamps, clamp holder base, and fixture linking the humeral stem with the main axial unit were designed and fabricated for this custom-designed rig. Finally, the rig was mounted on the ElectroForce machine by the M16 bolt as the base of the machine. The experimental testing setup was able to provide an approximate scenario of the implant under different joint reaction forces (JRF) and at various fixation methods.

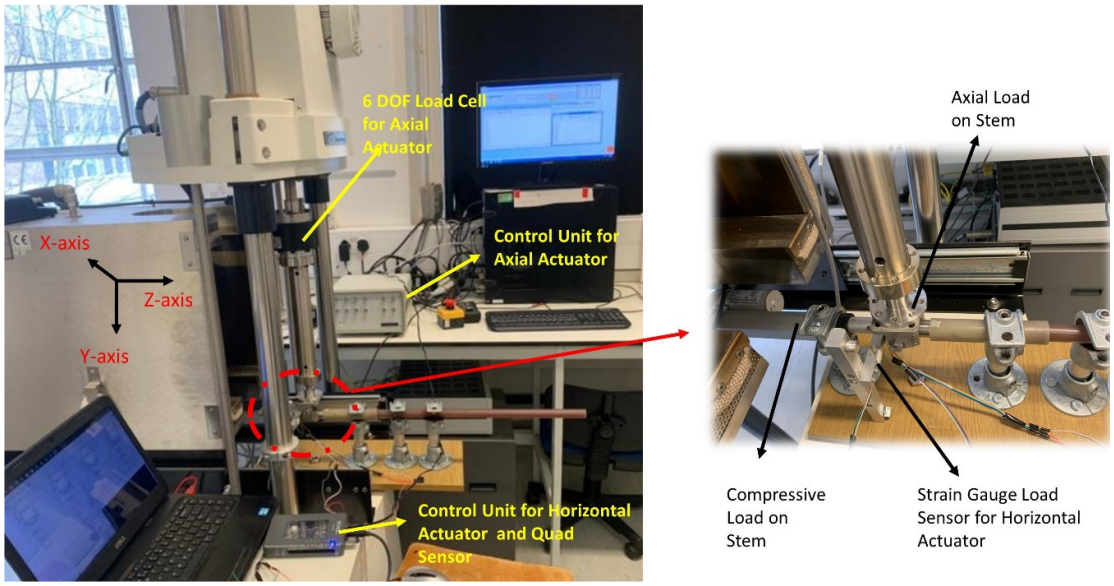

Figure 5. 2: Overall setup of the mechanical testing system: The axial actuator coupled the titanium stem and its associated load and displacement sensor connected to its control unit. The sandwiched load cell between implant and horizontal actuator and its control unit.

5.2.2 Load Cell Calibration

A strain gauge load cell for detecting the force through the horizontal actuator was connected to a 24-bit analog to digital converter (HX711) that converts the small strain change from the load cell into 24-bit changes in voltage between 0-5 V. The analog to digital converter was connected to the data acquisition device (NI My RIO) to retrieve and calibrate the load cell data. To calibrate the load cell, known weights were applied onto the load cell, exerting a force ranging from 10 N- 120 N as shown in

figure 5.3. Due to a linear relationship between strain gauge voltage output to force applied, a linear line of best fit was used to derive the voltage/force equation.

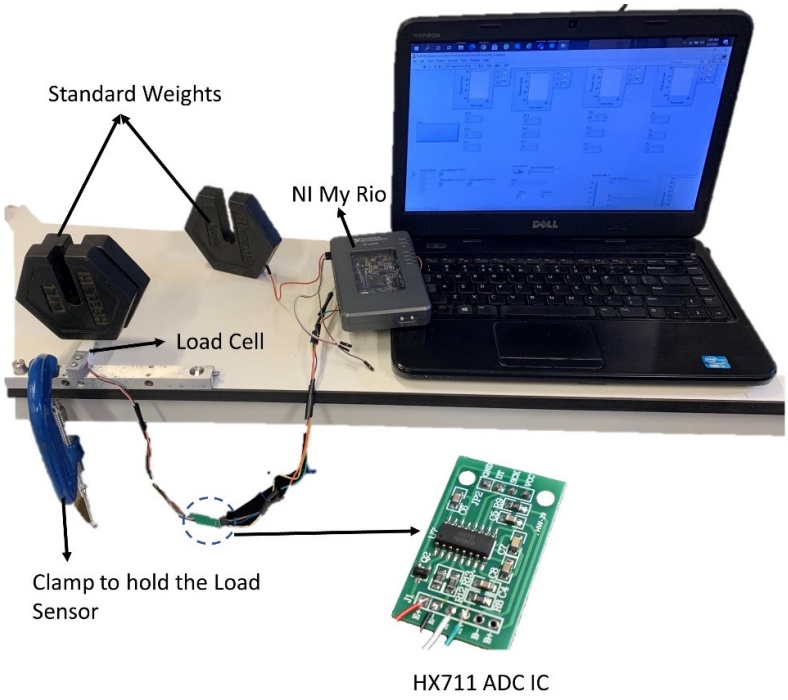

Figure 5. 3: Overview of the calibration setup of the Load cell.

For the calibration of the load cell of horizontal actuator. Figure 5.4 illustrates the calibrated output of the load cell. Strain gauge voltage outputs were collected at 0 to 120 N loads in increments of 10 N with each increment held for 10 seconds using a sampling rate of 10 Hz. Figure 5.4 highlights the well-fitted load cell calibration with the R^2 value of 0.9975.

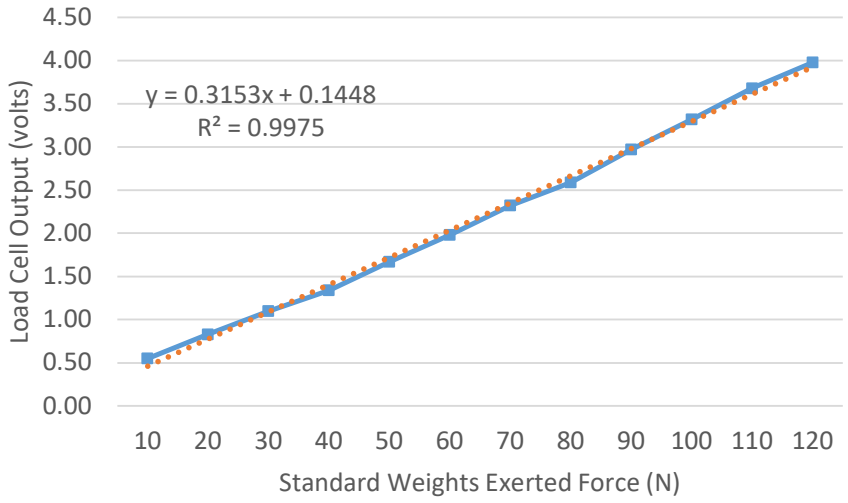

Figure 5. 4: Plot of the force applied against the load cell output voltage. Equation of the linear trend line derived and can be used to translate between voltage and force in newton.

To calibrate the load sensor that was associated with the axial actuator. The ElectroForce machine has a built-in mechanism for the calibration of its associated sensors i.e., TUNEIQ. By using that feature the load cell along with the displacement sensor was calibrated. In this TUNEIQ feature, the desired limits of the force, the execution frequency, and the type of loading are automatically tuned. In this work, the ElectroForce machine load cell was calibrated at a force ranging from 150-600 N at a frequency of 0.15 Hz.

5.2.3 Control Units of the Actuators

Two control units were used to provide real-time closed-loop control for the actuators. For the main axial load actuator and its associated sensors (load and displacement), a built-in controller with WinTest software was used. While for compressive force actuator and its load sensor a National Instruments Data Acquisition Card (My RIO 1900) with LABVIEW software was used. Both control units provided a fully digital proportional, integral, derivative, feedforward control. Figure 5.5 shows the schematic of our closed-looped control system for the performance of the actuator.

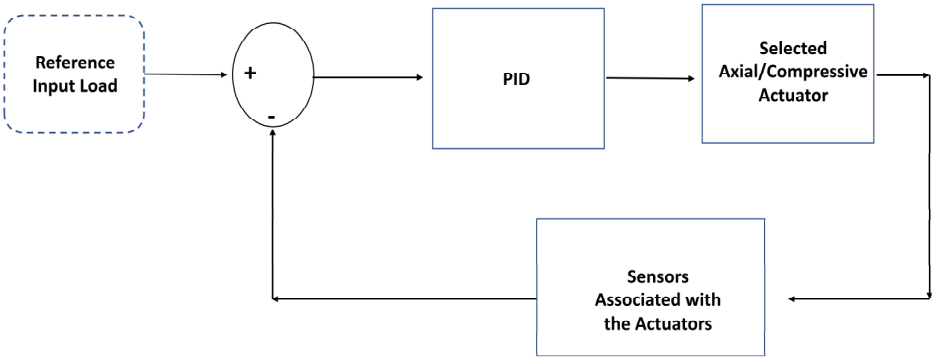

Figure 5. 5: A schematic of closed-loop control for the actuator 1 and 2 of the mechanical testing system using a proportional, integral, derivative controller.

To ensure the safety of the system during operation, the operating speed for the compressive force actuator (horizontal actuator) was kept to a minimum, and the stroke length limits were set from a minimum of 0 to 100 mm. Although the actuator has a maximum stroke length of 200 mm and speed of 44 mm/sec at no load, the speed was kept to 10 mm/sec which was achieved by lowering the applied input voltage. The axial actuator limits were assigned for load and displacement to ensure the system did not overload or damage the machine and implant/synthetic bone structure.

5.2.4 Humeral Stem Design

In this section, the design of the humeral stem along with the integration of the quad sensor for the loosening detection are described. As proposed, the sensors needed to be integrated into the stem to measure its localisation with respect to the magnet embedded in the cement restrictor (Chapter 3, 4). As described in chapter 4, the quad sensor configuration showed significantly better results in detecting linear and angular displacement along with compensating the tilt effect and enhancing the resolution of the system. Based upon the dimension of the quad sensor configuration and the dimension of the commercially available humeral stem of the elbow prostheses, a design of the humeral stem was developed that would integrate the quad sensor. A titanium alloy (Ti-6Al-4V) was used for manufacturing the humeral stem because the majority of the implants are manufactured from the same metal alloy and grade.

The humeral stem comprises of two parts. The first part is the inner tube in which the sensor is attached to the distal end and a small through-hole is used for the data and power wires to feed through to an external power source. The second part is the outer shell (figure 5.6a), in which the inner tube will be inserted (figure 5.6b) and will be hermetically sealed as shown in figure 5.6c.

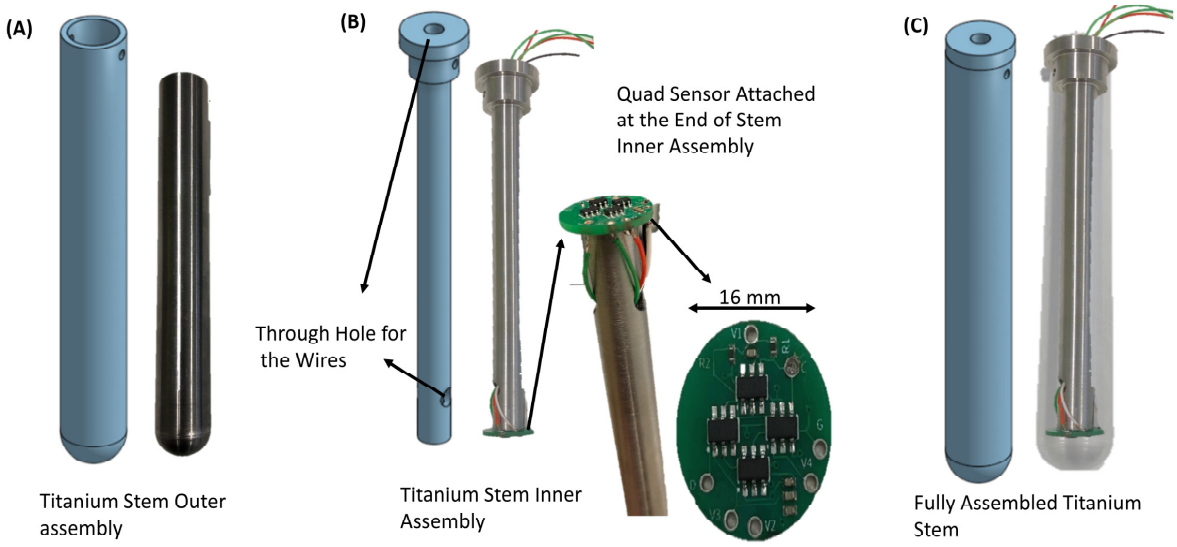

Figure 5. 6: Showing the Solidworks designed model and actual fabricated parts for (a) the outer shell of the titanium stem having a length of 150 mm and diameter of 20 mm. (b) the inner tube of the humeral stem along with printed circuit board (PCB) of the Quad Sensor configuration. (c) The assembly for the humeral stem.

The size of the PCB was kept minimum so that it can easily be inserted into the humeral stem. A total area of 10 mm is required for the quad sensor and 0402 packages were used for the auxiliary component of the sensors (pull-up resistors and capacitors). A two-layer PCB was designed with a diameter of 16 mm and was attached to the tip of the inner tube as shown in figure 5.6 b. The quad sensor data and power wires were connected to the NI DAQ card via a through-hole in the stem.

5.2.5 Humeral Stem Loosening Setup

The humerus bone of the elbow was simulated in the study using a polyurethane hollow cylinder (Sawbones Europe, Sweden), which has comparable mechanical properties to cortical bone (p= 0.2g/cc, compressive strength 18 MPa, compressive modulus 445 MPa, tensile strength 12MPa). The cylinder was machined to achieve comparable dimension to a humeral bone shaft with a length of 250 mm length, outer diameter of 18 mm outer diameter and a wall thickness of 2 mm. The material has been developed as a synthetic alternative to bone for mechanical testing studies and orthopaedic implant testing as an alternative to the cadaveric studies of the human bone [182]. The different loosening conditions were mimicked between the implant and bone by varying the cement mantle fixation. The three conditions that were mimicked in this study were:

- Fully Fixed: Attaining a strong mechanical bond between bone-cement and cement-implant interface with no gap.
- Loose: Attaining a strong mechanical bond only between bone-cement while keeping the cement-implant interface loose with no gap.
- Grossly loose (no cement): With no cement fixation and having a gap of 1 mm between bone and implant.

Figure 5.7 highlights the case study's three conditions.

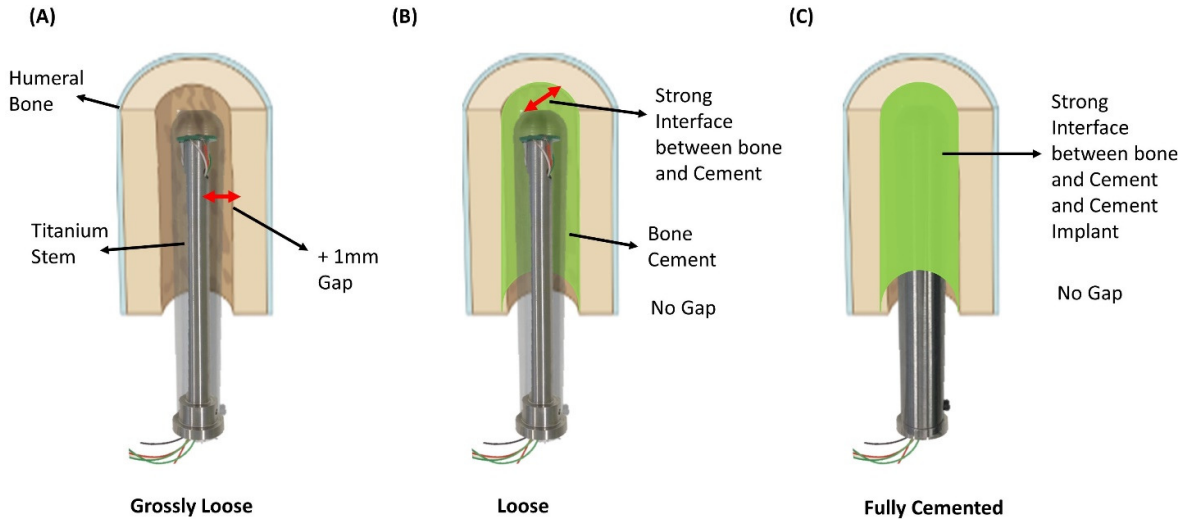

Figure 5. 7: (a) Implant and bone fixation setup during grossly loose condition having no cement mantle and a gap of 1mm. (b) Loose fixation setup, having strong bonding between bone and cement (c) Fully fixed setup with strong bonding between bone and implant via cement.

The cementless humeral stem fixation (grossly loose) was primarily achieved by pressing through the compressive force provided by the horizontal actuator. This constant compressive joint force held the implant in a fixed position and will provide extra stability. A total gap of 1mm is left between the implant and the bone wall, which would normally contain the cement mantle. At the end of the stem, the cement restrictor was placed keeping an adequate distance between the embedded sensor and magnet. The cement restrictor would normally be cemented into the bone, however for this fixation scenario the restrictor was attached to another polyurethane solid cylinder and the cylinder was well fixed by the clamp to ensure the restrictor did not move. Figure 5.8 highlights the setup for the grossly loose fixation.

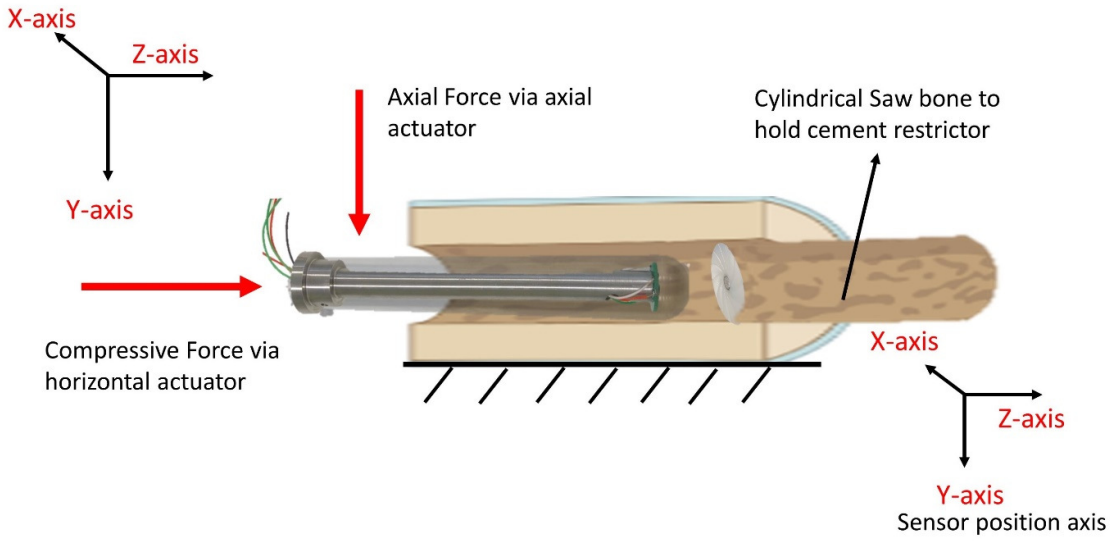

Figure 5. 8: Fixation of the cementless humeral stem via a press fit. Sensor's y axis was allign with the axial

To develop a slightly loose condition i.e., the implant detached from the cement and the only bond remained between the bone and cement alone. First, the bone specimen was fixed into a clamp and 3 holes of size 2.5mm were made at the medial side of the bone with 15 mm apart from each other as shown in figure 5.9. The reason for making these holes was that during cementing process air can be escaped through the holes and the cement can fill the internal bone space.

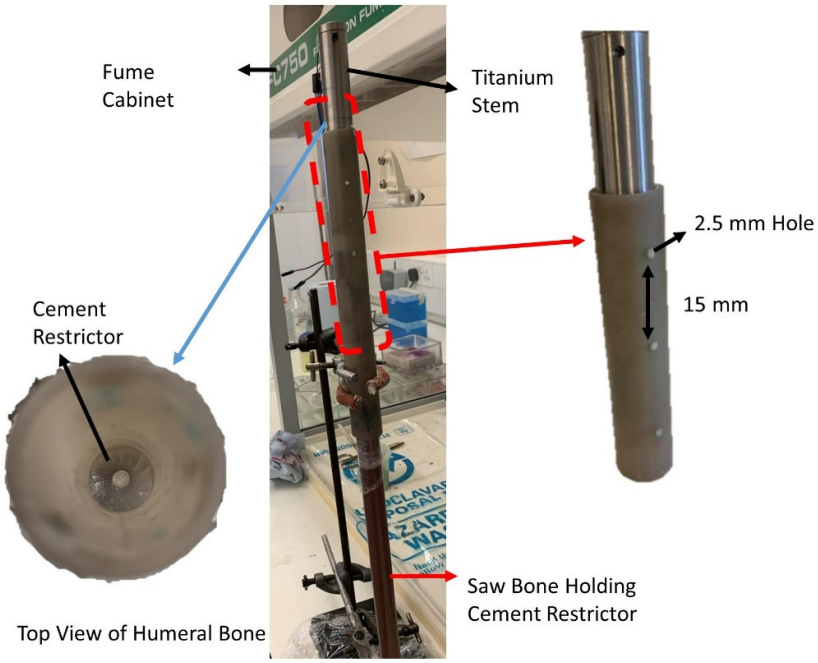

Figure 5. 9: Overview of the cementing setup to create a slightly loose fixation condition.

After setting up the bone specimen, the PMMA bone cement was prepared using a mixture of liquid monomer and methacrylicmethacrylate powder with a 1:2 ratio respectively. The mixture was carried out in fume cabinet (Airone FC 750 model, Safelab systems Ltd. Somerset, UK). Depending upon the size and length of bone 2 packs of bone cement were used (80 grams polymer and 40 ml monomer) and were carefully poured into the bone cylinder, where the other end was blocked by the cement restrictor to prevent the cement from leaking through, as shown in figure 5.10a.

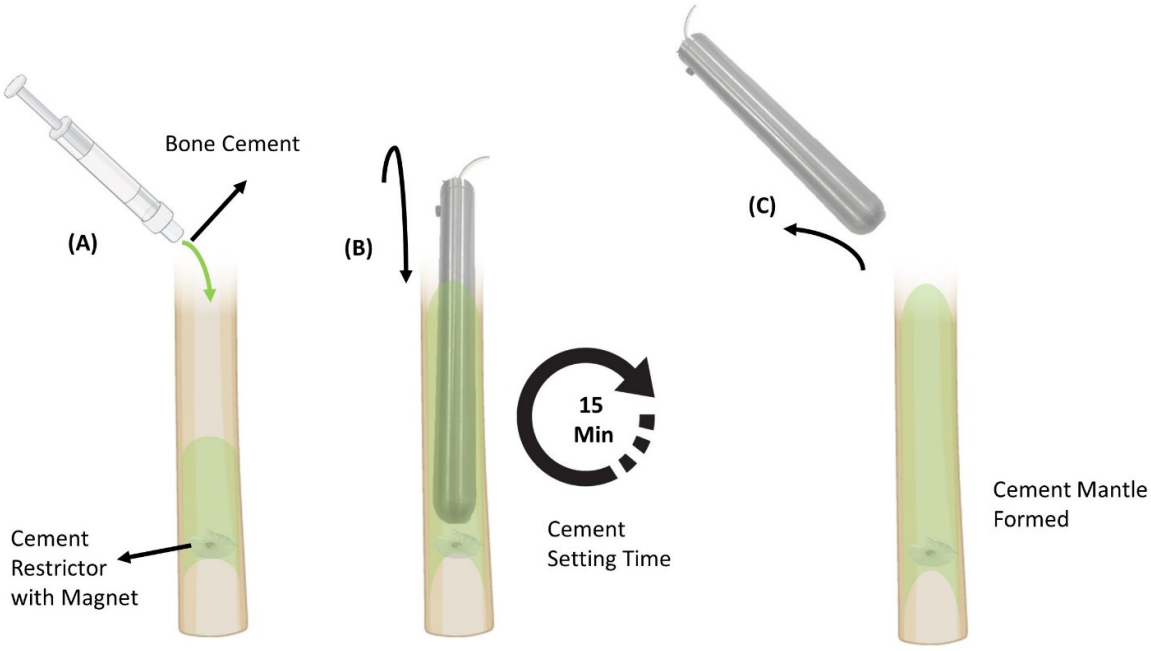

Figure 5. 10: (a) Insertion of the cement restrictor and bone cement in the humeral bone (b) Covered humeral stem inserted into the bone and left for 15 min (c) Strong bonding between humeral bone and cement mantle after removal of the stem.

Before inserting the titanium stem into the bone. The stem was covered with cling film and layer of Vaseline was applied to ensure the bone cement did not adhere to the stem surface. When the stem was inserted, any surplus cement seeped through the drilled holes on the humeral bone. This was to ensure cement had filled the bone cavity. The stem was removed after 15 minutes. This was the approximate time when the cement polymerises through an exothermic reaction during which the cement mantle increases in temperature. The cement mantle was left intact and fully bonded in the bone as shown in figure 5.10c.

Finally, for the fully cemented well-fixed humeral stem fixation i.e., attaining a strong bond between bone, cement and implant were attained following the same steps as described above for the slightly loose fixation. The only difference in the fully fixed fixation is that the stem was not covered in any

cling film or coated with Vaseline to ensure a fully bonded fixation. After insertion of the humeral stem, the stem was kept in the humeral bone until the cement was fully hardened as illustrated in figure 5.11c.

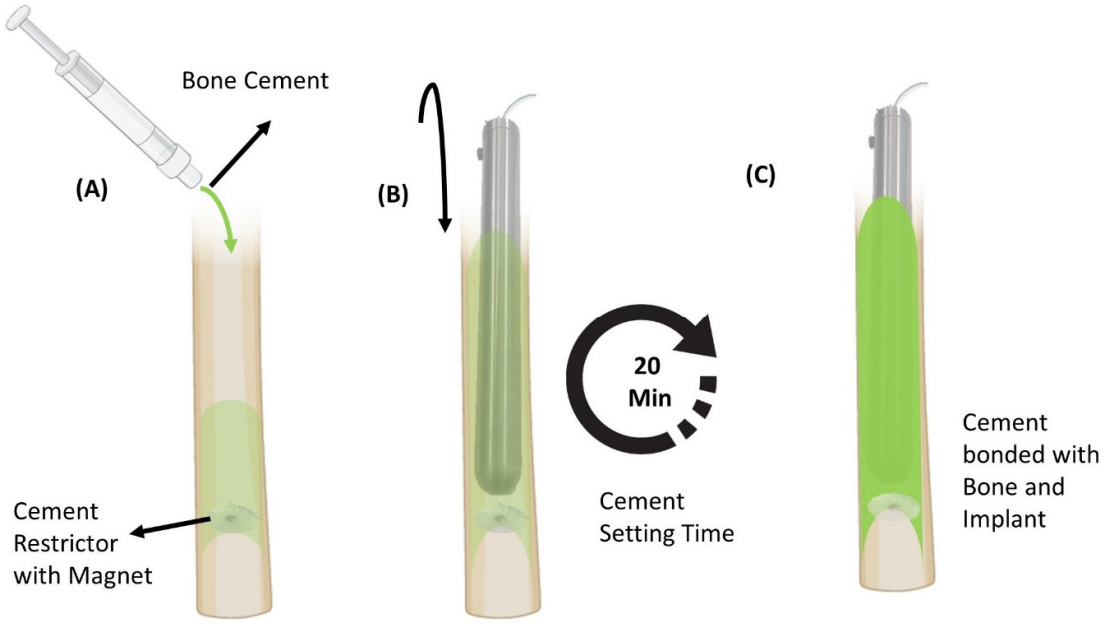

Figure 5. 11: Overall procedure for attaining the fully fixed implantation of the humeral stem.

5.2.6 Testing Protocol

All three types of loosening conditions were tested using the same procedure to ensure the repeatability and accuracy of the system. The testing protocol consists of three phases: pre-testing set up, testing, and post-testing. Figure 5.12 highlights the testing protocol in which pre-testing involves the preparation of bone specimens and setting up the rig and control system. The testing stage measures the response of the quad sensor system to the cyclic testing regime and the post-testing involves validation of the recorded data analysing the effect on the stem and bone after cyclic loading, disassembling, and re-assembling the system for the next experiment.

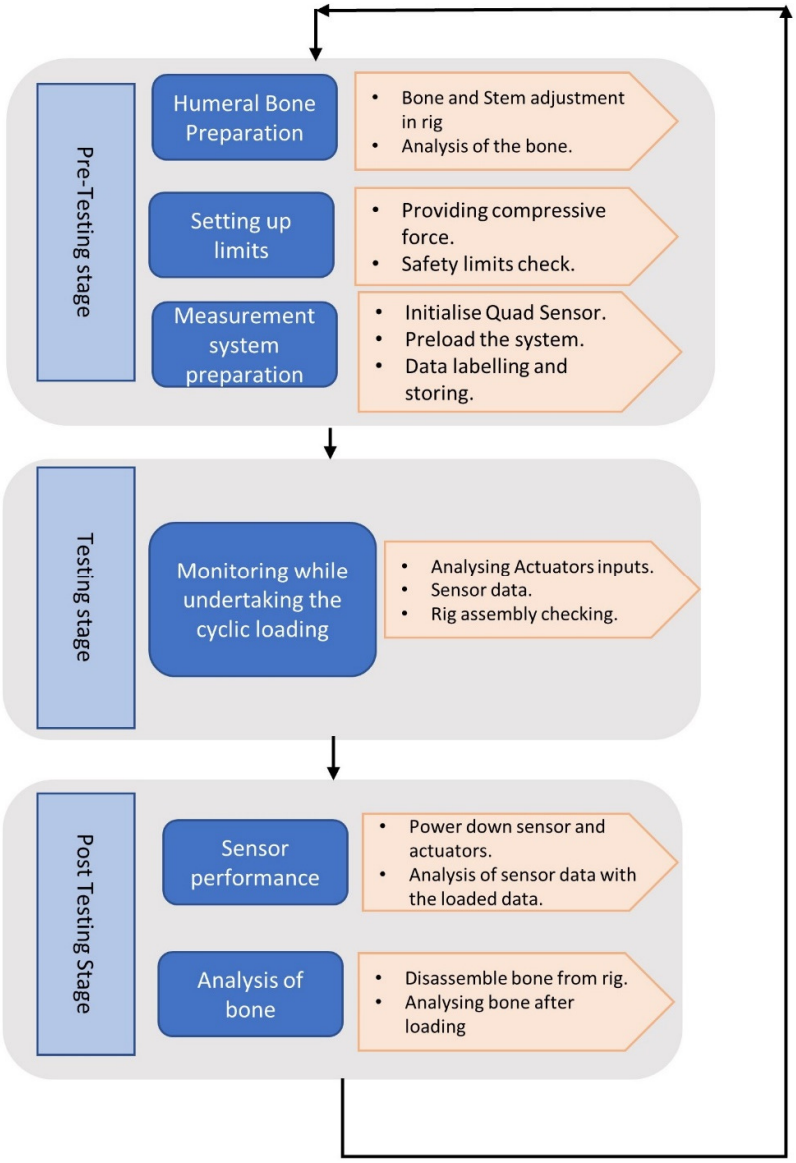

Figure 5. 12: Testing protocol for the detection of loosening at different implant fixation conditions

Pretesting consists of three phases. In the first phase, the humeral bone specimens were prepared, and the bone was analysed in terms of any cracks or deformity. Cement restrictor and humeral stem were inserted into the bone to mimic the real implant insertion and were placed onto the mechanical rig. The next phase was to provide the compressive joint force of 100 N via horizontal actuator and setting up the measurement system to control that force. Also, the quad sensor was initiated at this phase and was

configured as described in chapter 4. The last phase was the preparation and setting up the input parameters and limits for the axial load via axial actuator. The axial load of 250 N peak to peak was selected and rig safety limits were sets for both force and displacement. These limits will stop the experiment if reached and were set to protect the machine and implant. All the applied axial force and displacement were measured and collected along with the compressive force which was crucial for the post-processing and analysis stage.

The testing stage was conducted to analyse the sensor performance while undertaking the axial and compressive loading from both actuators. The input axial load from axial actuator was analysed from the WinTest software while for the horizontal actuator from the graphical interface made in LABVIEW. The system was set up for 3000 cycles at a loading frequency of 0.15 Hz, at a data sampling rate of 10 Hz.

The post-testing analysis was carried out in two phases to check the performance of the sensor in terms of any early signs of loosening detection. In the first phase, the data received from the sensors were analysed to check any changes in displacement change in each fixation scenario. After analysing the sensor data, they were overlapped or compared with the axial load data to check at which point the stem started to drift. In the second phase, the stem and bone were dismounted from the rig and were analysed in terms of any visual changes after loading.

5.3 Results

The following section outlines the results obtained from performing the experiments and firstly details the multiple sensor performance in detecting any early sign of loosening of all three-fixation followed by comparing the sensor results with the applied load and the time for the detection of loosening. Finally, the comparison of all three fixations with the visual qualitative analysis of any changes that occurred to the humeral bone after loading.

5.3.1 Grossly loose (no-cement) Implant

Figure 5.14 illustrates the detection mechanism of the quad sensor in all three axes when the humeral stem was under cyclic loading at a joint reaction force of 350 N in a grossly loose scenario.

Before starting the cyclic loading, each sensor of the quad configuration pointed that the magnet embedded in the cement restrictor is in the middle of all four sensors as shown in figure 5.13. According to the sensor selection criteria (chapter 4), as all sensors are pointing towards the middle, the magnetic field data from all four sensors (S1-S4) will be taken into consideration to detect any displacement in all three axes. From the cumulative data of all four sensors of the quad configuration the initial starting position of the stem concerning the cement restrictor was x=0.79 mm, y= -1.02 mm, and z=10.90.

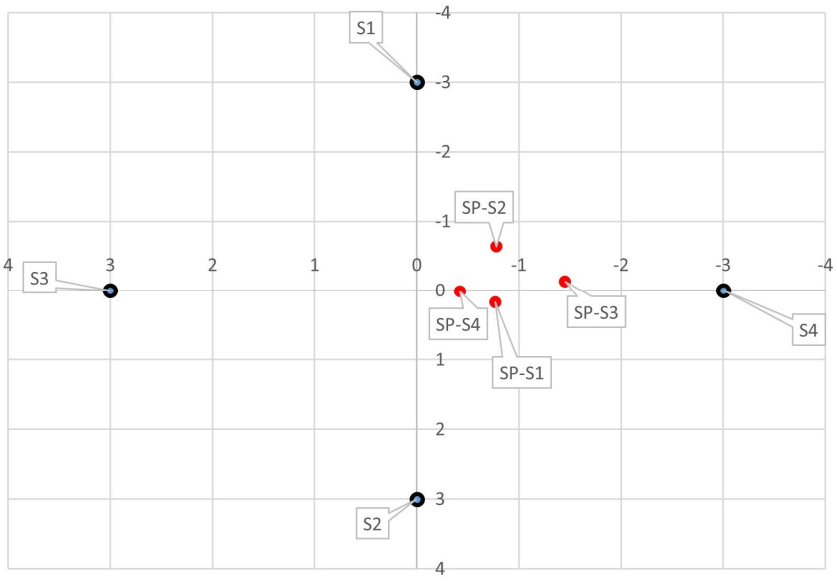

Figure 5. 13: Localisation of the humeral steam detected by each sensor of Quad-Sensor configuration with respect to a magnet at grossly loose fixation. S1-S4 are the position of the sensors while SP1-SP4 are the detected position of the stem.

In a grossly loose condition, the sensor detected the dynamic movement having an amplitude of 0.19±0.059 mm on the x-axis (figure 5.14a) and 0.40±0.062 mm on the y-axis (Figure 5.14b) while the z-axis remained constant (Figure 5.14c). This constant z- axis displacement shows that the stem was

moving linearly in both the x and y-axis (chapter 3 and 4). This dynamic movement for x and y remains the same during the whole loading period. Table 5.2 shows a summary of the movement of the stem in the x and y axes at every 1000 loading cycles along with the force exerted on the stem and the axial movement of the axial actuator.

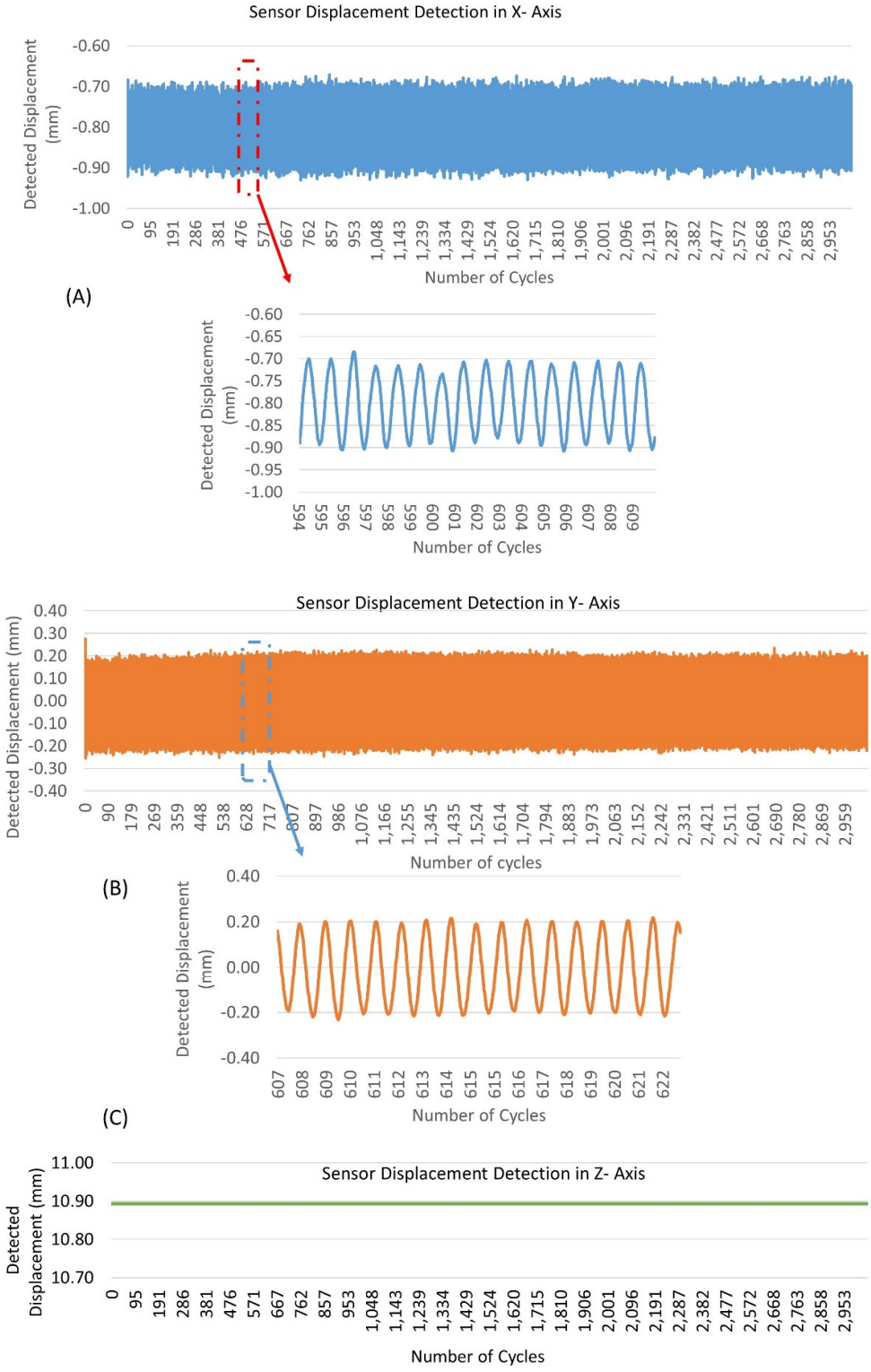

Figure 5. 14: Quad-Sensor displacement detection in (a) x-axis, (b) y-axis and (c) z-axis at grossly loose fixation.

Figure 5.15 (a & c) shows the exerted force from both actuators (axial and horizontal) remain the same during the whole loading cycle having a JRF of 350N while the axial displacement (figure 5.15 b) of axial actuator was 0.70±0.03 mm.

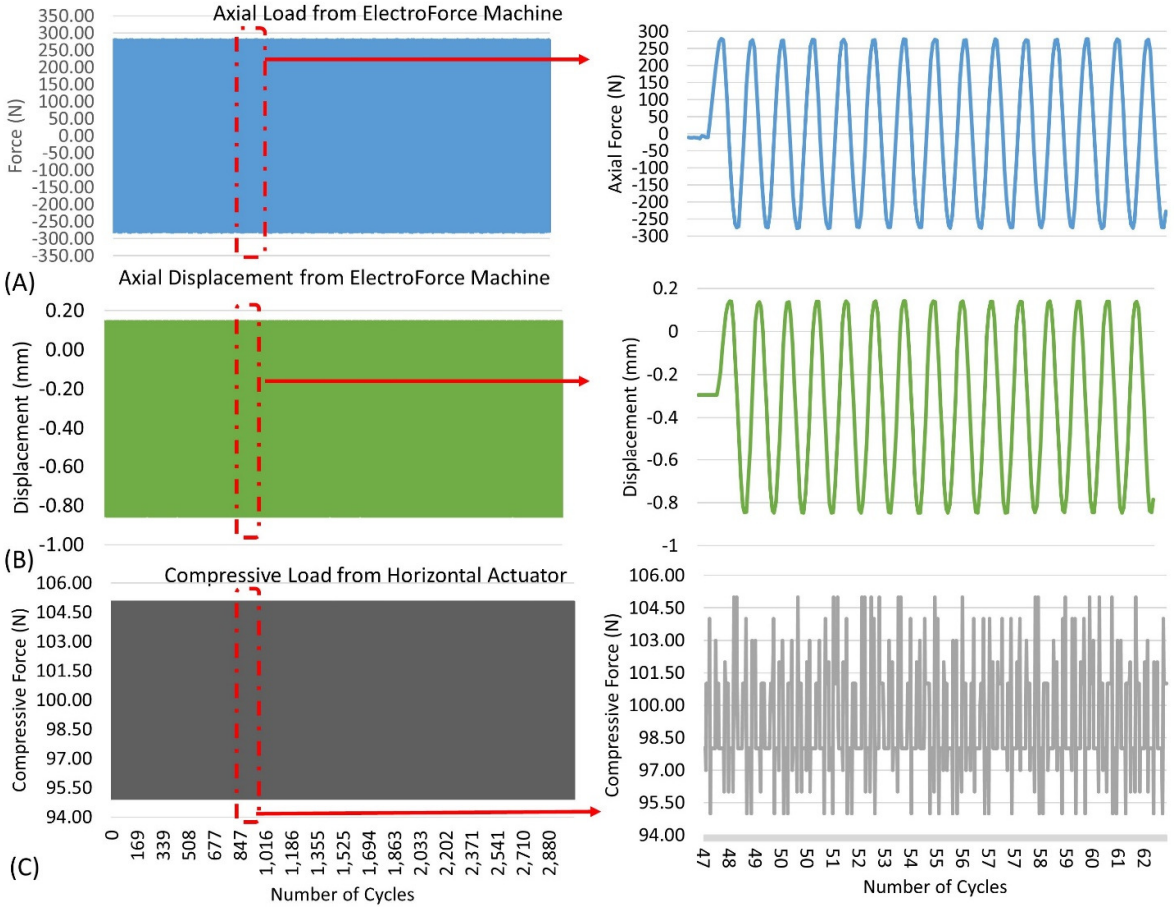

Figure 5. 15: (a) Axial force exerted by the axial actuator on the humeral stem. (b) Axial Displacement of Actuator during cyclic loading. (c) The compressive force exerted on the humeral stem by horizontal Actuator.

Table 5. 2: Quad-Sensor displacement detection in x/y axes along with JRF and axial displacement of the axial Actuator after every 1000 cycles at grossly loose fixation.

Cycles (x1000)	Sensor X-Axis Displacement	Sensor Y-Axis Displacement	Axial Force Peak-Peak	Axial Displacement	Compressive Force
0 (start)					
1	0.188±0.062	0.389±0.058	250±0.05	0.70±0.03	99.339±2.028
2	0.190±0.059	0.405±0.062	250±0.05	0.71±0.03	99.340±2.028
3	0.187±0.061	0.387±0.059	250±0.05	0.70±0.03	99.340±2.028

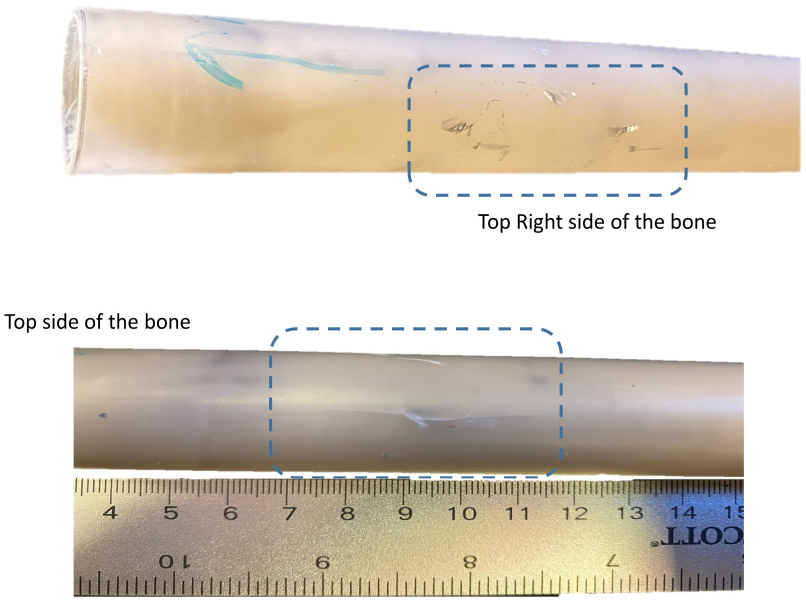

Figure 5. 16: Humeral bone after 3000 cycles of loading at a JRF of 350 N at grossly loose fixation.

Figure 5.16 shows that there were no major changes noticed on the humeral bone. One small crack on the top side of the bone which was where the holding screw held the bone in the clamp. There was also

a small deformity on the top right side due to the contact of the bone with clamp base while under loading.

5.3.2 Loose Implant

In the loose implant scenario, to detect the displacement of the stem in all axes, the magnetic field data from all the four sensors (S1-S4) of the quad sensor configuration was used. The selection of all four sensors was based on their localisation of the magnet which figure 5.17 shows that each sensor points to the magnet positions at the middle of quad configuration. Based upon the summed magnetic field of quad sensor the initial starting position of the stem with respect to the magnet was x= 0.24 mm, y= -1.02 mm, and z= 15.35.

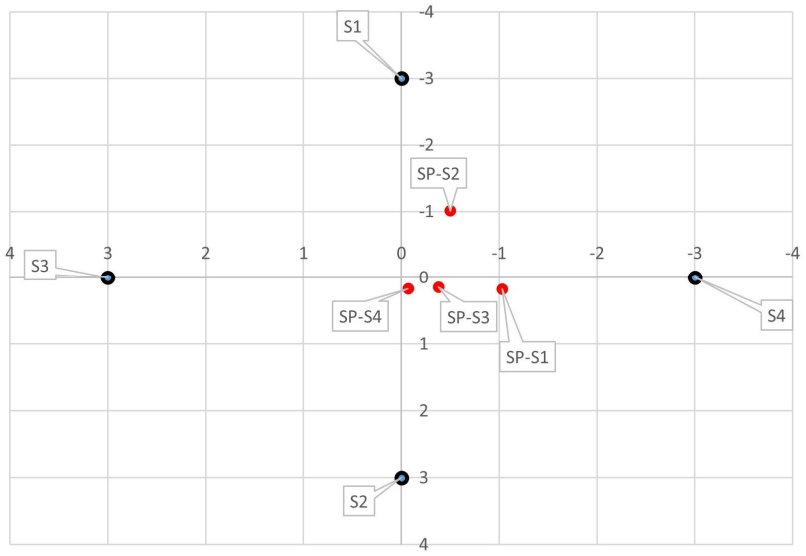

Figure 5. 17: Localisation of the humeral steam detected by each sensor of Quad-Sensor configuration with respect to a magnet at loose fixation. S1-S4 are the position of the sensors while SP1-SP2 are the detected position of the stem.

Figure 5.18 shows that the stem position during the whole phase of cyclic loading in all three axes. Figure 5.18c highlights that during the loose scenario the z-axis displacement remains the same illustrating that the displacement observed in other axes are linear.

In the partially loose scenario, the sensor initially detected no change in stem movement. After 1000 cycles a shift in x-axis position of 0.138±0.038 mm was detected by the sensor and another shift of 0.102±0.029 mm after 2000 cycles (figure 5.18a). Also, after second shift the stem started to move dynamically with an amplitude of 0.20±0.031 mm providing an early indication of loosening.

Figure 5.18b highlights the changes in the position of the stem in the y-axis during cyclic loading. Similar changes were noted in the y axis. Initially no movement was detected but after 2000 cycles the sensor detected the dynamic movement with an amplitude of 0.36±0.053 mm.

Table 5.3 also shows the comparison of the change in x- displacement with respect to JRF and axial displacement of the axial actuator. Table 5.3 also shows that when the axial displacement of the actuator started to change the sensor detected the change in stem movement as well. After 2000 cycles when the displaced amplitude of the axial actuator increased, the sensor detected an increase in amplitude as well in both axes.

Table 5. 3: Quad-Sensor displacement detection in x/y axes along with JRF and axial displacement of Actuator 2 after every 1000 cycles at loose fixation.

Cycles (1000)	**Sensor X-Axis Displacement**	**Sensor Y-Axis Displacement**	**Axial Force Peak-Peak**	**Axial Displacement**	**Compressive Force**
1	0.248±0.046	-1.02±0.051	250±0.05	0.40±0.05	99.339±2.028
2	0.138±0.038	-0.150±0.041	250±0.05	0.39±0.03	99.340±2.028
3	0.102±0.029	-1.034±0.045	250±0.05	0.65±0.03	99.340±2.028

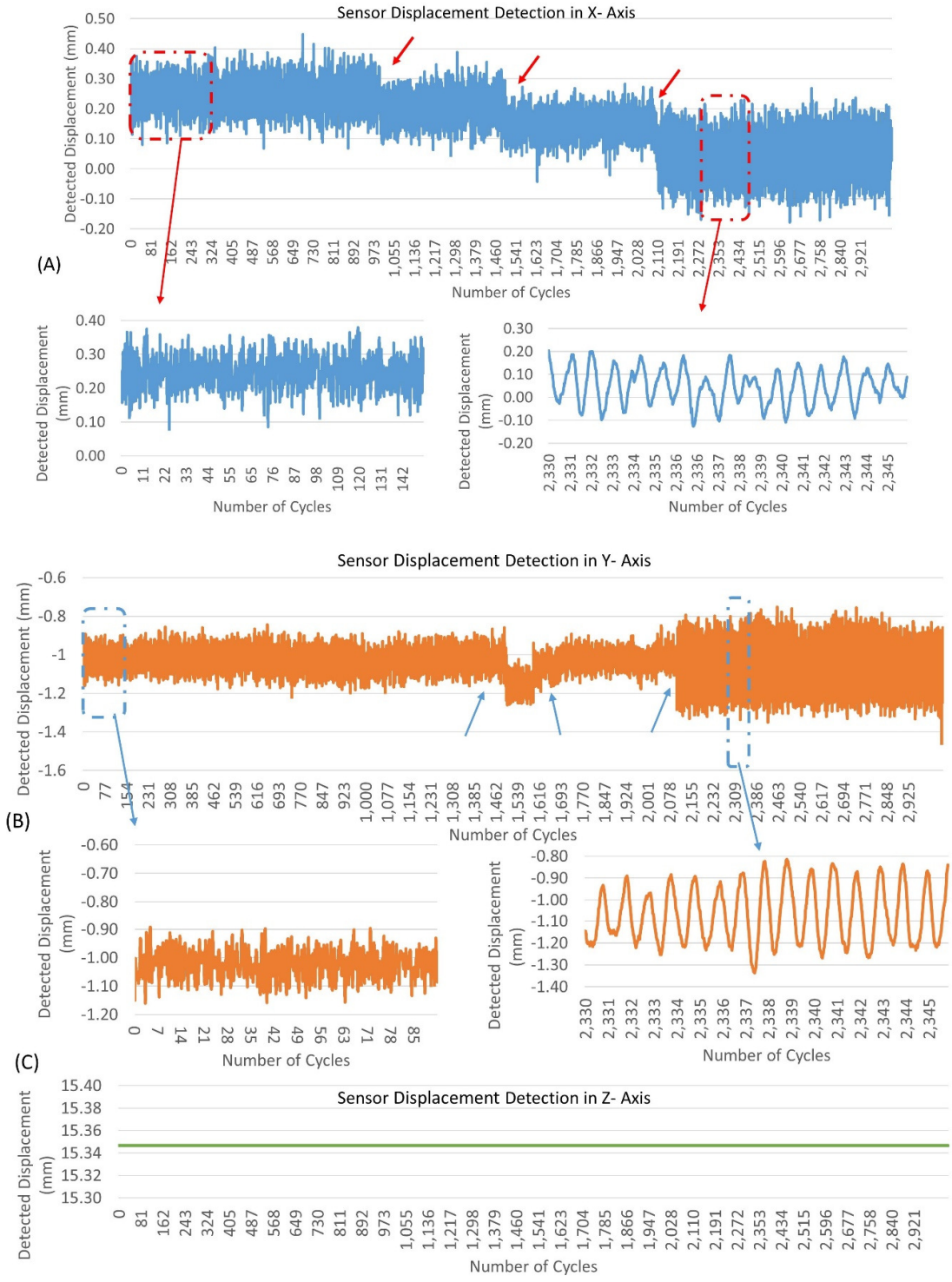

Figure 5. 18: Quad-Sensor displacement detection in (a) x-axis, (b) y-axis and (c) z-axis at loose fixation. The arrows in the graph point towards the early sign of loosening.

Figure 5.19 highlights a small change in the axial displacement of the actuator. During the initial 1000 cycles, the amplitude of the displacement remained the same but as the number of cycles increased the displacement increased to 0.20±0.04 mm. It was observed that as the axial displacement changes and increases, so too does the sensor detection as well. This infers that the implant is loosening leading to more movement, which was detected by the sensors (Table 5.3).

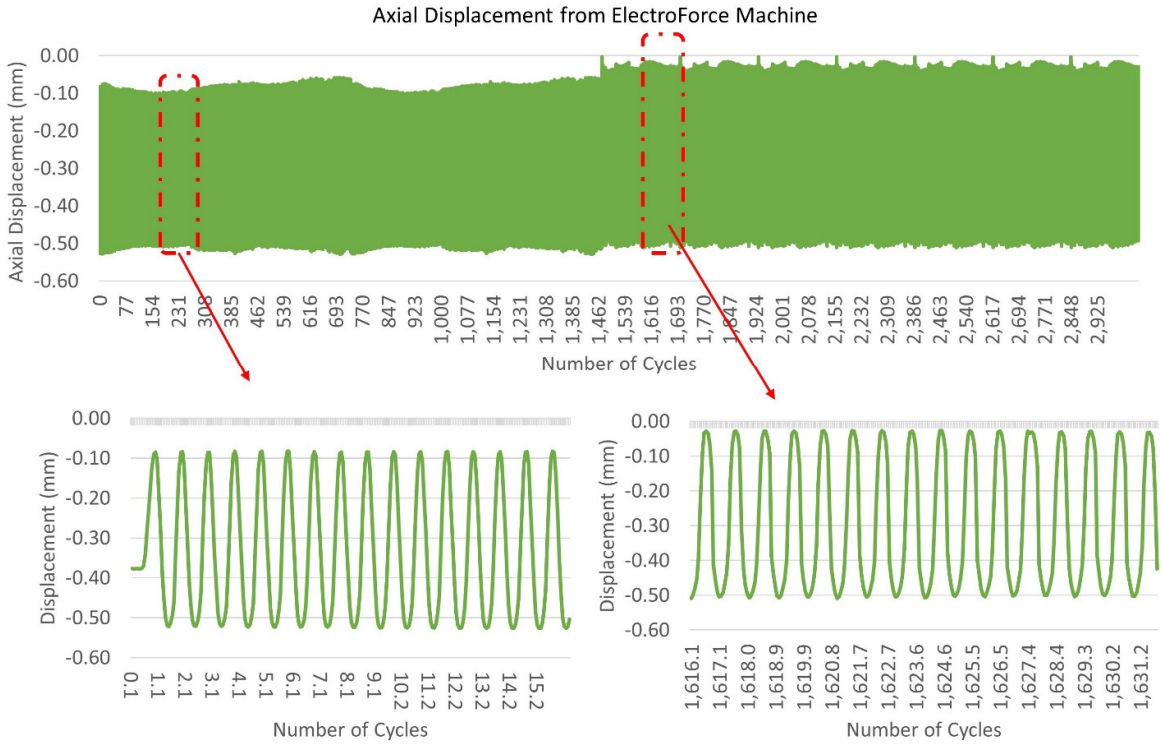

Figure 5. 19: Displacement of Axial Actuator 2 during a Loading Cycle

Figure 5.20a shows the pictorial effect on the bone after the cyclic loading. From the visual inspection of the bone and cement mantel after the experiment, it was observed that sections of the cement mantle separated from the bone (figure 5.20a). On inspection, it also appeared that the cement mantel was

thinner than 1 mm in places and small deformities were noted due to the clamp that held the bone specimen. No cracks were found on the bone during loose fixation conditions (figure 5.20b).

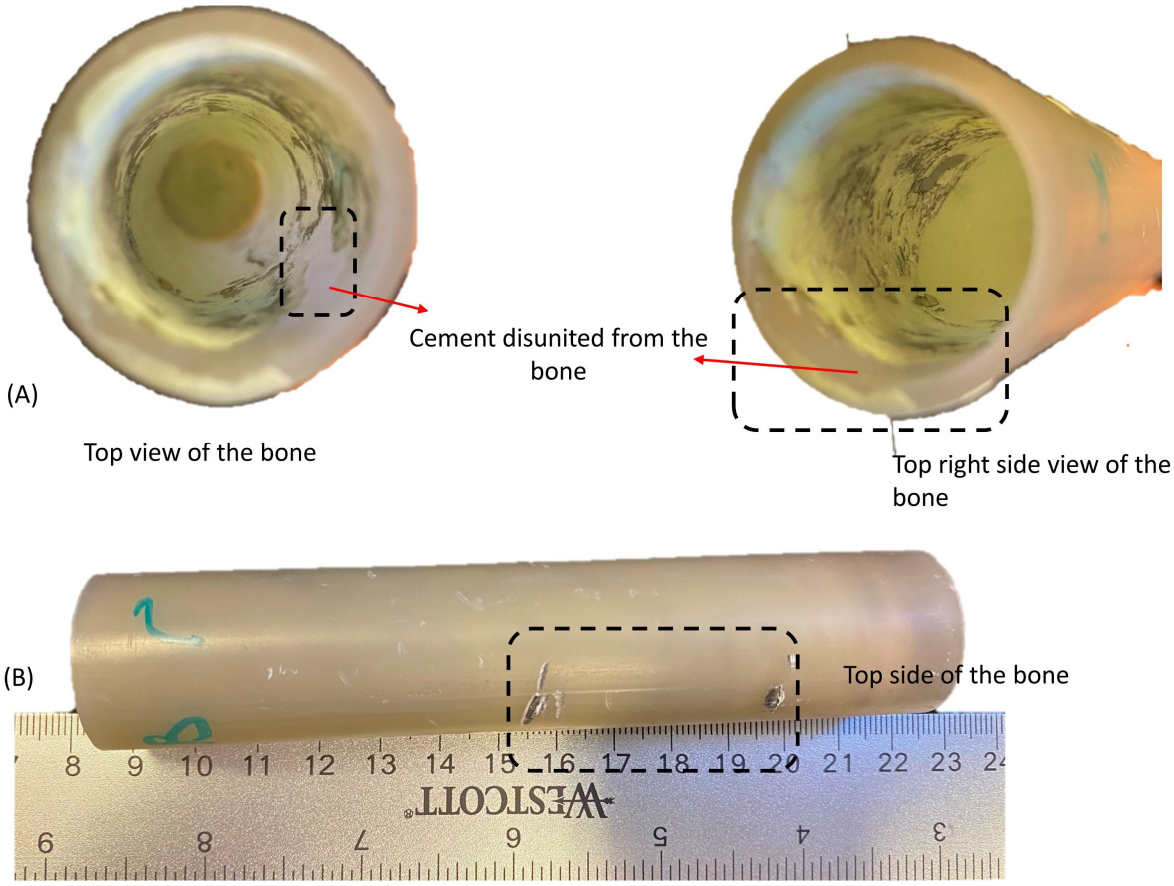

Figure 5. 20: (a) Cement mantle state after 3000 cycles of loading at a JRF of 350 N for the loose fixation scenario showing areas where the cement mantel separated from the bone during testing. (b) Humeral bone state after 3000 cycles of loading at a JRF of 350 N at loose fixation.

5.3.3 Fully Fixed Implant

In the fully fixed implant condition, figure 5.21 highlights the initial starting position of the stem with respect to the magnet embedded in the cement restrictor. In this case, the sensors (S1-S4) were pointing the position of the stem slightly tilted towards the sensor S3 and S4. According to the sensor selection criteria derived from chapter 4. To determine any changes in the position of the stem, magnetic field

data of S3 and S2 were considered while excluding the sensor S1 and S4 data. Based on sensor S3 and S2 data the initial starting position of the stem before the cyclic loading was x= 2.316 mm, y= 2.107, and z= 15.55 mm.

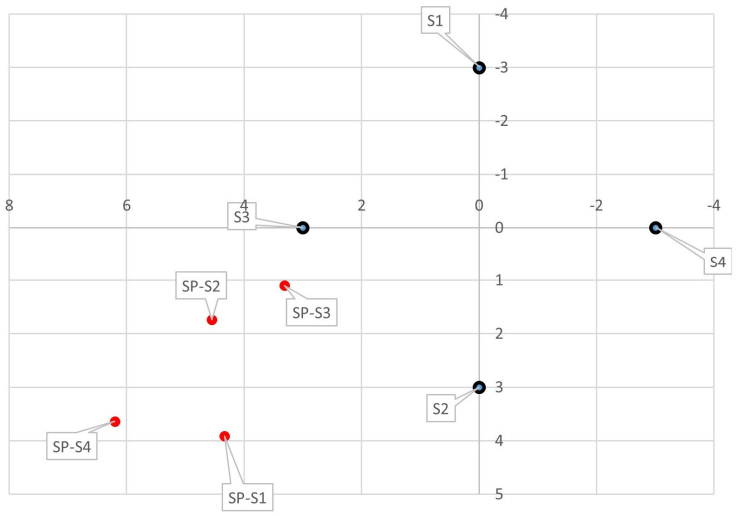

Figure 5. 21: Localisation of the humeral steam detected by each sensor of Quad-Sensor configuration with respect to a magnet at fully fixed fixation. S1-S4 are the position of the sensors while SP1-SP2 are the detected position of the stem.

In the fully fixed condition, no step change was detected by the sensor in all three axes, however, there was a displacement drift in the y axis noted (figure 5.22b). The position of the stem remained the same as it was at the beginning of the loading. Also, table 5.4 shows that the JRF remained the same as for all previous fixation experiments. For the axial actuator movement, the average displacement during the first 200 cycles was 0.29±0.06 mm, which then decreased by 0.10±0.03 mm to reach a new displacement of 0.18±0.03 mm and then remained the same during the end of cyclic loading as shown in figure 5.23. This decrease in axial displacement was due to the adjustment of the displacement sensors by the ElectroForce machine Table 5.4 shows all the sensor's responses during cyclic loading under fully fixed conditions.

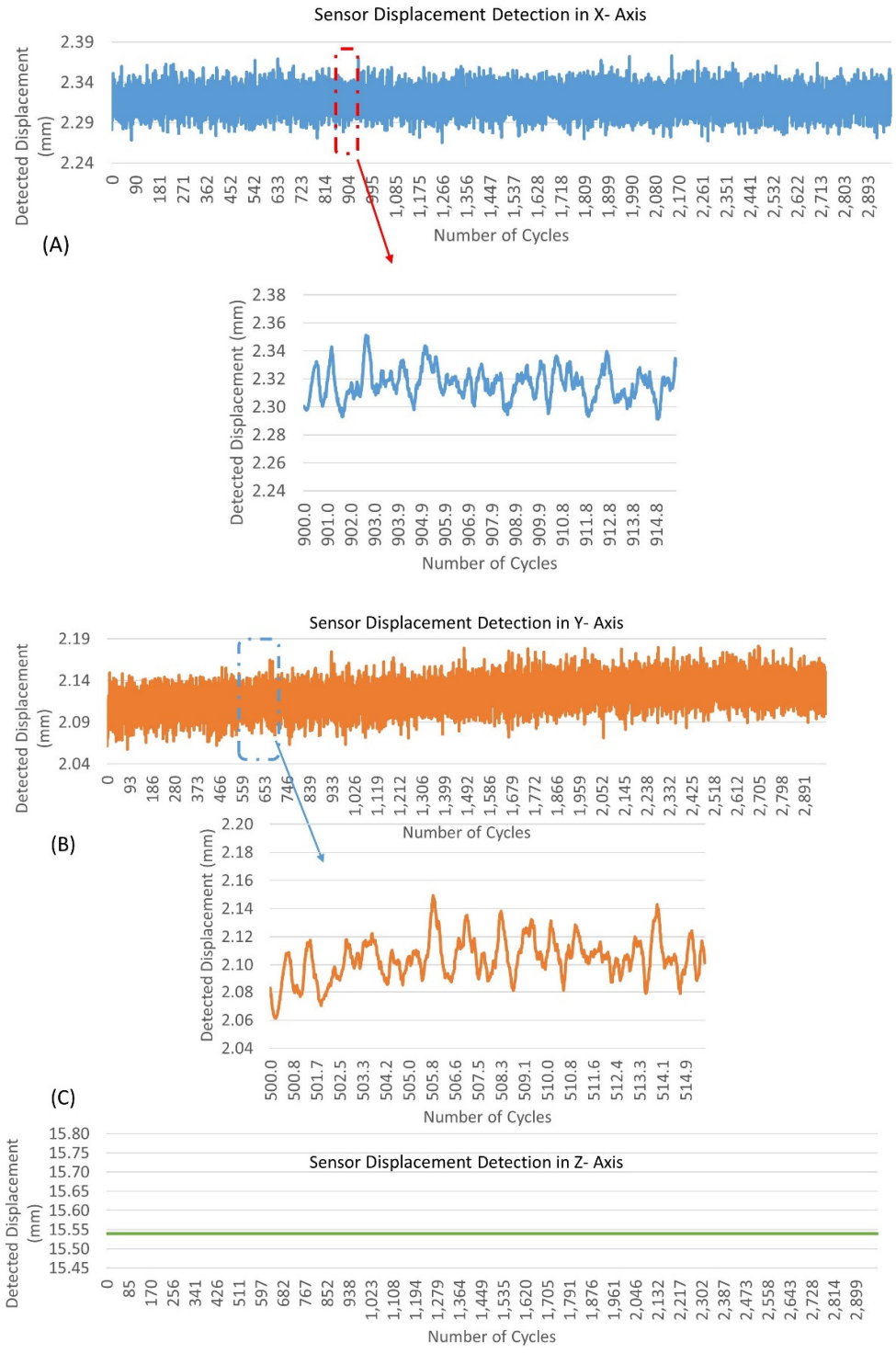

Figure 5. 22: Quad-Sensor displacement detection in (a) x-axis, (b) y-axis and (c) z-axis at fully fixed fixation.

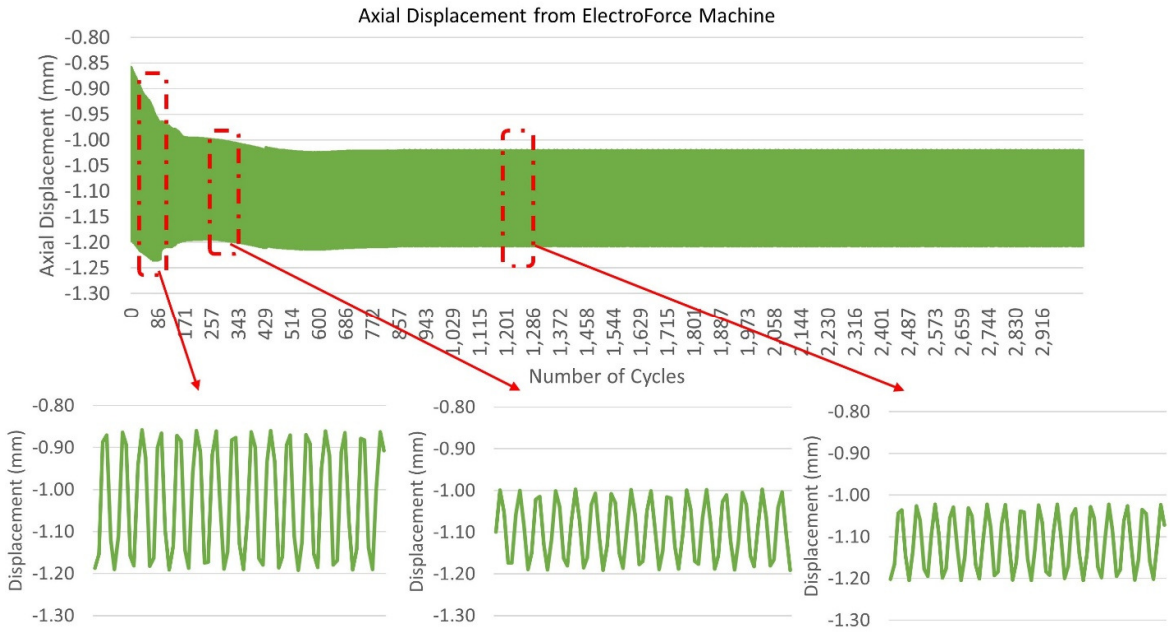

Figure 5. 23: Displacement of Axial actuator during Loading Cycle

Table 5. 4: Quad-Sensor displacement detection in x/y axes along with JRF and axial displacement of Actuator 2 after every 1000 cycles at fully fixed fixation.

Cycles (1000)	Sensor X-Axis Displacement	Sensor Y-Axis Displacement	Axial Force Peak-Peak	Axial Displacement	Compressive Force
1	2.316±0.012	2.107±0.013	250±0.05	0.29±0.06	99.339±2.028
2	2.318±0.013	2.116±0.014	250±0.05	0.18±0.03	99.340±2.028
3	2.316±0.013	2.132±0.013	250±0.05	0.17±0.03	99.340±2.028

The fixation was visually inspected post-testing where no cement separation or cracking was observed (figure 5.24 b). A small deformity at the top side of the bone was found due to clamping as shown in figure 5.23a.

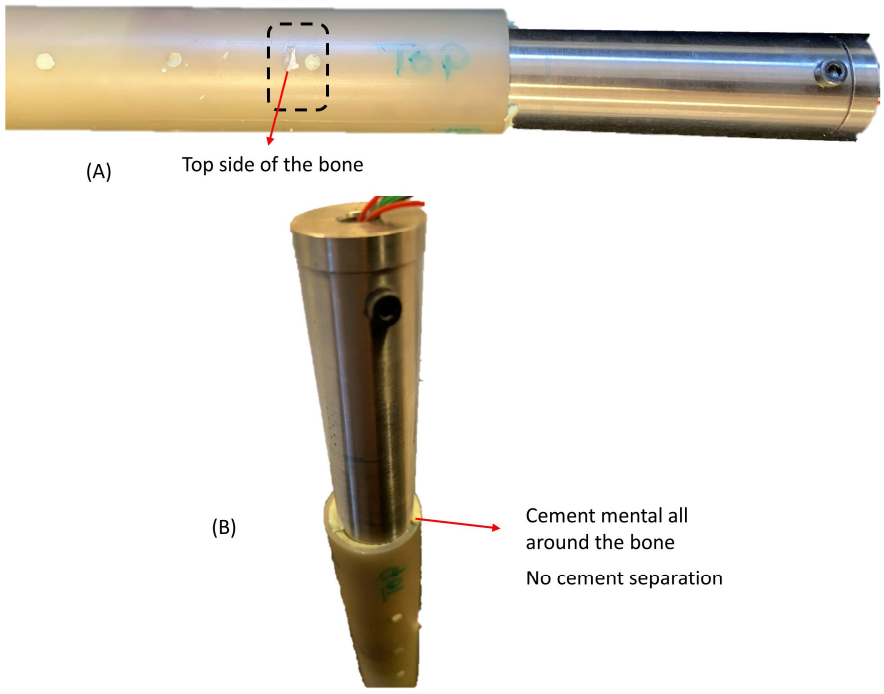

Figure 5. 24: (a) Humeral bone state after 3000 cycles of loading at a JRF of 350 N at loose fixation.(b) Cement mantle state after 3000 cycles of loading at a JRF of 350 N at loose fixation.

5.3.4 Comparison of all Fixation scenarios

Figure 5.25 shows the comparison of all three types of fixations in terms of sensor displacement detection in both x and y axes along with the axial displacement of the axial actuator. The grossly loose fixation showed higher movement at the implant tip in the x axis and y axis as compared to the loose and fully fixed implant and this correlated with an increase in axial displacement of the axial actuator compared to the other fixation scenarios. The partially fixed scenario showed an increase in x and y displacement over time, which also correlates with the change in displacement in the axial actuator. For the fully fixed scenario, any displacement changes at the implant tip was not detected. The axial displacement for the fully fixed implant was below 0.4 mm, indicating good fixation.

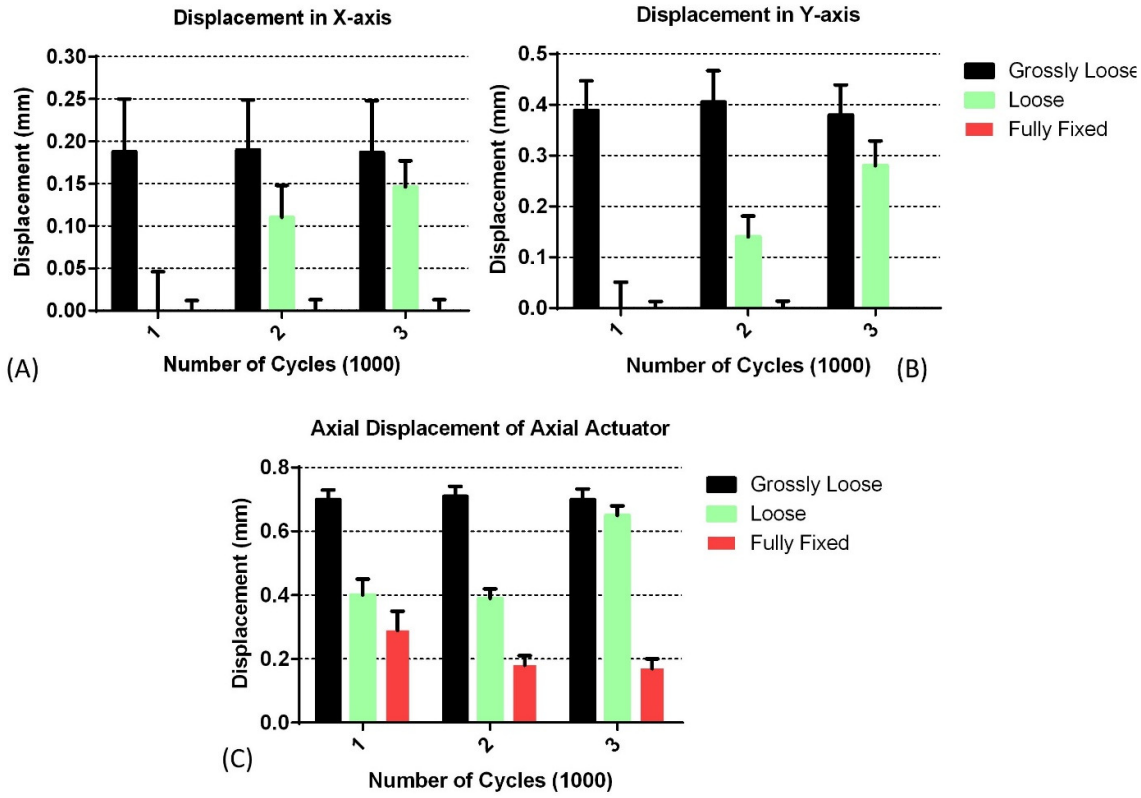

Figure 5. 25: Comparison of the displacement detected by Quad-Sensor under all three-fixation condition (a) Displacement changes in x-axis. (b) Displacement changes in y-axis. (c) Displacement detected by axial sensor of the actuator 2 during all three-fixation condition.

5.4 Discussion

A mechanical testing system was designed and fabricated to be used to simulate a clinically relevant loading scenario for close to reality detection of the elbow prostheses loosening at different fixation conditions. The main objective was to simulate the realistic loosening of the humeral stem of the elbow prostheses and to validate the quad sensor performance to detect early signs of loosening under a JRF of 350N.

The testing system was able to perform the controlled cyclic loading axially on the stem while a constant compressive joint force on the anterior side of the stem was applied. The humeral stem displacement at the tip was detected by the quad sensor as described in the previous chapter. The performance of the

quad sensor in terms of detecting early signs of loosening was evaluated against the axial displacement of the axial actuator at different fixation conditions.

Initially, at the grossly loose condition (no cement), which had a 1 mm gap between bone and implant. It was noted that the y displacement detected by the quad sensor and the axial displacement of the axial actuator was higher as compared to other fixations (figure 5.25). This was expected as the y sensor was aligned to detect axial movement. However, displacement in the x-axes was detected, which indicated movement in both axes. This may be for two reasons: firstly, the grossly loose scenario would result in free-moving body motion, resulting in out-of-plane movement. Secondly, it may be possible that a small misalignment of the y sensor to the axial direction resulting in the detection of both the x and y axes or a misalignment of the sensor with respect to the magnet. As one of the limitations of the detection technique is the starting orientation of the magnet/sensor. So, during the initial starting position, the sensor/magnet was not perfectly aligned which causes the stem to move in both x/y axes.

The sensor detection performance at the partially loose condition showed that after the first phase of cyclic loading (1000 cycles) the sensor detected a small change in implant position and after 2000 cycles the sensor detected an increase in displacement to 0.102±0.029 mm in the x-axis and 0.28±0.045 in y axis. The increase in axial displacement seems to indicate a change in fixation, where the structure became loose as a result. This is corroborated with the qualitative post-test visual observations that showed detachment of the cement mantle in sections of the bone. This early progression of loosening after few thousand cycles may be due to the low thickness of the cement mantle at 1mm. A thicker cement mantel could improve the longevity of the fixation, however, this would need to be explored further.

During fully cemented fixation no change in the position of the stem was observed only a slight drift in the y-axis (figure 5.22b) but its movement was within the noise range so the sensors were unable to detect that drift quantitatively. This may be due to creep behaviour in the cement [183]. This has meant that the implant was not tested from a fully fixed to loose position, this is a limitation and would require

a longer testing regime. Clinically, elbow implants loosen on average after 5-7 years. If translated to 150 cycles a day, would require testing to 300,000 – 420,000 cycles [178]. This was beyond the time constraints of this project.

5.5 Conclusion

A laboratory setup enabled, for the first time, to detect the humeral stem loosening of the elbow prostheses using multiple sensors embedded in the humeral stem, which highlighted that the sensor could detect fixation changes and so has the potential to detect early stem loosening at various fixation conditions.

The results indicated that for the grossly loose implant (no cement) the displacement detected by the sensor was high. Also, the system showed that when the stem could detect fixation changes and therefore detect changes in loosening progression. The design feature of the system should include a silicon covering on the clamps holding the bone to stop deformation from the experimental setup. Finally, the orientation of the sensor and magnet should be aligned so that all 4 sensors can be used to detect loosening.

6 Chapter 6

Investigation of a Non-radiographic, Non-invasive pH Sensor for Diagnosis of Septic loosening of Implantable Prostheses

This study was a collaboration between the Aston University Department of Chemical Engineering and Applied Chemistry and Mechanical Biomedical and Design and received a grant from the Aston Institute of Materials Research. In this collaborative work Hydrogel synthesis training was provided by the Department of Chemical Engineering

Summary

Implant associated infection is a serious challenge in the field of orthopaedic surgery and alongside aseptic loosening is one of the key factors in implant failure. These infections not only increase the risk of revision surgery but also lead to an adverse economic burden on patients as well. Currently, the diagnostic techniques that are applied to detect and study implant-associated infection (septic loosening) involve radiographic analysis, pathological assessment, and various blood culture tests. However, the result from these techniques are often not accurate and are unable to detect the infection in an early stage. Therefore, in this study, the aim was to develop an implantable sensor, which can detect early signs of infection around the implant by measuring a local change in pH value. A biocompatible hydrogel was synthesised that can respond to change in its surrounding pH values. The local pH value was determined by the degree of its swelling photographically. The sensor was calibrated at different pH buffer solutions and its response time along with reversibility were also tested. Finally, a magnet was embedded in the hydrogel to predict the degree of swelling non-photographically using a sensor. The chemical sensor showed a positive response towards change in different pH buffer solutions between pH 4.05, 5.5, 7, and 10. However, the reversibility of the sensor was only evident between pH 4.05 to pH 5.05. Change in magnet position with respect to pH did exhibit a correlation but the sensor formulation needs modifications to improve structural integrity and reversibility.

6.1 Introduction

Implant associated infection is a devastating disease because patients not only experience the physical and emotional trauma of revision surgery, they are also compounded with intensive postoperative care and treatment[137]. Currently, the rate of infection varies by the type of joints, hospitals, and surgeons. According to Mohajer et al *(2014)*, the rate of infection after primary joint replacement rages from 1 to 9 % (< 9 % in elbow implant, <2% in knee implant, and <1% in hip and shoulder implant) and significantly higher after revision surgery (<40%)[84]. Taking into account the infection rates and an increase in the number of joint replacement procedures, this shows a figure of about 4000-8000 infected implants annually. These infected implants not only increase the risk of morbidity and mortality but also increase the cost of managing the infected implant along with lowering quality of life[184]. According to Eric et al. *(2017),* from 2001 to 2009 the financial burden associated with treating infected implants (hips and knees) in the US was $320 million to $566 million over the 8 years. In 2020 it is expected to ramp up approximately $1.62 billion[185].

Implant associated infections are mainly caused by bacterial biofilms. Within the biofilm the microorganism organise themselves into a group of a complex three-dimensional matrix, resembling multicellular organisms and producing extracellular polymeric substances called polysaccharides. The orthopaedic implants of any type are vulnerable to hosting a biofilm[84]. Once the biofilm is firmly established on the non-living surface within the host, it is almost impossible to eradicate[186]. While systemic antibiotics can kill individual (planktonic) bacteria but they are of no use in eliminating biofilms because they have high resistance towards antibiotics and form a nidus for infection once the antibiotic therapy ceases[186, 187]. If the formation of biofilm is detected early it can be treated successfully by antibiotic, surgical irrigation, and debridement[138].

6.1.1 Infection Detection

Traditionally, the techniques used to identify implant-associated infection rely on intra-operative clinical diagnosis and infection-causing pathogen identification by examining different histopathological and physiological parameters[139]. Primarily, in clinical diagnosis, the surgeons first focus on the area of the implant that might have some sort of redness, swelling, and pain that are often related to an inflammatory response to infection. However, this inflammatory response also links with the normal wound healing process, which makes this method non-specific for implant-associated infection[139]. Different systemic inflammatory markers are also used that can differentiate normal wound healing response from infection response. These markers include the C- reactive protein test (CRP), leukocyte counts, erythrocyte sedimentation rate (ESR) along with pro-inflammatory cytokines and antimicrobial proteins[188]. Using these techniques, if the surgeon suspects an infection, synovial fluid is aspirated (arthrocentesis) along with blood samples for microbiology testing to identify infection. This is the most reliable method, however, the results take over 24 hours therefore antibiotics are typically administered at this stage as a precaution in case infection is present. However, due to the use of antibiotics the sensitivity of these markers reduces and in the process of extracting synovial fluid there is a risk of introducing bacteria to the surgical site via the skin [138, 188]. Acute infection typically occurs in the first few weeks post-surgery and is usually identified early. However low-level infection can occur months or even years later. Low-level infections are problematic as they usually develop slowly and a combination of tests are needed to confirm infection.

Currently, the initial method to identify infection is the radiographic study of the surrounding tissue around the implant. In which the presence of the infection is evidenced by bone erosion or by the presence of sinus tracks along the bone or implant[87]. However, these signs are only observed at the late stage of infection and these radiographic studies are not that sensitive in predicting early signs of infection. Another issue with these radiographic studies is excessive exposure to radiation along with high operational costs. Other techniques are also being developed, among them was detecting infection

by a change in temperature, different thermographic images of skins are taken and analysed to identify infection but this method is only applicable on the skin surface or near-surface wound[189]. Similar to this work an embedded sensor was developed to detect a change in temperature via an LCR tank circuit but that technique still lacks biocompatibility and sensitivity[139].

Recent studies in the implant-associated infection show that the bacterial colonised on the implant surface and the surrounding tissue around the implant has an acidic pH range from 4-7[190]. This acidic nature is because of the pathogen that is associated with making biofilms. Human blood pH ranges from 7.37 to 7.43[191]. In implant-associated infection, the most common pathogens are Staphylococcus aureus and Staphylococcus epidermis, their by-products are acidic in nature [89, 90]. Measuring and quantifying this change in pH in-vivo has the potential to identify the infection early. The main hurdle is to analyse this pH change non-invasively. There are a few radiographic methods that are used in estimating tissue's pH value but these methods have poor sensitivity and low resolution. Arifuzzaman et al *(2019)* developed a chemical-based pH-sensitive sensor to detect infection, non-invasively by measuring the degree of swelling of gel radiographically and using the movement of a tungsten rod from x-ray images. However, the main hurdle they faced is the uncertainty in reading the radiographs, which were reducing the pH sensing accuracy[138].

In this study, the aim was to develop an implantable sensor (Hydrogel) that can detect the early sign of infection non-invasively and non-radiographically. The sensor was designed to be embedded in the existing orthopaedic implant. The sensor working principle was based on the variation of gel size with respect to different pH values. This varying gel size will be measuring non-radiographically by embedding a magnet and computing the change in the magnet field via a magnet sensor. Embedding sensors in the existing orthopaedic implants have been done previously to measure different parameters including pressure, kinematics, position, and temperature. A similar type of embedding sensor was used in our previous work (chapter 3-5) to measure the position of the implant. In this work, the placement

of the magnet was changed i.e. inserting into the gel while the algorithm and calibration remain the same as of previous work i.e. single sensor single magnet configuration.

6.2 Material and Method

6.2.1 Hydrogel Disc Fabrication

Hydrogels are three-dimensional cross-linked materials that have the capability to absorb and hold large quantities of water without dissolving. Due to the presence of a large number of hydrophilic groups hydrogel has a higher absorption of water [192]. Hydrogels have unique properties of change in their volume size in response to different external stimuli such as temperature, electric current, and pH. Along, with the reversible response to the same stimuli, which makes them potential for a wide range of biomedical applications.

There are different techniques for the synthesis of hydrogel, the most common one is free-radical crosslinking copolymerization. In this technique, a non-ionic monomer is copolymerized with a small amount of cross-linker. To improve the swelling capacity of the gel an ionic monomer can also be added in the synthetic process [192].

In this chapter, the above-mentioned technique was used to cure the hydrogel. As the main aim was to develop a biocompatible pH sensing implantable sensor, biocompatible polymers were used, that can respond to the specified range of pH i.e. 4.05-7.0. Figure 6.1 illustrates the step-by-step process involved in the synthesis of the hydrogel. The polyacrylic acid-based hydrogel was developed because of its biocompatibility and pH response properties [193].

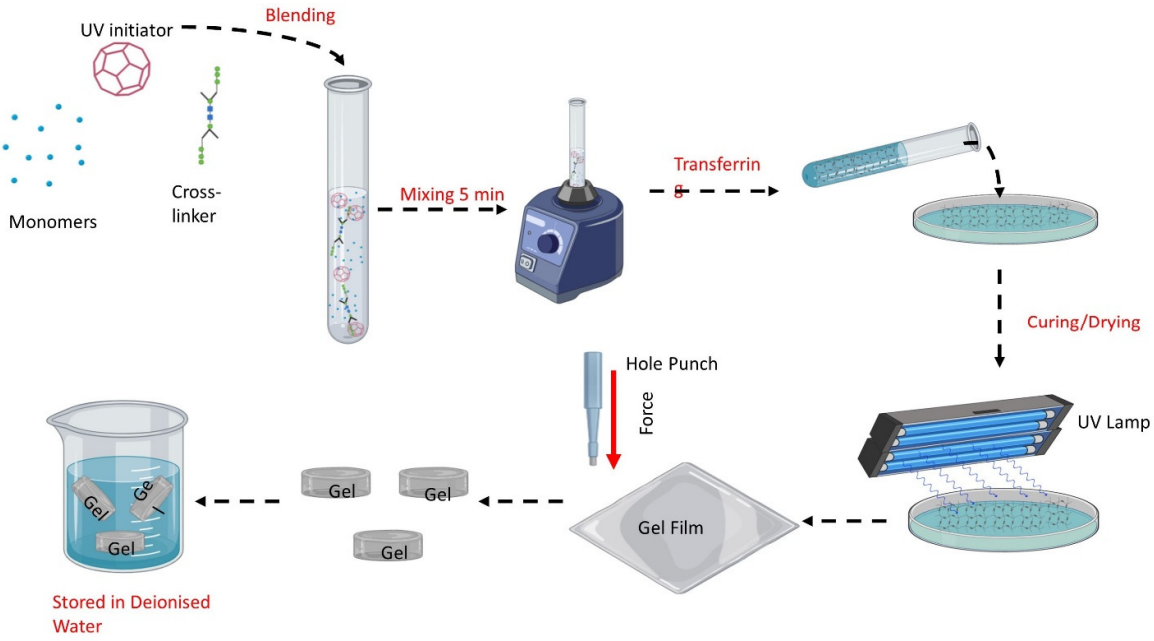

Figure 6. 1: Diagram illustrating the method employed to synthesis Hydrogel

The polyacrylic-based hydrogel was prepared from the photo-polymerization of monomers with a UV initiator and cross-linker. In this process first, the monomers acrylic acid and N, N-dimethylformamide (DMF) were blended with UV initiator (2-Ketoglutaric acid) along with cross-linker poly (ethylene glycol) diacrylate, average Mn 600(PEGDA600). DMF was used as a reagent solvent for synthesis and moisture absorption. 2- Ketoglutaric acid acted as UV initiator, which breaks off the carbon molecule at the alpha end and produces radical. The crosslinker was used to stabilise and improve the swelling capability of the gel. The solution was blended for 5 minutes to ensure the solute is completely mixed. The solution was transferred to the Petri dish and placed under 365 nm UV irradiation for polymerisation. The height of the hydrogel depends upon the size of the Petri dish. In this study, the Petri dish having a size of 150 mm diameter and 4 mm height was used. After polymerisation, the resulting hydrogel film was immersed in deionised water to remove any residue monomers. The hydrogel film was washed daily for 5 days to ensure the removal of any unreacted monomer. The circular punch hole was used to cut the hydrogel into disks. Finally, the disks were immersed in deionised water

for storage before testing and can be used for testing their performance under different pH buffer solutions. Table 1 shows the formulation of three different synthesis hydrogels based on their chemical composition weights. Their pH response was observed at different pH values ranging from 4.0-10.05. The weights selection of the chemical composition were based on Arifuzzaman et al, study on pH sensitive hydrogel [138].

Table 6. 1: Different Formulation and their Chemical Composition to Synthesis of the GEL

Formulation	Chemicals			
	Acrylic Acid	**DMF**	**PEGDA 600**	**2-Ketoglutaric acid**
1	3.75 grams	21 grams	0.50 grams	0.025 grams
2	4.02 grams	20.70 grams	0.36 grams	0.025 grams
3	4.02 grams	20.70 grams	0.30 grams	0.025 grams

6.2.2 Determination of Gelation

In order to determine, that the blended aqueous monomers, crosslinker, and UV initiators are polymerising and forming a solid 3-dimensional hydrogel, a degree of gelation is needed. Gelation is the process/time required in which the hydrogel is formed. To analyse the degree of gelation of the above mentioned 3 hydrogel formulations, samples of the blended solutions were taken, when they were under the UV irradiation during the process of polymerisation, at a regular time interval of 0.5 hours. Each sample was first placed in the deionised water for 24 hr at room temperature so that any unreacted monomer can be removed and each sample can attain the equilibrium. After 24 hrs, the portion of the sample which was polymerised was extracted, washed, and dried in the microwave oven from 2 – 3min depending upon its water content and the dried gel was weight. The extraction process was repeated

until the weight becomes constant. The monomers percentage that was converted into the hydrogel was determined by the following equation:

$$Degree\ of\ Gelation = \frac{m_d}{m_e} * 100 \qquad 1$$

Where m_d is the mass of the gel when dried while m_e is the mass of the gel when extracted from the deionised water.

6.2.3 Swelling Behaviour of Gel

The swelling properties of the gel were characterised by weight changes and geometric changes. The weight fraction (β) of the gel was measured in the swollen network by using equation 2.

$$\beta = \frac{(m - m_o)}{m_0} \qquad 2$$

Where m is the mass of gel at equilibrium state while m_0 is the weight of the fully dried gel. To analyse the weight and swelling response of gel at different pH values, the dried samples were fully immersed in the known pH buffer solution. The gel samples were kept in the solution until they attained equilibrium (>5 hours). After, equilibrium, the weights of the swollen gel was measured. A similar procedure was followed for other pH buffer solutions as well. By using equation 2 the degree of gels at the equilibrium state were characterised.

The geometric changes were carried out using photographic analysis. The change in the diameter of the gel was observed by video from a top view to record the time-lapse changes. Firstly, the gel was fully

immersed in a known pH solution, and photographs were taken at times 0, 1 hour, and 8 hours until the gel reached its equilibrium state. The diameters were measured from the time-lapse photos using ImageJ software. To accurately measure the diametric change of the gel, the gel submerged in the known pH solution was placed on top of the grid paper as shown in figure 6.2.

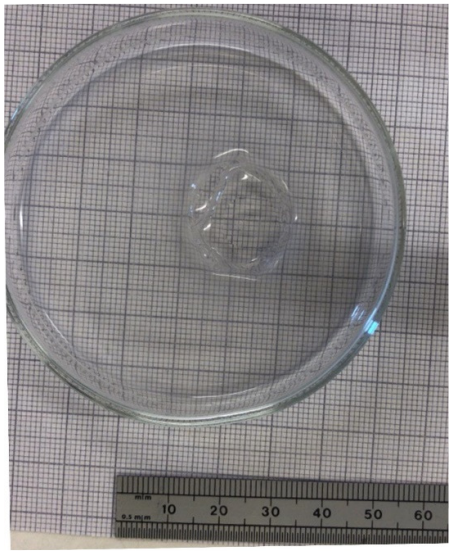

Figure 6. 2: Setup for detecting the geometric change of the hydrogel. With the reference to the grid lines, parameters were set up in ImageJ software and the diameter of the Gel was measured.

To check the response of gel at different pH values, the disk was removed from its previous pH buffer solution, washed two times by the new pH buffer solution, and then immersed in the new pH buffer solution, and left in the solution till it attains its equilibrium. Based on the variation of the diameter of gel at different pH values, the calibration curve was established.

6.2.4 Swelling Behaviour by Using Magnets

In this test, the change in gel size was measured magnetically by embedding a magnet in the gel using two different gel amalgamation types as shown in figure 6.3. The reason for synthesising these different gel amalgamation types was to analyse the bonding of the magnet with the gels. Furthermore, to check

the magnet adhesive response with the gel when exposed to different pH solutions. One of the types was exposed to an acidic medium while another to a basic medium and their response were analysed.

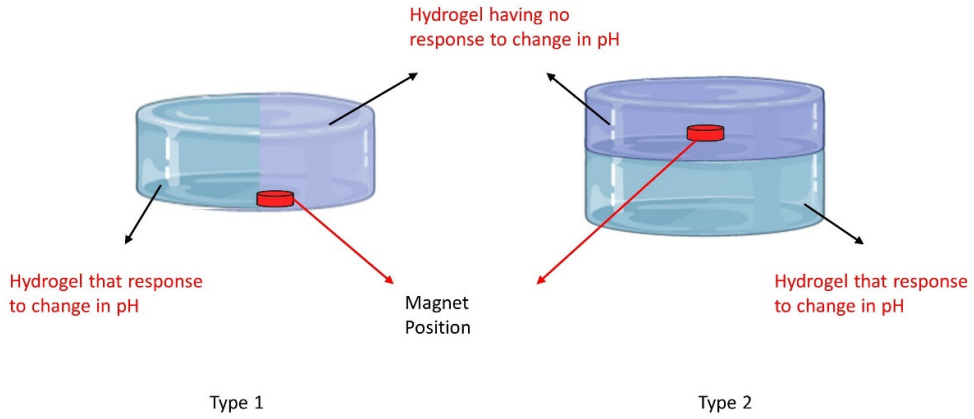

Figure 6. 3: Diagram illustrating the two types of magnet insertion in the gel and their amalgamation.

For synthesising such types of gels that contain magnets in them. First, the responsive gel is synthesised using a similar method as described in figure 6.1. When the gel is fully polymerised the magnets are placed on the gel. For type 1 at the side of the gel while for type 2 on top of the gel as shown in figure 6.4.

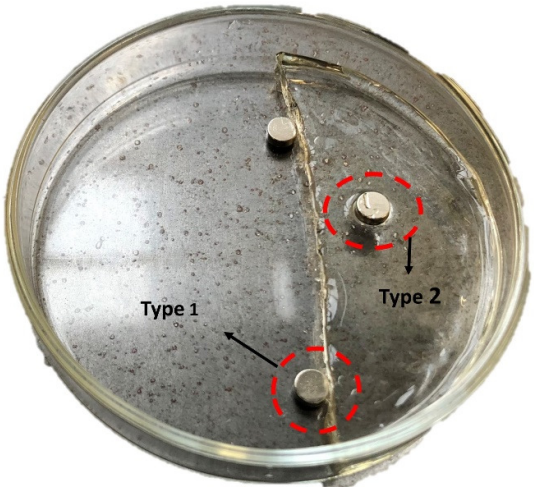

Figure 6. 4: Positioning of the magnet during magnet-based hydrogel synthesis

After positioning the magnet, the non-responsive gel solution is poured on top the previously synthesised gel and placed under UV irradiation. During the curing process, both gels interlinked with each other. This amalgamation process was to ensure the mechanical integrity and stability of the gel/magnet interface. Once the gel was made they were inserted into the deionised water and were washed for 5 days to remove any unreacted monomer. After 5 days, the gels were cut into circular shape disc using a circular punch hole and were ready for testing.

To measure the gel response at different pH buffer solutions, the gel was placed on titanium alloy and the sensor beneath that metal alloy. Titanium alloy was used because most of the orthopaedic implants are made of the same metal alloy. A National Instrument data acquisition card (MyRio) was used to retrieve data from the sensor. Figure 6.5 shows the schematics of the pH response detection method using a magnetic sensor.

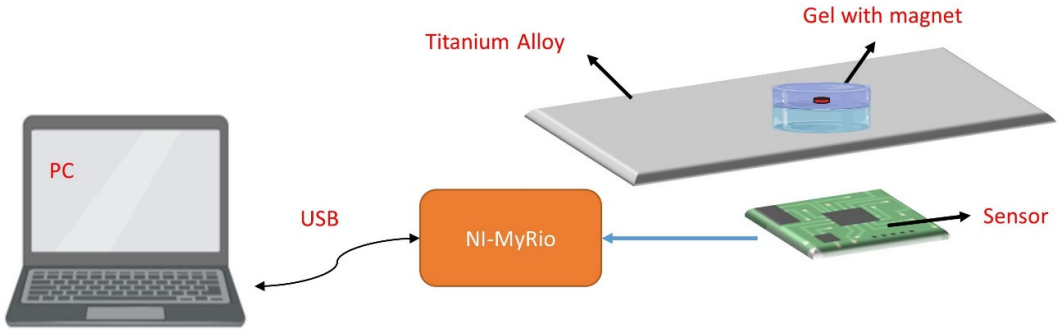

Figure 6. 5: Diagram illustrating the method to detect a change in pH response using a magnetic sensor

One of the samples of the magnet embedded gel was inserted into the pH solution from 5.0 (starting pH) to 10.0 and the variation of the gel size was measured by the displacement of the magnet. Another

sample was inserted into the pH solution from 5.0 (starting pH) to 4.05. The sampling rate of the system was 10 Hz and the gel response was recorded for 8 hours.

6.3 Results

6.3.1 Degree of Gelation

Figure 6.6 highlights the degree of gelation of the three hydrogels synthesised from different chemical compositions. It was observed that formulation 1, gelation was faster as compared to the other two. 90% of the formulation 1 monomer were converted into hydrogel within 2.5 hours of UV irradiation while for the other two formulations the gelation started after 4 hours of curing of it reached the final hydrogel from after 7.5 hours. It was observed that with the increase in the crosslinker content the degree of gelation can be increased figure 6.6.

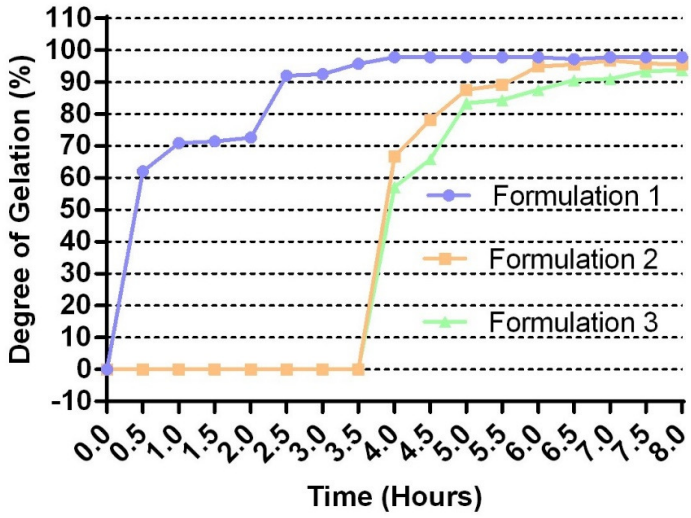

Figure 6. 6: Degree of Gelation of all Three Formulation of Hydrogels.

6.3.2 Swelling Behaviour of Gel

Figure 6.7 shows the dependency of the degree of swelling of the hydrogel by weight at different pH buffer solutions. The hydrogel synthesised from formulation 1, didn't show any change in its weight

content, it means that the formulation 1hydrogel was not absorbing any water. Similarly, the formulation 2 hydrogel response to the different pH buffer solutions was not promising and showed a moderate change in their weight highlighted in figure 6.7.

Compared to the previous two formulations, the hydrogel synthesised from formulation 3 showed a swelling response at different pH buffer solutions, and the weight of the gel increased from 5.3 times dry weight at pH 4.05 to 97.5 times dry weight at pH 10.0. Inspecting into the swelling ratio of the formulation 3 hydrogel, it shows that if the gel is in an acidic medium their water absorption capability will be less as compared to the basic medium.

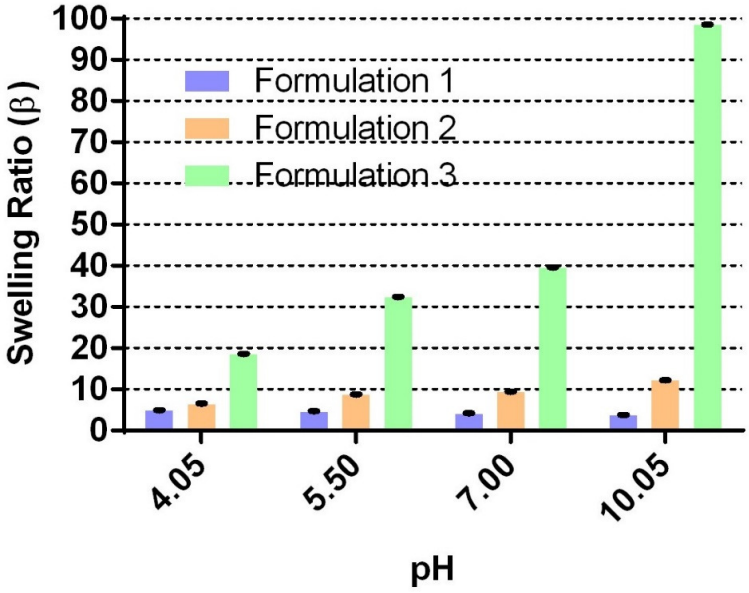

Figure 6. 7: Dependency of Degree of Swelling with respect to the weight fraction of all three Hydrogels

Figure 6.8 shows the geometric change of the hydrogel synthesised from the formulation 1 and 2. As highlighted in the previous section the formulation 1 and 2 didn't show any response to water absorption and increasing its weight. A similar response was observed photographically as well. As shown in figure

6.8 both formulation were submersed in the pH 10.05 buffer solution, hydrogel from formulation1 didn't show any change while for the formulation 2 hydrogel the diametric change was quite small.

Figure 6. 8: Dependency of Degree of Swelling by Diameter of the Hydrogels synthesised from formulation 1 and 2

Figure 6.9 shows the diametric change of the hydrogel synthesised from formulation 3. The gel diameter along with its water absorption capabilities increased with the pH of the solution becoming more basic in nature.

Figure 6. 9: Dependency of Degree of Swelling by Diameter of the Hydrogels synthesised from formulation 3

Figure 6.10, shows the quantitative change in diameter of the gel with respect to different pH solutions.

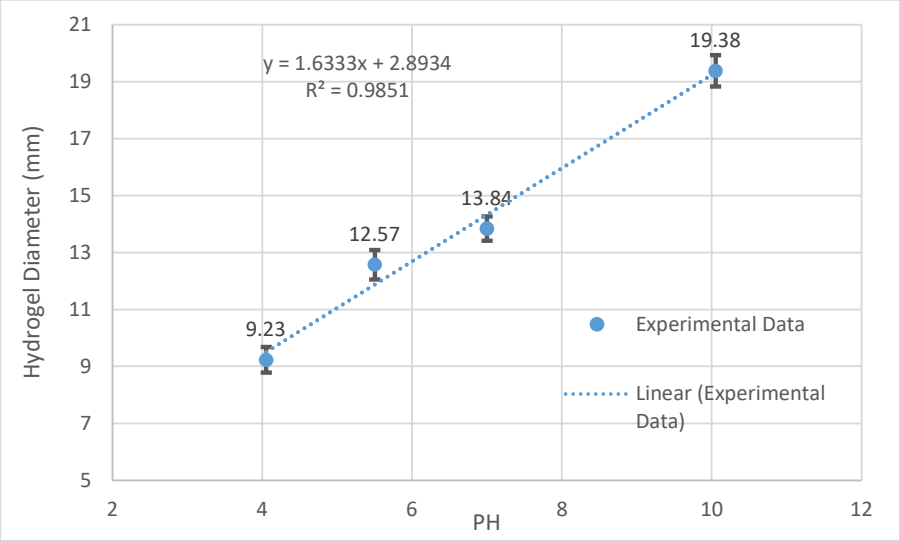

Figure 6. 10: Equilibrium Hydrogel Diameter in Standard pH buffer solutions (N=3).

Figure 6.10 shows that at the lower pH value of 4.05 the diameter of the gel swells from 9.23 mm to 19.38 mm at pH 10.0, showing a possible linear correlation. However, the data also indicated that the change in the gel diameter from pH 4.0 to pH 5.50 is higher as compared to the change in gel diameter from pH 5.50 to pH 7.0 some non-linearity. To assess the reversibility response of hydrogel, the gel was exposed alternatively to pH 5.50. It showed that the reversibility was only observed between pH 4.0 and pH 5.50. If the gel pH was above 5.50 it didn't show reversibility.

6.3.3 Swelling Behaviour Detection Using Magnet

As described in the methods section that the proposed mechanism to detect swelling behaviour of the hydrogel without any imaging or weight content method is by inserting a magnet into the gel that doesn't show any response to pH change and then amalgamating that gel to the responsive one (figure 6.3). Looking into the results obtained from the three synthesised hydrogels. For this particular magnet-based swelling behaviour detection, formulation 1 hydrogel was used in which magnet was insert, and then it was amalgamated with the formulation 3 hydrogel.

Figure 6.11a, shows the response of type 1 gel/magnet configuration. The gel was immersed in a pH 10.0 solution and its response was measured via magnet movement. It was observed that after 30 min the size of the gel starts to change in both x and y axes while the change in the z-axis was observed after 1.5 hours. The magnetic sensing system was detecting the changes in gel size in all three axes until the gel came to its equilibrium position. As highlighted in the figure 6.11a, it took 6 hours for the gel to come to its equilibrium position

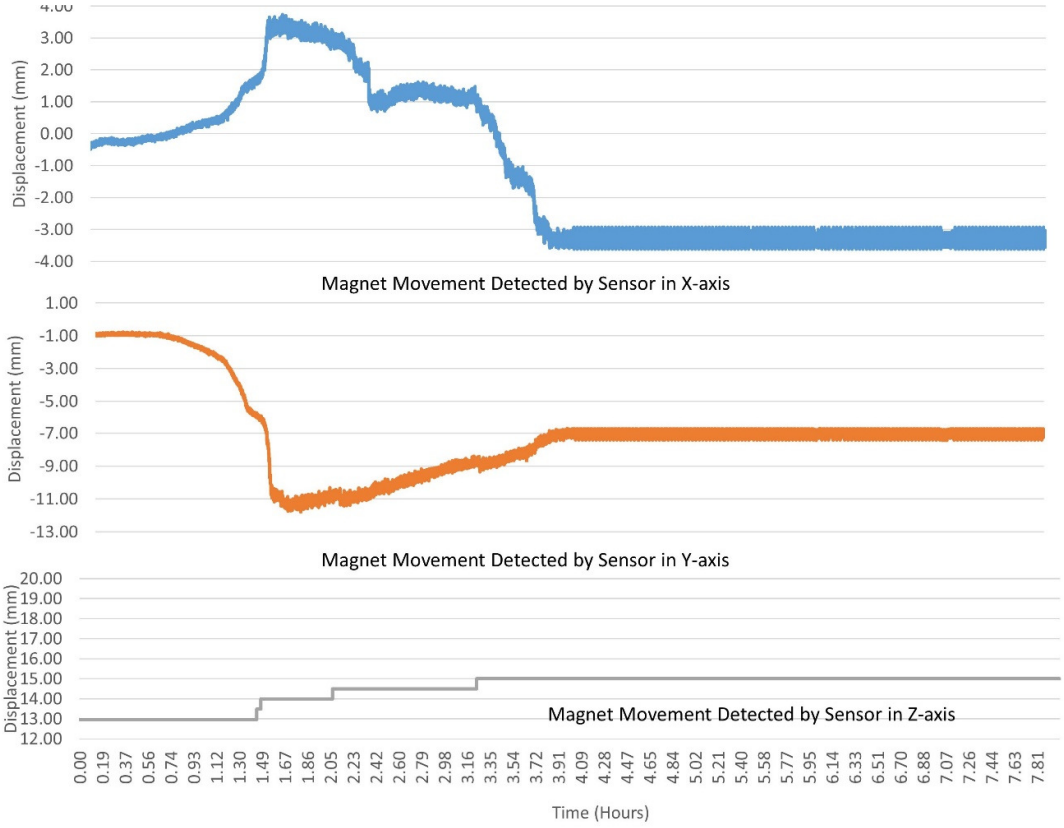

Figure 6. 11: Change in the magnet position with respect to the Type 1 merged gel at pH 10.05 buffer solution (N=1)

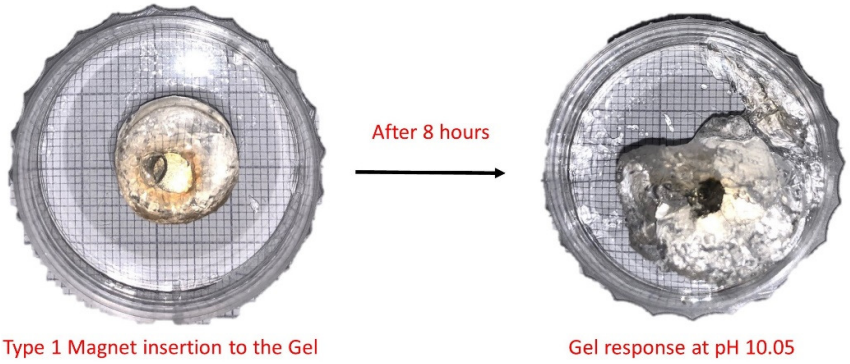

Figure 6. 12: Changes in the type 1 gel physical property before and after submerging in the pH buffer solution

As, from the previously observed results, at pH 10 the gel's water absorption ratio increases and it expands. As expected at pH 10.0, the gel expanded where the distance between the sensor and magnet increased as shown in figure 6.11 (Z-axis value). However, the gel with the magnet embedded showed a different response from the gel's response without the magnet at pH 10.0 solution (figure 6.12). Also, after 4 hours the gel was unable to maintain its mechanical stability and shape. The magnet also shifted in the x and y axes, showing a shift in position from the top plane (figure 6.11 and figure 6.12).

Figure 6.13, highlights the response of type 2 gel/magnet configuration. As in this type, the gels were merged axially. The merge gel was immersed at a pH of 4.0. It was observed that the gel response was not as fast as compared to the type 1 configuration. Also, the gel took 6.5 hours to come to its equilibrium state.

As from the previously observed results, when the gel is in acidic medium it contracts. The same response was observed by the magnetic sensing system, as the gel contracted the distance between the sensor and magnet decreased which was observed by the z-axis movement of the sensing system figure 6.13 z-axis movement. However, after reaching the equilibrium state the magnet separated completely

from the gel. Also, in this type 2 configuration, the lower part of the gel first started to contract and after 5 hours the upper part of the gel started to contract along with expansion in the lower part.

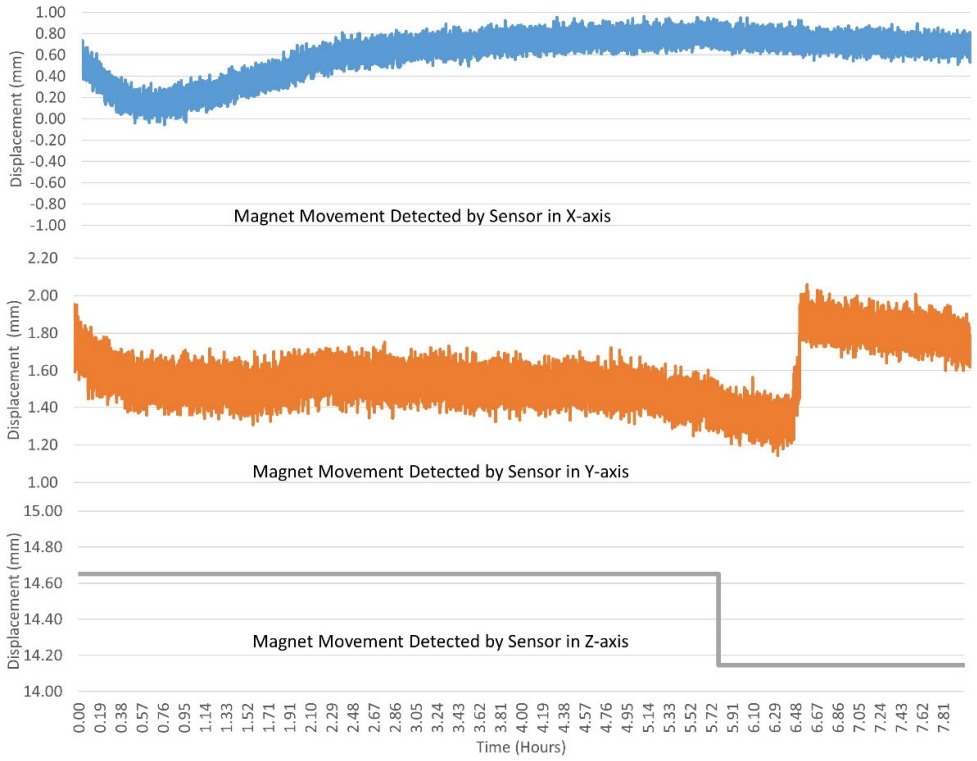

Figure 6. 13: Change in the magnet position with respect to the Type 2 merged gel at pH 4.05 buffer solution (N=1)

Figure 6.14 highlights the physical changes of the type 2 gel/magnet configuration. Compared to the gel contraction observed from formation 3 alone, with this gel type the contraction was more noticeable along with the slow response time

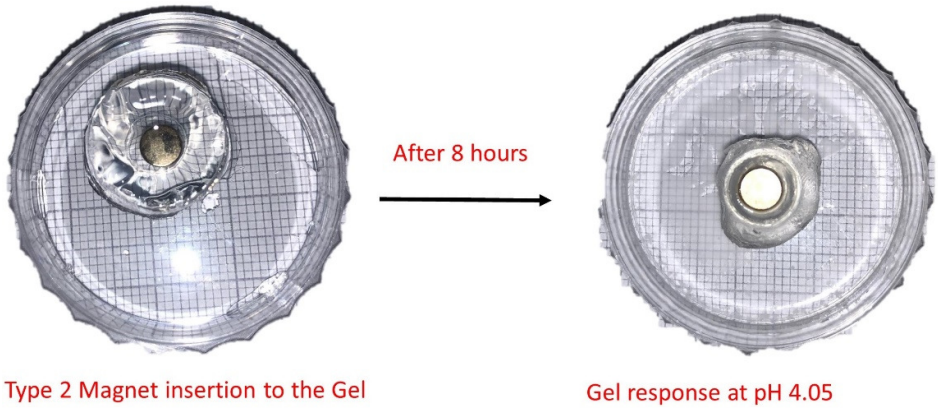

Figure 6. 14: Changes in the type 2 gel physical property before and after submerging in the pH buffer solution

6.4 Discussion

The work presented in this chapter shows the feasibility of utilising a magnet-based chemical sensor for detecting the infection via the change in pH value. Three types of hydrogels were synthesised by varying their chemical compositions. The experimental results showed that the hydrogel having a higher cross-linker content polymerises much faster compared to lower cross linker-content figure 6.6. Also, the results highlighted that the gel with a higher cross-linker showed less/no response to the change in pH compared to the lower content figure 6.7. Also, the synthesised gel highlighted that the weight fraction of the gel decreases in the acidic medium while it increases gradually as the gel media becomes more basic. Also, the result demonstrated that the diameter of the gel decreased in an acidic medium and increased in a basic medium, but still in order to make a calibrated curve that fits well with the actual pH value, there is a need for modification in the formulation. The reversibility was only observed when the gel was immersed between pH 4.0 and pH 5.5. Beyond this range, the gel didn't show any reversibility. Future research is needed to determine the ideal formulation that can establish a suitable calibration curve that fits with the Henderson- Hasselbalch equation and achieve reversibility.

Finally, two types of merging gel were synthesised with an embedded magnet. The magnet responds as were hypothesised, that when the gel is in an acidic medium it will contract resulting in decreasing the distance between the sensor and magnet, and in a basic medium it will expand and will increase the distance between sensor and magnet. But when the gel reached its equilibrium state it did not keep its stability and shape figure 6.12 and figure 6.14. Therefore, to detect the pH response via magnet movement, the system requires adherence of magnet at the outer boundary of gel rather than embedding in the gel.

6.5 Conclusion

The synthesis and application of a magnet-based chemical sensor for detecting infection via pH change were carried out showing the potential of using this application in infection detection. The pH-sensitive gel was demonstrated to show its swelling response at different pH buffer solutions. This is the first magnetic-based infection detection method that can detect the early sign of infection without any radiographs or invasively taking samples. This magnet-based chemical sensor has the potential not only to detect but eradicating the sensed infection by an actively drug-releasing mechanism which most of the hydrogel are capable of along with further understanding the cause of prosthetic joint infection.

7 Chapter 7

Discussion and Future Work

The primary aim of this thesis was to design a novel diagnostic measuring system that can easily be integrated into the commercially available elbow prosthesis making it "smart" and provide highly accurate in-vitro prosthesis loosening information both aseptic and septic without any radiographic exposure or contact. Different configurations of sensors and magnets were designed to detect the migration of the prostheses in multiple axes, with a final quad configuration developed. A detection algorithm combined with different noise filtering was used to refine the output signal that demonstrated the feasibility of highly accurate detecting aseptic loosening through the proposed system. A mechanical testing rig was designed, manufactured, and used to simulate a variety of realistic prostheses loosening scenarios under a loading cycle, in which the proposed detection was validated by integrating into a humeral component as part of the smart elbow prosthesis. In a separate design, a biocompatible hydrogel was synthesised to detect the infection around the prosthesis by measuring the change in pH around the implant. The developed magnetic detection method was integrated with the hydrogel to detect changes in gel diameter as a function of pH changes and therefore could detect early signs of septic loosening.

7.1 Implantable Loosening Detection System

The following sections outline the concluding discussion about the detection technique sensor configuration, algorithms, and its design for the detection of loosening of elbow prostheses.

7.1.1 Single Sensor Single Magnet Configuration

In this configuration, the magnetic sensor was placed at the tip of the humeral stem while the magnet was embedded in the cement restrictor. These positions were based on the clinical finding which highlights that majority of the radiolucent lines are observed near the tip of the elbow prosthesis after

loosening [158]. Therefore, the sensor component was placed near the vicinity of the tip, and to detect its relative position, a magnet was embedded in the cement restrictor. The way the migration of the humeral stem was detected by correlating the magnetic field received from the magnet and converting that field data into the implant position parameter (Chapter 3). Migration of the component was detected in multiple axes with a resolution of 0.3 mm linearly and 0.50 angularly both under quasi-static and dynamic motion. The accuracy of the detecting system was affected when the distance between the sensor and magnet was increased. Beyond 15 mm Z-Distance (distance between sensor and magnet), the noise in the detected measurement along with the detection error started to increase (Chapter 3, Figure 3.20).

The effect of the biomaterials was also investigated (chapter 3, Table 3.4), finding a negligible effect of the biomaterials on the detection technique. With different types of motion (quasi-static and dynamic) the percentage error of detection was 3 % for quasi-static while 10 % for dynamic movement detection. The higher percentage error in the dynamic movement was due to the lower operating frequency of the system. The system can detect the motion when it is moved below 0.5 Hz. Any motion above this range the system was able to detect the change but was unable to quantify displacement accurately (Appendix A.1).

The magnetic field of the magnet varies non-orthogonal (lack of orthogonal alignment) when it is moved in any direction in the spatial plane. This feature adds non-linearity and crosstalk to the magnetic field value received by the sensor (Chapter 3, section 3.3.1). Also, comparing it to the other sensor types (eddy current and capacitive sensor), a similar kind of non-linearity and crosstalk is observed when detecting the targeted object in multiple axis [194-196]. The algorithm linked with the single sensor configuration eliminated the crosstalk effect along with non-linearity. The configuration can detect the linear movement ranging from 0.3 -4.00 mm while angular from 0.5 – 4.0 degrees. Although it can detect linear movement beyond 4 mm, the range was selected as at this point implants are grossly loose and can be detected on a plain radiograph [99]. So, the whole focus was detecting the migration as low

as possible. While in angular movement the maximum it can detect was 4.0 degrees with an error of 0.475±0.90 mm. That error was due to the tilting effect of the magnet. Also, comparing to the other detection tools, none of them have been reported in the literature to differentiate between linear and angular loosening. This configuration showed the capacity of differentiating between linear and angular movement both in quasi-static and dynamic movement (Chapter 3, Figure 3.21). The resolution of the detection technique is far superior to the normal x-ray. As the x-rays can only confirm loosening when the implant is shifted 2 mm or more (Chapter 2, Table 2.5). At that point, the implant is considered to be grossly loose. This configuration provided the base for detection of an early sign of aseptic loosening without exposure to x-rays.

There were two major limitations encountered by the single sensor configuration. The first one was the tilt effect and there is no compensation for any starting non-parallel alignment between the sensor and magnet. For proper detection of the migration, the sensor and magnet need to be perfectly aligned with each other, any misalignment the error in the measurement is increased by 0.22-13 % depending upon the degree to which it is misaligned (Chapter 3, Table 3.3 and Appendix A.2) There was a need for further development/ improving the sensing algorithm and configuration design to compensate for any small tilting effect. As highlighted in the literature, positioning of the implant is essential for the effectiveness of TEA. During surgery, there is always a risk of malpositioning of the implant. This malpositioning can occur due to incorrect selection of the native flexion-extension axis [197] or by incorrect selection of implant stem size. To use the proposed detection technology the tilting/malpositioning of the implant needs to be addressed.

A second limitation is possible environmental effects. The system performance can be affected if it encounters an external magnetic field. The magnetic field strength decreases with increasing distance away from the magnet. However, as long as the external magnetic field variations are at an appropriate distance from the sensor, it will not cause any disturbances to the sensor measurement. To enhance the

system performance the configuration along with the detection algorithm was modified by introducing additional sensors and using different filtering techniques (Chapter 4).

7.1.2 Dual Sensor Single Magnet Configuration

One of the limitations of the single sensor configuration was the high noise content in the detected migration.

Various methods could be adopted to reduce the background noise of the magnetic sensor. The simplest one is by operating the system in a magnetically shielded room. This method limits its usage to the specific laboratory environment and also adds the additional cost of room development. Another method is by designing and fabricating a new type of magnetic sensor using multilayer thin films however they are hard to design and fabrication is expensive [198]. For reducing the background environmental noise, a dual sensor configuration was designed, in which one sensor detects the environmental magnetic field while another the field emitted for the magnet embedded in the restrictor. The subtraction method [168] was linked with the detection algorithm along with a wavelet filter to reduce the noise. In comparison to the previously mentioned method, this technique for reducing the background is less expansive and does not involve any changes to the sensor's design.

However, empirically the dual sensor configuration actually downgraded the system performance compared to the single sensor configuration (Chapter 4, Table 4.2). This downgrading was due to the difference in the magnetic field measured by the sensors. As both were not detecting a similar magnetic field. The dual sensor configuration introduces as much as 10 % noise along with increasing the error in detection by 30 %. For compensating for this, newer sensors configuration were designed in which all the sensors needed to experience the same magnetic field.

7.1.3 Quad Sensor Single Magnet Configuration

To improve the system performance and compensate for the tilting effect of the single sensor a multi sensor configuration (Quad sensor) was designed. In the quad sensor, 4 sensors were placed in a cross

formation and it was hypothesised that the data from the sensor which has common axes will be subtracted with each other to cancel out the background noise. The quad sensor demonstrated better performance in noise cancelation as all the sensors experienced the same magnetic field and after using the subtraction method followed by averaging the resultant field the SNR value was improved from 44 dB to 71 dB. Also, the RMS error was kept to a minimum of 0.020. This configuration also increased the resolution of the detection measurement to 0.15 mm along with compensating the tilting effect. The tilting effect was resolved by introducing sensor-specific criteria with which the system was able to detect angular movement up to 4 degrees implant shift. The system can detect beyond this range but after a shift of 4 degrees, the implant is easily detected by x-ray. In a single sensor configuration, there was an error in the detection measurement due to misalignment of the sensor and magnet that restricted the operating range of the system. In quad sensor configuration, sensor and magnet don't need to be aligned and the detection was observed without any introduction of additional error (Appendix A.2).

The quad sensor configuration achieved the resolution of detection migration equivalent to the RSA method. RSA is currently considered to be a gold standard for detecting aseptic loosening having a precision of 0.29 mm translation and 0.66 degree rotation. The main disadvantage of RSA is that it is limited to the laboratory conditions and the approach necessitates patients' being exposed to several radiographs each time. Furthermore, continuous implant monitoring is required to understand the implant performance and to determine what may be causing the implant to loose, which is not possible with the RSA method.

In comparison to the other detection technologies such as Eddy current sensors and capacitive sensors which are utilise to access implant migration. These detection mechanisms are highly sensitive, with a detection migration resolution of 0.15 mm from Eddy current sensor and 0.25 mm for the capacitive sensor [120, 127]. Both of these methods are affected by the misalignment along with the crosstalk effect when used to detect migration in more than one axis. Also, these techniques have not been used under

the clinical environment and the effect of the biometrical on the detected measurement still needs to be analysed.

Having all these advantages over the other diagnostics tool. The quad sensor configuration experience a few limitations as well, which need to be resolve in order to use it for clinical studies. Currently, the system is only able to detect the linear and angular movement of the stem without determining the orientation of the stem. This is essential for the initial calibration of the system. An improper position of the sensory component with respect to the magnet at the initial setup will introduce an error in the detection mechanism. Another limitation is the effect of an external magnetic field which can alter the magnetic field of the magnet and introduce error or false positives in the detection measurements. An introduction of another sensor separate from the quad can be used to detect any other source of magnetic field apart from the magnet's one. One of the implications for this limitation is that the patient may not be able to be imaged using MRI (Magnetic Resonance Imaging), which uses powerful magnetic fields of 2 Tesla to up to 7 Tesla for soft tissue imaging. Although MRI is not routine in orthopaedics, it can be an important diagnostic tool for tumour detection, cardiovascular investigations, and other soft tissue pathologies. The magnetic field strengths in these systems could cause the small permanent magnet to dislodge, which may cause injury. For health and safety that the patient will be exempt from using such systems, similar to patients who have implanted pacemakers or other implanted devices that are contraindicated for MRI [199].

Operating frequency is another factor that limits its usage. The normal gait of the human elbow is between 1 – 2 Hz the current detectable operating frequency is between 0.1-0.5 Hz. For the static movement detection the current operating range is suitable but to detect dynamic along with using it for other implant performance i.e. kinematics detection the operating frequency needs to be enhanced. Currently, the system signal transmission and powering are wired and further work is needed to develop a wireless power and data transmission which will be outlined later in this chapter.

Another major limitation of the detection technique is the movement of the restrictor rather than the stem itself. Which creates a false positive response by the detection system highlighting that the stem has moved.

Although the migration of the restrictor still identifies the weakening of the bonding between cement mantle and bone. There is a need for a mechanism to differentiate between cement restrictor migrations and stem migration[200]. Looking into the migration of the Hardinge restrictor, which is 6 times lower than the biodegradable restrictor [201] and in one of the studies the restrictor migration was 0.20 mm after 1 year of implantation[200]. This implies that restrictor migration is less likely, however, this is not certain and will need to be addressed under further development of the system.

7.1.4 Performance of the system under load testing environment

In order to further validate the loosening detection system in clinically relevant loading scenarios, a mechanical testing rig was designed and manufactured based on the ASTM F2028-17 guidelines set for the loosening behaviour of a shoulder glenoid implant under load controlled cyclic loading, and a contact compressive joint reaction force (Chapter 5). Arguably the glenoid shoulder implant has similar loading traits to the elbow: both experience 3 axis loading and translation in the joint, both experience compressive force from surrounding musculature, and both experience similar loading magnitudes. The humeral stem was designed based on the dimensions of the commercially available elbow implant stem, a quad sensor was embedded in the stem and was mounted onto the rig (Chapter 4, 5).

Three different fixation scenarios were mimicked, and the performance of the quad sensor was analysed at a joint reaction force of 600 N at 3000 cycles. Based on the measured displacements from the sensors, the system can differentiate between the different loosening conditions, along with detecting changes in loosening in the partially loosed condition (Chapter 5, Figure 5.18). The detection system correlates with the axial movement of the testing rig. As the axial displacement started to increase the system was also able to detect that change.

Early progression of loosening detected in the partially loose fixation was due to weak/thinner cement mantle between bone and implant after 3000 cycles. Observations post-testing showed bonding was detached at several areas of the bone (Chapter 5, Figure5.20). However, no detected changes were observed in the fully cemented condition after 3000 cycles. It was hoped that the system would detect changes in displacement as the fixation became loose. However, post-testing observations found no cement cracking or visible signs of loosening. This is likely due to the low number of cycles tested. At 3000 cycles, this most likely would be analogous to the first few days or weeks after surgery. In order to simulate mid-to-long-term testing regimes, the number of cycles should be increased. Although the cyclic loading behaviour of the elbow joint is not known, hip simulations are tested to 3 million to represent up to 5 years of loading. A review of the literature and critique of relevant biomechanical studies is needed to collate an estimate of loading cycles to estimate 5 years after surgery, which is typically the time elbow implants begin to loosen. Although only speculative, it may need to be tested to 100,000's cycles or more. A further study is needed to analyse the detection performance and stem failure at a higher number of loading cycles, detecting changes from fully fixed to completely loose. However, testing to 3000 cycles has given valuable insight into the different movement behaviours of different fixations, which confirms the hypothesis that fully loose, partially loose, and fully fixed systems can be differentiated, even at this early stage post-operatively.

Comparing to the studies conducted by Arami et al *(2018)* and Alshuhri et al *(2018)* [202, 203], where similar types of fixations were created (fully fixed, loose, grossly loose) by using vibrometry to detect the loosening. Both studies were able to differentiate the loosening based on the harmonics and power density spectrum of the vibrometry system but none of them were able to detect quantitatively the shifting of the implant along with the direction of the implant loosening progression.

7.1 .5 Implantable Septic Loosening Detection System

Incorporating the useful aspect of the sensor configuration to detect aseptic loosening, a new chemical sensor (hydrogel) was synthesised to detect the early sign of infection by detecting the local pH change

around the implant (Chapter 6). Combining the chemical sensor with the magnetic sensor gave the non-radiographic technique for detecting infection. Comparing to Arif. et al *(2019)* [138] pH detecting hydrogel, the chemical sensor synthesised in the study showed a similar pH response but no reversibility was detected. However, after the amalgamation of the magnetic sensor with the chemical sensor, the gel response along with its physical stability were weaken and required a new formulation for maintaining its mechanical stability and chemical response.

7.2 Outlook of the Thesis

Although this Ph.D. work successfully provided the foundation for using the magnetic sensing mechanism to detect early signs of loosening (septic and aseptic) without any radiographic exposure and minimal modification in the implant design, there are further aspects that merit investigation.

One particular aspect recommended for future work is further optimisation of the detection measurement, to detect initial orientation in multiple axes. The Jacobian matrix prediction error has merit for detecting the orientation of the system. A similar technique was used by Taylor et.al *(2019)* for detecting the orientation of multiple magnets [204]. Having these features will not only aid in the initial calibration of the system but will provide accurate information for properly placing the implant during implantation.

Another aspect worth analysing is to differentiate between implant migrations and cement restrictor migration. Machine learning techniques (supervised and unsupervised) will further improve the detection capability by training and validating the system with different migration of both components. Thus, the machine learning technique is recommended for further enhancing the detection measurements.

Although the mechanical testing rig provided the clinically relevant loading cycle, there is a need for modification in the design. Firstly, the holding clamps need to be redesigned so that they do not affect the deformity of the bone sample. Secondly, the rig is only providing the compressive joint reaction

force, to simulate the realistic patterns of elbow movement during various ADL, more actuators and force sensors are recommended. This will provide more degrees of freedom to the elbow movement and would be able to simulate the 3D elbow JRF more realistically.

For infection detection, a change in the formulation of the hydrogel is required which not only maintains its physical integrity but also can be adhered to the surface of the implant without a need of an external source.

Finally, for using this proposed method in cadaveric or in-vivo experiments, the measurement system needs to be integrated into the final Self-Powered Smart Implant (SPSI) highlighted in figure 7.1. Which will have a data fusion system and algorithm for both septic and aseptic loosening along with the supplementary electronic for wireless data transmission and remote/self-powering. For wireless power transmission, the system will follow the same protocol used for other implantable device such non-radiative capacitive coupling, inductive coupling and magnetic resonance coupling or the implant can be integrated with energy harvesting unit to generate its own power by using vibration energy or thermal energy [205-207].

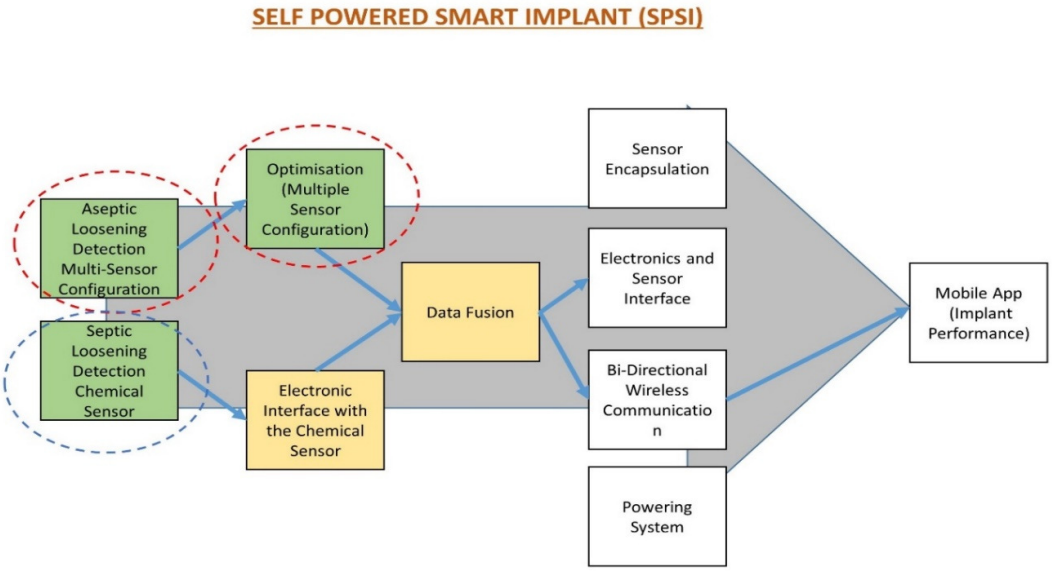

Figure 7. 1: Overview of the Self-Powered Smart Implant

This SPSI will not be limited to the elbow prostheses loosening detection but can be easily adapted to other major joint designs as well. Minor modifications of the sensor and magnet could simply meet the constraints of the other prostheses.

Reference:

1. Angst, F., et al., *Comprehensive assessment of clinical outcome and quality of life after total elbow arthroplasty.* Arthritis Care & Research, 2005. **53**(1): p. 73-82.
2. Filh, G.M. and M.V. Galvão, *POST-TRAUMATIC STIFFNESS OF THE ELBOW.* Revista Brasileira de Ortopedia, 2010. **45**(4): p. 347-354.
3. Murena, L., et al., *History and Evolution of Elbow Arthroplasties*, in *Elbow Arthroplasty : Current Techniques and Complications*, F. Castoldi, G. Giannicola, and R. Rotini, Editors. 2020, Springer International Publishing: Cham. p. 3-13.
4. Sanchez-Sotelo, J., *Elbow rheumatoid elbow: surgical treatment options.* Current reviews in musculoskeletal medicine, 2016. **9**(2): p. 224-231.
5. Fevang, B.T., et al., *Results after 562 total elbow replacements: a report from the Norwegian Arthroplasty Register.* J Shoulder Elbow Surg, 2009. **18**(3): p. 449-56.
6. Jenkins, P.J., et al., *Total elbow replacement: outcome of 1,146 arthroplasties from the Scottish Arthroplasty Project.* Acta Orthop, 2013. **84**(2): p. 119-23.
7. Gay, D.M., et al., *Indications and reoperation rates for total elbow arthroplasty: an analysis of trends in New York State.* J Bone Joint Surg Am, 2012. **94**(2): p. 110-7.
8. Key, M. *MEASUREMENT of RANGE of MOTION of the ELBOW and FOREARM*. 2016; Available from: https://musculoskeletalkey.com/measurement-of-range-of-motion-of-the-elbow-and-forearm/.
9. Stroyan, M. and K.E. Wilk, *The Functional Anatomy of the Elbow Complex.* Journal of Orthopaedic & Sports Physical Therapy, 1993. **17**(6): p. 279-288.
10. Snell, R.S., *Clinical anatomy for medical students*. 2004, Philadelphia: Lippincott Williams & Wilkins.
11. Standring, S., *Gray's anatomy : the anatomical basis of clinical practice*. 2016.
12. Zuccon, G., et al., *Design and Performance of an Elbow Assisting Mechanism.* Machines, 2020. **8**(4).
13. Kaufmann, R.A., J.L. D'Auria, and J. Schneppendahl, *Total Elbow Arthroplasty: Elbow Biomechanics and Failure.* J Hand Surg Am, 2019. **44**(8): p. 687-692.
14. Kincaid, B.L. and K.-N. An, *Elbow joint biomechanics for preclinical evaluation of total elbow prostheses.* Journal of Biomechanics, 2013. **46**(14): p. 2331-2341.
15. Austin Ramme, E.S. *Evaluation and Management of Elbow Osteoarthritis*. 2015; Available from: http://www.cancertherapyadvisor.com/shoulder-and-elbow/evaluation-and-management-of-elbow-osteoarthritis/article/627183/.
16. Nicol, A.C., Berme, N., Paul J.P. *biomechanical analysis of elbow joint function*. in *Proceeding of the IMechE Conference on Joint Replacement of the Upper Extremity. Institute of Mechanical Engineers*. 1977. London.
17. Halls, A.A. and A. Travill, *TRANSMISSION OF PRESSURES ACROSS THE ELBOW JOINT.* Anat Rec, 1964. **150**: p. 243-7.
18. Heidari, B., *Rheumatoid Arthritis: Early diagnosis and treatment outcomes.* Caspian Journal of Internal Medicine, 2011. **2**(1): p. 161-170.
19. Luokkala, T. and A.C. Watts, *Total elbow arthroplasty.* Bone & Joint 360, 2017. **6**(6): p. 2.
20. Mody, G.M. and P.M. Brooks, *Improving musculoskeletal health: Global issues.* Best Practice & Research Clinical Rheumatology, 2012. **26**(2): p. 237-249.
21. Loeser, R.F., et al., *Osteoarthritis: A Disease of the Joint as an Organ.* Arthritis and Rheumatism, 2012. **64**(6): p. 1697-1707.
22. Johnson, et al., *The Stanmore total elbow replacement for rheumatoid arthritis.* Journal of Bone & Joint Surgery, British Volume, 1984. **66-B**(5): p. 732.
23. Sanchez-Sotelo, J., *Total Elbow Arthroplasty.* The Open Orthopaedics Journal, 2011. **5**: p. 115-123.
24. Kudo, H., K. Iwano, and J. Nishino, *Cementless or hybrid total elbow arthroplasty with titanium-alloy implants: A study of interim clinical results and specific complications.* The Journal of Arthroplasty, 1994. **9**(3): p. 269-278.
25. Ebramzadeh, E., et al., *The cement mantle in total hip arthroplasty. Analysis of long-term radiographic results.* J Bone Joint Surg Am, 1994. **76**(1): p. 77-87.

26. Morrey, B.F., et al., *Total elbow arthroplasty. A five-year experience at the Mayo Clinic.* J Bone Joint Surg Am, 1981. **63**(7): p. 1050-63.
27. Saber-Samandari, S., C.C. Berndt, and K.A. Gross, *Selection of the implant and coating materials for optimized performance by means of nanoindentation.* Acta Biomaterialia, 2011. **7**(2): p. 874-881.
28. Prkić, A., et al., *Total elbow arthroplasty is moving forward: Review on past, present and future.* World Journal of Orthopedics, 2016. **7**(1): p. 44-49.
29. Soni, R.K. and M.E. Cavendish, *A review of the Liverpool elbow prosthesis from 1974 to 1982.* Journal of Bone & Joint Surgery, British Volume, 1984. **66-B**(2): p. 248.
30. Dee, R., *TOTAL REPLACEMENT ARTHROPLASTY OF THE ELBOW FOR RHEUMATOID ARTHRITIS.* Journal of Bone & Joint Surgery, British Volume, 1972. **54-B**(1): p. 88.
31. de Vos, M., *Total elbow arthroplasty. A historical and contemporary perspective*. 2016, [Sl: sn].
32. Malone, A.A., A.J.N. Taylor, and I.S. Fyfe, *Successful outcome of the Souter-Strathclyde elbow arthroplasty.* Journal of Shoulder and Elbow Surgery, 2004. **13**(5): p. 548-554.
33. Aldridge, J.M., et al., *Total elbow arthroplasty with the Coonrad/Coonrad-Morrey prosthesis.* Journal of Bone & Joint Surgery, British Volume, 2006. **88-B**(4): p. 509.
34. Petscavage, J.M., A.S. Ha, and F.S. Chew, *Radiologic Review of Total Elbow, Radial Head, and Capitellar Resurfacing Arthroplasty.* RadioGraphics, 2011. **32**(1): p. 129-149.
35. Gschwend, N., N.H. Scheier, and A.R. Baehler, *Long-term results of the GSB III elbow arthroplasty.* Journal of Bone & Joint Surgery, British Volume, 1999. **81-B**(6): p. 1005.
36. Cesar, M., et al., *GSB III total elbow replacement in rheumatoid arthritis.* Journal of Bone & Joint Surgery, British Volume, 2007. **89-B**(3): p. 330.
37. Rydholm, U., et al., *Surface replacement of the elbow in rheumatoid arthritis. Early results with the Wadsworth prosthesis.* Journal of Bone & Joint Surgery, British Volume, 1984. **66-B**(5): p. 737.
38. Ljung, P., L. Lidgren, and U. Rydholm, *Failure of the Wadsworth elbow: Nineteen cases of rheumatoid arthritis followed for 5 years.* Acta Orthopaedica Scandinavica, 1989. **60**(3): p. 254-257.
39. van der Lugt, J.C.T. and P.M. Rozing, *Systematic review of primary total elbow prostheses used for the rheumatoid elbow.* Clinical Rheumatology, 2004. **23**(4): p. 291-298.
40. Mori, T., et al., *Kudo type-5 total elbow arthroplasty in mutilating rheumatoid arthritis.* Journal of Bone & Joint Surgery, British Volume, 2006. **88-B**(7): p. 920.
41. Cusick, M.C., et al., *Accuracy and Reliability of the Mayo Elbow Performance Score.* The Journal of Hand Surgery, 2014. **39**(6): p. 1146-1150.
42. Singh, J.A. and R. Ramachandaran, *Sex Differences in Characteristics, Utilization and Outcomes of patient undergoing Total Elbow Arthroplasty: A Study of the U.S. Nationwide Inpatient Sample.* Clinical rheumatology, 2016. **35**(3): p. 723-731.
43. Day, J.S., et al., *Prevalence and projections of total shoulder and elbow arthroplasty in the United States to 2015.* J Shoulder Elbow Surg, 2010. **19**(8): p. 1115-20.
44. Castoldi, F., G. Giannicola, and R. Rotini, *Elbow Arthroplasty: Current Techniques and Complications*. 2020: Springer.
45. Day, J.S., et al., *Prevalence and projections of total shoulder and elbow arthroplasty in the United States to 2015.* Journal of Shoulder and Elbow Surgery, 2010. **19**(8): p. 1115-1120.
46. Singh, J.A., et al., *Sex and surgical outcomes and mortality after primary total knee arthroplasty: a risk-adjusted analysis.* Arthritis care & research, 2013. **65**(7): p. 1095-1102.
47. Zhou, H., et al., *Total Elbow Arthroplasty in the United States: Evaluation of Cost, Patient Demographics, and Complication Rates.* Orthop Rev (Pavia), 2016. **8**(1): p. 6113.
48. Giannicola, G., et al., *Change in Quality of Life and Cost/Utility Analysis in Open Stage-related Surgical Treatment of Elbow Stiffness.* Orthopedics, 2013. **36**(7): p. e923-e930.
49. Krukhaug, Y., et al., *A survivorship study of 838 total elbow replacements: a report from the Norwegian Arthroplasty Register 1994-2016.* J Shoulder Elbow Surg, 2018. **27**(2): p. 260-269.
50. Hendricks, T.J., A.C.M. Chong, and R.P. Cusick, *The Cost of Routine Follow-Up in Total Joint Arthroplasty and the Influence of These Visits on Treatment Plans.* Kans J Med, 2018. **11**(3): p. 59-66.
51. Voloshin, I., et al., *Complications of total elbow replacement: A systematic review.* Journal of Shoulder and Elbow Surgery, 2011. **20**(1): p. 158-168.

52. Welsink, C.L., et al., *Total Elbow Arthroplasty: A Systematic Review.* JBJS Reviews, 2017. **5**(7): p. e4-e4.
53. Klug, A., et al., *Trends in total elbow arthroplasty: a nationwide analysis in Germany from 2005 to 2014.* International Orthopaedics, 2018. **42**(4): p. 883-889.
54. Luokkala, T. and W.A. C., *Total elbow arthroplasty.* Bone & Joint 360, 2017. **6**(6): p. 2-10.
55. Gay, D.M., et al., *Indications and Reoperation Rates for Total Elbow Arthroplasty: An Analysis of Trends in New York State.* JBJS, 2012. **94**(2): p. 110-117.
56. Woolf, A.D. and B. Pfleger, *Burden of major musculoskeletal conditions.* Bulletin of the World Health Organization, 2003. **81**(9): p. 646-656.
57. LROI, *Netherland-LROI-Annual Report.* 2018.
58. UK_NJR, *UK_NJR 15th Annual Report*. 2018.
59. Portuguese Arthroplasty Register, *1st Annual Report, June 2009 - May 2010*. 2010.
60. New Zealand Orthopaedic Association, *New Zealand Orthopaedic Association ANNUAL REPORT 2016 – 2017*. 2017.
61. NorwegianNationalAdvisoryUnit onArthroplasty andHipFractures, *Report June 2018*. 2018.
62. Sanchez-Sotelo, J., *Primary elbow arthroplasty: problems and solutions.* Shoulder & elbow, 2017. **9**(1): p. 61-70.
63. Gschwend, N., B.R. Simmen, and Z. Matejovsky, *Late complications in elbow arthroplasty.* Journal of Shoulder and Elbow Surgery, 1996. **5**(2, Part 1): p. 86-96.
64. Little, C.P., A.J. Graham, and A.J. Carr, *Total elbow arthroplasty.* Journal of Bone & Joint Surgery, British Volume, 2005. **87-B**(4): p. 437.
65. Prkic, A., et al., *Why does total elbow arthroplasty fail today? A systematic review of recent literature.* Archives of Orthopaedic and Trauma Surgery, 2017. **137**(6): p. 761-769.
66. Joon Park, R.S.L., *Biomaterials: An Introduction*. 2007, New York, NY, USA: Springer Science,Business Media.
67. Ratner, B.D., et al., *Biomaterials Science: An Introduction to Materials in Medicine*. 1997: Elsevier Science.
68. Arora, M., et al., *Polymethylmethacrylate bone cements and additives: A review of the literature.* World journal of orthopedics, 2013. **4**(2): p. 67-74.
69. McKellop, H.A., et al., *The origin of submicron polyethylene wear debris in total hip arthroplasty.* Clin Orthop Relat Res, 1995(311): p. 3-20.
70. Goldberg, S.H., et al., *Modes of wear after semiconstrained total elbow arthroplasty.* J Bone Joint Surg Am, 2008. **90**(3): p. 609-19.
71. Lee, B.P., R.A. Adams, and B.F. Morrey, *Polyethylene Wear After Total Elbow Arthroplasty.* JBJS, 2005. **87**(5): p. 1080-1087.
72. Kwaees, T.A., et al., *Cementation technique for elbow arthroplasty; an international survey.* Journal of orthopaedics, 2019. **16**(6): p. 459-462.
73. Emara, A.K., et al., *Femoral Stem Cementation in Hip Arthroplasty: The Know-How of a "Lost" Art.* Current Reviews in Musculoskeletal Medicine, 2021. **14**(1): p. 47-59.
74. Bain, G.I., et al., *Management of Mason type-III radial head fractures with a titanium prosthesis, ligament repair, and early mobilization. Surgical technique.* J Bone Joint Surg Am, 2005. **87 Suppl 1**(Pt 1): p. 136-47.
75. Waanders, D., et al., *The mechanical effects of different levels of cement penetration at the cement–bone interface.* Journal of Biomechanics, 2010. **43**(6): p. 1167-1175.
76. D, S., *Revision total elbow arthroplasty in the presence of bone deficiency* in *Operative elbow surgery*. 2012, Expert Consult. p. 695–716.
77. Herren, D.B., et al., *Modeling and Finite Element Analysis of a New Revision Implant for the Elbow.* Clinical Orthopaedics and Related Research®, 2004. **420**: p. 292-297.
78. Kodama, A., T. Mizuseki, and N. Adachi, *Kudo type-5 total elbow arthroplasty for patients with rheumatoid arthritis.* Bone & Joint Journal, 2017. **99-B**(6): p. 818.
79. King, G.J.W., et al., *In vitro stability of an unconstrained total elbow prosthesis: Influence of axial loading and joint flexion angle.* The Journal of Arthroplasty, 1993. **8**(3): p. 291-298.

80. Sjöden, G.O.J., A. Lundberg, and G.A. Blomgren, *Late results of the Souter-Strathclyde total elbow prosthesis in rheumatoid arthritis 6/19 implants loose after 5 years.* Acta Orthopaedica Scandinavica, 1995. **66**(5): p. 391-394.
81. Herren, D.B., S.W. O'Driscoll, and K.-N. An, *Role of collateral ligaments in the GSB-linked total elbow prosthesis.* Journal of Shoulder and Elbow Surgery, 2001. **10**(3): p. 260-264.
82. Kwak, J.-M., K.-H. Koh, and I.-H. Jeon, *Total Elbow Arthroplasty: Clinical Outcomes, Complications, and Revision Surgery.* Clinics in orthopedic surgery, 2019. **11**(4): p. 369-379.
83. Futai, K., et al., *In vivo three-dimensional kinematics of total elbow arthroplasty using fluoroscopic imaging.* International Orthopaedics, 2010. **34**(6): p. 847-854.
84. Al Mohajer, M. and R.O. Darouiche, *The expanding horizon of prosthetic joint infections.* Journal of Applied Biomaterials & Functional Materials, 2014. **12**(1): p. 1-12.
85. Prasad, G. and A.A. Ali, *An overview and challenges of revision total elbow arthroplasty.* Orthopaedics and Trauma, 2020. **34**(4): p. 235-243.
86. Widmer, A.F., *New Developments in Diagnosis and Treatment of Infection in Orthopedic Implants.* Clinical Infectious Diseases, 2001. **33**(Supplement_2): p. S94-S106.
87. Zimmerli , W., A. Trampuz , and P.E. Ochsner *Prosthetic-Joint Infections.* New England Journal of Medicine, 2004. **351**(16): p. 1645-1654.
88. Osmon, D.R., et al., *Diagnosis and Management of Prosthetic Joint Infection: Clinical Practice Guidelines by the Infectious Diseases Society of Americaa.* Clinical Infectious Diseases, 2013. **56**(1): p. e1-e25.
89. Legout, L. and E. Senneville, *Periprosthetic Joint Infections: Clinical and Bench Research.* The Scientific World Journal, 2013. **2013**: p. 549091.
90. Zimmerli, W. and P. Sendi, *Orthopaedic biofilm infections.* APMIS, 2017. **125**(4): p. 353-364.
91. Brady, R.A., et al., *Infections of Orthopaedic Implants and Devices*. Springer Berlin Heidelberg: Berlin, Heidelberg. p. 1-41.
92. Thomas, B., *The role of bacterial biofilms in chronic infections.* APMIS, 2013. **121**(s136): p. 1-58.
93. Marić, S. and J. Vraneš, *Characteristics and significance of microbial biofilm formation.* Periodicum Bilogorum, 2007. **109**: p. 115-121.
94. Gbejuade, H.O., A.M. Lovering, and J.C. Webb, *The role of microbial biofilms in prosthetic joint infections.* Acta Orthopaedica, 2015. **86**(2): p. 147-158.
95. Eid, A., *Infected orthopedic implants.* The Egyptian Orthopaedic Journal, 2016. **51**(3): p. 187-198.
96. Unosson, E., *Antibacterial strategies for titanium biomaterials*. 2015, Acta Universitatis Upsaliensis.
97. Apostu, D., et al., *Current methods of preventing aseptic loosening and improving osseointegration of titanium implants in cementless total hip arthroplasty: a review.* The Journal of international medical research, 2018. **46**(6): p. 2104-2119.
98. Paterson, M., P. Fulford, and R. Denham, *Loosening of the femoral component after total hip replacement. The thin black line and the sinking hip.* Journal of Bone & Joint Surgery, British Volume, 1986. **68-B**(3): p. 392.
99. Morrey, B.F., R.A. Adams, and R.S. Bryan, *Total replacement for post-traumatic arthritis of the elbow.* Journal of Bone & Joint Surgery, British Volume, 1991. **73-B**(4): p. 607.
100. Borjali, A., et al., *Detecting mechanical loosening of total hip replacement implant from plain radiograph using deep convolutional neural network.* arXiv preprint arXiv:1912.00943, 2019.
101. T., v.d.L.J.C., et al., *Migration of the humeral component of the Souter-Strathclyde elbow prosthesis.* The Journal of Bone and Joint Surgery. British volume, 2010. **92-B**(2): p. 235-241.
102. Valstar, E.R., E.H. Garling, and P.M. Rozing, *Micromotion of the Souter-Strathclyde total elbow prosthesis in patients with rheumatoid arthritis.* Acta Orthopaedica Scandinavica, 2002. **73**(3): p. 264-272.
103. Ten Brinke, B., et al., *The accuracy and precision of radiostereometric analysis in upper limb arthroplasty.* Acta orthopaedica, 2017. **88**(3): p. 320-325.
104. Newberg, A.H. and S.M. Wetzner, *Digital subtraction arthrography.* Radiology, 1985. **154**(1): p. 238-239.

105. Ovesen, O., et al., *The diagnostic value of digital subtraction arthrography and radionuclide bone scan in revision hip arthroplasty1 1No benefits or funds were received in support of this study.* The Journal of Arthroplasty, 2003. **18**(6): p. 735-740.
106. Temmerman, O.P., et al., *Accuracy of diagnostic imaging techniques in the diagnosis of aseptic loosening of the femoral component of a hip prosthesis: a meta-analysis.* J Bone Joint Surg Br, 2005. **87**(6): p. 781-5.
107. Apple, J.S., et al., *Digital subtraction arthrography of the prosthetic hip.* Southern medical journal, 1986. **79**(7): p. 808-810.
108. Love, C., et al., *Radionuclide Bone Imaging: An Illustrative Review.* RadioGraphics, 2003. **23**(2): p. 341-358.
109. Mandalia, V., et al., *Evaluation of patients with a painful total knee replacement.* Journal of Bone & Joint Surgery, British Volume, 2008. **90-B**(3): p. 265.
110. Talbot, B.S. and E.P. Weinberg, *MR Imaging with Metal-suppression Sequences for Evaluation of Total Joint Arthroplasty.* RadioGraphics, 2016. **36**(1): p. 209-225.
111. Lohmann, C.H., et al., *Imaging in peri-prosthetic assessment: an orthopaedic perspective.* EFORT Open Reviews, 2017. **2**(5): p. 117-125.
112. Mushtaq, N., et al., *Radiological Imaging Evaluation of the Failing Total Hip Replacement.* Frontiers in surgery, 2019. **6**: p. 35-35.
113. Tam, H.H., et al., *SPECT-CT in total hip arthroplasty.* Clinical Radiology, 2014. **69**(1): p. 82-95.
114. Li, P.L.S., N.B. Jones, and P.J. Gregg, *Vibration analysis in the detection of total hip prosthetic loosening.* Medical Engineering & Physics, 1996. **18**(7): p. 596-600.
115. Georgiou, A.P. and J.L. Cunningham, *Accurate diagnosis of hip prosthesis loosening using a vibrational technique.* Clinical Biomechanics, 2001. **16**(4): p. 315-323.
116. Ruther, C., et al. *A New Approach for Diagnostic Investigation of Total Hip Replacement Loosening*. in *Biomedical Engineering Systems and Technologies*. 2013. Berlin, Heidelberg: Springer Berlin Heidelberg.
117. Unger, A.C., et al., *Acoustic monitoring (RFM) of total hip arthroplasty - Results of a cadaver study.* European journal of medical research, 2009. **14**(6): p. 264-271.
118. Cachão, J.H., et al., *Altering the Course of Technologies to Monitor Loosening States of Endoprosthetic Implants.* Sensors, 2020. **20**(1).
119. Davies, J.P., M.K. Tse, and W.H. Harris, *In vitro evaluation of bonding of the cement-metal interface of a total hip femoral component using ultrasound.* J Orthop Res, 1995. **13**(3): p. 335-8.
120. Khokle, R.P., K.P. Esselle, and D.J. Bokor, *Design, Modeling, and Evaluation of the Eddy Current Sensor Deeply Implanted in the Human Body.* Sensors (Basel, Switzerland), 2018. **18**(11): p. 3888.
121. Khokle, R.P., et al., *Eddy Current–Tunneling Magneto-Resistive Sensor for Micromotion Detection of a Tibial Orthopaedic Implant.* IEEE Sensors Journal, 2019. **19**(4): p. 1285-1292.
122. Arpaia, P., F. Clemente, and A. Zanesco, *Low-Invasive Diagnosis of Metallic Prosthesis Osseointegration by Electrical Impedance Spectroscopy.* IEEE Transactions on Instrumentation and Measurement, 2007. **56**(3): p. 784-789.
123. Cachão, J.H., et al., *Altering the Course of Technologies to Monitor Loosening States of Endoprosthetic Implants.* Sensors, 2020. **20**(1): p. 104.
124. G. Hamid et al. *Non-Invasive Failure Diagnosis of Aseptic Loosening via Piezoresistive Bone Cement and Electrical Impedance Tomography*. 2020.
125. Burton, A.R., P. Sun, and J.P. Lynch, *Bio-compatible wireless inductive thin-film strain sensor for monitoring the growth and strain response of bone in osseointegrated prostheses.* Structural Health Monitoring, 2019: p. 1475921719831452.
126. McGilvray, K.C., et al., *Implantable microelectromechanical sensors for diagnostic monitoring and post-surgical prediction of bone fracture healing.* J Orthop Res, 2015. **33**(10): p. 1439-46.
127. Soares dos Santos, M.P., et al., *Towards an effective sensing technology to monitor micro-scale interface loosening of bioelectronic implants.* Scientific Reports, 2021. **11**(1): p. 3449.
128. Arvieux, C. and H. Common, *New diagnostic tools for prosthetic joint infection.* Orthopaedics & Traumatology: Surgery & Research, 2019. **105**(1, Supplement): p. S23-S30.

129. Cyteval, C. and A. Bourdon, *Imaging orthopedic implant infections.* Diagnostic and Interventional Imaging, 2012. **93**(6): p. 547-557.
130. Saeed, K., *Diagnostics in prosthetic joint infections.* Journal of Antimicrobial Chemotherapy, 2014. **69**(suppl_1): p. i11-i19.
131. Springer, B.D., *The Diagnosis of Periprosthetic Joint Infection.* The Journal of Arthroplasty, 2015. **30**(6): p. 908-911.
132. Greidanus, N.V., et al., *Use of Erythrocyte Sedimentation Rate and C-Reactive Protein Level to Diagnose Infection Before Revision Total Knee Arthroplasty: A Prospective Evaluation.* JBJS, 2007. **89**(7): p. 1409-1416.
133. Parham, S. and Z. Werner, *Diagnosis of Periprosthetic Joint Infections in Clinical Practice.* The International Journal of Artificial Organs, 2012. **35**(10): p. 913-922.
134. Trampuz, A., et al., *Advances in the laboratory diagnosis of prosthetic joint infection.* Reviews in Medical Microbiology, 2003. **14**(1): p. 1-14.
135. Andrej, T., et al., *Microcalorimetry: a novel method for detection of microbial contamination in platelet products.* Transfusion, 2007. **47**(9): p. 1643-1650.
136. Trampuz, A., et al., *Sonication of Removed Hip and Knee Prostheses for Diagnosis of Infection.* New England Journal of Medicine, 2007. **357**(7): p. 654-663.
137. Ehrlich, G.D., et al., *Engineering Approaches for the Detection and Control of Orthopaedic Biofilm Infections.* Clinical orthopaedics and related research, 2005(437): p. 59-66.
138. Arifuzzaman, M., et al., *An implanted pH sensor read using radiography.* Analyst, 2019. **144**(9): p. 2984-2993.
139. Karipott, S.S., et al., *An Embedded Wireless Temperature Sensor for Orthopedic Implants.* IEEE Sensors Journal, 2018. **18**(3): p. 1265-1272.
140. Khan, M.M.K., et al., *A New Diagnostic Technique to Detect Early Migration of Joint Prostheses.* IEEE Access, 2021. **9**: p. 7021-7032.
141. Fevang, B.-T.S., et al., *Results after 562 total elbow replacements: A report from the Norwegian Arthroplasty Register.* Journal of Shoulder and Elbow Surgery, 2009. **18**(3): p. 449-456.
142. Barnsley, L. and L. Barnsley, *Detection of aseptic loosening in total knee replacements: a systematic review and meta-analysis.* Skeletal Radiol, 2019. **48**(10): p. 1565-1572.
143. Bergmann, G., F. Graichen, and A. Rohlmann, *Hip joint loading during walking and running, measured in two patients.* Journal of Biomechanics, 1993. **26**(8): p. 969-990.
144. Arami, A., et al., *Instrumented Knee Prosthesis for Force and Kinematics Measurements.* IEEE Transactions on Automation Science and Engineering, 2013. **10**(3): p. 615-624.
145. Khan, M.A., M. Serpelloni, and E. Sardini. *Optimized power harvesting module for an autonomous sensor system implanted in a total knee prosthesis*. in *2017 IEEE International Instrumentation and Measurement Technology Conference (I2MTC)*. 2017.
146. Fleming, A.J., *A review of nanometer resolution position sensors: Operation and performance.* Sensors and Actuators A: Physical, 2013. **190**: p. 106-126.
147. Preethichandra, D.M.G. and K. Shida. *A simple interface circuit to measure very small capacitance changes in capacitive sensors*. in *Proceedings of the 17th IEEE Instrumentation and Measurement Technology Conference [Cat. No. 00CH37066]*. 2000.
148. Du, W.Y., *Resistive, Capacitive, Inductive, and Magnetic Sensor Technologies* ed. 1. 2014.
149. Wang, T., C. Kang, and G. Chai, *Low-Frequency Noise Evaluation on a Commercial Magnetoimpedance Sensor at Submillihertz Frequencies for Space Magnetic Field Detection.* Sensors, 2019. **19**(22): p. 4888.
150. Lenz, J. and S. Edelstein, *Magnetic sensors and their applications.* IEEE Sensors Journal, 2006. **6**(3): p. 631-649.
151. C., S., et al., *Modern integrated silicon Hall sensors.* Sensor Review, 1998. **18**(4): p. 252-257.
152. Hall, E.H., *On a New Action of the Magnet on Electric Currents.* American Journal of Mathematics, 1879. **2**(3): p. 287-292.
153. Hsiao, H.-S., et al., *Characteristics of magnetic sensor with assembly errors in a rotary recording system.* Microsystem Technologies, 2020. **26**(1): p. 89-94.
154. Ripka, P. and M. Janosek, *Advances in Magnetic Field Sensors.* IEEE Sensors Journal, 2010. **10**(6): p. 1108-1116.

155. Arami, A., J. Miehlbradt, and K. Aminian, *Accurate internal–external rotation measurement in total knee prostheses: A magnetic solution.* Journal of Biomechanics, 2012. **45**(11): p. 2023-2027.
156. Cheung, E.V. and S.W. O'Driscoll, *Total elbow prosthesis loosening caused by ulnar component pistoning.* J Bone Joint Surg Am, 2007. **89**(6): p. 1269-74.
157. Kiran, M., A. Jariwala, and C.A. Wigderowitz, *Evaluation of the Cementation Index as a Predictor of Failure in Coonrad-Morrey Total Elbow Arthroplasty.* Advances in Orthopedic Surgery, 2014. **2014**: p. 243823.
158. Cil, A., et al., *Revision of the humeral component for aseptic loosening in arthroplasty of the shoulder.* The Journal of Bone and Joint Surgery. British volume, 2009. **91-B**(1): p. 75-81.
159. Aziz, S.M., M. Grcic, and T. Vaithianathan, *A Real-Time Tracking System for an Endoscopic Capsule using Multiple Magnetic Sensors*, in *Smart Sensors and Sensing Technology*, S.C. Mukhopadhyay and G.S. Gupta, Editors. 2008, Springer Berlin Heidelberg: Berlin, Heidelberg. p. 201-218.
160. Schott, C., et al., *Novel Magnetic Displacement Sensors.*
161. Arora, R., *I2C Bus Pullup Resistor Calculation*. 2015.
162. Camacho, J.M. and V. Sosa, *Alternative method to calculate the magnetic field of permanent magnets with azimuthal symmetry.* Revista mexicana de física E, 2013. **59**: p. 8-17.
163. Hu, C., M.Q.H. Meng, and M. Mandal, *A Linear Algorithm for Tracing Magnet Position and Orientation by Using Three-Axis Magnetic Sensors.* IEEE Transactions on Magnetics, 2007. **43**(12): p. 4096-4101.
164. Acharya, D., et al., *Application of adaptive Savitzky–Golay filter for EEG signal processing.* Perspectives in Science, 2016. **8**: p. 677-679.
165. Huang, H., S. Hu, and Y. Sun, *A Discrete Curvature Estimation Based Low-Distortion Adaptive Savitzky–Golay Filter for ECG Denoising.* Sensors, 2019. **19**(7): p. 1617.
166. Niculescu, M., et al., *Evolution of Cementation Techniques and Bone Cements in Hip Arthroplasty*, in *Handbook of Bioceramics and Biocomposites*, I.V. Antoniac, Editor. 2016, Springer International Publishing: Cham. p. 859-899.
167. Zimmer Biomet, *Comprehensive Segmental Revision System*. 2016. p. 3-4.
168. Wöltgens, P.J.M. and R.H. Koch, *Magnetic background noise cancellation in real-world environments.* Review of Scientific Instruments, 2000. **71**(3): p. 1529-1533.
169. Cai, C. and P.d.B. Harrington, *Different Discrete Wavelet Transforms Applied to Denoising Analytical Data.* Journal of Chemical Information and Computer Sciences, 1998. **38**(6): p. 1161-1170.
170. Srivastava, M., C.L. Anderson, and J.H. Freed, *A New Wavelet Denoising Method for Selecting Decomposition Levels and Noise Thresholds.* IEEE Access, 2016. **4**: p. 3862-3877.
171. March, L., et al., *Burden of disability due to musculoskeletal (MSK) disorders.* Best Practice & Research Clinical Rheumatology, 2014. **28**(3): p. 353-366.
172. Hoy, D.G., et al., *The global burden of musculoskeletal conditions for 2010: an overview of methods.* Annals of the Rheumatic Diseases, 2014. **73**(6): p. 982.
173. Palazzo, C., et al., *Risk factors and burden of osteoarthritis.* Annals of Physical and Rehabilitation Medicine, 2016. **59**(3): p. 134-138.
174. Maggs, J. and M. Wilson, *The Relative Merits of Cemented and Uncemented Prostheses in Total Hip Arthroplasty.* Indian J Orthop, 2017. **51**(4): p. 377-385.
175. Gao, X., M. Fraulob, and G. Haïat, *Biomechanical behaviours of the bone-implant interface: a review.* Journal of the Royal Society, Interface, 2019. **16**(156): p. 20190259-20190259.
176. Abdelgaied, A., J. Fisher, and L.M. Jennings, *A comprehensive combined experimental and computational framework for pre-clinical wear simulation of total knee replacements.* Journal of the Mechanical Behavior of Biomedical Materials, 2018. **78**: p. 282-291.
177. Ali, M., et al., *Influence of hip joint simulator design and mechanics on the wear and creep of metal-on-polyethylene bearings.* Proceedings of the Institution of Mechanical Engineers, Part H: Journal of Engineering in Medicine, 2016. **230**(5): p. 389-397.
178. Kiene, J., et al., *A physiological dynamic testing machine for the elbow joint.* The open orthopaedics journal, 2013. **7**: p. 78-85.
179. King, G.J., et al., *Motion and laxity of the capitellocondylar total elbow prosthesis.* J Bone Joint Surg Am, 1994. **76**(7): p. 1000-8.

180. Dunning, C.E., et al., *Simulated active control produces repeatable motion pathways of the elbow in an in vitro testing system.* J Biomech, 2001. **34**(8): p. 1039-48.
181. F2028., A.S., *Standard test methods for the dynamic evaluation of glenoid loosening or disassociation.* 2004, ASTM International: West Conshohocken.
182. Hetaimish, B.M., *Sawbones laboratory in orthopedic surgical training.* Saudi Med J, 2016. **37**(4): p. 348-53.
183. Waanders, D., et al., *The effect of cement creep and cement fatigue damage on the micromechanics of the cement–bone interface.* Journal of Biomechanics, 2010. **43**(15): p. 3028-3034.
184. Alijanipour, P. and J. Parvizi, *Infection post-total knee replacement: current concepts.* Current reviews in musculoskeletal medicine, 2014. **7**(2): p. 96-102.
185. Wagner, E.R., et al., *Comparison of the hospital costs for two-stage reimplantation for deep infection, single-stage revision and primary total elbow arthroplasty.* Shoulder & Elbow, 2017. **9**(4): p. 279-284.
186. Neut, D., et al., *Detection of Biomaterial-Associated Infections in Orthopaedic Joint Implants.* Clinical Orthopaedics and Related Research®, 2003. **413**: p. 261-268.
187. Grant, S.S. and D.T. Hung, *Persistent bacterial infections, antibiotic tolerance, and the oxidative stress response.* Virulence, 2013. **4**(4): p. 273-283.
188. B., F., et al., *The value of synovial biopsy, joint aspiration and C-reactive protein in the diagnosis of late peri-prosthetic infection of total knee replacements.* The Journal of Bone and Joint Surgery. British volume, 2008. **90-B**(7): p. 874-878.
189. Chanmugam, A., et al., *Relative Temperature Maximum in Wound Infection and Inflammation as Compared with a Control Subject Using Long-Wave Infrared Thermography.* Advances in Skin & Wound Care, 2017. **30**(9): p. 406-414.
190. Wang, F., et al., *X-Ray Excited Luminescence Chemical Imaging of Bacterial Growth on Surfaces Implanted in Tissue.* Advanced healthcare materials, 2015. **4**(6): p. 903-910.
191. Ahn Jin, K., *Chapter 27 - Acidosis*, in *Comprehensive Pediatric Hospital Medicine*, L.B. Zaoutis and V.W. Chiang, Editors. 2007, Mosby: Philadelphia. p. 125-132.
192. Ahmed, E.M., *Hydrogel: Preparation, characterization, and applications: A review.* Journal of Advanced Research, 2015. **6**(2): p. 105-121.
193. Halacheva, S.S., et al., *Injectable Biocompatible and Biodegradable pH-Responsive Hollow Particle Gels Containing Poly(acrylic acid): The Effect of Copolymer Composition on Gel Properties.* Biomacromolecules, 2014. **15**(5): p. 1814-1827.
194. Shi, H., Y. Wang, and J. Lin, *Optimized Design and Calibration of the Triaxis Induction Magnetometer with Crosstalk and Nonorthogonality Compensation.* Journal of Sensors, 2016. **2016**: p. 1810636.
195. Wang, H., et al. *A low-cost, high-performance, soft tri-axis tactile sensor based on eddy-current effect*. in *2017 IEEE SENSORS*. 2017.
196. Pyo, S., J. Choi, and J. Kim, *Flexible, Transparent, Sensitive, and Crosstalk-Free Capacitive Tactile Sensor Array Based on Graphene Electrodes and Air Dielectric.* Advanced Electronic Materials, 2018. **4**(1): p. 1700427.
197. Colin, P.M., et al. *Implant alignment in total elbow arthroplasty: conventional vs. navigated techniques*. in *Proc.SPIE*. 2009.
198. Liou, S., et al., *Picotesla Magnetic Sensors for Low-Frequency Applications.* IEEE Transactions on Magnetics, 2011. **47**: p. 3740-3743.
199. Dill, T., *Contraindications to magnetic resonance imaging.* Heart, 2008. **94**(7): p. 943.
200. Alfaro-Adrián, J., H.S. Gill, and D.W. Murray, *Cement migration after THR. A comparison of charnley elite and exeter femoral stems using RSA.* J Bone Joint Surg Br, 1999. **81**(1): p. 130-4.
201. Wembridge, K.R. and A.J. Hamer, *A Prospective Comparison of Cement Restrictor Migration in Primary Total Hip Arthroplasty.* The Journal of Arthroplasty, 2006. **21**(1): p. 92-96.
202. Arami, A., et al., *Knee Implant Loosening Detection: A Vibration Analysis Investigation.* Annals of biomedical engineering, 2018. **46**(1): p. 97-107.
203. Alshuhri, A.A., et al., *Non-invasive vibrometry-based diagnostic detection of acetabular cup loosening in total hip replacement (THR).* Medical Engineering & Physics, 2017. **48**: p. 188-195.
204. Taylor, C.R., H.G. Abramson, and H.M. Herr, *Low-Latency Tracking of Multiple Permanent Magnets.* IEEE Sensors Journal, 2019. **19**(23): p. 11458-11468.

205. Ledet, E.H., et al., *Smart implants in orthopedic surgery, improving patient outcomes: a review.* Innovation and entrepreneurship in health, 2018. **5**: p. 41-51.
206. Khan, S.R., et al., *Wireless Power Transfer Techniques for Implantable Medical Devices: A Review.* Sensors (Basel, Switzerland), 2020. **20**(12): p. 3487.
207. Hannan, M.A., et al., *Energy harvesting for the implantable biomedical devices: issues and challenges.* BioMedical Engineering OnLine, 2014. **13**(1): p. 79.

Appendices

Appendix 1: Detection Algorithm Performace at Different Frequency

The stem was moved 1 mm dynamically in the y-axis keeping the other two axes constant at three different frequencies (0.5 Hz, 1 Hz, and 2 Hz). Figure A.1 highlights that the system detected accurately the movement when operated in 0.5 Hz at 1 Hz the there was detection with higher error while at 2 Hz the system was unable to detect.

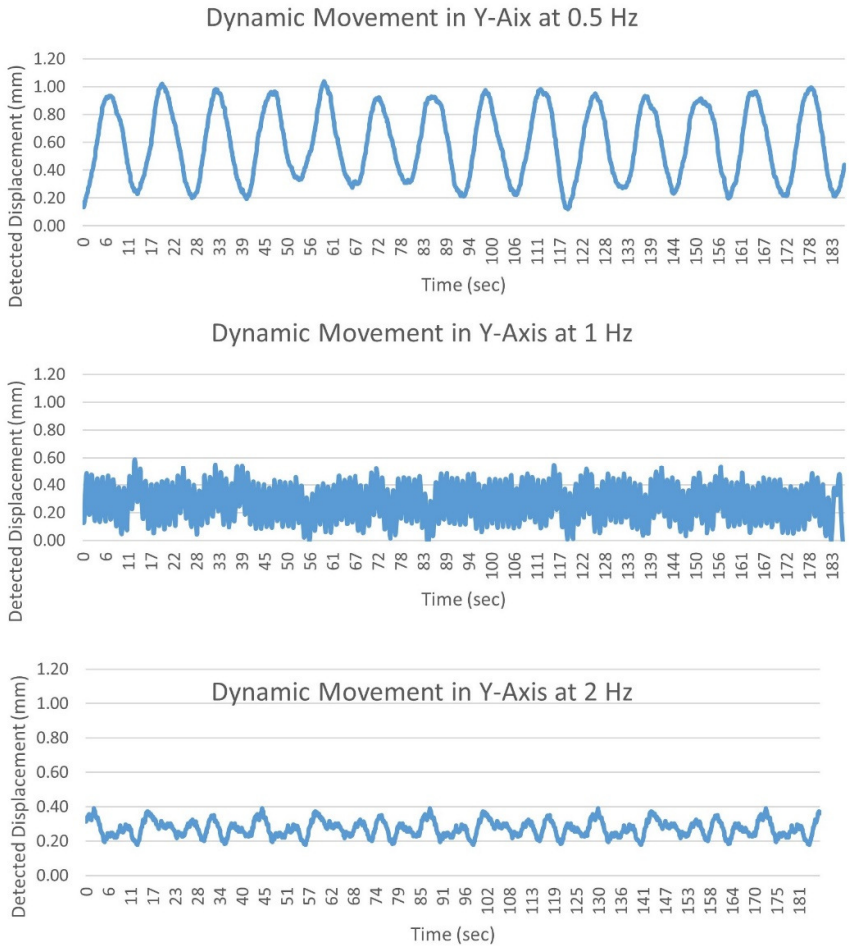

Figure A. 1: System Detection performance at three different frequencies.

Appendix 2: Comparison of Sensor Detection performance when malposition

Figure A.2 highlights that the stem did not align with the magnet i.e. Implant is malposition due to the tilt effect all four sensors have an error in detecting accurately the displacement of the implant. While combining all sensor data i.e. Quad configuration compensated the titling effect and accurately detect the movement with minimum standard deviation error.

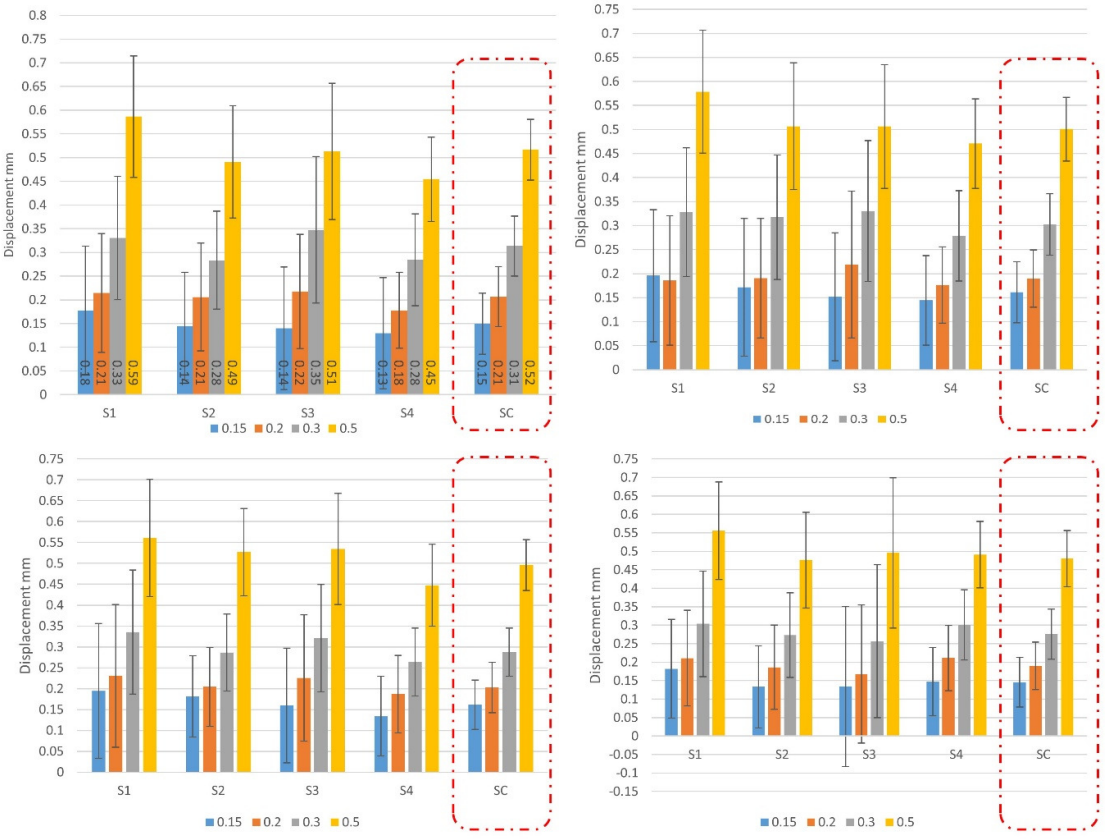

Figure A. 2: Sensor performance in detecting linear movement (0.15,0.20,0.30, and 0.50 mm) offset from the axis.

Appendix 3: Technical drawings of the Humeral Stem.

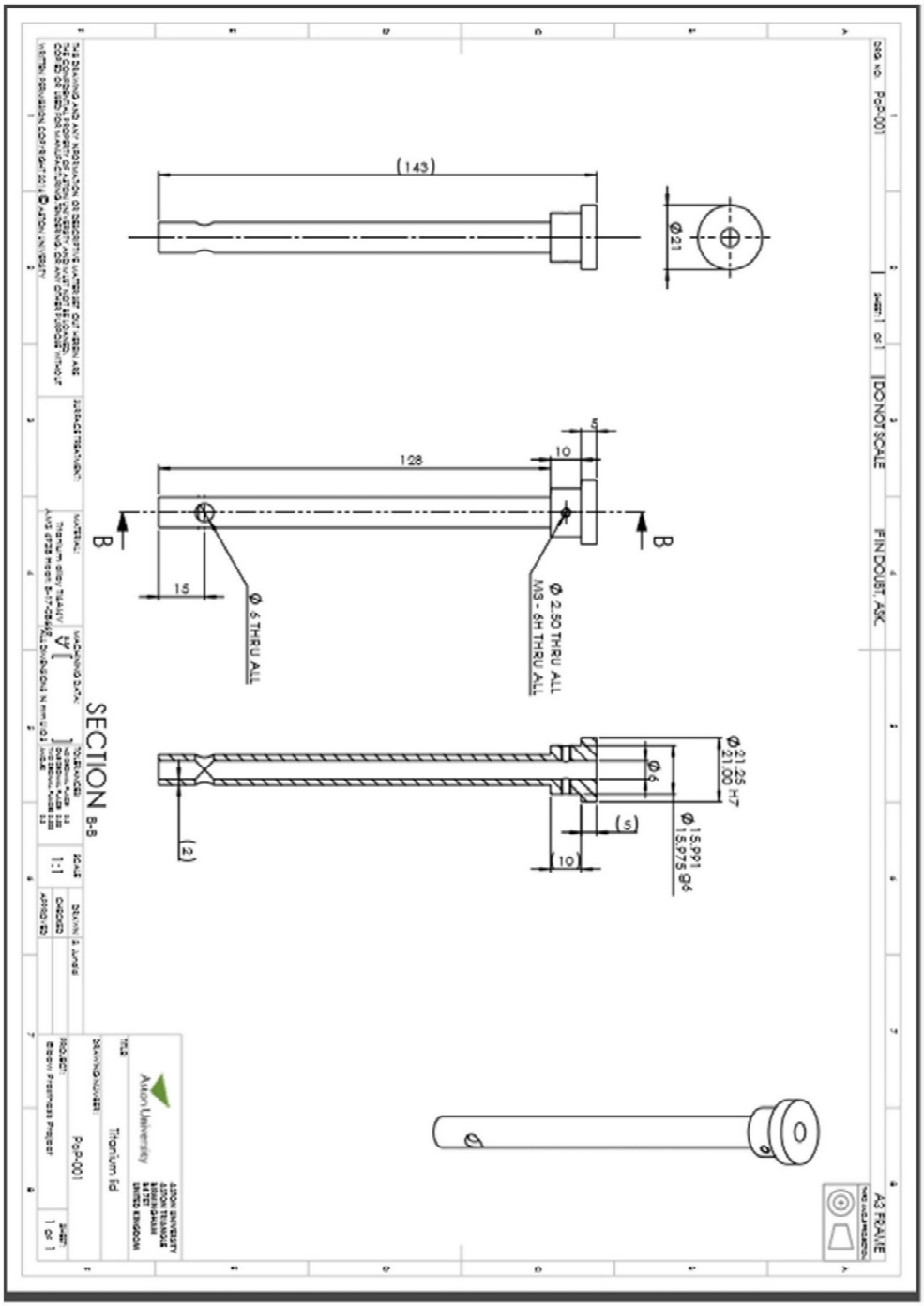

Figure A. 3. Technical Drawing for the Inner Tube of the Humeral Stem.

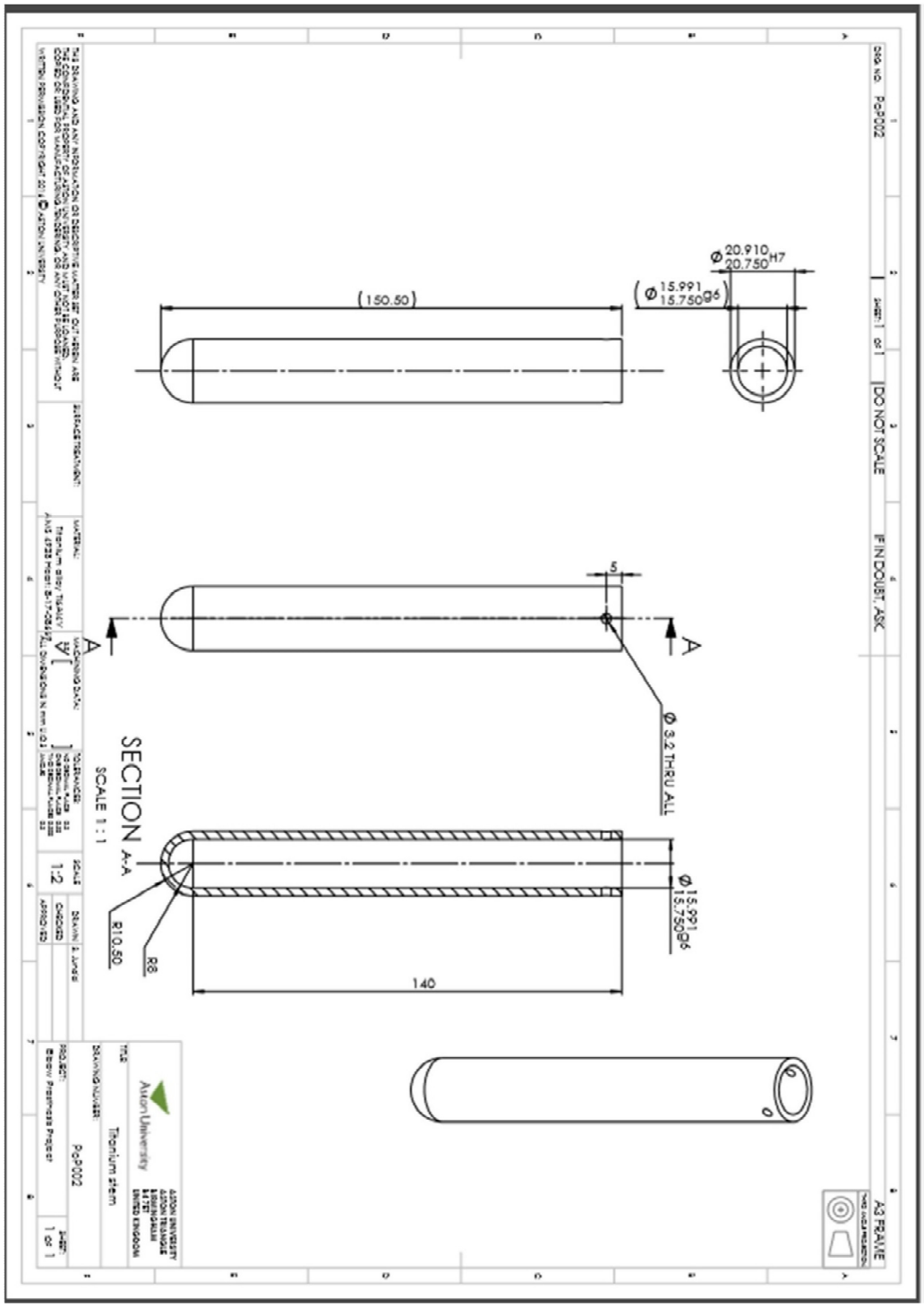

Figure A. 4: Technical Drawing for the Outter shell of Humeral Stem.

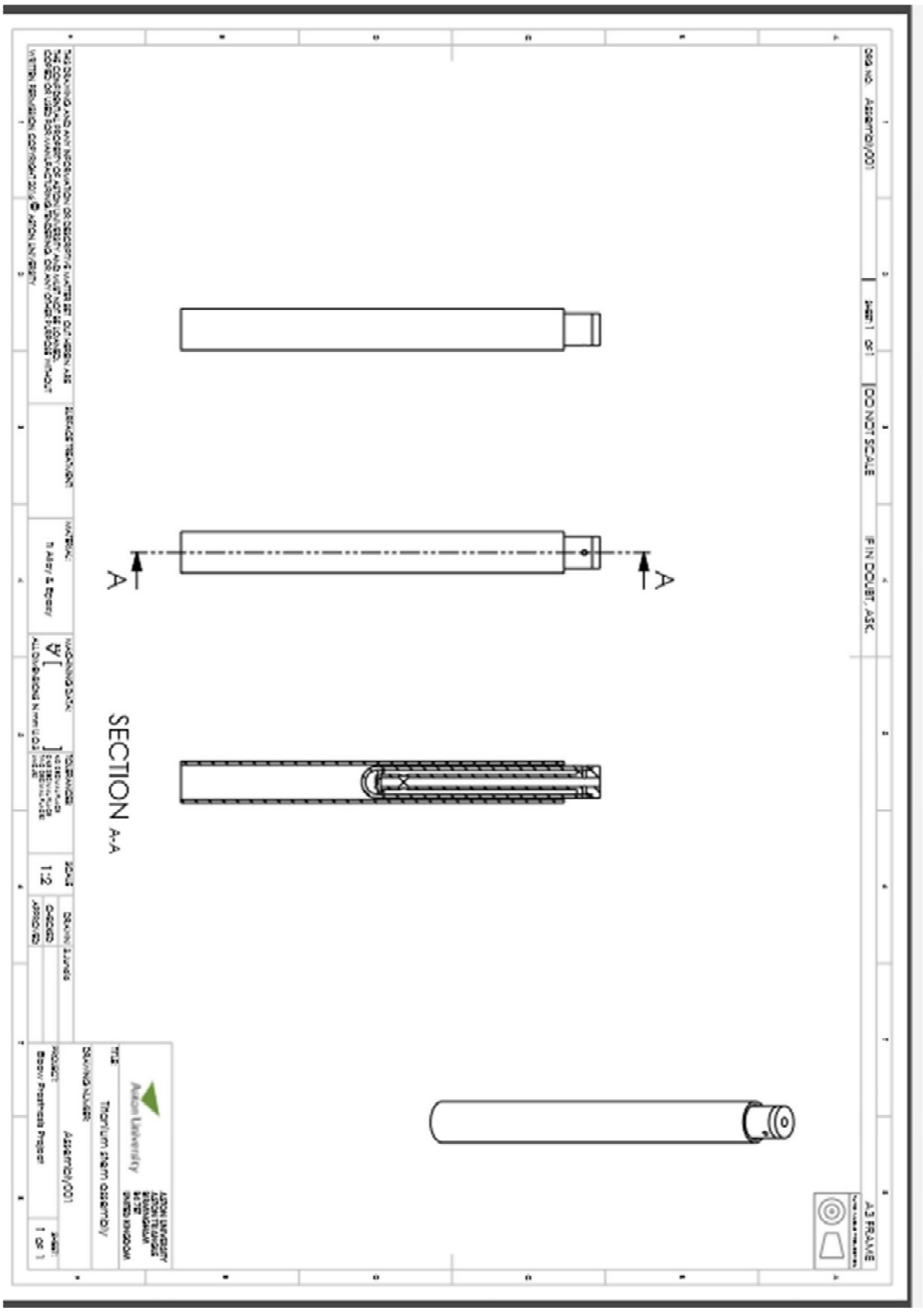

Figure A. 5: Technical Drawing for the Assembly of Humeral Stem

Appendix 3: Orthopaedic Research Society Conference Posters

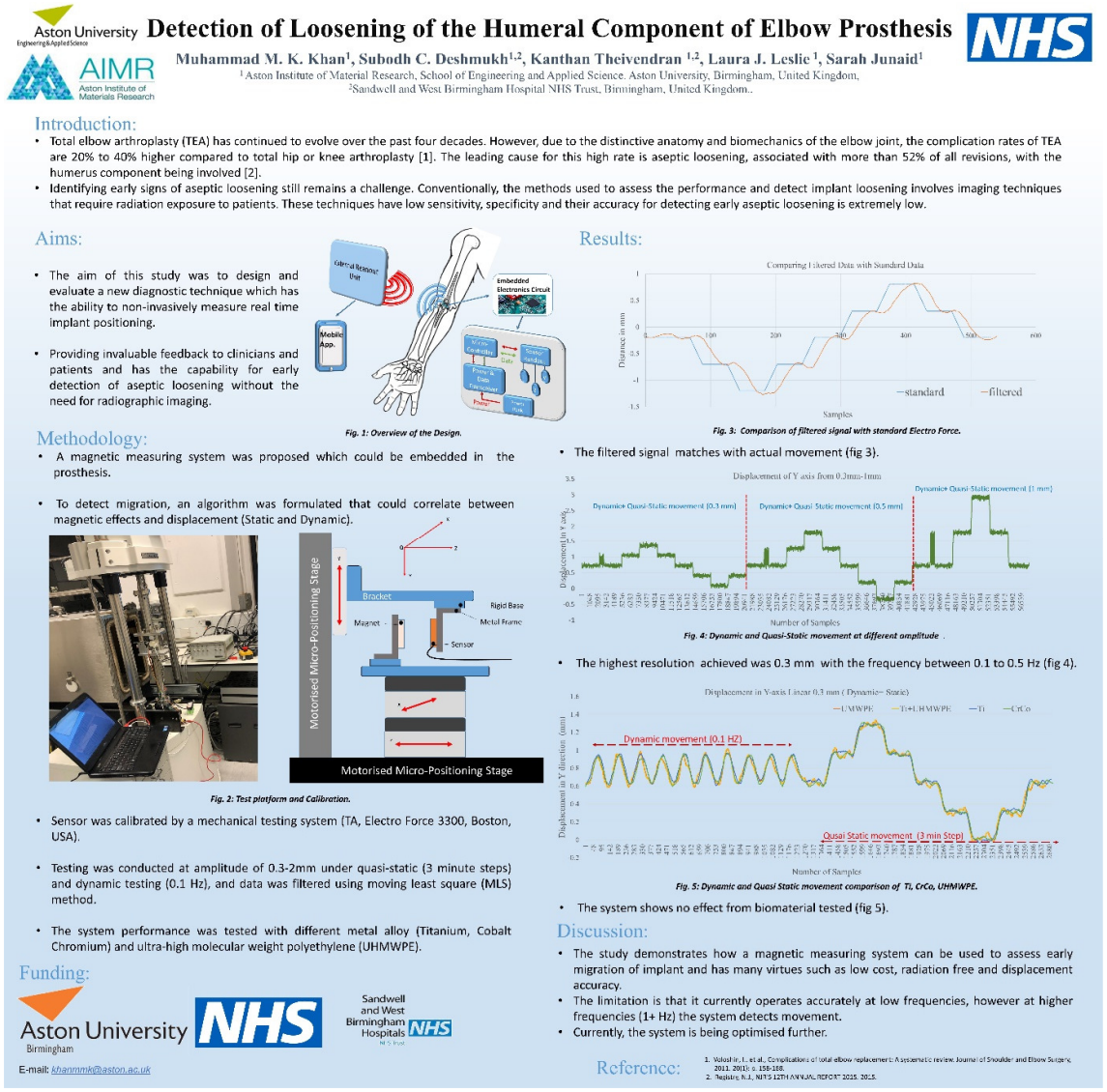

Figure A. 6: ORS Annual Meeting Poster 2019.

Non-Invasive, Non-Radiographic Technique for Detecting Micro-Motion In Total Joint replacement Loosening

Muhammad M. K. Khan[1], Subodh C. Deshmukh[1,2], Kanthan Theivendran [1,2], Laura J. Leslie [1], Sarah Junaid[1]

[1] Aston Institute of Material Research, School of Engineering and Applied Science. Aston University, Birmingham, United Kingdom,
[2]Sandwell and West Birmingham Hospital NHS Trust, Birmingham, United Kingdom..

Introduction:

- Currently, the leading cause of revise surgery in total joint replacement (TJR) is aseptic loosening [1],which not only increases the revision burden but puts patients in emotional and physical trauma[2].

	United Kingdom	Australia	New Zealand	Portugal	Norway	Netherland
THA Primary	996,272	440,841	118,993	4,384	1,902.08	215,380
THA Revision	106,360	57,819	17,348	648	31,515	28,639
Burden %	**9.64**	**11.59**	**12.72**	**12.86**	**14.21**	**11.73**
TKA Primary	1,091,636	544,075	93,963	4,110	81,861	201,454
TKA Revision	68,233	48,502	7,390	278	7,501	19,045
Burden %	**5.88**	**8.18**	**7.29**	**6.33**	**8.39**	**8.63**
TSA Primary	30,841	29,068	8,250	111	7,707	10,174
TSA Revision	3,480	3338	637	9	754	1,104
Burden %	**10.13**	**10.30**	**7.16**	**7.5**	**8.91**	**9.78**
TEA Primary	2,884	2738	515	13	867	508
TEA Revision	820	536	35	1	451	221
Burden %	**22.13**	**16.37**	**6.36**	**7.14**	**34.21**	**30.31**

Fig. 1: Revision Burden of different joint arthroplasty at various nation wide arthroplasty registries.

Objectives

- Investigate the use of magnetic fields and magnetic sensors to accurately monitor implant migration.
- Test the effect of biomaterials used in TJR and different migration parameters i.e. static, dynamic, linear and angular.

Methodology:

- A magnetic measuring system was proposed which could be embedded in the commercially available implant.
- To detect migration, an algorithm was formulated that could correlate between magnetic effects and displacement (Static and Dynamic).

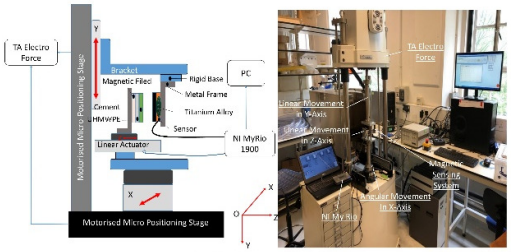

Fig. 2: Test platform and Calibration.

Funding:

Aston University Birmingham
Sandwell and West Birmingham Hospitals NHS

E-mail: khanmmk@aston.ac.uk

Results:

- Calculated displacement (Fig.3), showed good correlation with the actual movement.
- System was able to detect single axes movement (Fig.3) along with multiple axes movement (Fig.4).

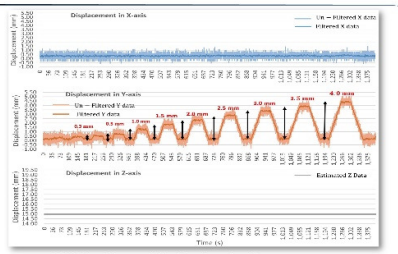

Fig. 3: Linear Movement in Y-axis keeping other axis movement constant

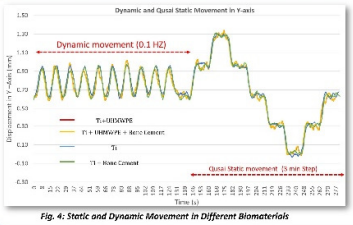

Fig. 4: Static and Dynamic Movement in Different Biomaterials

- System was able to detect both static and dynamic movement (Fig.4) with the resolution of 0.3 mm.
- There was negligible effect of biomaterials on the proposed system (Fig.4).

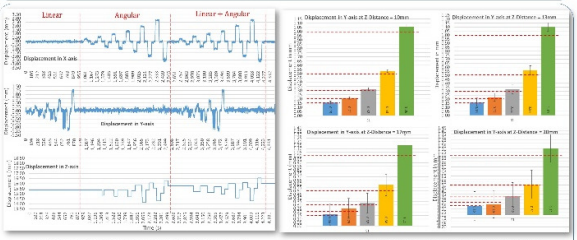

Fig. 5a:Linear and Angular movement in multiple axis

Fig. 5b:Resolution of the sensing system at different Distance

- The system can detect multiple axes movement, along with differentiating between linear and angular movement (Fig.5a)
- With increase of the distance the %error and % standard deviation increases (Fig.5b)

Significance:

- To minimise the revision rate it is necessary to detect early implant migration of the implant > 150 micron.
- This study highlights, that the magnetic measuring system can detect implant migration up to 0.3 mm with the working range.
- With further study, it may to possible to detect much small migration along with reducing the of error with increase in distance.

Reference:

1. Registry, N.J., NJR 5 14T I ANNUAL REPORT 2017
2. Registry, N.J., NJ 5 15TH ANNUAL REPORT 2015. 2015.

Figure A. 7: ORS Annual Meeting Poster 2020.

Appendix 4: LabView Code for Data Retrieving from Magnetic Sensor